BOUNDARY LAYER FLOW OVER DIRECTIONAL GROOVED SURFACE WITH SPANWISE HETEROGENEITY

A THESIS SUBMITTED TO THE UNIVERSITY OF MANCHESTER
FOR THE DEGREE OF DOCTOR OF PHILOSOPHY
IN THE FACULTY OF SCIENCE AND ENGINEERING

2019

Fang Xu
School of Engineering
Department of Mechanical, Aerospace and Civil Engineering

Blank page

Contents

Word Count: 49189

List of Tables

List of Figures

Abstract

In this thesis, both vortical structures and the secondary flow in boundary layers over convergent-divergent riblets (C-D riblets) are experimentally studied.

The development of the laminar boundary layer over C-D riblets is studied using dye visualisation and mono-/stereoscopic particle image velocimetry (PIV). C-D riblets are observed to generate a spanwise flow from the diverging line towards the adjacent converging line, leading to a weak recirculating secondary flow in cross-stream planes across the boundary layer which creates a downwelling over the diverging region and an upwelling over the converging region. The fluid inside riblet valleys follows a helicoidal path and it also interacts with the crossflow boundary layer. The boundary layer development over the riblet section is divided into a developing stage followed by a developed stage. With a decreased riblet height at the converging line and a linear spanwise height variation, the intensity of the induced secondary flow over the converging region is significantly reduced, while the flow field characteristics over the diverging region are basically preserved.

The turbulent boundary layers developing over C-D riblets with three different heights of $h^+ = 8$, 14 and 20 are studied in the longitudinal plane and the cross-stream plane. Although a logarithmic region is observed in the velocity profiles, Townsend's outer-layer similarity hypothesis is not valid. The coherent structures over C-D riblets are revealed in three perspectives, including spanwise vortices, vortex packets and uniform momentum zones, which help to obtain new insights into the vortical activities at different scales. While an increased riblet height affects the entire turbulent boundary layer over the converging region, the impact on the diverging region is largely confined within the near-wall region. In the cross-stream plane, a riblet height increase results in a wider downwelling region, a stronger spanwise flow, a narrower upwelling region and a stronger decelerating effect. Overall, the higher C-D riblets generate a more intense secondary flow, and the mechanism of an increasing riblet height is attributed to the greater capability of deeper yawed microgrooves.

Declaration

No portion of the work referred to in this thesis has been submitted in support of an application for another degree or qualification of this or any other university or other institute of learning.

Copyright Statement

Acknowledgements

Firstly, I would love to express my sincere gratitude and appreciation to my PhD supervisors, Professor Shan Zhong and Dr. Shanying Zhang for their strong supports during my entire PhD career. In the past three years, their dedicated and insightful guidance have helped me immensely. Without their hard effort, I cannot have consistent new advances or get problems resolved quickly, or even enter the world of fluid physics. They provide in-depth discussions and detailed revisions on the referred journal papers. They communicate with me sincerely and encourage me to focus on the flow mechanism. I am sincerely grateful to have my excellent PhD supervisors.

I would like to acknowledge the President's Doctoral Scholar Award from the University of Manchester for providing the financial support and a wealth of training courses. My sincere thanks go to the MACE workshops in Pariser Building and George Begg Building. I would not be able to have rigs and conduct experiments smoothly without the warm assistance from technicians including Philip Oakes, Andrew Kennaugh, David Golding, William Storey, Eddie Whitehouse, Brian Clancy, Kevin Totton, Stuart Mcintyre, Ross Holmes, Melanie Ward, et al. A special acknowledgement goes to Timothy Craft who provided valuable remarks and constructive suggestions to my research. I would also like to thank Beverley Knight and Abbie Hicking of my department for their administrative support.

I would like to thank my colleagues past and present: Haiping Tian, Emanuele Spinosa, Ulises Figueroa, Tongbiao Guo, Yuanye Zhou, Qiang Liu, Bo Wen, Jinmiao Guo, Xiaodong Chen, Pengcheng Quan, Huan Zhao, etc., for their support and our friendship. The discussions among us greatly broaden my horizon and provide insights to my researches.

I express my deepest gratitude to my family members, to my parents (Shanyu Xu, Chun Zhang), parents-in-law (Yushun Li, Yuhong Xie) and other close relatives. It is very challenging being away from the family to pursue a PhD career abroad. I cannot thank them enough for their understanding, support and encouragement all through my

life. Although I am not good enough at this stage, I am trying to do better and make greater contributions to mankind.

Finally, I would like to thank my wife, Li Li, for her love and caring towards me. Although we are separated at almost two ends of the planet, me at the University of Manchester and she at the University of Melbourne, we believe firmly that we can overcome difficulties and successfully fulfil our PhD candidatures.

Symbols and Abbreviations

Latin symbols

$A_{\Delta U}$ (ms^{-1})	amplitude of induced velocity
A_{ω_y} (s^{-1})	amplitude of vorticity
A_g (m^2)	groove cross section
B (1)	log-law constant
H_r (m)	roughness element height
H_y (m)	wall-normal height
h (m)	riblet height
h_p (m)	riblet protrusion height
K (1)	acceleration parameter
L (m)	length of riblet section
L_x (m)	streamwise length scale
L_z (m)	spanwise width
l (m)	streamwise length
N (1)	number of PIV snapshots
N_{UMZ} (1)	number of uniform momentum zones
p_{up} (1)	probability of common-flow-up event
R (1)	spatial correlation function
Re_θ (1)	momentum thickness Reynolds number
Re_τ (1)	friction Reynolds number
Re_l (1)	Reynolds number based on streamwise length
S (m)	spanwise spacing
s (m)	riblet spacing
s_x (m)	riblet spacing projected in x direction
s_z (m)	riblet spacing projected in z direction
TIU (m^2s^{-1})	total induced velocity
Tu (1)	turbulence intensity

t_{UMZ} (m)	thickness of uniform momentum zones
U_∞ (ms^{-1})	freestream velocity
U_c (ms^{-1})	convection velocity
u (ms^{-1})	streamwise velocity
v (ms^{-1})	wall-normal velocity
W (m)	width of riblet section
$W_{\Delta U}$ (m)	width of converging/diverging region
W_x (m)	streamwise width
W_r (m)	high roughness strip width
w (ms^{-1})	spanwise velocity
w_c (m)	riblet crest width
w_r (m)	riblet root width
x (m)	streamwise coordinate
y (m)	wall-normal coordinate
y_d (m)	zero-plane displacement
z (m)	spanwise coordinate

Greek symbols

α (1)	inclination angle
γ (1)	riblet yaw angle
ΔU (ms^{-1})	difference in time-averaged streamwise velocity
δ (m)	boundary layer thickness ($99\%U_\infty$)
θ (m)	boundary layer momentum thickness
κ (1)	von Kármán constant
Λ (m)	riblet wavelength
λ_{ci} (s^{-1})	swirling strength
ν (m^2s^{-1})	kinematic viscosity
Π (1)	population density of vortices
σ (1)	standard deviation
ω_x (s^{-1})	vorticity in y-z plane
ω_y (s^{-1})	vorticity in x-z plane
ω_z (s^{-1})	vorticity in x-y plane

Superscript

$+$	normalisation in wall units

$'$	fluctuating component

Subscript

p	prograde vortex
r	retrograde vortex
ref	reference point of correlation origin
rms	root mean square
s	smooth wall

Other symbols

$\lvert\cdot\rvert$	absolute value
$\rightarrow$	vector
–	ensemble average
~	dispersive component
$\langle\cdot\rangle_\Lambda$	secondary-flow-scale spatial averaging
$\langle\cdot\rangle_r$	roughness-scale spatial averaging

Abbreviations

C-D riblets	convergent-divergent riblets
CL	converging line
DL	diverging line
DNS	direct numerical simulation
DV	dye visualisation
FP	flat plate
HMP	high momentum pathway
HWA	hot-wire anemometry
LDA	laser Doppler anemometry
LES	large eddy simulation
LMP	low momentum pathway
OFI	oil film interferometry
POD	proper orthogonal decomposition
PIV	particle image velocimetry
PSP	pressure-sensitive paint
p.d.f.	probability density function
sPIV	stereoscopic particle image velocimetry

TNTI	turbulent/non-turbulent interface
TSP	temperature-sensitive paint
UDV	ultrasonic Doppler velocimetry
UMZ	uniform momentum zone

Chapter 1

Introduction

1.1 Motivation

In the past few decades, the drag reduction on flight vehicles have received extensive attention in the aviation industry. For a civil or commercial transport aircraft, approximately 50% of the total drag in cruise is contributed by the skin friction drag [134]. Therefore, a reduction in the skin friction drag would contribute to a lower fuel consumption and a larger maximal total range, which are associated with the direct operating costs for airlines. In *Flightpath 2050 Vision* formulated by the Advisory Council for Aviation Research and Innovation in Europe (ACARE), the European Commission (EU) predicted that air traffic will increase by about 4.8% each year [82]. Therefore, the International Air Transport Association (IATA) has taken an ambitious goal in reducing CO_2 emissions, i.e. a reduction of the net aviation CO_2 emissions by 50% by 2050 relative to the 2005 levels. By 2050, *Flightpath 2050 Vision* aims to achieve a 90% reduction in NO_x emissions and a 65% reduction in the perceived noise [82]. To achieve these challenging goals, novel flow control techniques may be adopted by the new generation of aircraft.

The boundary layer flow is a common wall-bounded flow, which can be further divided into the laminar boundary layer and the turbulent boundary layer. The laminar boundary layer is steady and can be characterised by the theoretical Blasius solution. In contrast, the turbulent boundary layer is composed of a hierarchy of coherent structures of different scales. These coherent structures are related to Reynolds stresses and the turbulence kinetic energy, determining the velocity profile and the wall-shear stress. The turbulent boundary layer at a low or moderate Reynolds number is populated by

hairpin vortices. The hairpin vortices are typically composed of one or two streamwise-aligned legs connected to a spanwise-oriented head with the same rotation sense as the mean shear. Hairpin vortices are typically grouped together in an orderly manner to form vortex packets, which are at boundary-layer scale and inclined downstream. At high Reynolds numbers, superstructures with streamwise length scales an order of magnitude larger than the boundary layer thickness can be observed in the turbulent boundary layer.

The skin friction drag originates from the moving fluid adjacent to the wall surface due to the no-slip condition. The flow control strategies aiming to reduce the skin friction drag can be classified into two categories including laminar flow control and turbulent drag reduction. Laminar flow control intends to delay the transition and maintain a longer section with laminar state. This is achieved by mitigating adverse pressure gradients or damping the disturbance modes leading to instability. However, at high Reynolds numbers or over high roughness surfaces, laminar flow control strategies are not applicable. In the turbulent flow, some commonly applied drag reduction techniques are the suction/blowing, the adjustment of fluid viscosity, the suppression of near-wall cycles of streamwise streaks and the modification of large-scale streamwise vortices. Flow control strategies can be classified as active and passive, depending on whether or not additional energy is added to the flow field. At the present time, the active flow control strategies are in some sense less desirable in engineering applications considering the added system complexity.

The surface pattern of longitudinal (streamwise-aligned) riblets, as a promising passive flow control technique, has been applied to reduce the wall-shear stress without introducing excessive form drag. The optimal drag reduction can reach approximately 10% for longitudinal blade riblets [15]. The drag reduction mechanism of longitudinal riblets is attributed to the dampened near-wall turbulence fluctuations inside riblet grooves and over riblet crests [125]. However, considering the production and maintenance costs, longitudinal riblets have not been applied on the wall surface of a civil or commercial transport aircraft at the current stage [139]. By improving the riblet coating technique and reducing maintenance costs, longitudinal riblets may be used commercially in the future [140].

Besides spanwise homogeneous longitudinal riblets, the directional grooves can be arranged heterogeneously in the spanwise direction. Based on the surface patterns observed on certain parts of shark skin, Koeltzsch et al. [79] proposed the surface pattern

of convergent-divergent riblets (C-D riblets). C-D riblets are composed of spanwise alternating left-yawed and right-yawed riblet grooves, and this surface pattern is capable of inducing large-scale perturbations in the entire boundary layer without introducing excessive form drag [79, 72]. The generation of the large-scale secondary flow makes C-D riblets inherently different from longitudinal riblets. The relatively smaller form drag makes C-D riblets more likely to be applied in engineering applications than conventional vortex generators. It is envisaged that C-D riblets may be adopted in future engineering applications in the aspects of drag reduction, separation inhibition and heat transfer augmentation. To date, there have been some research on the flow field characteristics and the drag reduction effect in the wall-bounded turbulent flow over C-D riblets [115, 113, 25, 73, 72]. However, the flow topology in the laminar boundary layer over C-D riblets and inside riblet valleys is still unknown. There is no study on the effects of C-D riblets on the characteristics of coherent structures including hairpin vortices, hairpin packets and uniform momentum zones.

1.2 Aims and objectives

The following study aims to experimentally investigate the characteristics of laminar and turbulent boundary layers over C-D riblets. The main objectives of the PhD project are as follows:

- To reveal the flow topology of both micro-scale and large-scale vortical structures in the laminar boundary layer, and to study the effects of changing riblet wavelength.
- To examine the effects of spanwise height variations in the laminar boundary layer over C-D riblets.
- To investigate the effects of C-D riblets on the secondary flow and vortical structures in the turbulent boundary layer, and to study the effects of changing riblet height.

1.3 Methodology

To fulfil these objectives, a series of experiments are conducted in the PhD project, including:

- Dye visualisation and mono-/stereoscopic particle image velocimetry (PIV) measurements in laminar boundary layers over C-D riblets with different riblet wavelengths.
- Mono-PIV measurements in laminar boundary layers over C-D riblets with spanwise height variations.
- Mono-/stereoscopic PIV measurements in turbulent boundary layers over C-D riblets with different riblet heights.

1.4 Publication list

- F. Xu, S. Zhong, and S. Zhang. Vortical structures and development of laminar flow over convergent-divergent riblets. *Physics of Fluids*, 30(5):051901, 2018.
- F. Xu, S. Zhong, and S. Zhang. Vortical structures of laminar boundary layer over convergent-divergent riblets with spanwise height variations. In *21st Australasian Fluid Mechanics Conference*, Adelaide, Australia, 2018.
- F. Xu, S. Zhong, and S. Zhang. Statistical analysis of vortical structures in turbulent boundary layer over directional grooved surface pattern with spanwise heterogeneity. *Physics of Fluids*, 31(8):075100, 2019.
- F. Xu, S. Zhong, and S. Zhang. Secondary flow in turbulent boundary layer over directional grooves with spanwise heterogeneity.

1.5 Thesis structure

This thesis is to be presented in the *Journal Format* which has its result context provided in the format of several journal and conference papers, following the guidance of the *'Presentation of Theses Policy'* of University of Manchester. An inclusion of these papers highlights the author's contributions to the field of directional grooves with spanwise heterogeneity (C-D riblets). All academic papers to be presented in this thesis were written by the author, under the guidance of the main supervisor, Professor Shan Zhong, and the secondary supervisor, Dr. Shanying Zhang. A detailed description of the author's contribution will be presented at the beginning of each result chapter.

Chapter 2 reviews the literatures which are related to the project. We incorporate brief reviews on four important topics, including coherent structures, longitudinal riblets, C-D riblets, and surface patterns with spanwise heterogeneity. The progress of coherent structures in wall-bounded flow is summarised. Advances in research on riblet surfaces including longitudinal riblets and C-D riblets are presented. Some representative studies of different types of surface patterns with spanwise heterogeneity are introduced.

Chapter 3 overviews the research methodologies including the experimental apparatus and measurement techniques, including the water flume and flat plate facilities, riblets parameters and manufacturing, dye visualisation experiment, PIV setups and processing, and validation of baseline smooth-wall boundary layers.

Chapter 4 presents results on vortical structures and the development of laminar boundary layer over C-D riblets using dye visualisation and mono-/stereoscopic particle image velocimetry. The flow topology is proposed and the effect of riblet wavelength is analysed. In the absence of the interference of complex turbulent events, the use of a laminar boundary layer achieves a clearer flow topology, allowing for a better understanding of the associated flow physics to be established.

Chapter 5 discusses the effects of spanwise height variation of C-D riblets on the vortical structures in the laminar boundary layer. The riblet height is reduced in the converging region, which resembles the height distribution of the bird secondary flight feathers.

Chapter 6 analyses the statistical characteristics of vortical structures in turbulent boundary layer over C-D riblets. The effects of riblet height on the characteristics of vortical structure is also revealed by studying three different heights of $h^+ = 8$, 14 and 20. Several features of vortical structures, such as the population of spanwise vortices, the spatial correlation function and uniform momentum zones, are studied using mono-PIV measurements in the longitudinal plane.

Chapter 7 relates to the turbulent secondary flow in the cross-stream plane over C-D riblets with three different heights. Stereoscopic PIV measurements are conducted in the cross-stream plane. A categorisation of surface patterns with spanwise heterogeneity is also proposed by synthesising two previous classification methods.

Chapter 8 summarises the main findings of the above-mentioned studies and proposes some suggestions for future work.

Blank page

Chapter 2

Literature Review

To provide a better understanding of the results presented in the thesis, related literatures are reviewed in the following four aspects:

- Coherent structures
- Longitudinal riblets
- Convergent-divergent riblets
- Spanwise heterogeneous surface patterns

2.1 Coherent structures

In the early stage, turbulence was considered as a random phenomenon which originates from the sensitivity of the fluid to the initial and boundary conditions. However, from multiple flow visualisation experiments, it was noticed that the vortical structures in the wall-bounded turbulent flow are not completely random [78]. The progress of turbulent flow knowledge is mainly due to the understanding of coherent structures. Robinson [133] defined coherent structures as *"a three dimensional region of the flow over which at least one fundamental flow variable (velocity component, density, temperature, etc.) exhibits significant correlation with itself or with another variable over a range of space and/or time that is significantly larger than the smallest local scales of the flow"*. Coherent structures are defined operatively, i.e. by describing the method through which the structure is identified and isolated. For instance, the velocity field obtained by particle image velocimetry (PIV), conditional sampling or proper orthogonal decomposition (POD) can be applied to identify coherent structures. Adrian [3] and

Smits et al. [137] proposed that coherent structures can be classified into the following categories:

1. near-wall cycle of streamwise vortices,
2. horseshoe/hairpin vortices,
3. large scale motions,
4. very large scale motions.

Coherent structures play a fundamental rule in producing Reynolds stresses and turbulence kinetic energy and determining the velocity profile and wall-shear stress. In this section, coherent structures of different length scales in the canonical wall-bounded turbulent flows are reviewed, including zero-pressure-gradient boundary layer, channel and pipe.

2.1.1 Near-wall cycle of streamwise vortices

Streamwise vortices are also referred to as streamwise streaks or low-speed streaks. They are the spanwise alternating high and low-speed strips which exist in the region very close to the wall surface. The early researches on the near-wall cycle of streamwise vortices were primarily advanced by two research groups, one led by Kline from Stanford University and the other led by Brodkey from Ohio State University.

Kline et al. [78] conducted a seminal work on the near-wall streamwise streaks using hydrogen bubble flow visualisation technique. In the near-wall region, spatial- and temporal-dependent coherent motions were first discovered and termed as 'low-speed streaks'. Due to vortex stretching, the low-speed streamwise streaks tend to gradually lift up, oscillate and consequently break up into smaller structures [see Figure 2.1]. The burst is defined as the oscillation and breakup of the uplifted streamwise streaks which transport the low-speed fluid to the outer layer [78]. The streamwise length is about 1000 in viscous wall units, and the spanwise spacing between two adjacent streaks is around 100 in viscous wall units. The evolution of these streamwise streaks was referred to by later researchers as the near-wall cycle of streamwise vortices. The mechanisms of formation and breakup of streamwise streaks are shown in Figure 2.2. There exists an inherent breakup frequency, i.e. a linear relationship between the bursting frequency and the wall-shear stress expressed using the friction velocity U_τ.

Corino & Brodkey [33] applied flow visualisation using colloidal particles and a high-speed camera to investigate the streamwise vortices in the turbulent pipe flow.

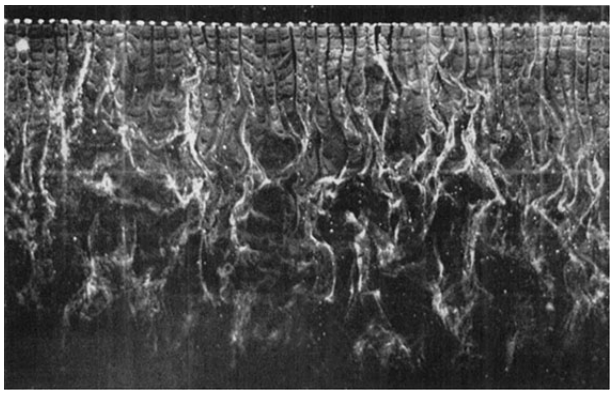

Figure 2.1: Flow visualisation of streamwise streaks using hydrogen bubble technique (Kline et al. [78]).

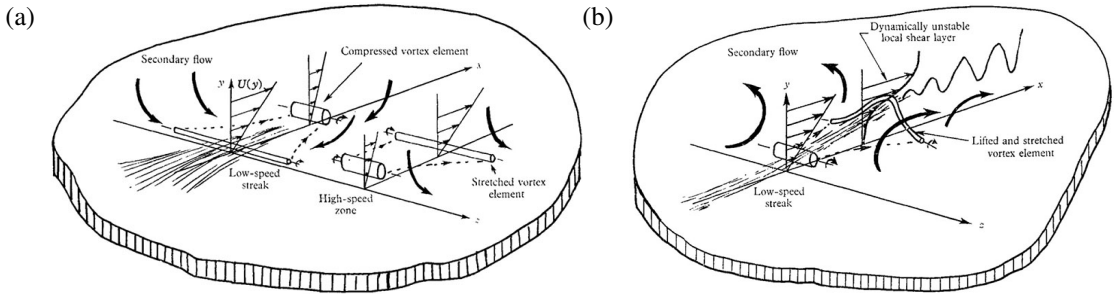

Figure 2.2: The proposed mechanisms of (*a*) formation, (*b*) breakup of low-speed streaks (Kline et al. [78]).

The bursting of low-speed streamwise streaks lifts up the fluid, giving rise to ejection events. Corino & Brodkey [33] related the ejection to the local deceleration and subsequent acceleration of the fluid [see Figure 2.3a]. The ejection events account for around 20% of total time and contribute to 70% of total turbulence production (Reynolds shear stress). The sweep events, in which the high-speed fluid in the outer region is brought down towards the wall, were identified for the first time [see Figure 2.3b].

Kim et al. [74] applied hydrogen-bubble visualisation and hot-wire anemometry to investigate the boundary layer. Essentially all the turbulence production occurs during the bursting events at $0 < y^+ < 100$. The association between the bursting events and the instantaneous inflectional instability of velocity profile is revealed. The instability triggers the ejection events, while the sweep events produce stabilising effects on the local fluid and re-establish low-speed streaks. The bursting is modelled and divided into the following three stages:

1. lifting of low-speed streak, forming an inflexional instantaneous velocity profile,

2. rapid growth of an oscillation motion downstream of the inflexional zone,

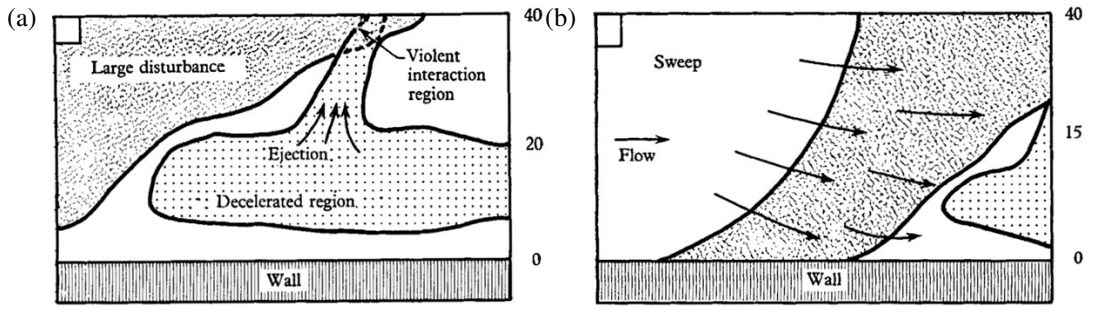

Figure 2.3: Schematic of (*a*) ejection event, (*b*) sweep event (Corino & Brodkey [33]).

3. more chaotic fluctuations (breakup) and then return to the mean velocity profile shape.

Wallace et al. [158] applied hot-film probes to investigate the turbulence production process in the fully developed channel flow. At $y^+ \approx 15$, there is a positive contribution of 70% from the ejections and sweeps respectively, while the interaction between them has a negative contribution of -40%.

Lu & Willmarth [88] applied a cross-wire probe to measure the fluctuating velocity components u' and v'. These velocity components are partitioned into a Cartesian plot of u' versus v'. The ejections are associated with $Q2$ events ($u' < 0$, $v' > 0$), while the sweeps are associated with $Q4$ events ($u' > 0$, $v' < 0$). These $Q2$ and $Q4$ events were found to be the primary contributors to the Reynolds stress.

Offen & Kline [116] conducted dye visualisation and hydrogen bubble measurements to study the interaction between the near-wall streaks and the fluid in the logarithmic region. The lift-up is intrigued by the disturbance which originates in the logarithmic region, while such disturbance is related to the interaction of the earlier upstream bursting with the fluid in the logarithmic region. Based on these findings, the near-wall cycle was proposed for the first time and termed as 'circulatory motions'. The regenerative process was described as *"the interaction between bursts and the flow in the logarithmic region produces sweeps which, in turn, influence the generation of bursts farther downstream"*. The near-wall cycle is self-sustaining since the low-speed streamwise streaks are formed and maintained autonomously from the dynamics of boundary layer.

Later on, Offen & Kline [117] proposed a model of the 'bursting cycle' which incorporates both ejection and sweep events. The above-mentioned three stages in bursting [74] are summarised as one type of flow structure, i.e. the stretched and uplifted vortices mentioned by Kline et al. [78]. The coherent motions in the outer

region are driven by the small-scale near-wall vortices. Kline et al. [78] mentioned that *"the turbulence processes near the wall are due to nearby interactions; they are not driven directly by the large-scale motions which are observed as 'bulges' in the superlayer"*.

Blackwelder & Kaplan [17] proposed the variable interval time-averaging (VITA) technique to detect bursting. This technique applies a discriminator based on $u'_{rms}(t) > k\overline{u'_{rms}}$, where *rms* indicates the root mean square and k is a threshold parameter which is larger than 1. The bursting period was observed to scale with inner variables.

Praturi & Brodkey [124] proposed a different driving mechanism from that proposed by Offen & Kline [117]. The outer region transverse motions are considered to be the driving force for the small-scale near-wall motions. The proposed mechanism of the interaction between incoming high-speed fluid in the outer region and the low-speed near-wall fluid is shown in Figure 2.4.

Jiménez & Pinelli [69] studied the turbulent channel at moderate Reynolds numbers of $Re_\tau = 201$, 428 and 633. The near-wall turbulence production process is observed to sustain even without any input from the core flow [see Figure 2.5]. The artificial numerical manipulations of the outer flow were observed to have little effect on the near-wall turbulence production process. The wall serves to provide the mean shear, but it is not directly linked to the turbulence generation. This finding is in direct contrast to the other studies which suggest a coupled dynamic process between the near-wall and outer regions. It is expected that there is a competition among different mechanisms for near-wall turbulence production, and the auto-generation process overwhelms the others at these moderate Reynolds numbers.

The generally accepted regeneration process of the near-wall cycle is shown in Figure 2.6. For high Reynolds number flows, Marusic et al. [93] summarised that the structures which modulate the near-wall cycle have not been fully identified, and the interaction mechanisms may vary at different Reynolds numbers.

2.1.2 Hairpin vortices

The hairpin/horseshoe vortices, which play a key role in the turbulence production and transportation, are prevalent in the turbulent boundary layer [133]. A hairpin vortex is typically composed of either one or two streamwise-aligned legs connected to a spanwise-oriented head which has the same rotation as the mean shear [3]. Some of the studies which contribute to a deeper understanding of hairpin vortices are reviewed.

Theodorsen [145] first proposed the schematic of hairpin/horseshoe vortices and

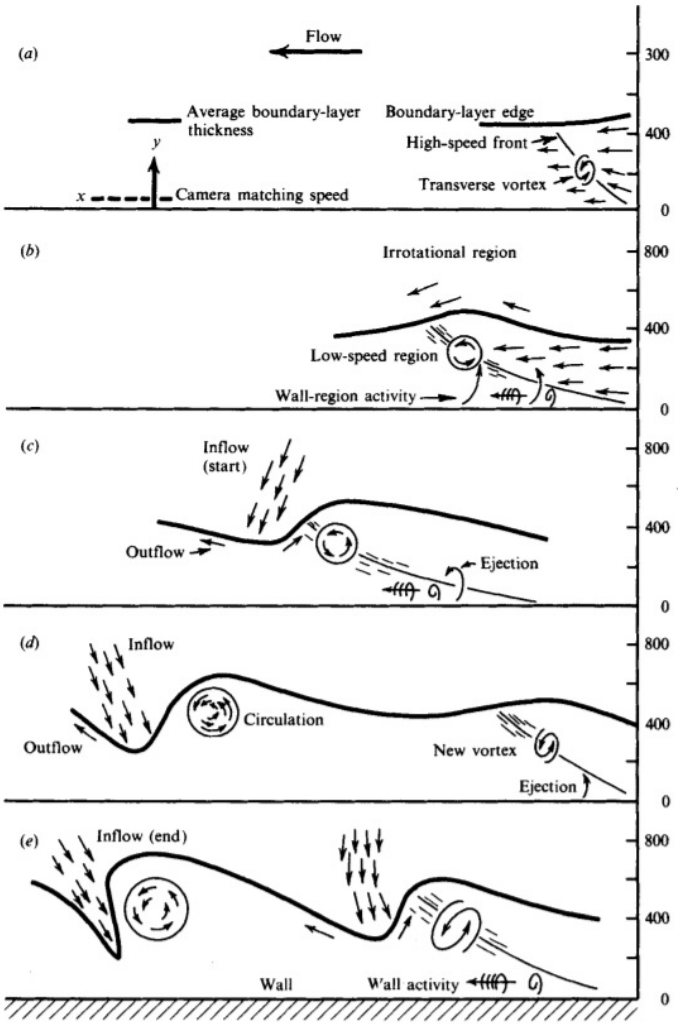

Figure 2.4: Schematic of interaction mechanism between fluid in the outer region and near-wall motions (Praturi & Brodkey [124]).

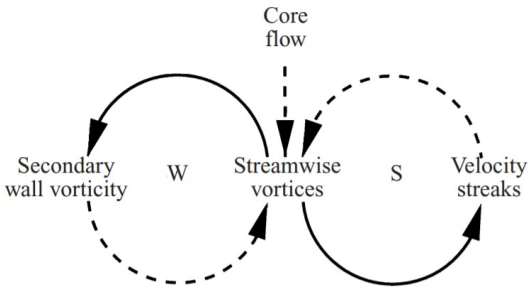

Figure 2.5: Schematic of the proposed auto-generation mechanism for turbulence production in the near-wall region (Jiménez & Pimelli [69]).

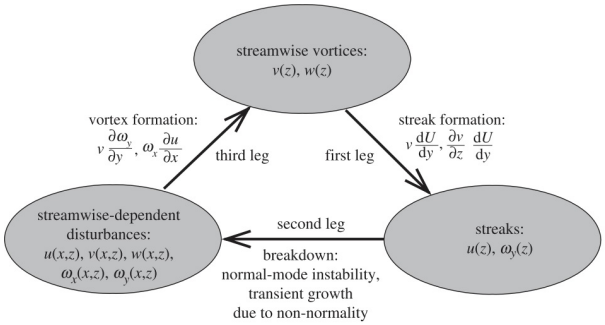

Figure 2.6: Schematic of self-sustaining process of near-wall turbulence structures (Kim [75]).

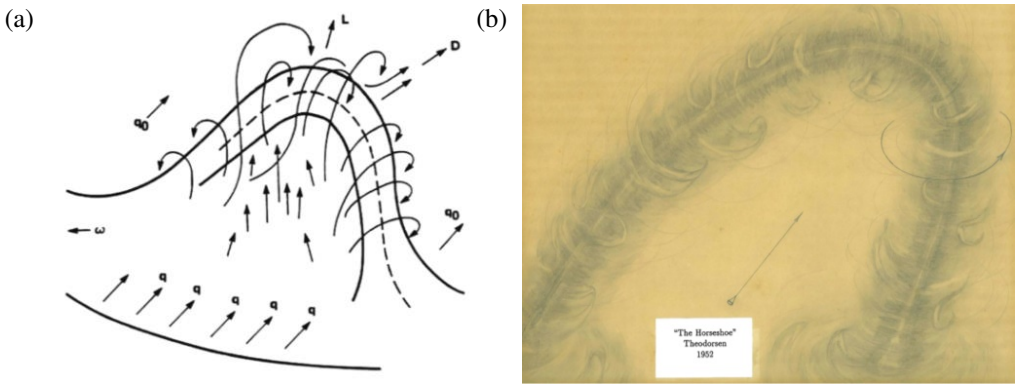

Figure 2.7: (*a*) Aroused hairpin in the near-wall region, (*b*) vortices in the shape of hairpin (Theodorsen [145]).

considered these structures as the building blocks of the turbulent flow. The proposed schematic of hairpin vortices is shown in Figure 2.7. Later on, Townsend [148, 149] proposed the attached eddy hypothesis, which assumed the streamwise-elongated double-coned vortex which is attached to the wall. Figure 2.8 shows the schematic of Townsend's attached vortices. Some researchers believe that the horseshoe/hairpin vortex and the attached eddy are essentially the same structure, with attached eddy viewed as headless horseshoe [119].

One compelling evidence of the existence of hairpin vortices was provided by Bandyopadhyay [12] and Head & Bandyopadhyay [57]. In their experiments, an inclined light sheet was applied to visualise hairpin vortices in the turbulent boundary layer with $500 < Re_\theta < 17500$. The 45° inclined hairpin vortices are produced in a regular sequence, and the hairpin heads form an interface with an angle of around 20° to the wall surface [see Figure 2.9]. Figure 2.10 reveals the effects of Reynolds number (Re) on the shapes of vortex structures in the turbulent boundary layer, revealing different degrees of stretching. At very low Re, the vortices are less elongated and termed

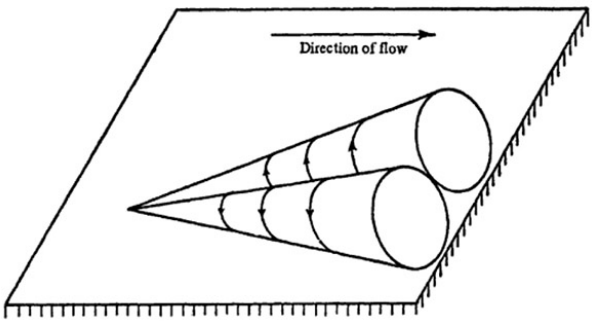

Figure 2.8: Schematic of attached eddy (Townsend [149]).

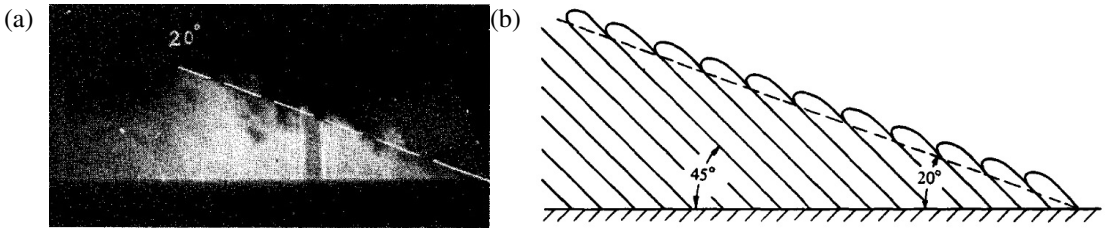

Figure 2.9: (*a*) Flow visualisation image of turbulent boundary layer at $Re_\theta = 14500$, with crossflow from right to left (Bandyopadhyay [12]). (*b*) Schematic of hairpin vortices which are inclined at 45° to the wall surface (Head & Bandyopadhyay [57]).

as 'vortex loops'. As *Re* increases, the vortices are elongated along the streamwise direction, and these stretched vortices are termed as 'horseshoe vortices' or 'vortex pairs'.

Perry et al. [123] observed the Λ-shaped vortex structures downstream of a vibrating trip wire, as shown in Figure 2.11. The turbulent spot was suspected to be composed of an array of Λ-shaped vortices. These Λ-shaped vortices in the turbulent spot are similar to the hairpin vortices in the turbulent boundary layer [57].

Moin & Kim [102] and Kim & Moin [76] investigated the existence of hairpin

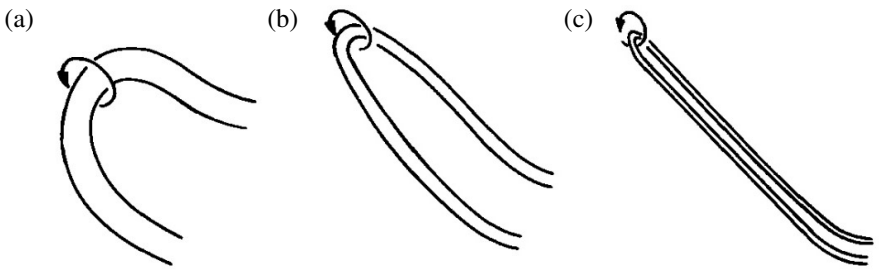

Figure 2.10: Effect of Reynolds number (*Re*) on features of hairpin vortex in the outer region at (*a*) very low *Re*, (*b*) moderate *Re*, (*c*) high *Re* (Head & Bandyopadhyay [57]).

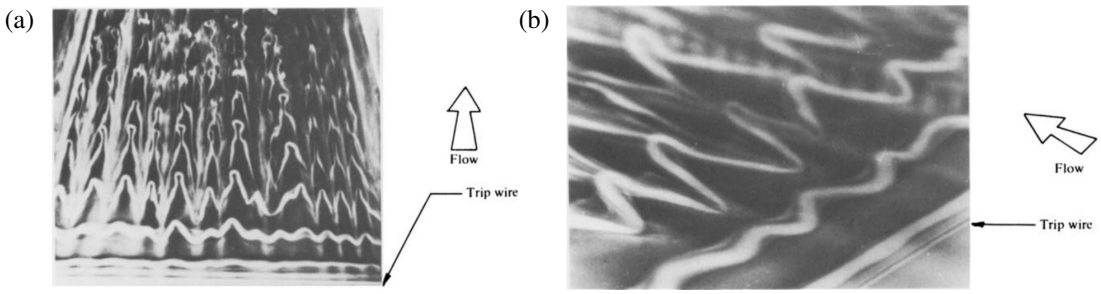

Figure 2.11: Smoke visualisation of Λ-shaped vortices in (*a*) front view, (*b*) perspective view (Perry et al. [123]).

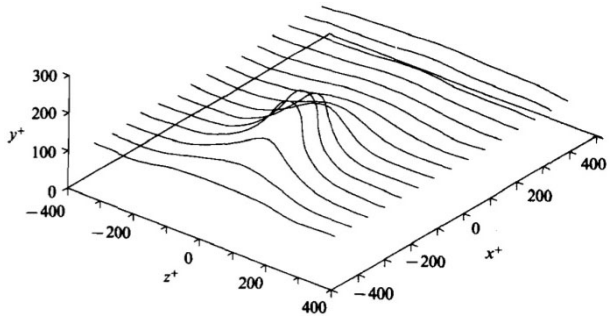

Figure 2.12: Vortex lines in turbulent channel indicating existence of hairpin vortices (Kim & Moin [76]).

vortices in the turbulent channel flow using large eddy simulation (LES) and direct numerical simulation (DNS). This work, at an early stage, demonstrates the importance of numerical simulation in understanding fluid physics. The 45° inclined hairpin vortices are identified by the vortex lines, as shown in Figure 2.12. These well-organised vortical structures are generated from the roll-up of sheets of transverse vorticity and associated with the bursting process.

Acarlar & Smith [1, 2] examined the development of hairpin vortices produced by hemispherical protrusions or fluid injection. The hairpin vortex patterns observed in the turbulent boundary layer were also obtained in these experiments which introduce perturbations to the developing laminar boundary layer. For the hemisphere perturbation [1], two types of vortices were generated, with standing vortices formed at the upstream stagnation point and hairpin vortices in the wake region of the hemisphere [see Figure 2.13]. Measurements using hot-film anemometry further indicate that the velocity profile in a distance downstream of the hemisphere protuberance is remarkably similar to the velocity profile in the turbulent boundary layer. The fluid injection was applied to investigate the generation of hairpin vortices [2], which is attributed to the break-up and roll-up of shear layers [see Figure 2.14]. The stretching of horseshoe

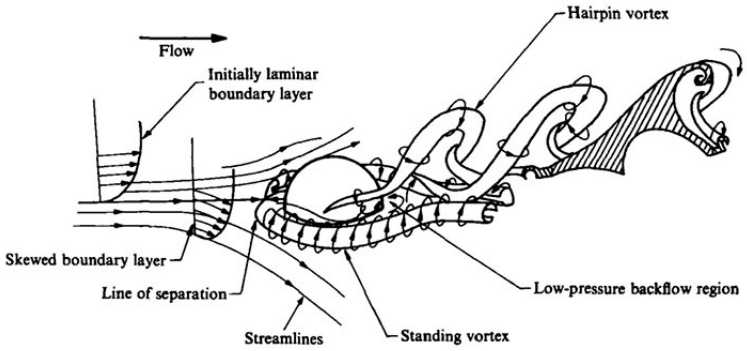

Figure 2.13: Schematic of standing vortex and hairpin vortices generated by hemisphere protrusions (Acarlar & Smith [1]).

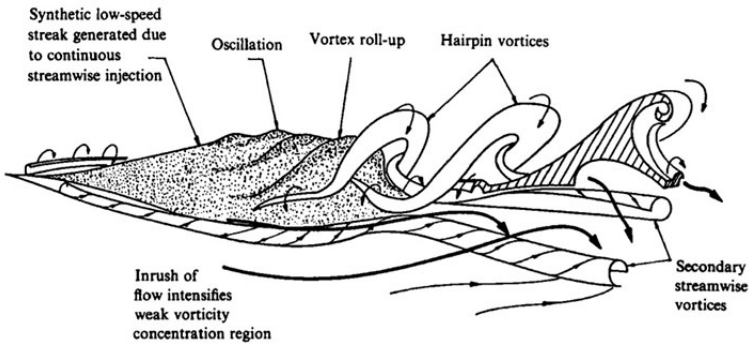

Figure 2.14: Schematic of synthetic low-speed streak breakup generating hairpin vortices (Acarlar & Smith [2]).

vortices by the wall shear layer makes these structures elongated into hairpin vortices. Between the counter-rotating legs of the older hairpin vortex, there exists an accumulation and lift-up of low-momentum fluid as a consequence of lateral pressure gradients, which is observed as low-speed streaks [78]. There is a strong interaction between the primary hairpin vortices and the secondary vortices.

Haidari & Smith [56] examined the generation and growth of single hairpin vortices by controlling the surface fluid injection through a slot. The regeneration process occurs when the injection velocity exceeds the critical value. The new hairpin vortex is produced by both lateral deformation of the vortex lines of older hairpins and viscous-inviscid interaction induced by surface fluid ejection [see Figure 2.15].

Robinson [133] presented a schematic of vortex patterns at different wall-normal distances [see Figure 2.16]. The buffer region is dominated by streamwise vortices, while the wake region is occupied by hairpins vortices. The logarithmic region consists of both hairpins and streamwise vortices. The dynamics of streamwise and hairpin vortices contribute to the turbulence production and momentum transportation between

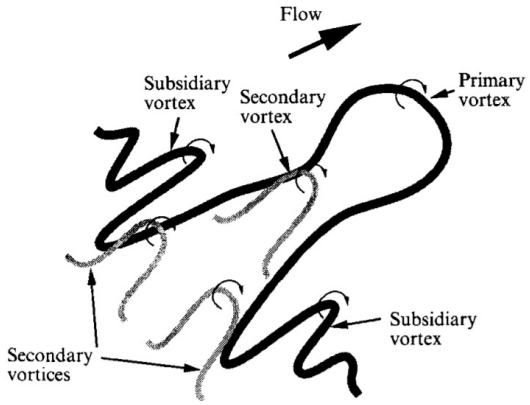

Figure 2.15: Schematic of hairpin vortices hierarchy (Haidari & Smith [56]).

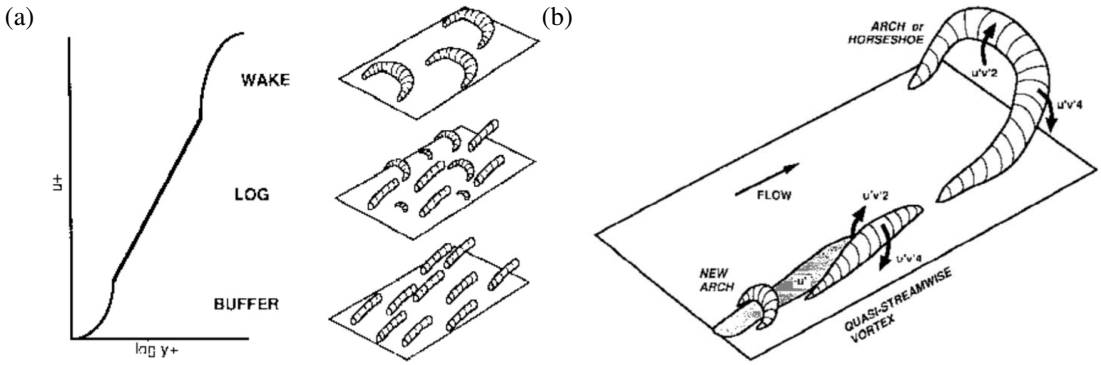

Figure 2.16: (*a*) Idealised schematic of vortical structures for low Reynolds number boundary layers. (*b*) Ejection/sweep motions of streamwise/hairpin vortices in the inner/outer region (Robinson [133]).

the inner layer and the outer layer.

Wu & Moin [167, 168] simulated the genuine spatially developing turbulent boundary up to $Re_\theta = 940$. The instantaneous flow fields in the transitional and turbulent regions are dominated by hairpin vortices [see Figure 2.17]. This study provides the first direct evidence to the dominance of hairpin vortices in the form of the Navier-Stokes equations.

Although hairpin vortices have been extensively observed in turbulent flows at low Reynolds numbers, there is no dominance of hairpin vortices at high Reynolds numbers. Schlatter et al. [136] applied direct numerical simulation (DNS) to study the turbulent boundary layer at $Re_\theta = 4300$. The vortical structures are complex and irregular, with only few hairpin-shaped vortices [see Figure 2.18]. At high Reynolds numbers, the amorphous vortical structures are termed as 'vortex clusters' [see Figure 2.19], which can be further categorised into the wall-attached type and the wall-detached type [39, 68].

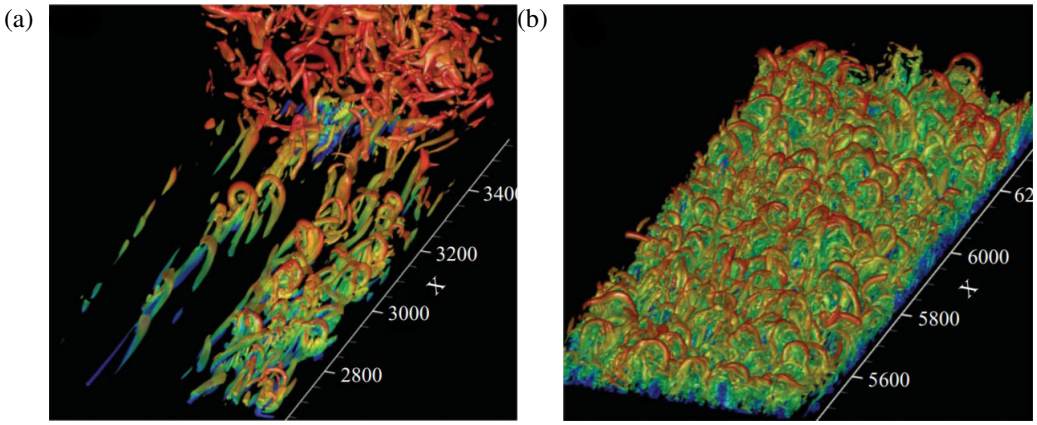

Figure 2.17: Instantaneous vortical structure in (*a*) transitional region at $2625 \leq x/\theta_0 \leq 3562$, (*b*) turbulent region at $5437 \leq x/\theta_0 \leq 6375$, where θ_0 is the inlet boundary layer momentum thickness (Wu & Moin [167]).

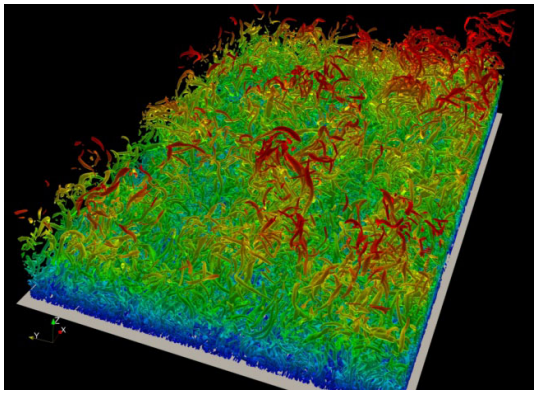

Figure 2.18: Instantaneous vortical structures (λ_2 criterion) in turbulent boundary layer at $Re_\theta = 4300$ (Schlatter et al. [136]).

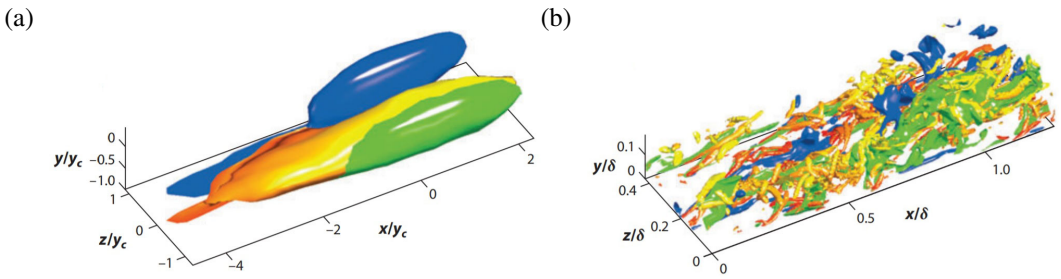

Figure 2.19: (*a*) Structure of the averaged Reynolds shear stress indicating vortex cluster, (*b*) an instantaneous realisation of the same object at $Re_\tau = 934$, where blue and green objects are conditioned on the presence of sweeps and ejections, respectively (Jiménez [68]).

Research	Type of flow	Region of interest	Key observation
Theodorsen [145]	theoretical	single hairpin	propose schematic of hairpin/horseshoe vortices
Townsend [148, 149]	Theoretical	single hairpin	put forth attached eddy hypothesis
Head & Bandyopadhyay [57]	turbulent BL ($Re_\theta = 17500$)	entire BL	strong evidence of hairpin vortices using light sheet
Perry [123]	laminar BL ($Re_\theta = 316-439$)	near-wall region	visualise Λ-shaped stretched horseshoe vortices
Moin & Kim [102, 76]	turbulent channel ($Re_\tau = 180$)	entire channel	LES/DNS revealing 3D structure of hairpin vortices
Acarlar & Smith [1, 2]	laminar channel	near-wall region	hemisphere/fluid inject to generate hairpin vortices
Haidari & Smith [56]	laminar BL ($Re_\theta = 330,440$)	near-wall region	generation of hairpin vortices from perturbation
Robinson [133]	turbulent BL	entire BL	review on multiple types of hairpin vortices
Wu & Moin [167]	turbulent BL ($Re_\theta = 950$)	entire BL	DNS revealing populated hairpin vortices (forest)
del Álamo [39]	turbulent channel ($Re_\tau = 1900$)	logarithmic layer	amorphous structures as 'vortex clusters' at high Re
Schlatter et al. [135]	turbulent BL ($Re_\theta = 4300$)	entire BL	irregular vortices no hairpin dominance at high Re

Table 2.1: List of some representative work on hairpin vortices. The boundary layer is abbreviated as BL.

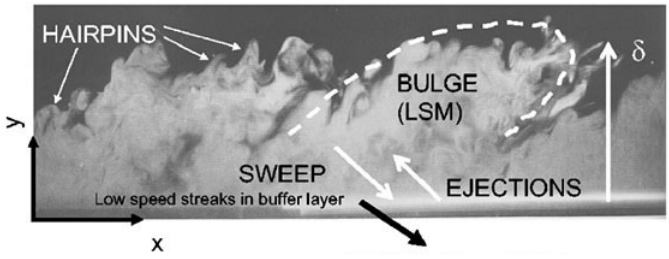

Figure 2.20: Smoke visualisation of vortical structures showing bulges (large-scale motions) in the turbulent boundary layer (Falco [46]).

Table 2.1 summarises the primary contributions of the above-mentioned studies on the understandings of hairpin vortices.

2.1.3 Large-scale motions

Large-scale motions (LSMs) refer to the flow features with length scales comparable to the dominant length scale in the wall-bounded flow (boundary layer thickness, channel height or pipe radius) in the logarithmic layer and the outer layer. By analysing the temporal correlation of the streamwise velocity component downstream of a circular cylinder [53], Townsend [149] first recognised the existence of LSMs in the turbulent flow. In the experiments by Kovasznay et al. [80], Falco [46], Brown & Thomas [21] and Murlis et al. [104], the turbulent bulges having streamwise extent of $2\delta - 3\delta$ and spanwise extent of $\delta - 1.5\delta$ were also observed. The inclined coherent structures in the shape of bulges constitute LSMs [see Figure 2.20]. The irrotational region between two adjacent bulges leads to the intermittency in the turbulent flow.

Meinhart & Adrian [96] conducted PIV measurements in the turbulent boundary layer at $Re_\theta = 6845$. In the outer region, there exist growing zones of relatively uniform streamwise momentum, which are referred to as uniform momentum zones (UMZs). There are usually several vertically aligned UMZs in the turbulent flow.

Zhou et al. [182] applied direct numerical simulation (DNS) to study the formation and evolution of hairpin packets in the turbulent channel flow. When the primary hairpin vortex is above the threshold strength, new hairpin vortices are generated both upstream and downstream of the primary hairpin vortex, and these vortices form a coherent hairpin packet which propagates coherently [see Figure 2.22]. This auto-generation process is believed to be the key aspect in the turbulence generation process. The UMZs are formed by the streamwise alignment of hairpin packets which grow and generate new hairpins as they propagate downstream [182].

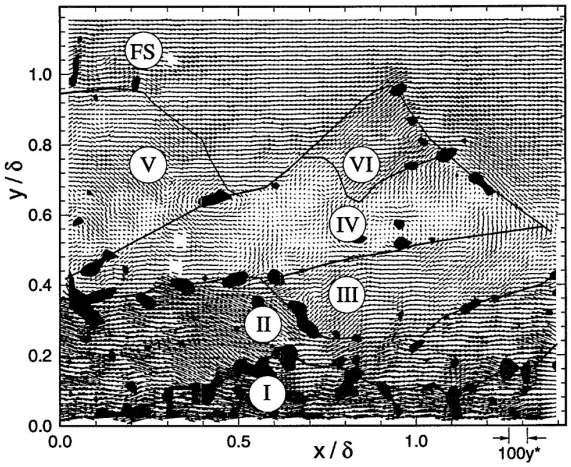

Figure 2.21: Instantaneous velocity field in the turbulent boundary layer with convection velocity of $0.9U_\infty$ subtracted (Meinhart et al. [96]).

Adrian et al. [4] conducted PIV measurements to confirmed that the low momentum streaks which are induced by the streamwise-aligned hairpin packets are recognised as UMZs in the longitudinal plane. The turbulent boundary layer is consisted of young, slowly advecting hairpin packets in the near the wall and old, rapidly advecting packets away from the wall [see Figure 2.23].

There does not exist a simple one-to-one correspondence between UMZs and turbulent bulges [77]. Within one bulge, there may exist several hairpin packets at different stages of growth. The LSMs are generated by a group of hairpin packets travelling at approximately the same convection velocity [10].

2.1.4 Very-large-scale motions/superstructures

Very-large-scale motions (VLSMs), or superstructures, refer to the features with streamwise length scales of $O(10\delta)$, which is larger than the large-scale motions (LSMs) in the logarithmic region of wall-bounded flow. The term 'VLSM' is used when referring to internal flows including pipes and channels, while the term 'superstructure' is used when referring to external flows such as turbulent boundary layers.

Kim & Adrian [77] observed VLSMs in the outer layer of fully developed turbulent pipe. Hairpins are aligned coherently in groups to form long packets, and then these packets are aligned coherently to form VLSMs [see Figure 2.24]. The bimodal distribution in the pre-multiplied spectrum of the streamwise velocity is shown in Figure 2.25. Here, the wave number is pre-multiplied in the spectrum to obtain a logarithmic plot, in which equal areas under the curve correspond to equal energies. The low

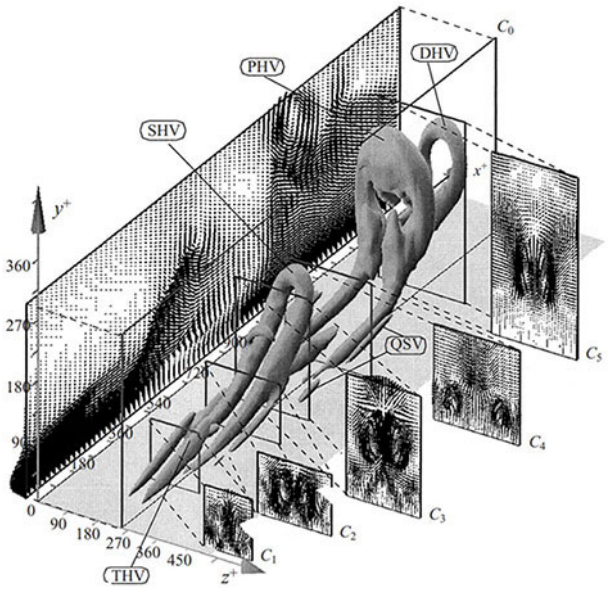

Figure 2.22: The sequence of hairpin vortices including primary hairpin vortex (PHV), secondary hairpin vortex (SHV), tertiary hairpin vortex (THV) and downstream hairpin vortex (DHV) (Zhou et al. [182]).

wave number mode scales with outer variables [see Figure 2.25a], while the high wave number mode scales with inner variables [see Figure 2.25b]. The streamwise length of the VLSMs in the logarithmic layer is around $12 - 14$ times the pipe radius.

Hutchins & Marusic [64] conducted turbulent boundary layer measurement using a spanwise aligned hot-wire rake. The streamwise velocity fluctuations over a certain spanwise range were projected in time through Taylor's hypothesis [144]. The meandering superstructures, which are indicated by the positive and negative streamwise velocity fluctuations, extend over 20δ in the streamwise direction [see Figure 2.26].

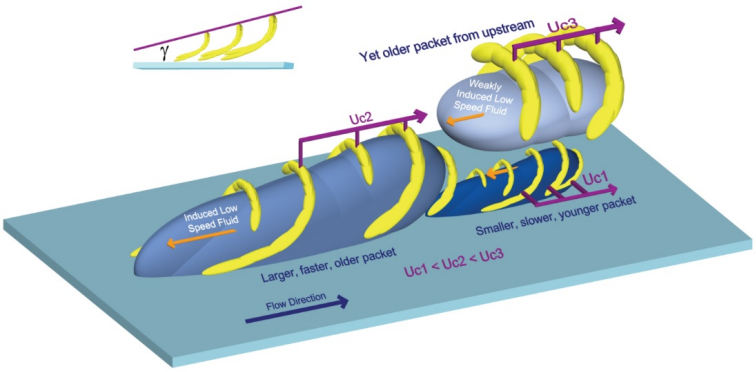

Figure 2.23: Conceptual scenario of hairpin packets and cane-type vortices growing up from the wall (Adrian et al. [4]).

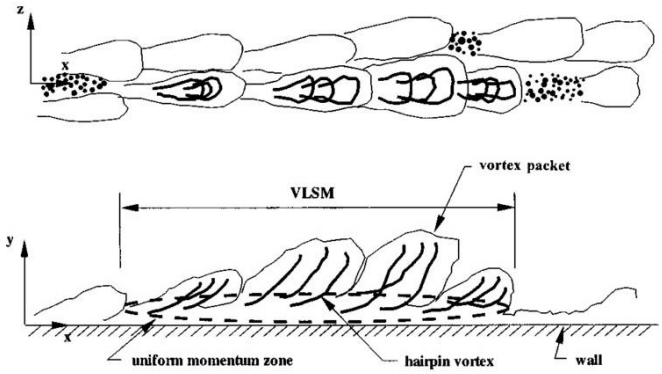

Figure 2.24: Conceptual model of generation of very-large-scale motions (Kim & Adrian [77]).

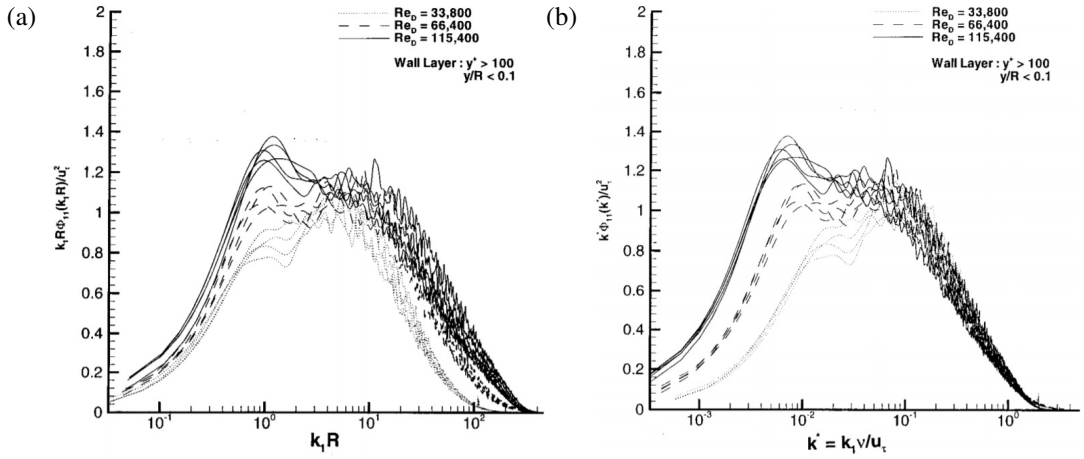

Figure 2.25: Bimodal distribution of the pre-multiplied spectrum with dimensionless using (*a*) inner variables, (*b*) outer variables (Kim & Adrian [77]).

Hutchins & Marusic [64] also revealed the existence of superstructures in the atmospheric turbulent boundary layer at $Re_\tau = 6.6 \times 10^5$ [see Figure 2.27].

Guala et al. [55] revealed the existence the VLSMs with wavelengths of $8R - 16R$ (R is the pipe radius) in the outer region of the fully developed turbulent pipe flow. Half of the turbulence kinetic energy and more than half of the Reynolds shear stress are contained in the energetic VLSMs. Later on, Balakumar & Adrian [10] studied the VLSMs in turbulent channel flows and the superstructures in turbulent boundary layer flows. Figure 2.28 shows the scale separation between the LSMs and the VLSMs (superstructures). In the wall-bounded flow of pipe, channel and boundary layer, the behaviours and mechanisms of VLSMs (superstructures) are considered to be essentially the same. The wavelength of the spectral peak, i.e. the wavelength of VLSMs carrying the highest energy density, is approximately $13h - 15h$ (h is the

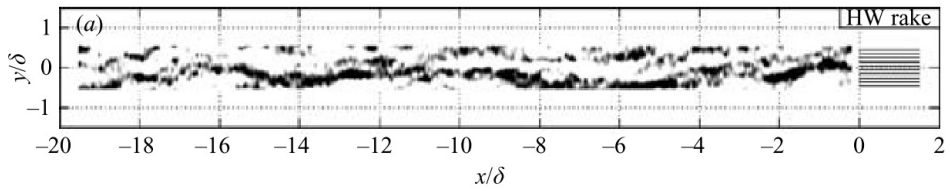

Figure 2.26: Meandering superstructures in the turbulent boundary layer (Hutchins & Marusic [65]).

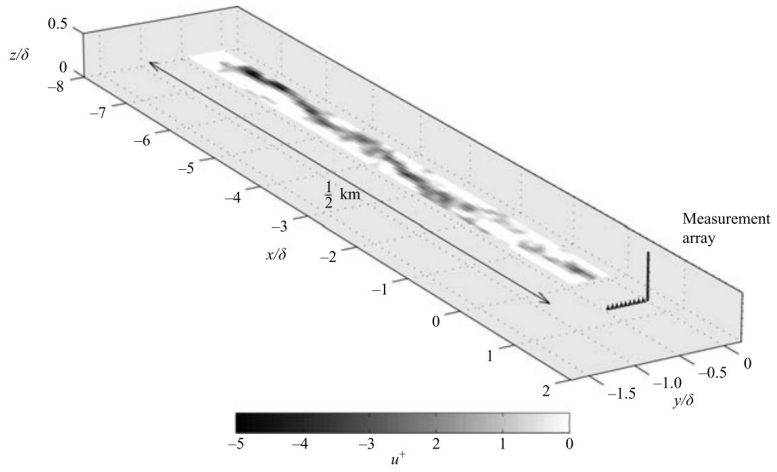

Figure 2.27: Meandering superstructures in the atmospheric turbulent boundary layer (Hutchins & Marusic [65]).

channel height) in the channel flow. The superstructures of $6\delta - 8\delta$ (δ is the boundary layer thickness) in the turbulent boundary layer are shorter than the corresponding VLSMs in the pipe flow and the channel flow.

2.2 Longitudinal riblets

Longitudinal riblets are the microgrooves which are aligned in the streamwise direction [see Figure 2.29]. The longitudinal riblets are a well-known passive drag reduction technique in the turbulent boundary layer. This surface pattern is inspired by the skin of fast-swimming sharks covered with streamwise-aligned corrugated dermal denticles [see Figure 2.30].

In early stages before fully understanding of the drag reduction mechanism, the longitudinal riblets have been applied in engineering applications, e.g. the rowing shell by US rowing team in 1984 Summer Olympic and the hull of challenge boat Stars & Stripes as the best challenger for the America's Cup 87, although it is uncertain

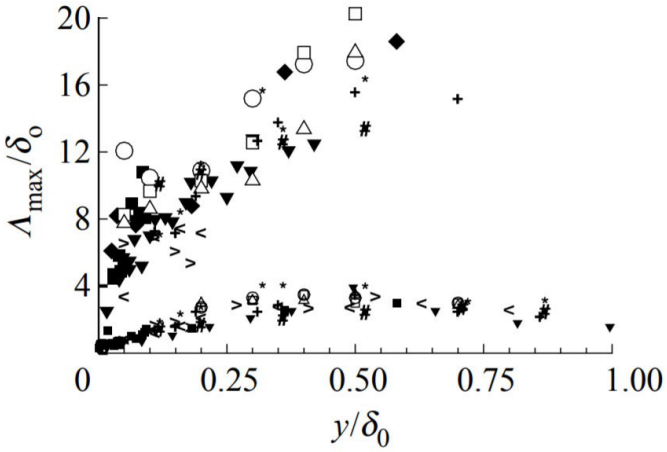

Figure 2.28: Wavelength of the spectral peaks in different wall-bounded turbulent flows of pipe, channel and boundary layer (Balakumar & Adrian [10]).

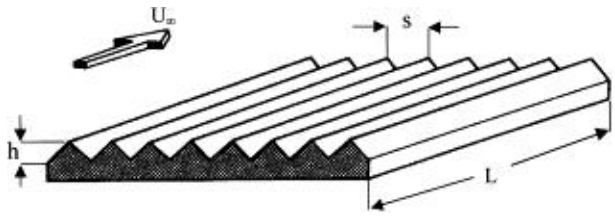

Figure 2.29: Sketch of riblet geometry (Viswanath [155]).

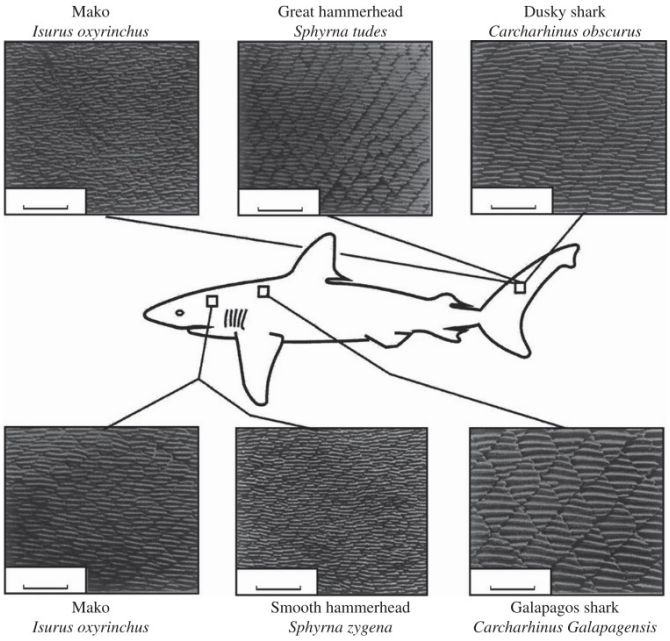

Figure 2.30: Scale patterns on fast-swimming sharks (Dean & Bhushan [38]).

whether longitudinal riblets played any real role [49]. In the aeronautical industry, Coustols & Schmitt applied longitudinal riblets to a complete $1/11$ scale Airbus A320 model [35]. About two-thirds of the wetted model surface was covered by longitudinal riblets, leading to a total drag reduction of up to 1.6% at cruising conditions [131]. The flight test using Airbus A320 with riblet films covering 75% of the wetted surface achieved a similar drag reduction rate as the wind tunnel test [132]. The researchers in Lufthansa placed square patches with longitudinal riblets on the fuselage and leading edge of the wings of two A340-300s aircraft [84]. The reduction in the skin-friction drag is estimated to be more than 1%. Ball [11] estimated that a transparent plastic film with longitudinal riblets helps to reduce the drag of aircraft by up to 8%, which corresponds to around 1.5% fuel saving. However, the direct operative cost including the installation and maintenance of riblets is comparable to the performance benefits, which blocks the potential wide application of these riblets in aeronautics [11, 131]. To date, longitudinal riblets have not been applied to aircraft surfaces in commercial airlines.

2.2.1 Optimisation of riblet parameters

There have been numerous studies on the optimisation of longitudinal riblets in terms of the drag reduction effect [159, 161, 160, 15]. Most of these studies were conducted by changing the riblet spacing s^+ and height h^+ with a changing freestream velocity. Here, the dimensions of riblets are expressed in viscous wall units, i.e. riblet spacing $s^+ = sU_\tau/\nu$ and riblet height $h^+ = hU_\tau/\nu$, where U_τ is the friction velocity and ν is the kinematic viscosity. In most experiments, the force balance is utilised to measure the total wall-shear stress. The difference of the wall-shear stress between longitudinal riblets and the smooth-wall case at similar flow conditions can be applied to determine the drag reduction effect.

The general shape of the drag reduction curve of longitudinal riblets is shown in Figure 2.31. At a small riblet spacing, the drag reduction ratio is proportional to the riblet size, and this region is commonly referred to as the 'viscous' regime. In the viscous regime, the contribution of non-linear terms inside riblet grooves and around riblet crests is negligible [49]. The drag reduction effect saturates as riblets get larger, and the maximum drag reduction occurs as the viscous region 'breaks down'. When the size of riblet teeth further increases, the longitudinal riblets behave as a standard k-type roughness surface, and the drag turns larger than that over the smooth-wall case.

The first systematic study on the drag reduction effect of longitudinal riblets was

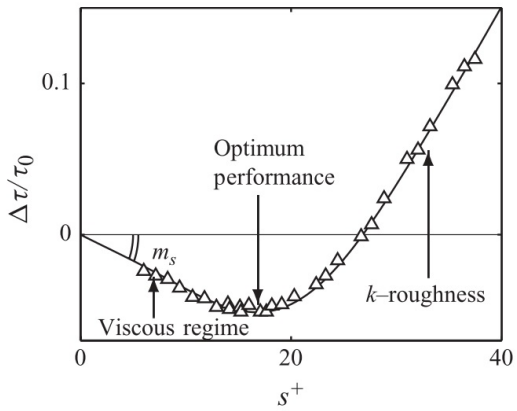

Figure 2.31: Drag reduction ratio of longitudinal sawtooth riblets with 60° peak sharpness as a function of riblet spacing s^+ (García-Mayoral & Jiménez [50]).

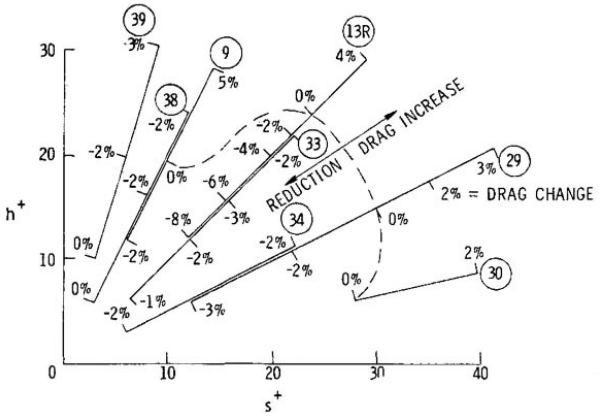

Figure 2.32: Drag reduction effect as a function of h^+ and s^+ for sawtooth riblets (Walsh [161]).

conducted by Walsh [159, 161] and Walsh & Lindemann [160]. The drag reduction effect of sawtooth riblets with various s^+ and h^+ was evaluated in a water towing tank [161]. The maximum drag reduction of 8% is achieved at $h^+ = 10$ and $s^+ = 15$ [see Figure 2.32]. It is observed that the peak curvature of sawtooth riblets has a significant effect on the drag reduction performance. For sawtooth riblets with valley curvature, the maximum drag reduction occurs at $h^+ = 8 - 12$ and $s^+ = 15 - 20$.

Bechert et al. [15] provide a systematic experimental evaluation of the drag reduction effect of longitudinal riblets with different parameters. The drag reduction curves on the right column of Figure 2.33 are replotted using data in Bechert et al. [15]. The triangular riblet teeth [see Figure 2.33a] are considered as a durable shape, with the maximum drag reduction of 5% occurring at $h/s \approx 1$ and $\alpha \approx 60°$. Scallop can refer to any form of concave shape, and thus there does not exist a standard scalloped profile

[see Figure 2.33c]. Ideally, the riblet crest should be thin and sharp, but the scalloped riblets with measurable tip thicknesses also produce favourable results. The scalloped geometry are observed to achieve a maximum drag reduction of 6.5% at $h/s \approx 0.7$. The blade longitudinal riblets [see Figure 2.33e] are observed to achieve a maximum drag reduction of 9.9% at $h/s \approx 0.5$ and $t/s = 0.02$. Although the drag reduction of blade riblets is the most favourable, the low durability of blade teeth should be considered in engineering practice.

Given the shape of longitudinal riblets, the viscous-scaled riblet spacing (s^+) and riblet height (h^+) are often applied to predict the drag reduction ratio. However, it is difficult to compare the drag reduction effect for different riblet shapes. The values of s^+ corresponding to the maximum drag reduction effect have a scatter of around 40% [49]. In order to deal with this problem, García-Mayoral & Jiménez [49] synthesised available datasets and proposed the groove cross section (A_g) which considers the riblet geometry as the geometric parameter. Figure 2.34 shows the definition of the groove cross section A_g. For the longitudinal riblets, the alternative scaling $l_g^+ = \sqrt{A_g^+}$ provides a better collapse of 10% scatter on the data as compared to the riblet spacing s^+, and the maximum drag reduction occurs at $l_g^+ \approx 11$ [see Figure 2.35].

2.2.2 Drag reduction mechanism

Walsh [159, 161] first attributed the drag reduction mechanism of longitudinal riblets to the restricted oscillation and the inhibited growth of low-speed streaks. The near-wall region consists of low- and high-speed streaks [78], and the average lateral spacing of low-speed streaks is approximately 30 in viscous wall units [74]. When the riblet spacing is much lower than the transverse extent of low-speed streaks, the eruption of low-speed streaks is dampened by the longitudinal riblets, leading to reduced wall-shear stress.

Using conformal mapping, Bechert & Bartenwerfer [14] provides a theoretical analysis based on the riblet geometry and the velocity profile. The protrusion height h_p is defined as the distance between the riblet crest and the apparent origin of the time-averaged velocity profile. Since the riblets obstructs the crossflow, the apparent origin of the velocity profile locates between the riblet crest and the riblet valley. The protrusion heights of the longitudinal flow h_{pl} and the spanwise crossflow h_{pc} are shown in Figures 2.36a and 2.36b, respectively. Based on theoretical analysis, Luchini et al. [89] proposed the parameter $\Delta h = h_{pl} - h_{pc}$, which considers the origin difference between the longitudinal flow and the spanwise crossflow. In other work, $\Delta h = h_{pl} - h_{pc}$

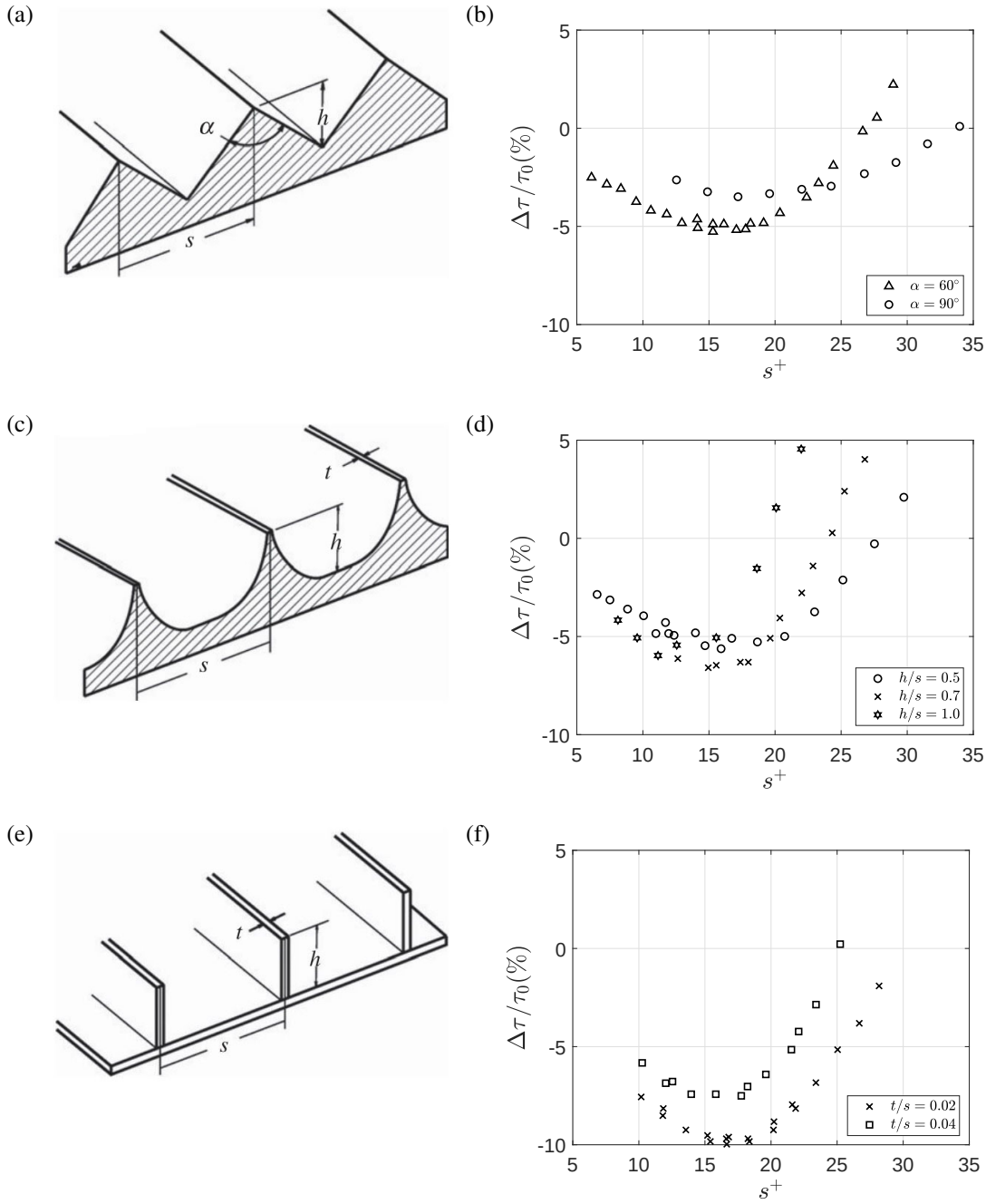

Figure 2.33: Schematic of riblet dimensions and drag reduction ratio for (*a, b*) sawtooth riblets, (*c, d*) scallop riblets, (*e, f*) blade riblets (replot using data in Bechert et al. [15]).

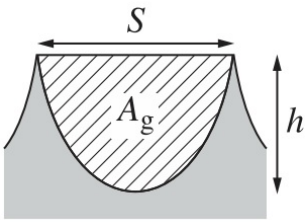

Figure 2.34: Definition of the groove cross section of riblets A_g/s^2 (García-Mayoral & Jiménez [49]).

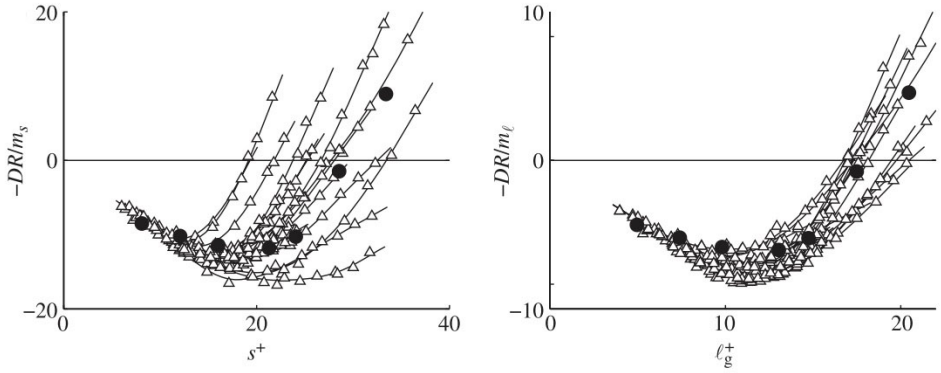

Figure 2.35: Drag-reduction curves of diverse longitudinal riblets, reduced to a common viscous slope as a function of the spacing s^+ (left) and as a function of the square root of the groove cross section l_g^+ (right) (García-Mayoral & Jiménez [49]).

quantitatively indicates the difference of impedance between the longitudinal flow and the spanwise crossflow. When $\Delta h > 0$, i.e. $h_{pl} > h_{pc}$, the viscous dissipation in the spanwise crossflow is higher than that in the longitudinal flow, contributing to lower turbulence fluctuations in the near-wall region.

Pulles et al. [125] conducted measurements in both water channel and wind tunnel facilities using laser Doppler anemometer (LDA) and hot-wire anemometer, respectively. The near-wall turbulence fluctuations over longitudinal riblets are lower than those over the smooth wall [see Figure 2.37]. The decreased turbulence fluctuations in the near-wall region over riblets have been observed in the experiments by Choi [28], Vukoslavčević et al. [157], Park & Wallace [120] and Suzuki & Kasagi [143]. Further analysis on the high-order parameters including the skewness and flatness also reveals that the turbulence fluctuations mainly reside above riblet grooves [157]. The drag reduction effect of longitudinal riblets was attributed to the restricted spanwise movement of streamwise vortices [28], while the deteriorated drag-reducing effect was related to the enhanced turbulent momentum transport [143].

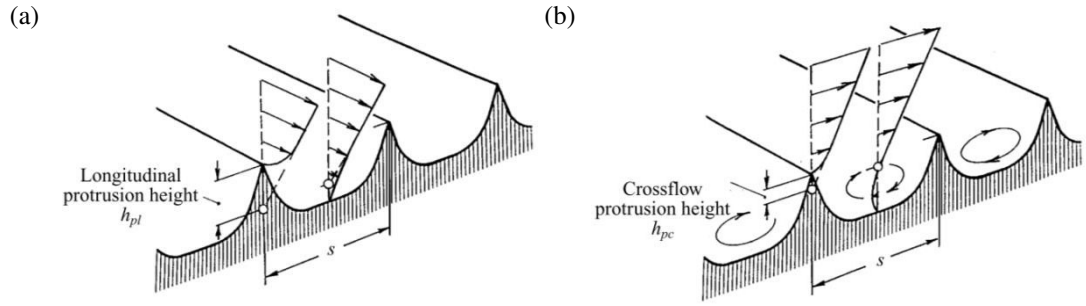

Figure 2.36: Protrusion height of the (a) longitudinal flow h_{pl}, (b) spanwise crossflow h_{pc} over longitudinal riblets (Bechert et al. [15]).

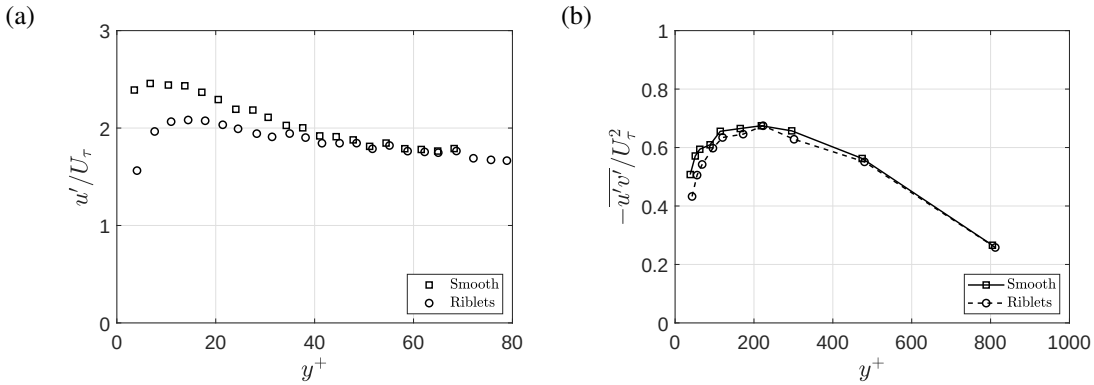

Figure 2.37: (a) Streamwise turbulence fluctuations u' as a function of inner coordinate y^+ in water channel with $U_\infty = 0.14m/s$, (b) Reynolds shear stress $-\overline{u'v'}$ as a function of inner coordinate y^+ in wind tunnel with $U_\infty = 9.8m/s$ (replot using data in Pulles et al. [125]).

Flow visualisation techniques have been applied to investigate the near-wall vortical structures over longitudinal riblets. Using the synchronised smoke-wire technique, flow visualisation images for drag decreasing and increasing cases are shown in Figure 2.38 [85]. For the drag decreasing case, the freestream velocity $U_\infty = 3m/s$ corresponds to a normalised riblet spacing of $s^+ = 25.2$. The spanwise extent of streamwise vortices is larger than the riblet spacing, making these vortices reside above riblets. The turbulence fluctuations in the grooves are relatively small, and only the small areas of the tips experience high shear stress. Besides, the riblets impede the spanwise movement of streamwise vortices. It should be mentioned that the interaction between streamwise vortices and riblet crest leads to the secondary flow. However, the induced secondary flow has a small scale and weak intensity, thus its contribution to the increase in the wall-shear stress is not significant. The wall-shear stress is decreased when the riblet spacing is smaller than the spanwise extent of streamwise vortices. For the drag increasing case, the higher freestream velocity $U_\infty = 5m/s$ leads to a larger

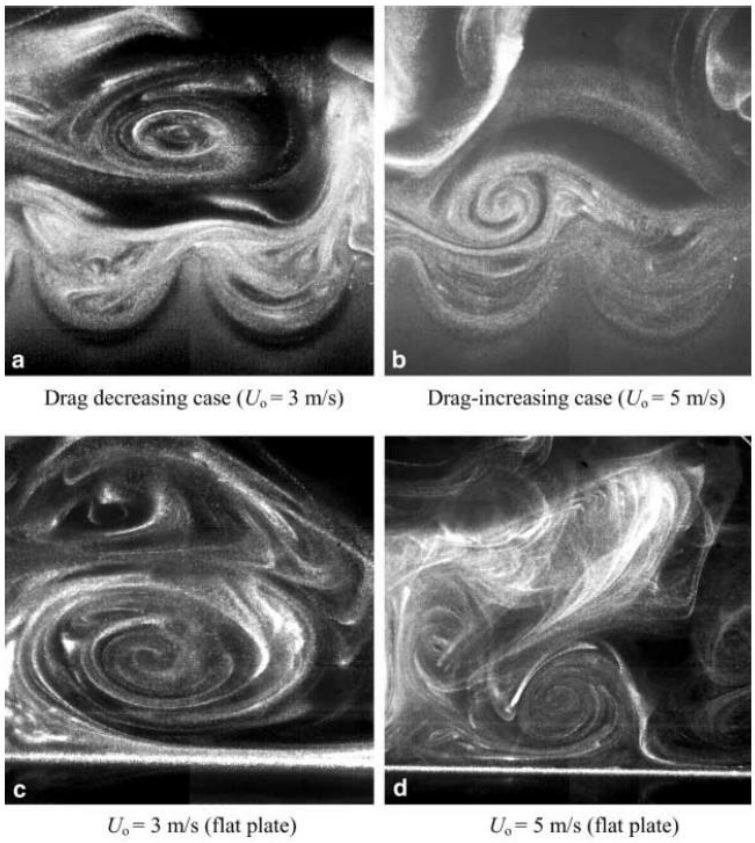

Figure 2.38: Flow visualisation images of streamwise vortices in the cross-stream plane. The riblet spacing in viscous wall units is $s^+ = 25.2$ for the drag reducing case and $s^+ = 40.6$ for the drag increasing case (Lee & Lee [85]).

riblet spacing of $s^+ = 40.6$. The streamwise vortices are observed to penetrate into riblet teeth, leading to more intense velocity fluctuations inside grooves and an increased wall-shear stress over riblets.

The dampened spanwise turbulence fluctuations have also been observed in numerical simulations [27, 51, 42]. As shown in Figure 2.39 by El-Samni et al. [42], at the optimal riblet spacing of $s^+ = 17.7$, the spots which have high Reynolds shear stress reside above riblet crests, while at the larger riblet spacing of $s^+ = 40.6$, the high stress eddies penetrate inside the grooves. The large riblet spacing permits the coherent structures above the riblet crests to push high-speed fluid into grooves. The numerical simulations results are qualitatively similar to the flow visualisation observations in Figure 2.38.

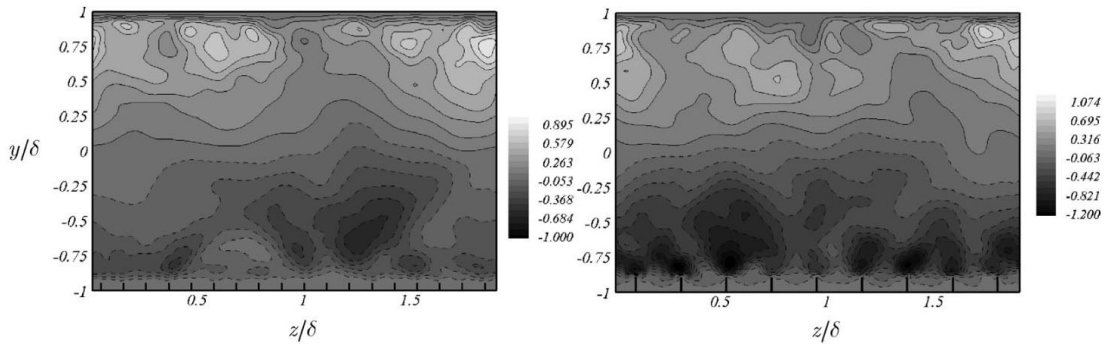

Figure 2.39: Contours of Reynolds shear stress over longitudinal riblets with $s^+ = 17.7$ in drag reducing case (left) and $s^+ = 40.6$ in drag increasing case (right) in turbulent channel flow (El-Samni et al. [42]).

2.3 Convergent-divergent riblets

Convergent-divergent riblets (C-D riblets) are the surface pattern which is composed of a spanwise array of strips with left-yawed and right-yawed microgrooves arranged in an alternating manner [see Figure 2.40]. Due to the potential for reducing surface friction drag [25] and inhibiting flow separation [87, 126], C-D riblets have attracted considerable research attentions in the recent few years [79, 113, 72, 173, 174, 71, 175]. The key parameters of C-D riblets include the riblet wavelength (Λ), riblet yaw angle (γ), riblet spacing (s), riblet height (h), riblet section length (L) and riblet section width (W), as shown in Figure 2.41. The converging line (CL) and the diverging line (DL) are defined from the interfaces between adjacent strips, and the converging/diverging region is referred to the region close to the converging/diverging line. The yaw angle is defined as the acute angle between microgrooves and the converging/diverging line [see Figure 2.40].

The surface patterns of C-D riblets were inspired by some roughness patterns observed in nature, including shark skins and bird flight feathers. As shown in Figure 2.42, the diverging riblet pattern was observed upstream of shark hearing sensors, while the converging pattern was found upstream of shark sensory receptors [79]. Figure 2.43 shows the diverging riblet pattern which was observed on the secondary flight feathers of birds [25]. In addition, on the bird flight feathers, there exists a spanwise variation of the surface height, with a reduced riblet height away from the middle (diverging) region. By analysing scanning electron microscope (SEM) photos of mature pigeon flight feathers in Figure 2.44, Chen et al. [25] revealed a reduced roughness height from 130μm near the feather shaft (i.e. diverging region) to around 30μm at the

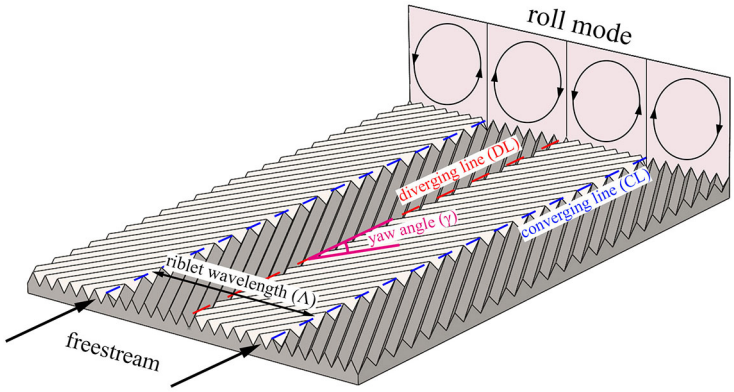

Figure 2.40: Schematic diagram of convergent-divergent riblets (C-D riblets) and the induced time-averaged roll mode (Xu et al. [175]).

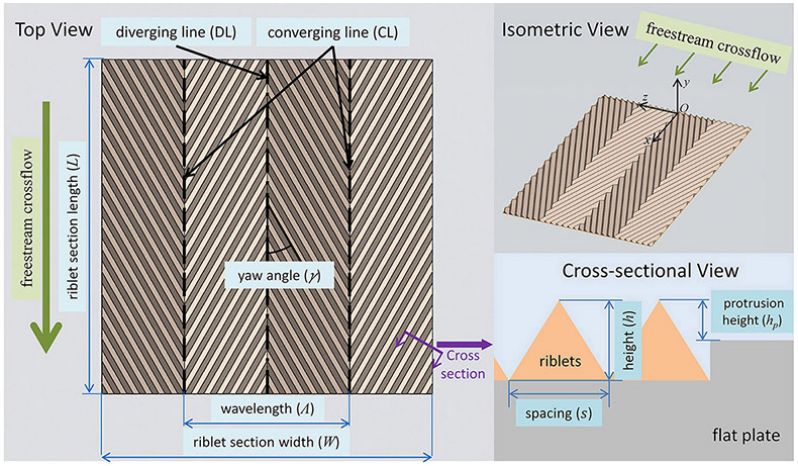

Figure 2.41: Schematic diagram of key geometric parameters of C-D riblets (Xu et al. [173]).

outer fringe (i.e. converging region). Similar height variation in the spanwise direction was observed on the flight feathers of other bird species.

The characteristics of the flow field over C-D riblets were first experimentally studied by Koeltzsch et al. [79]. The flow in a pipe, with inner surface fitted by $\pm 45^\circ$ yawed microgrooves [see Figure 2.45], was investigated using hot-wire anemometer. An increase in the local streamwise velocity and a decrease in turbulence fluctuations were observed over the diverging riblet pattern, and the opposite effect was found over the converging riblet pattern.

Later on, researchers at the University of Melbourne conducted a series of experiments on C-D riblets in the turbulent boundary layer. Nugroho et al. [113] obtained the distributions of the streamwise velocity component using a single-normal hot-wire probe, revealing similar characteristics as reported by Koeltzsch et al. [79]. The effect

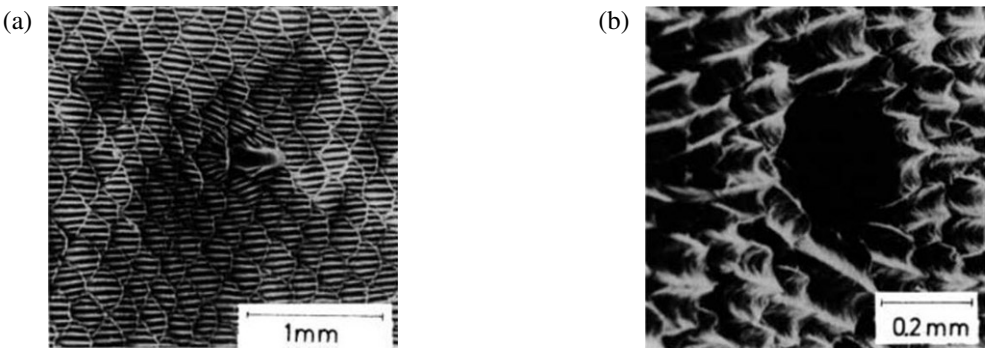

Figure 2.42: (*a*) Converging riblet patterns upstream of the sensory receptors of sharks, (*b*) diverging patterns upstream of the hearing sensors of sharks (Koeltzsch et al. [79]).

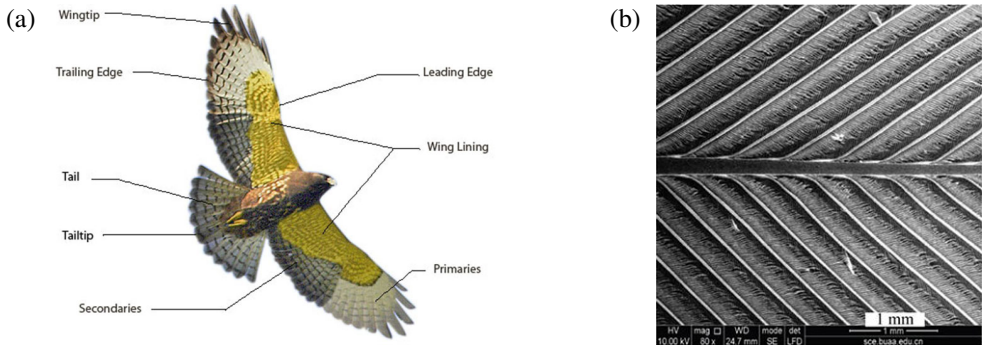

Figure 2.43: (*a*) Configuration of bird wing and tail feathers (Avian Report). (*b*) Microscopic structure of bird flight feathers (Chen et al. [25]).

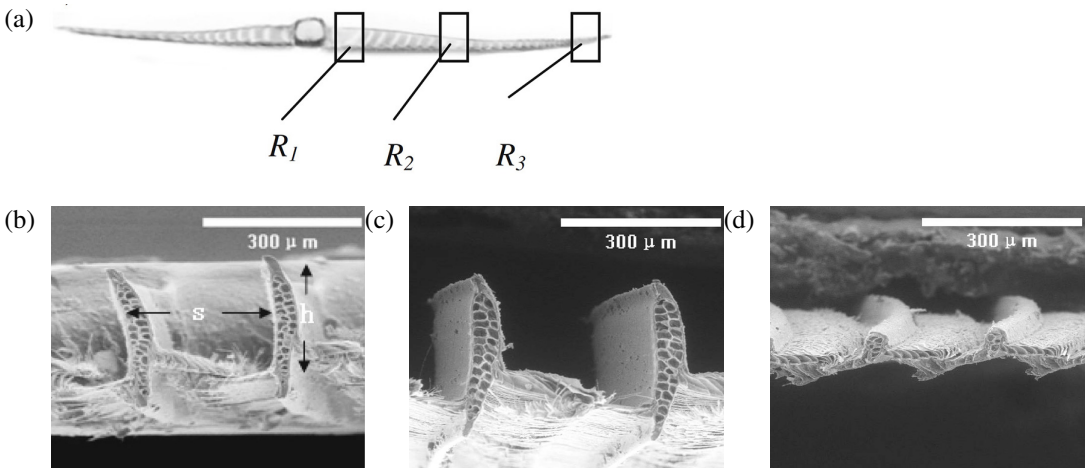

Figure 2.44: (a) Cross-sectional view of a pigeon secondary flight feather. (b)-(d) Scanning electron microscope (SEM) image of bird flight feather cross-section in *R*1/*R*2/*R*3 region (Chen et al. [25]).

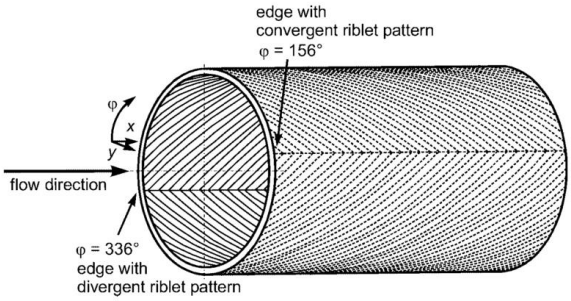

Figure 2.45: Divergent and convergent riblet patterns inside pipe channel (Koeltzsch et al. [79]).

of some parameters of C-D riblets on the boundary layer flow was studied, including the yaw angle, the streamwise fetch length and the viscous-scaled riblet height. Both increasing the yaw angle and increasing the viscous-scaled riblet height lead to stronger spanwise variations. An analysis on the pre-multiplied energy spectra indicates that the coherent structures have been modified radically over C-D riblets [see Figure 2.46]. Using a cross-wire anemometer, Nugroho et al. [114] revealed the presence of a time-averaged large-scale counter-rotating roll mode in cross-stream plane [see Figure 2.47]. Their finding was confirmed and extended by Kevin et al. [72] with stereoscopic PIV measurements. The roll mode seems to have gathered the low-speed fluid and relocated the very-large-scale streamwise structures and features with high vortical activities over the converging region. In accordance to the sense of rotation of the counter-rotating roll mode, the fluid in the region over the diverging line appears to be directed towards the wall (downwash), whereas the fluid in the region over the converging line is seen to be directed away from the wall (upwash). With large field of view measurements in all orthogonal planes, Kevin et al. [71] confirmed that C-D riblets result in formation of large-scale coherent structures over the converging region, which dictate the instantaneous behaviour of the roll mode and share some characteristics, such as meandering and breaking, displayed by the superstructures observed in canonical smooth-wall flows.

It should be addressed that there exists an inherent difference between C-D riblets and longitudinal (streamwise) riblets. The spanwise length scale of the secondary flow induced by longitudinal riblets has the same order as that of the riblet spacing (s) [28, 51]. The effects of longitudinal riblets are known to be confined in the vicinity of the riblet surface via suppression of streamwise vortical structures in the near-wall region. In contrast, the spanwise length scale of the secondary flow produced by C-D riblets is comparable to the riblet wavelength (Λ) or the boundary layer thickness

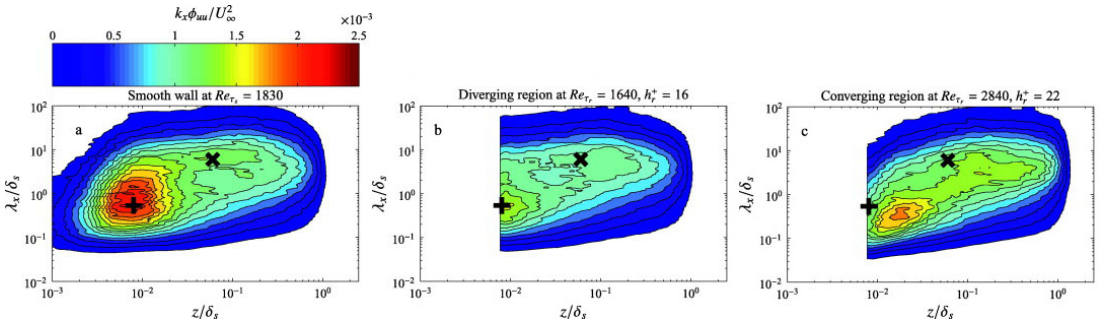

Figure 2.46: Contours of pre-multiplied energy spectra of streamwise velocity fluctuations for the smooth wall (left), the diverging region (middle), and the converging region (right) (Nugroho et al. [113]).

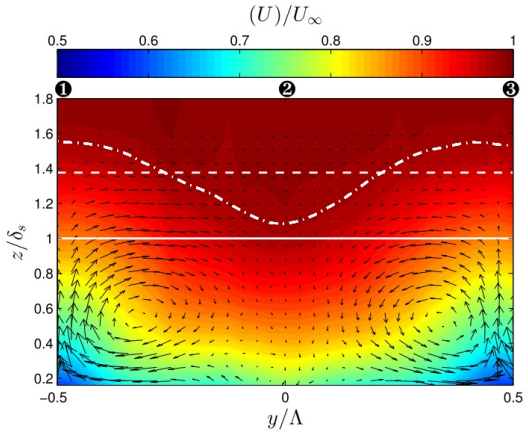

Figure 2.47: Contour of the time-averaged streamwise velocities and in-plane velocity vectors in the cross-stream plane over C-D riblets (Nugroho et al. [114]).

(δ) [72], which could be one or two orders of magnitude larger than that of the riblet spacing (s). As such, the whole boundary layer can be affected [113].

The drag reduction effect of C-D riblets on the flow field has been explored by some researchers. Chen et al. [25] carried out an experiment in a fully-developed turbulent pipe flow, and reported that the pipes covered with spanwise arrays of C-D riblets with diminishing heights towards their edges yield a drag reduction. With an optimal yaw angle of 30° and an optimal riblet height of 20 in viscous wall units, a 21% drag reduction was achieved [see Figure 2.48], which is significantly larger than what longitudinal riblets could ever offer (8% in Walsh [161], 9.9% in Bechert et al. [15]). By applying the modified Clauser method to the time-averaged streamwise velocity profile, an estimation of local wall-shear stress reveals a drag reduction over the diverging line and a drag increase over the converging line [113, 72, 175]. However, in the turbulent boundary layer, the net drag over C-D riblets is estimated to be slight

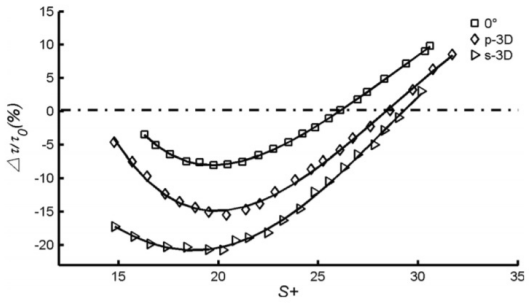

Figure 2.48: Drag reduction ratio of pipe flow with C-D riblets as a function of riblet spacing s^+ (Chen et al. [25]).

larger [113]. Thus, the mechanism of the significant drag reduction effect of C-D riblets reported by Chen et al. [25] still needs further exploration.

The surface pattern of C-D riblets has been tentatively applied to some engineering applications. Liu et al. [87] conducted a linear cascade machine experiment, demonstrating that C-D riblets fitted on blade suction surfaces can reduce pressure losses by suppressing flow separation at low Reynolds numbers. Quan et al. [126] applied C-D riblets behind the leading edge of a double ramp model at a freestream Mach number of 5, revealing that C-D riblets are capable of suppressing shock-induced flow separation and improving pressure recovery in the downstream flow field. These two applications of C-D riblets are intended to reduce the pressure drag in the separated flow field, rather than reducing the skin-friction drag. The skin-friction drag was not measured in these studies.

Table 2.2 summarises the parameters of the studies on C-D riblets.

2.4 Spanwise heterogeneous surface patterns

A roughness surface is heterogeneous when its characteristic length scale is comparable to the dominant length scale in the flow field (boundary layer thickness, channel half height or pipe radius). With surface roughness elements arranged in a spanwise alternating manner, the spanwise heterogeneous surfaces can induce a large-scale secondary flow in the cross-stream plane. The surface heterogeneity can be composed of roughness strip, elevated elements, convergent-divergent riblets, free-slip surface, etc. Spanwise heterogeneous surfaces are encountered in multiple actual scenes, including river beds [162, 163], damaged turbine blades [97, 13], rivet arrays on aircraft, etc. Such roughness patterns have been investigated as a promising passive flow control method in engineering applications.

Research	Model	Measure	Riblet section (m)	Λ (mm)	h (h^+) (mm)	s (s^+) (mm)	γ (deg)
Koeltzsch et al. [79]	pipe	hot-wire	0.2 (L), 0.07 (R)	440	0.152 (19)	0.152 (19)	45
Nugroho et al. [115]	plate	hot-wire	3.09 (L), 0.885 (W)	147.5	0.5 (17)	0.675 (23)	30
Nugroho et al. [112]	plate	hot-wire	3.09 (L), 0.885 (W)	147.5	0.5 (13/24)	0.675 (18/32)	10
Nugroho et al. [113]	plate	hot-wire	5.15 (L), 0.885 (W)	147.5	0.5 (6.7 – 24.4)	0.675 (9 – 33)	10/30
Chen et al. [24]	pipe	pressure gauge	0.4 (L), 0.026 (R)	40	0.06 (9 – 18)	0.1 (15 – 30)	30
Chen et al. [25]	pipe	pressure gauge	0.6 (L), 0.026 (R)	40	0.06 (9 – 18)	0.1 (15 – 30)	0 – 60
Kevin et al. [73]	plate	PIV	5.15 (L), 0.885 (W)	147.5	0.5 (18)	0.675 (24)	20
Kevin et al. [72]	plate	PIV	5.15 (L), 0.885 (W)	147.5	0.5 (18)	0.675 (24)	20
Liu et al. [87]	blade	five-hole probe	0.018 (L), 0.0455 (W)	6.5	0.08	0.3	30
Xu et al. [173]	plate	dye, PIV	0.09 (L), 0.09 (W)	30/36/45	2.4	3	30
Xu et al. [174]	plate	PIV	0.09 (L), 0.09 (W)	45	2.4	3	30
Kevin et al. [71]	plate	PIV	5.15 (L), 0.885 (W)	147.5	0.5 (19)	0.675 (26)	20
Quan et al. [126]	double ramp	PSP, TSP	0.02 (L), 0.033 (W)	11	0.039/0.078	0.3	30
Xu et al. [175]	plate	PIV	0.5 (L), 0.25 (W)	83.33	0.8/1.4/2 (8/14/20)	2 (20)	30

Table 2.2: A summary of experimental parameters in existing studies on C-D riblets. PIV - particle image velocimetry, PSP - pressure-sensitive paint, TSP - temperature-sensitive paint. L and W are the streamwise length and the spanwise width of the riblet section, respectively. Λ is the riblet spacing, h is the riblet height, s is the riblet spacing and γ is the riblet yaw angle. The superscript $+$ indicates the length scale in wall units.

In this section, some representative work on the surface patterns with spanwise heterogeneity are outlined, including alternating roughness strips, variation in wall-shear stress, alternating free-slip and no-slip strips, periodically elevated roughness elements and randomly elevated roughness elements. The surface pattern of convergent-divergent riblets is elaborated in Section 2.3 and will not be repeated here. A further categorisation of these surface patterns with spanwise heterogeneity, in the aspects of surface geometry, roll mode and secondary flow generation mechanism, can be found in Section 7.5.

2.4.1 Alternating roughness strips

Wang & Cheng [162] investigated the secondary flow over spanwise alternate rough and smooth strips in an open channel. Cellular secondary flows are observed to extend to the whole channel, with downwelling over the rough strip and upwelling over the smooth strip. The near-wall streamwise velocity above the rough strip is lower than that over the smooth strip. At a higher vertical station, the relation between the streamwise velocity and the roughness reverses, i.e. a larger streamwise velocity occurs above the rough strip than that over the smooth strip. Thus, there exists a larger vertical gradient of the streamwise velocity over the rough strip.

Willingham et al. [166] investigated the turbulent boundary layer over a flat plate with spanwise alternating high-roughness and low-roughness strips. The drag imposed on the flow field by the roughness surface is computed with the equilibrium logarithmic law. The stress jump across these streamwise-aligned roughness strips induces a spanwise turbulent mixing, which serves as the source of the secondary flow. The width of the high roughness strip is observed to have a strong impact on the secondary flow pattern. Counter-rotating vortices of the same scale of the boundary layer are observed in the cross-stream plane, with downwelling over the high roughness area and upwelling over the low roughness area. With a similar setting of spanwise alternating high and low roughness strips, Anderson et al. [6] confirmed that the secondary flow is driven and sustained by the spatial gradients in Reynolds stresses, i.e. Prandtl's secondary flow of the second kind. The imbalance between production and dissipation of the turbulent kinetic energy leads to secondary convection velocities.

Bai et al. [9] studied the turbulent boundary layer over a flat plate with spanwise alternating high and low roughness strips [see Figure 2.49]. Large-scale counter-rotating roll-modes are observed in the cross-stream plane, with upwelling over the low roughness strip and downwelling over the high roughness strip. The streamwise velocity

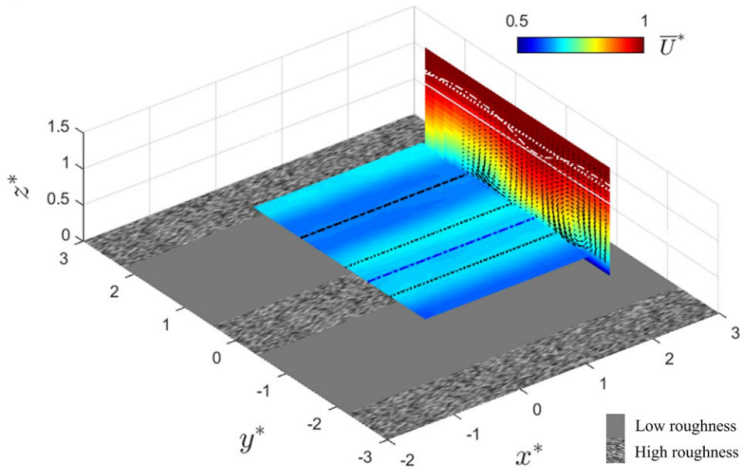

Figure 2.49: The time-averaged streamwise velocity in the wall-parallel plane and the cross-stream plane over alternating roughness strips (Bai et al. [9]).

increases over the high roughness strip and decreases over the low roughness strip. The Reynolds stresses and instantaneous turbulent events also exhibit spatial preferential features.

2.4.2 Variation in wall-shear stress

In numerical simulation, different wall-shear stress values can be assigned to the adjacent streamwise-aligned strips. Chung et al. [31] investigated the turbulent channel flow with laterally alternating patches of high and low wall-shear stress [see Figure 2.50]. The spanwise stress jump, which induces a spanwise flow from the high shear area to the low shear area, serves as the driving force of the secondary flow. Counter-rotating roll mode is observed in the crossflow. With a spanwise spacing of $S/\delta_s \leq 3.14$, a large wall-normal velocity transports the low momentum fluid away from the wall, which leads to a relatively lower streamwise velocity over the low wall-shear stress region. When the spanwise spacing turns larger than 6.28 ($S/\delta_s \geq 6.28$), a higher streamwise velocity is observed over the low wall-shear stress region, which is attributed to its lower resistance.

2.4.3 Alternating free-slip and no-slip area

Türk et al. [151] and Stroh et al. [142] investigated the flow field over a flat surface with spanwise alternating no-slip and free-slip strips in a turbulent channel flow. At

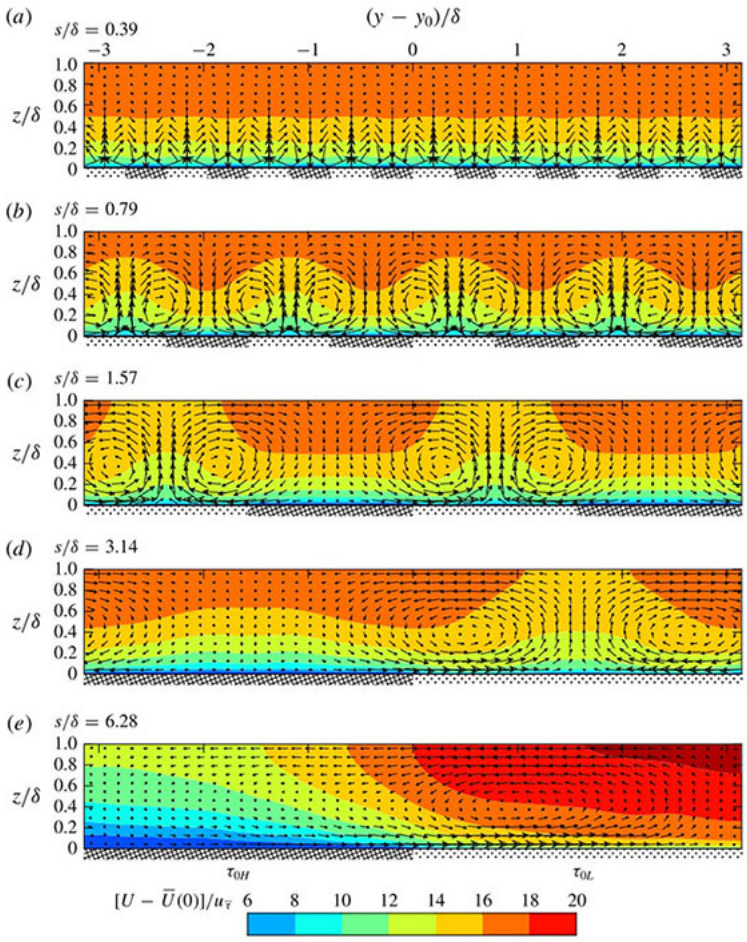

Figure 2.50: The time-averaged streamwise and in-plane velocities in the cross-stream plane over strips with spanwise variation in wall-shear stress (Chung et al. [31]).

a small spanwise spacing, a pair of counter-rotating vortices is observed to extend to the distance of roughly one wavelength in the wall-normal direction, with upwelling over the no-slip area and downwelling over the free-slip area [see Figure 2.51]. When the spanwise spacing approaches the half channel height, the secondary flow extends to the entire half depth. The mechanism of the secondary flow is attributed to the near-wall spanwise flow from the free-slip area to the no-slip area. Interestingly, a further increase in the spanwise spacing leads to a large-scale flow with reversed rotational direction, i.e. upwelling over the free-slip area and downwelling over the no-slip area. In this case, the tertiary vortical motion at a higher wall-normal station is recognised as the large-scale secondary flow, which has the opposite rotational direction as compared to the near-wall vortical motion over the intersection between the free-slip area and the no-slip area.

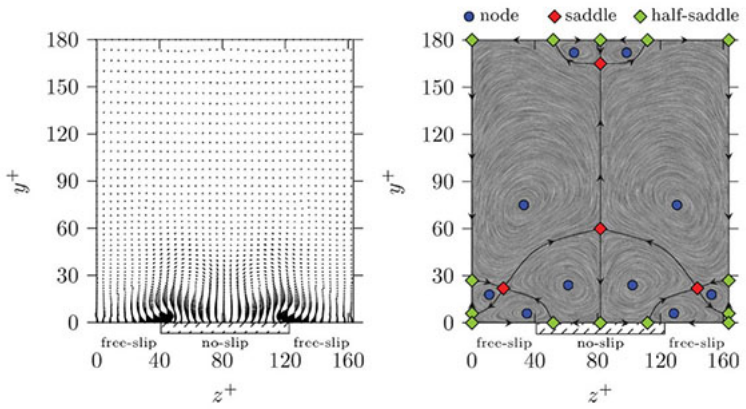

Figure 2.51: The secondary flow motion in the cross-stream plane over alternating free-slip and no-slip areas for $L^+ = 162$ and $L/W = 2$ at $Re_\tau = 180$ (Stroh et al. [142]).

2.4.4 Periodically elevated elements

Wang & Cheng [163] investigated the secondary flow over spanwise-periodical rectangular ridges in an open channel flow. In the cross-stream plane, the secondary flow is composed of a pair of counter-rotating vortices. Downwelling is observed both over the ridge middle and over the trough middle, whilst upwelling occurs above the transition between the trough and the ridge.

Vanderwel & Ganapathisubramani [152] investigated the secondary motions in turbulent boundary layers over streamwise-aligned Lego bricks with different spanwise spacings [see Figure 2.52]. When the spanwise spacing is larger than 0.5δ, the δ-scale counter-rotating recirculation zones which flank the elevations are observed. When S is comparable to δ, the upwelling with a lower streamwise velocity is observed over the elevated roughness strips, whilst the opposite is obtained between roughness elements. The downwelling is observed in the region close to the wall surface over the middle section of the roughness element, which is aligned with the result in Wang & Cheng [163].

Yang & Anderson [178] investigated the vortical structures in a channel flow with periodic streamwise-aligned pyramidal obstacles. A domain-scale counter-rotating roll mode is observed in the outer layer at a large spanwise spacing, with upwelling over the smooth wall and downwelling near the pyramidal obstacles. Since the ratio between the roughness element width and the spanwise spacing is relatively small, a downwelling secondary flow is observed in the regions over the roughness elements and near the step changes. For a small spanwise spacing of $S/H = 0.64$, the large-scale counter-rotating vortices vanish. Upwelling occurs above the elements while

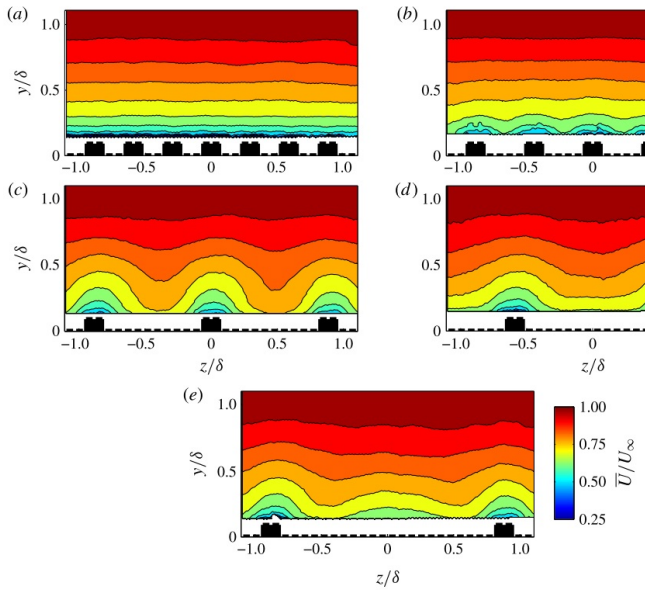

Figure 2.52: Contours of time-averaged streamwise velocity in the cross-stream plane over periodically elevated elements with different spanwise spacings (Vanderwel & Ganapathisubramani [152]).

downwelling arises near the step changes. Two pairs of counter-rotating vortices are observed in one spanwise spacing, with one pair close to the wall and the other at a higher station.

Medjnoun et al. [95] investigated the turbulent boundary layer over spanwise-periodical rectangular smooth ridges. Compared to the smooth-wall case, a net drag increase is observed over the spanwise heterogeneous surface. The logarithmic law region exists in the mean velocity profile, but the mean velocity and variance profiles are observed to not collapse in the outer region.

Awasthi & Anderson [8] investigated the turbulent channel flow over a surface with spanwise varying topographic height. The spanwise heterogeneous topographies are constructed by the outer product of one array featuring Gaussian distribution and the other array featuring harmonic distribution. Domain-scale counter-rotating vortices are observed in the cross-stream plane, with upwelling over the low roughness region and downwelling over the high roughness area. Steeper and shorted structures are observed over the high roughness region.

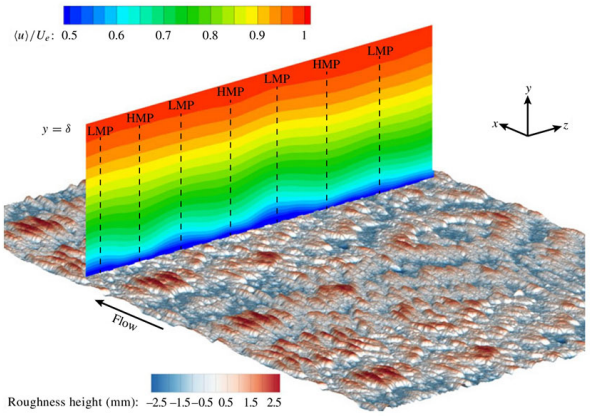

Figure 2.53: The time-averaged streamwise velocity in the cross-stream plane over randomly elevated roughness elements (Barros & Christensen [13]).

2.4.5 Randomly elevated roughness elements

Mejia-Alvarez et al. [97] and Barros & Christensen [13] studied the turbulent boundary layer over the replica of a damaged turbine blade under foreign-material deposition. The spanwise heterogeneity generates spanwise-alternating low- and high-momentum pathways [see Figure 2.53]. The high-momentum pathway (HMP) or low-momentum pathway (LMP) refers to the region where the time-averaged streamwise momentum is excessive and insufficient, respectively, as compared to the spatial-temporal-averaged (spanwise-time-averaged) streamwise momentum. In the ensemble-averaged flow field, upwelling occurs over the low-momentum pathway (LMP) and downwelling occurs over the high-momentum pathway (HMP), with swirling motions in the region between these pathways.

2.5 Summary

In summary, the drag reduction of a civil aircraft is of great interest to the academia and the aviation industry. Some novel flow control techniques may be applied to achieve the challenging goal of reducing the skin-friction drag. In the turbulent flow, the complexity of coherent structures including streamwise vortices, hairpin vortices, large-scale motions and very-large-scale motions/superstructures increases the difficulty of achieving the goal.

There is only limited work on the boundary layer flow over C-D riblets, compared to the extensive research and insight into the skin-friction drag reduction effect of

longitudinal riblets. The flow topology of the laminar boundary layer flow over C-D riblets is still unknown, especially inside riblet valleys. The effects of C-D riblets on the characteristics of coherent structures including hairpin vortices, hairpin packets and uniform momentum zones have not been studied. The attempt of the project is to understand the flow physics and to benefit future engineering applications of C-D riblets.

From a broader perspective, the surface pattern of C-D riblets belongs to the spanwise heterogeneous surface patterns. The surface geometry of spanwise heterogeneity varies widely. In the cross-stream plane, the boundary-layer-scale roll mode can be induced by different types of spanwise heterogeneity. In addition, the generation mechanism of the large-scale roll mode may vary for different types. Therefore, the synthesis and categorisation of the surface patterns with spanwise heterogeneity would be of benefit to the relevant researchers.

Chapter 3

Research Methodology

In this section, the setup of experiments is introduced in the following five aspects:

- Water flume and flat plate facilities
- Parameters and manufacturing of C-D Riblets
- Dye visualisation experiment
- Particle image velocimetry
- Smooth-wall boundary layers validation

3.1 Water flume and flat plate facilities

3.1.1 Water flume

The experiments are conducted in a low-speed water flume at the School of Mechanical, Aerospace and Civil Engineering, the University of Manchester. Figure 3.1 shows an overview of the experimental facilities, and Figure 3.2 shows a schematic diagram of the water flume. The water flume is $3.64m$ long and it has a $0.305m \times 0.305m$ cross-sectional area. Both the side walls and the bottom floor of the test section are made of transparent glass to allow measurements from two sides or underneath the water flume. The fluid is driven from the holding tank to the entry tank by a centrifugal pump, which is controlled by an ABB^{TM} digital inverter. To achieve a flow field with a low turbulence level, after passing through straightener vanes and honeycomb, the water goes through four inlet screens which are arranged in a decreasing order of mesh size. Adjustable permeable grate is installed at the outlet of the flume, and circular holes on the

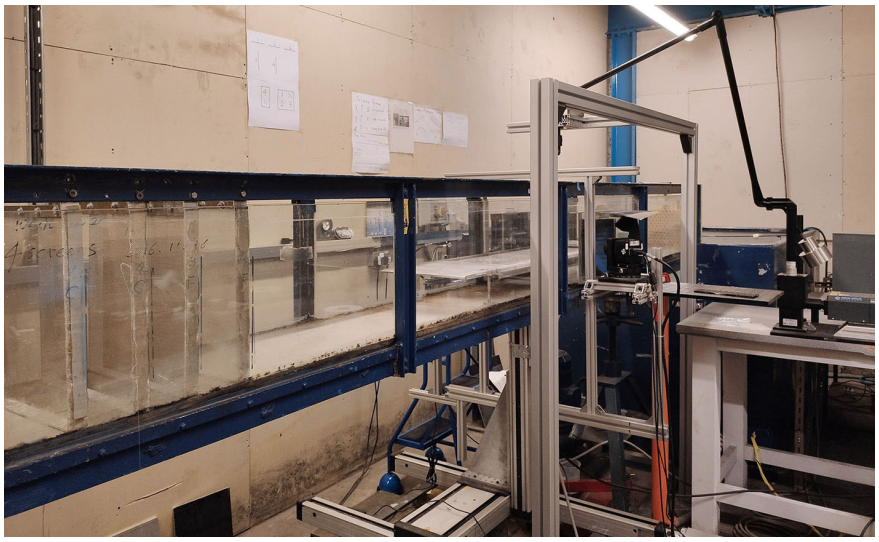

Figure 3.1: Perspective view of the experimental facilities. The setting shown is for stereoscopic PIV measurements in the boundary layer.

permeable grate are carefully adjusted to ensure equal velocity (mass flux) on all water levels. Freestream velocity and the level of water in the test section are controlled by both RPM (revolutions-per-minute) of centrifugal pump and the level set of adjustable permeable grate. The range of freestream velocity is between 0 and $0.3m/s$. To reduce the breeding of bacteria and parasites, a water circulation between the holding tank and the entry tank is applied on a daily basis.

3.1.2 Flat plate in laminar boundary layer

An aluminium flat plate (1380mm long, 300mm wide, 6mm thick) is applied to generate the laminar boundary layer in the water flume. The flat plate is installed horizontally in the water flume with its test surface facing downward. The $1:5$ super-elliptical leading edge helps reduce flow separation or transition from the leading edge. The height of the flat plate can be adjusted by four screws, and a slight negative inclination angle is applied to ensure stable attached boundary layer. A rotational flap at the trailing edge also helps reduce streamwise pressure gradient. On the flat plate, there is a hole with a diameter of $D = 132mm$ and the centre locating at $x = 715mm$ downstream of the leading edge [see Figure 3.3]. A disc plate containing $90mm \times 90m$ convergent-divergent riblets can be installed into the hole using two screws. The stereoscopic PIV data confirms the two-dimensional characteristics of the boundary layer flow across the width of the convergent-divergent riblet section. In the laminar boundary layer,

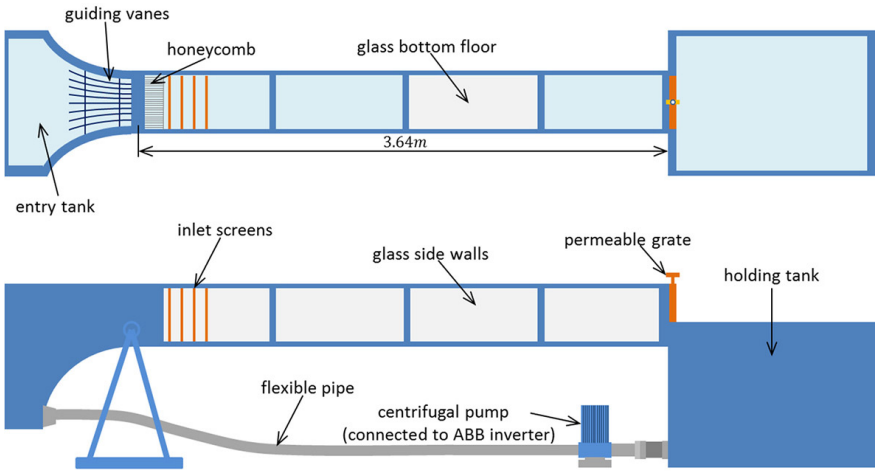

Figure 3.2: Schematic diagram of the water flume in the top view (upper) and the side view (lower).

Figure 3.3: Front view of the flat plate test surface in the laminar boundary layer. The disc plate is not installed in the $D = 132mm$ hole.

based on PIV measurement results, the freestream velocity is set as $U_\infty = 0.1m/s$ and the turbulence intensity in the freestream crossflow is about 0.2%.

3.1.3 Flat plate in turbulent boundary layer

In the turbulent boundary layer experiments, a 1350mm-long flat plate with its test section facing upward is designed [see Figure 3.4]. A super-elliptical leading edge is applied to avoid flow separation from the leading edge. Two angle irons are mounted on the bottom of the flat plate, which help to avoid plate bending along the streamwise direction. The inclination angle of the flat plate can be adjusted by four steel legs with threads placed on the bottom floor of the water flume. There exists a small gap

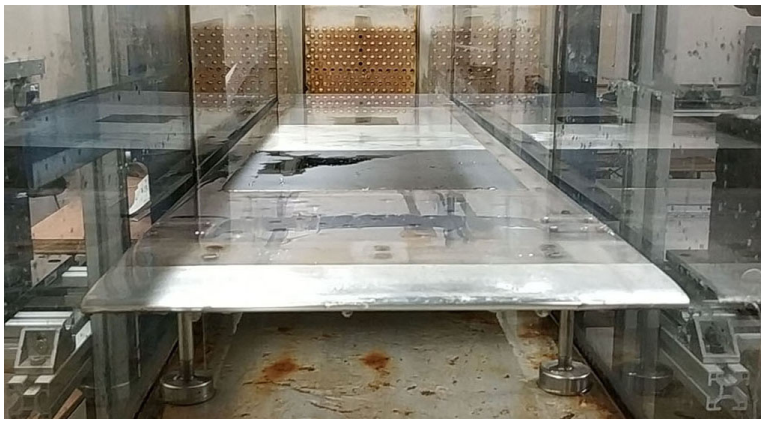

Figure 3.4: Front view of the flat plate test surface in the turbulent boundary layer. The cavity is filled with tiles having smooth surfaces.

between the flat plate and each side wall of the water flume, which restrains the growth of the side wall boundary layers along the flat plate. A cavity with dimensions of $500mm \times 250mm \times 6mm$ (in length, width and depth respectively) starts at $550mm$ from the leading edge. Rectangular tiles with either a smooth surface or rough pattern as the upper surfaces are inserted into the cavity of the flat plate. Compared to the flat plate in Section 3.1.2, the current new design of the flat plate can have a larger section with C-D riblets.

3.2 Parameters and manufacturing of C-D Riblets

3.2.1 Riblets with three different wavelengths

C-D riblets with three different riblet wavelengths are applied in the laminar boundary layer experiment in Chapter 4. The surface pattern is machined on the upper surface of a disc plate ($D = 132mm$), which can be flush-mounted into the test plate as an insert [see Figure 3.5]. The disc plate containing the C-D riblets is made with clear resin using $3D$ printing technique with an accuracy of $\pm 25\mu m$. The surface with C-D riblets can be of good quality by building the supports required by $3D$ printing on the opposite side. The thickness of the disc plate insert is $6mm$, which ensures that there is no step between the insert and the flat plate. The centre of this disc is located at $715mm$ downstream of the leading edge of the test plate.

The cross-sectional shape of the riblets is triangular with $s = 3mm$ and $h = 2.4mm$. The protrusion height (h_p) of convergent-divergent riblets is $1.2mm$, which indicates that the smooth wall levels with half of the riblet height ($h_p = h/2$). The blockage

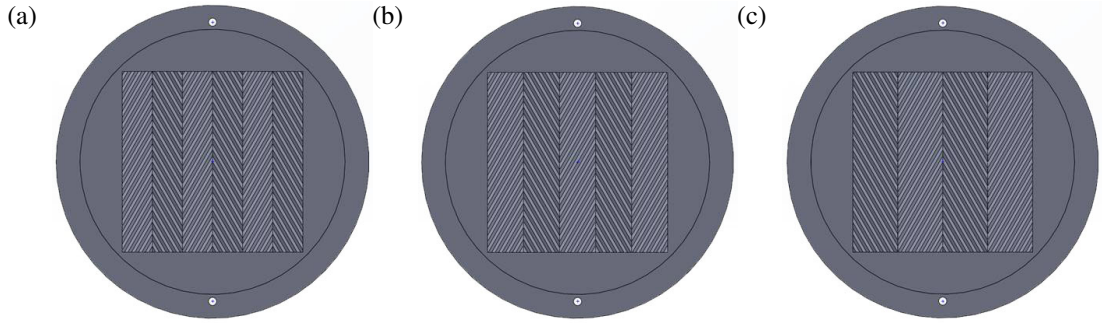

Figure 3.5: Schematic of disc plate with C-D riblets as the upper surface with riblet wavelength of (a) $\Lambda = 30mm$, (b) $\Lambda = 36mm$, (c) $\Lambda = 45mm$.

ratio, i.e. the protrusion height of the riblets to the flat plate boundary layer thickness (h_p/δ_{FP}), is about 9% at the start of the riblet section. With both the layer thickness and the particles diameter being set as $25\mu m$, the resolution of $3D$ printing (approximately % of the riblet spacing or the riblet height) is considered excellent for the present setup. The angle between tilted riblets and the freestream direction is the yaw angle (γ). The yaw angle of $\gamma = 30^\circ$, which was justified by Chen et al. [25] as the optimal value in reducing the skin-friction drag in their turbulent pipe flow experiment, is adopted in this experiment. The overall length and width of the riblet section is $L = 90mm$ by $W = 90mm$. Riblet sections with a wavelength of $30mm$, $36mm$ and $45mm$ are tested in this experiment. The total number of riblet wavelengths accommodated on the disc plate is hence 3.0, 2.5 and 2.0 respectively.

3.2.2 Riblets with spanwise height variations

C-D riblets with spanwise height variations are applied in the laminar boundary layer experiment in Chapter 5. The riblet section starts at $x = 0.67m$ from the leading edge of the flat plate. To investigate the effect of spanwise riblet height variation, three types of C-D riblet patterns are designed, as shown in Figure 3.6. The riblet height along the diverging line $h_{DL} = h$ is $2.4mm$ for all three cases. The riblet height in the longitudinal plane along the converging line h_{CL}, as indicated in Figure 3.6, has three values of $2.4mm$ (uniform height), $1.2mm$ (half height) or 0 (zero height), and a linear variation of the riblet height is designed in the spanwise direction. The smooth wall levels with half of the adjacent riblet height, i.e. the protrusion height h_p is $h_{DL}/2$ ($h_{CL}/2$) for the wall surface adjacent to the diverging line (converging line).

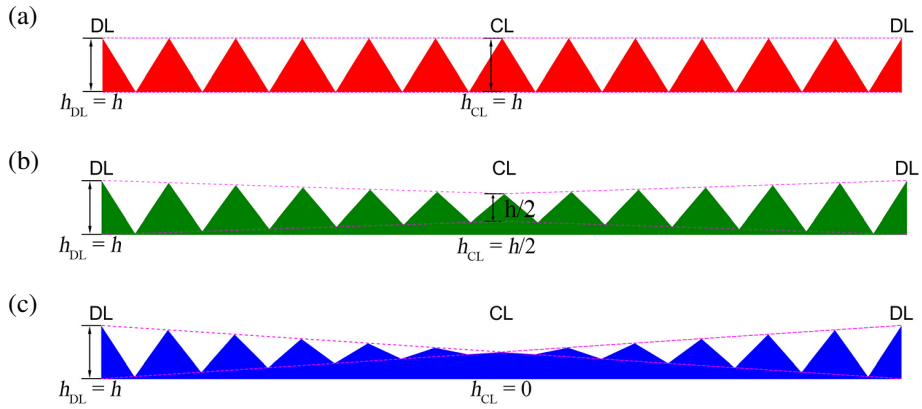

Figure 3.6: Cross-sectional view in the cross-stream (y-z) plane of C-D riblets with (a) $h_{CL} = h$, (b) $h_{CL} = h/2$, (c) $h_{CL} = 0$. Dashed lines indicate a linear variation of the riblet height along the spanwise direction.

3.2.3 Riblets with three different heights

C-D riblets with three different riblet heights are applied in the turbulent boundary layer experiments in Chapter 6 and Chapter 7. C-D riblets are machined on rectangular tiles using 3D printing technique, as shown in Figure 3.7. The layer thickness and particle diameter are set as $25\mu m$, and black resin is used to reduce the surface reflection of the laser light. These riblet tiles can be inserted into the cavity of the flat plate to form the surface pattern. The riblet section is $500mm$ in length and $250mm$ in width. The riblet wavelength (Λ) is $83.33mm$, which is 2.55 times of the turbulent boundary layer thickness over the smooth wall (δ_s) at the measurement station. Across the span of the cavity, three riblet wavelengths are accommodated. The yaw angle (γ), which is defined as the angle between the yawed grooves and the freestream direction, is selected as 30° based on the optimal value proposed by Chen et al. [25]. In the experiment, C-D riblets with three different heights (h), i.e. $0.8mm$, $1.4mm$ and $2mm$, and the same riblet spacing (s) of $2mm$ are tested. In all cases, the smooth wall is levelled with the mid height of the riblets. The blockage ratio, i.e. the riblet height to the boundary layer thickness of the smooth wall (h/δ_s), is 2.4%, 4.3% and 6.2% respectively at the measurement station. Over a homogeneous rough-wall surface, the outer-layer similarity is expected to hold for all these three height values (h/δ_s) [170, 47]. As indicated in Figure 3.7, the riblets have trapezoidal teeth with a width of $0.4mm$ at the crest (w_c) and $0.8mm$ at the root (w_r). The trapezoidal shape of the C-D riblets is chosen for some particular reasons. First, the flat instead of curved riblet surface is chosen, since the former will be easier to machine in engineering applications. Besides, to reduce

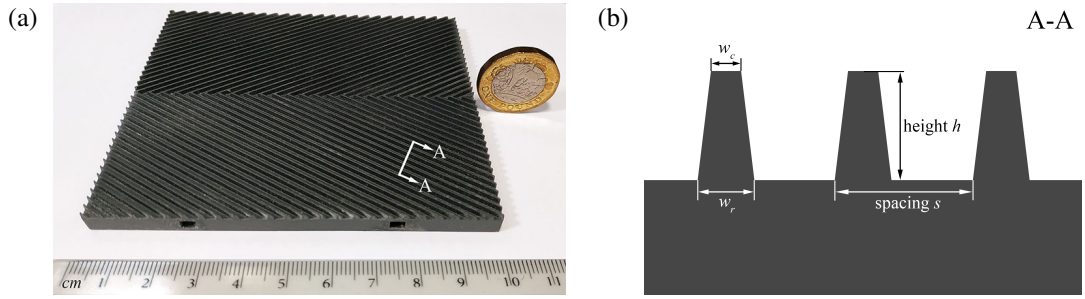

Figure 3.7: (*a*) Perspective view of a tile with C-D riblets on its upper surface. A £1 coin on its side is displayed for visual comparison. (*b*) Sectional view of C-D riblets along $A-A$, showing the trapezoidal profile of riblet teeth.

damage or corrosion, a sharp riblet crest is not applied. Also, a wider root than crest is selected to enhance the durability of the riblet teeth.

The riblet height can be expressed in wall units using the local friction velocity (U_τ) and the kinematic viscosity (ν) as $h^+ = hU_\tau/\nu$. To ensure consistency, the friction velocity over the smooth wall ($U_{\tau s}$) is applied in the normalisation. Along the streamwise length of the riblet section, the normalised riblet height (h^+) in wall unit varies by less than 6.3%. At the measurement station, the riblet height of 0.8*mm*, 1.4*mm* and 2.0*mm* corresponds to approximately 8, 14 and 20 in wall units respectively, and the riblet spacing in wall units is $s^+ = sU_\tau/\nu = 20$. Hereafter, these C-D riblets are referred to as $h^+ = 8$, $h^+ = 14$ and $h^+ = 20$ riblets respectively. García-Mayoral & Jiménez [49] proposed to use the groove cross section (A_g) to characterise the drag reduction effect of longitudinal riblets. The values of $A_g^{+1/2} = \sqrt{A_g\nu^2/U_\tau^2}$ for the trapezoidal riblets tested in these experiments are 10.6, 14 and 16.7 respectively. Unlike the $h^+ = 8$ or $h^+ = 14$ riblets which stay within the viscous sublayer and the buffer layer, the riblets with $h^+ = 20$ approach the lower bound of the log-law region.

Note that the present study and the work by Nugroho et al. [113] investigate the effect of riblet height from two complementary aspects. In the study, the freestream velocity is kept the same (the same baseline turbulent boundary layer), and the change in h^+ is obtained by changing the physical height (h) of C-D riblets. Since the riblet spacing remained the same, the ratio h/s varied from 0.4 to 1.0. By contrast, in the work by Nugroho et al. [113], the height of riblets was kept constant, and the riblet height in wall units (h^+) was changed by varying the freestream velocity. In their study, the baseline turbulent boundary layers were different, whilst the ratio h/s remained constant [113].

3.3 Dye visualisation experiment

The dye visualisation technique is capable of qualitatively indicating fluid motion inside riblet valleys, which is difficult to obtain with other measurement techniques. The setup of the dye visualisation experimental system includes dye injection, illumination and image acquisition. The dye is obtained by mixing rhodamine B, alcohol and water. The density of the dye is adjusted to a density similar to water. After adding a drop of dye to the water, the dye remains approximately suspended. Figure 3.8 shows the drawings of the disc plate with holes and the dye injection cavity. In the present experiment, the dye is fed from a $3D$ (three-dimensional) printed cavity through five rubber tubes, which are connected to the five dye injection orifices on the disc plate located at a distance of $10mm$ upstream of the riblet section. The flow rates through these five holes can be individually adjusted by the clips on the rubber tubes. The flow rates remain relatively low to ensure minimal interference to the flow field and to indicate the flow topology of the surface flow. The dye is attached to the wall surface upstream of the riblet section. Since the disc plate can be rotated 180° to swap converging and diverging lines, five holes are designed on each side of the disc plate. The dye flow rate through each rubber tube can be individually controlled using tube clips. The top side of the disc plate with convergent-divergent riblets remains translucent, whereas the bottom side is painted white to increase the contrast of dye images. The remaining part of the disc plate is painted black.

During the experiment, the riblet section is illuminated using four white light-emitting diode (LED) light sources through the glass side walls of the flume. To avoid producing shadows of dye streaklines on the riblet surface, lighting from the top is not used. The dye visualisation images are captured using a Canon $D70$ SLR camera fitted with a Canon EF-S $18-135mm$ $F3.5-5.6$ IS lens. The camera is operated using a remote control mode to minimise its movement. The aperture of the camera lens is set as 11.0 in the side view and 5.6 in the top view. The smaller aperture used for the side view enables a larger depth of view across the span.

3.4 Particle image velocimetry

3.4.1 Measurement principle

Particle image velocimetry (PIV) is an optical measurement technique which allows simultaneous measurements of the entire velocity field in a region. A PIV system

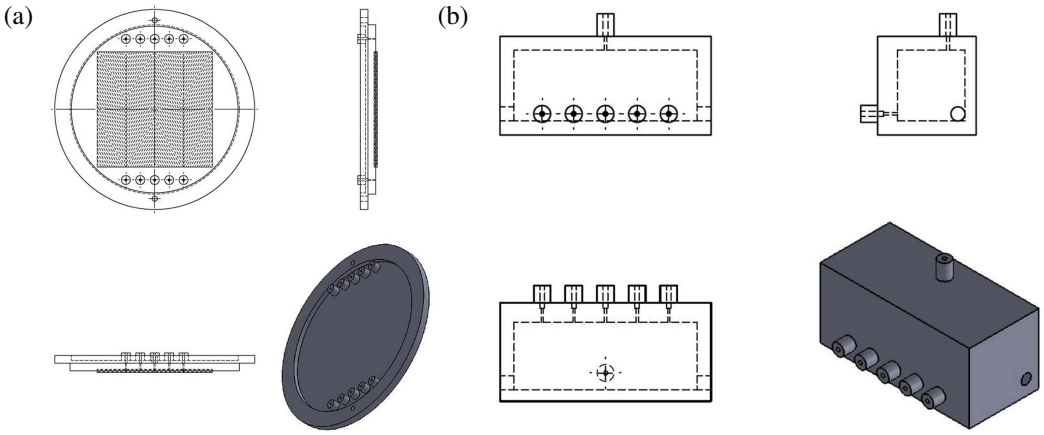

Figure 3.8: Drawing of dye visualisation facilities of (a) disc plate with five holes, (b) dye injection cavity.

has three subsystems including seeding, illumination and recording [see Figure 3.9]. The seeding subsystem is composed of sufficiently small tracer particles which should faithfully follow the fluid. The density of tracer particles is comparable to that of the working fluid. The laser (light amplification by stimulated emission of radiation) system is usually applied as the illumination source. The tracer particles are illuminated in the same plane or volume of the flow field for multiple times (at least twice) within a known time interval(s). The recording system records the light scattered by tracer particles on a sequence of frames on the camera(s). The charge-coupled device (CCD) cameras are commonly used to record image data. An electronic synchroniser is usually applied to regulate the above-mentioned three subsystems.

In a mono-PIV system, the light scattered by tracer particles is recorded on two frames (an image pair) on a CCD camera. To extract the displacement vectors in the measurement plane, each frame is divided into a set of small areas, i.e. interrogation windows. For each interrogation window, the local displacement of tracer particles ($\vec{r}$) can be calculated using the spatial statistical cross-correlation function [see Figure 3.10]. Given $\vec{x}_i$ as the position vector in an image frame, the image intensity field can be defined as

$$I(\vec{x}) = \sum_{i=1}^{N} V_0(\vec{x}_i)\tau(\vec{x}-\vec{x}_i), \tag{3.1}$$

where $V_0(\vec{x}_i)$ is the transfer function associate with the light intensity at $\vec{x}_i$, and $\tau(\vec{x})$ is the point spread function of the imaging lens, which is commonly assumed to follow a Gaussian distribution. The cross-correlation function of two interrogation windows in

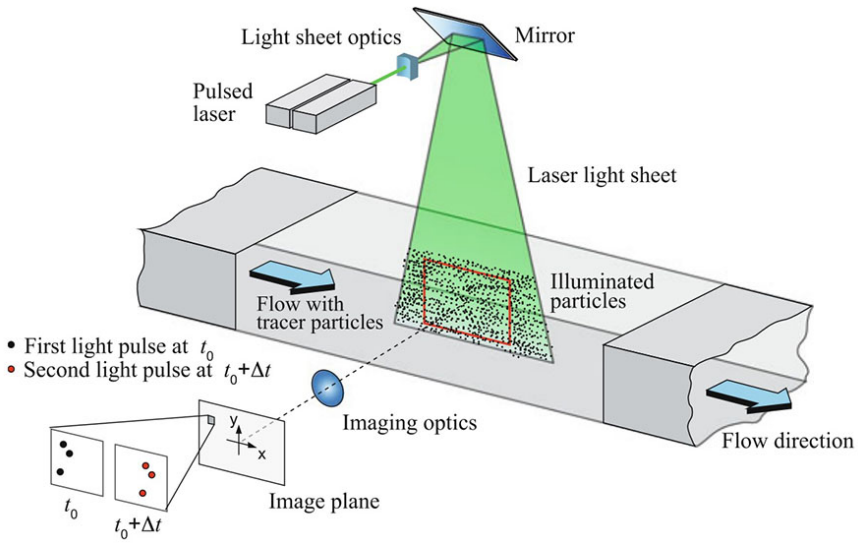

Figure 3.9: Schematic of mono-PIV experimental setup (Raffel et al. [129]).

frame A and frame B is

$$R(\vec{s}) = \langle I_A(\vec{x}) I_B(\vec{x}+\vec{s}) \rangle, \tag{3.2}$$

where $\vec{s}$ is the separation vector in the correlation plane, and $\langle \cdot \rangle$ is the spatial averaging over the interrogation window. The local displacement vector $\vec{r}$ is calculated to reach the maximum of the correlation peak. In practice, the cross-correlation function is commonly calculated using fast Fourier transform (FFT) algorithms and following an iterative process with two levels of interrogation windows of decreasing sizes.

Given the time interval between two frames (Δt) and the image magnification factor (M) obtained by calibration, the local in-plane velocity vectors can be calculated as $\vec{u} = M\vec{r}/\delta t$. The calibration is performed by placing an object of known length in the light sheet plane, which helps transform the image displacement into world coordinates. In order to obtain more displacement vectors, the neighbouring interrogation windows can be partially overlapped.

In a stereoscopic PIV system, two cameras are arranged with separate viewing angles to extract the out-of-plane-axis displacement component. To align each lens principal axis with the principal view direction, each camera is mounted on an adaptor, and the plane of the camera sensor is tilted to intersect the image plane, lens plane and object plane in a common line, i.e. to satisfy the Scheimpflug criterion [see Figure 3.11]. The calibration is performed by taking images of a flat calibration plate placed in the light sheet plane and several other parallel planes.

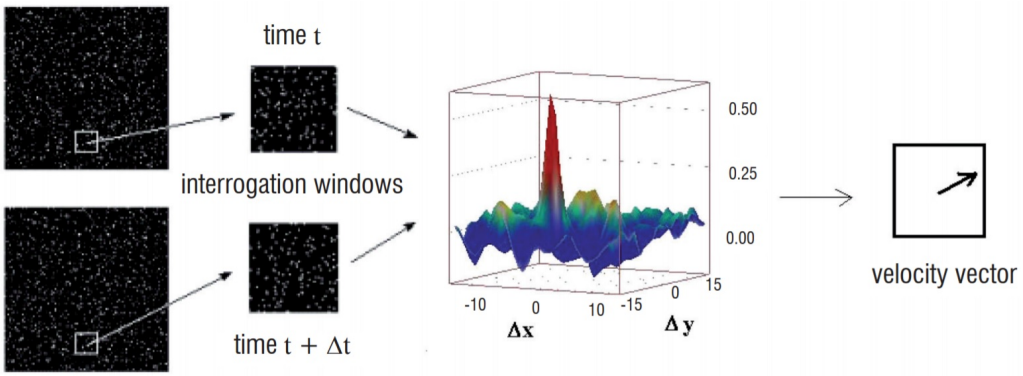

Figure 3.10: Cross-correlation of a pair of interrogation windows to obtain the displacement (Brossard et al. [20]).

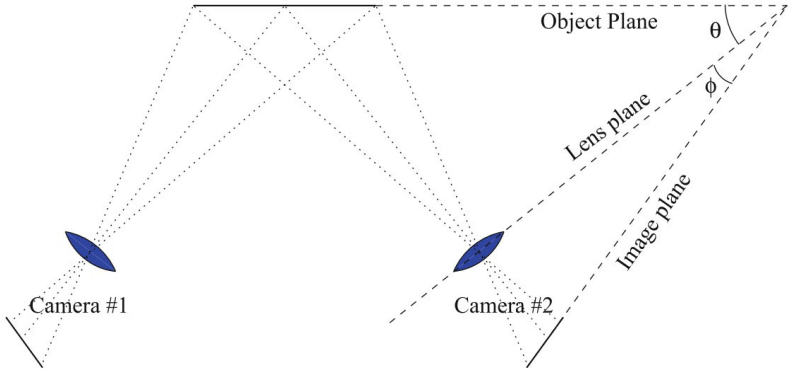

Figure 3.11: Stereoscopic imaging configuration satisfying Scheimpflug criterion (Raffel et al. [129]).

3.4.2 Applied PIV system

The TSI^{TM} PIV system applied in the related experiments is composed of a New Wave Solo-PIV 120 laser generator, a laser pulse synchroniser (Model 610036) and two CCD cameras. The Solo-PIV 120 laser generator is capable of firing two laser pluses in a rapid succession with a maximum power of $135mJ$ and a pulse width of $3 \sim 5ns$ at a repetition rate up to $15Hz$. The CCD cameras have a 12-bit intensity dynamic range and a maximum resolution of 2352×1768 (4 Mega) pixels. The cameras are capable of recording images at a frame rate of up to $16Hz$. The $532 \pm 10nm$ bandpass filter is installed on each of the Nikon AF $50mm$ $f/1.8D$ camera lens to further improve the image quality by reducing the intensity of the background light. The Dantec Dynamics HGS-10 (Hollow Glass Spheres) particles with a mean diameter of $10\mu m$ and density of $1.1 \times 10^3 kg/m^3$ are used as the seeding particles, which follow the motion of the fluid with high fidelity. To reduce the laser reflection and improve the quality of PIV

images near the wall, the riblet section is coated with a matt black paint. The thickness of the matt black paint is negligible and does not affect the measurement results. The reader is referred to Section 4.4.5, Section 5.3.3, Section 6.3.3 and Section 7.3.3 to obtain the detailed parameters of each specific PIV setup.

In each experiment, the PIV image pairs are processed using TSI^{TM} Insight 4G software to obtain the velocity vector fields. Prior to the PIV processing, a background image calculated by ensemble-averaging all available images is subtracted from each image. In the longitudinal plane or the cross-stream plane, due to high disparity in the displacements of particles in the near-wall flow and the freestream, the image deformation algorithm is applied during the processing.

The uncertainty of velocity component is estimated using the Peak Ratio (PR) method, which uses the Peak to noise Peak Ratio (PPR) to determine the uncertainty, and incorporates particle seeding density, pre-processing of image, pixel displacement and other possible sources to calculate uncertainty [23]. The PR method has been calibrated and incorporated in TSI^{TM} Insight 4G software. The PR method assumes that the errors in pixel displacement follow a Gaussian distribution. Therefore, the uncertainty is expressed with a corresponding confidence level.

3.5 Smooth-wall boundary layers validation

3.5.1 Laminar boundary layer characterisation

The freestream velocity is set as $U_\infty = 0.1m/s$ and the turbulence intensity in the freestream crossflow is about 0.2%. The Reynolds number based on the streamwise distance of the measurement station ($l = 715mm$) from the leading edge of flat plate ($Re_l = U_\infty l/\nu$) is 7.15×10^4, and the Reynolds number based on the momentum thickness ($Re_\theta = U_\infty \theta/\nu$) is 165.

The Blasius profile presents the theoretical solution of the steady two-dimensional laminar boundary layer over a flat plate placed parallel to the freestream [18]. The laminar boundary layer in the present experiment is compared with the Blasius profile. Figure 3.12 shows that the velocity profile measured at $x = 0.715mm$ fits well with the Blasius solution obtained assuming that the boundary layer starts from the leading edge, confirming that the boundary layer under investigation is close to a zero-pressure-gradient laminar boundary layer. Due to the surface reflection of the laser light, PIV data points in the region of $y/\delta < 0.1$ are not available.

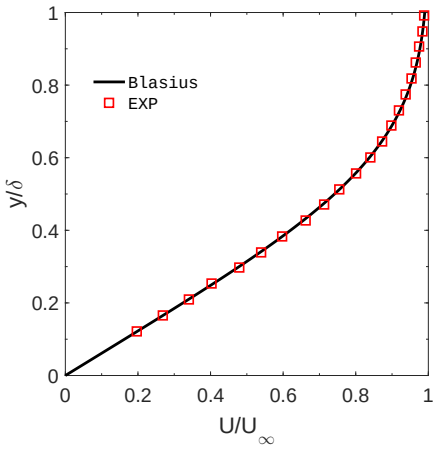

Figure 3.12: Comparison of the measured streamwise velocity profile in the laminar boundary layer with the Blasius profile.

3.5.2 Turbulent boundary layer characterisation

Similar to sandpaper or turbulator tape, the rod can be used as a tripping device to induce turbulence in the downstream region. The baseline turbulent boundary layer is tripped by a $4mm$ diameter rod installed $75mm$ downstream of the leading edge of the flat plate. The inclination angle of the flat plate is adjusted to zero degree to minimise the pressure gradient in the freestream region. The freestream velocity (U_∞) is $0.2m/s$. The turbulence intensity in the freestream region is around 0.7%, which is acceptable considering the low Reynolds number in the water flume. The acceleration parameter ($K = \nu(dU_\infty/dx)/U_\infty^2$) is approximately 5×10^{-8} in the measurement section. At the measurement station of $x = 450mm$, the boundary layer thickness (δ_s) is $32.5mm$ and the friction velocity ($U_{\tau s}$) is $9.75 \times 10^{-3} m/s$. The momentum thickness Reynolds number (Re_θ) is 723 and the friction Reynolds number (Re_τ) is 320.

A strategy is followed to establish the zero-pressure-gradient condition. The inclination angle of the flat plate can be adjusted by four steel legs with threads, and these legs were placed on the bottom floor of the water flume [see Figure 3.13]. In order to obtain an acceleration parameter ($K = \nu(dU_\infty/dx)$) close to zero, the inclination angle was adjusted multiple times. In the baseline case, the value of $K = 5 \times 10^{-8}$ in the test section ensures that the streamwise pressure gradient is nominally zero. The current velocity decay profile is found to be aligned with the reference case [164] in the outer region [see Figure 3.14], which confirms the zero-pressure-gradient condition.

Figure 3.15 shows the time-averaged streamwise velocity profile (U^+) of the turbulent boundary layer. For clarity of presentation, the data points in the high y^+ region

Figure 3.13: Front view of the leading edge and supporting thread legs of the flat plate. The test section of the plate is on the upper side and not shown here.

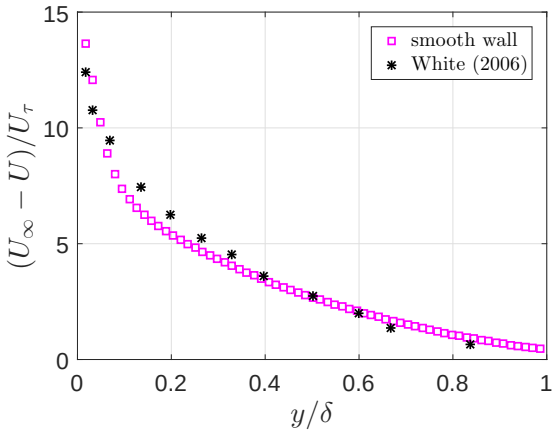

Figure 3.14: Time-averaged streamwise velocity defect profile $(U_\infty - U)/U_\tau$ as a function of outer coordinate y/δ.

are down-sampled. The friction velocity U_τ is estimated using the Clauser method [32]. The profiles of wind tunnel datasets at $Re_\theta = 617$ (Erm et al. [45]) and at $Re_\theta = 697$ (Erm et al. [44]) are utilised for comparison. DNS datasets at $Re_\theta = 670$ (Spalart [138]) and at $Re_\theta = 800$ (Wu et al. [167]) are also applied as references. The normalised mean velocity profile follows the log-law in the region of $30 < y^+ < 120$. Good consistency is well preserved in the inner layer, while some differences exist among these datasets in the wake region of $y^+ > 300$. Besides the minor difference in the Reynolds number, some other factors, e.g. the numerical method used to introduce turbulence, numerical discretisation scheme and resolution in simulations or the tripping device used to trigger laminar-turbulent transition in experiments [44], may also contribute to the discrepancies of the turbulent boundary layer. Overall, the baseline streamwise velocity profile is in good alignment with the reference profiles.

Figure 3.16 compares profiles of turbulence intensities of u'^+_{rms} and v'^+_{rms} (*rms* refers to the root mean square) with four reference datasets at similar Reynolds numbers.

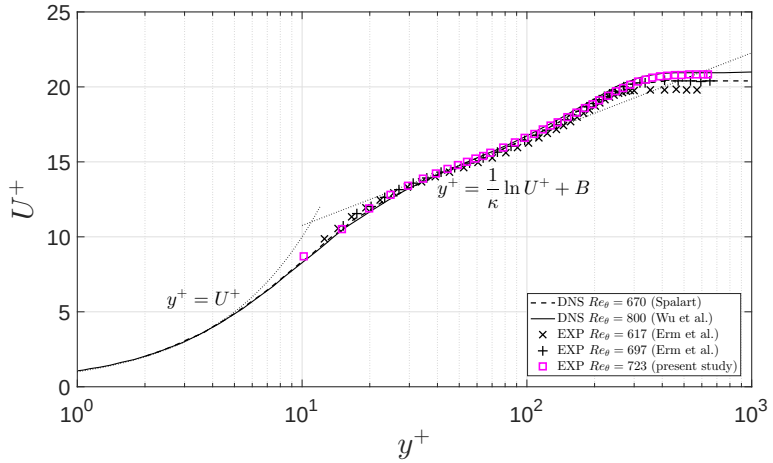

Figure 3.15: Time-averaged streamwise velocity profile U^+ as a function of inner coordinate y^+ of the turbulent boundary layer.

Overall, the profiles of turbulence intensities in the present experiment are quite comparable with these references. The peak value and its vertical position are similar among these datasets. Interestingly, the present turbulence intensity profiles are closer to the experimental data [45, 44] than the numerical simulation results [138, 167]. In the region outside the boundary layer, turbulence intensities of u'^+_{rms} and v'^+_{rms} in the present experiment are slightly larger than those in the aforementioned studies. In the experiments by Erm et al. [45, 44], the etched lengths of the hot-wire probe (l) are $1mm$ and $0.9mm$, which correspond to the normalised lengths (l^+) of approximately 32 and 29, respectively. Cameron et al. [22] mentioned that the hot-wire length of 22 viscous units or less should be applied for measuring velocity fluctuations in the near-wall region. Thus, the lower near-wall peak of u'^+_{rms} in the reference experiments by Erm et al. [45, 44] can be attributed to the problems with the hot-wire length.

Figure 3.17 compares profiles of the Reynolds shear stress ($-\overline{u'v'}^+$) of the turbulent boundary layer with four reference datasets [45, 138, 44, 167]. Despite the general agreement with these reference datasets in the profile shape, the peak value of $-\overline{u'v'}^+$ is slightly lower in the present experiment. At a low Reynolds number, Erm et al. [44] revealed that the Reynolds shear stress profile is affected by the parameters of the tripping device. Thus, the minor variation of $-\overline{u'v'}^+$ may be attributed to the selection of the tripping device and its instalment station.

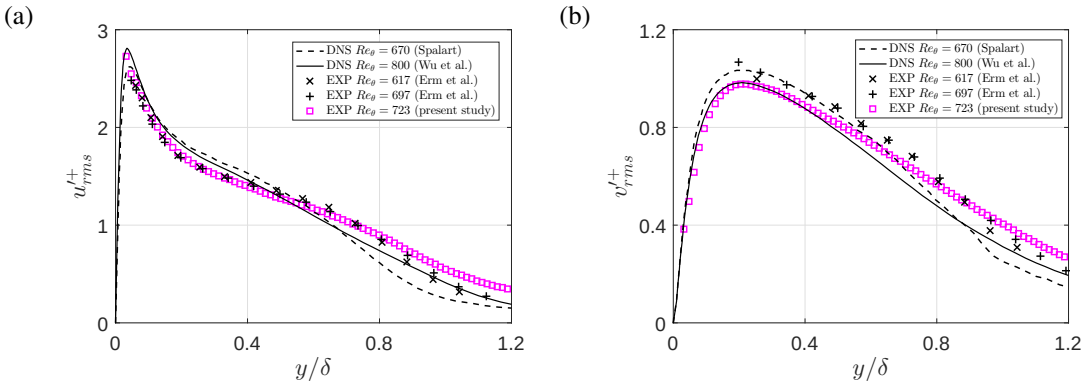

Figure 3.16: Turbulence intensity of (*a*) streamwise component u'^+_{rms}, (*b*) wall-normal component v'^+_{rms}, as a function of outer coordinate y/δ of the turbulent boundary layer.

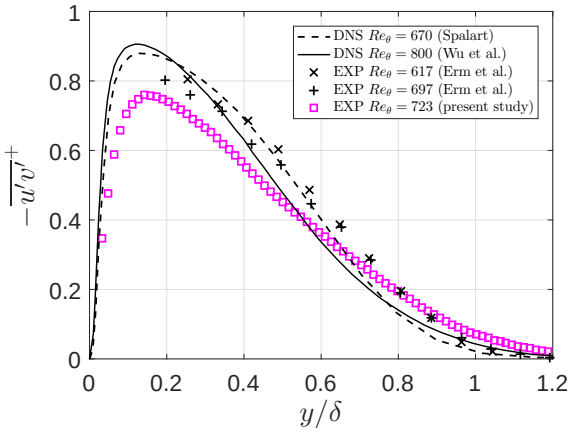

Figure 3.17: Reynolds shear stress $-\overline{u'v'}^+$ as a function of outer coordinate y/δ of the turbulent boundary layer.

Chapter 4

Vortical Structures and Development of Laminar Boundary Layer over Convergent-Divergent Riblets

F. Xu, S. Zhong, and S. Zhang. Vortical structures and development of laminar flow over convergent-divergent riblets. *Physics of Fluids*, 30(5):051901, 2018.

Submitted: 02 March 2018

Accepted: 11 April 2018

Published Online: 02 May 2018

DOI: 10.1063/1.5027522

Author	Fang Xu	Shan Zhong	Shanying Zhang
Rig design and setup	60%	15%	25%
Experimental measurement	60%	15%	25%
Paper writing	60%	25%	15%
Review feedback	60%	25%	15%
Overall	60%	20%	20%

Table 4.1: Author contribution to this peer-reviewed paper.

4.1 Abstract

In this work, the development of a laminar boundary layer over a rectangular convergent-divergent riblet section with a finite streamwise length is studied experimentally using

dye visualisation and PIV in a water flume. The flow topology over this highly directional spanwise roughness is established from this study. It is shown that convergent-divergent riblets generate a spanwise flow above the riblets from the diverging line towards the adjacent converging line. This consequently leads to the formation of a weak recirculating secondary flow in cross-stream planes across the boundary layer that creates a downwash motion over the diverging line and an upwash motion over the converging line. It is found that the fluid inside the riblet valley follows a helicoidal path and it also interacts with the crossflow boundary layer hence playing a key role in determining the structure of the secondary flow across the boundary layer. The impact of riblet wavelength on vortical structures is also revealed for the first time. A larger riblet wavelength is seen to produce a stronger upwash/downwash and hence a more intense secondary flow as well as a stronger deceleration effect on the crossflow. Furthermore, the streamwise development of the flow over the riblet section can be divided into a developing stage followed by a developed stage. In the developing stage, the magnitude of induced streamwise velocity and vorticity over the converging line continue to increase, whereas in the developed stage the values of these parameters remain essentially unchanged.

4.2 Nomenclature

$A_{\Delta U}$ (ms^{-1})	amplitude of induced velocity
A_{ω_y} (s^{-1})	amplitude of vorticity
h (m)	riblet height
h_p (m)	riblet protrusion height
L (m)	length of riblet section
l (m)	streamwise coordinate of the centre of riblet section
Re_θ (1)	momentum thickness Reynolds number
Re_l (1)	Reynolds number based on l
s (m)	riblet spacing
s_x (m)	riblet spacing projected in x direction
s_z (m)	riblet spacing projected in z direction
Tu (1)	turbulence intensity
U_∞ (ms^{-1})	freestream velocity
u (ms^{-1})	streamwise velocity
v (ms^{-1})	wall-normal velocity

W (m)	width of riblet section
$W_{\Delta U}$ (m)	width of converging/diverging region
w (ms^{-1})	spanwise velocity
x (m)	streamwise coordinate
y (m)	wall-normal coordinate
z (m)	spanwise coordinate
ν (m^2s^{-1})	kinematic viscosity
δ (m)	boundary layer thickness $(99\%U_\infty)$
γ (1)	riblet yaw angle
Λ (m)	riblet wavelength
λ_{ci} (s^{-1})	swirling strength
$\langle\lambda_{ci}\rangle$ (s^{-1})	signed swirling strength
ω_x (s^{-1})	vorticity in y-z plane
ω_y (s^{-1})	vorticity in x-z plane
ω_z (s^{-1})	vorticity in x-y plane
θ (m)	boundary layer momentum thickness

Abbreviation	
CL	converging line
DL	diverging line
FP	flat plate
PIV	particle image velocimetry
TIU	total induced velocity

4.3 Introduction

Longitudinal (streamwise) riblets have been studied since 1980s [159, 160] and a large volume of research work has been undertaken in laminar boundary layers [26, 40, 127], transitional boundary layers [54], and turbulent boundary layers [28, 81, 15]. The drag reduction performance and the control mechanism of longitudinal riblets are well-understood. It has been reported that longitudinal riblets are capable of delivering a reduction of surface friction drag around 10% in a turbulent boundary layer [161, 15]. The drag reduction mechanism of longitudinal riblets is attributed to the damping of crossflow fluctuations [51, 52, 42] or the uplift of turbulent streamwise vortices above the riblet valley [27, 143, 85, 50]. There are some comprehensive reviews of the

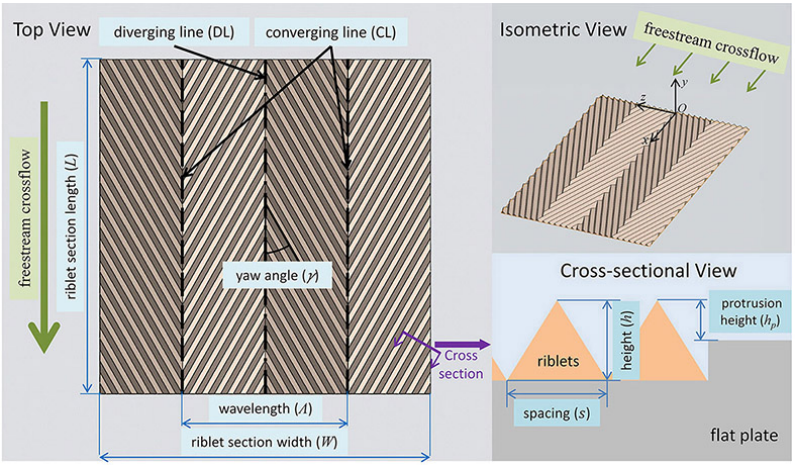

Figure 4.1: Schematic diagram of convergent-divergent riblets parameters. Converging line (*CL*) and diverging line (*DL*) are defined intuitively from the arrangement of the riblets relative to the freestream direction. The converging/diverging region is referred to the region close to the converging/diverging line.

advances in research on longitudinal riblets [155, 38, 49].

Convergent-divergent riblets studied in this paper are new types of directional surface roughness patterns which begin to attract research attention more recently. For these types of surface patterns, sections of riblets with a negative yaw angle and a positive yaw angle with respect to the freestream direction are arranged in an alternative manner in the spanwise direction, see Figure 4.1. The patterns of convergent-divergent riblets are inspired by nature. Converging riblet patterns are found upstream of the sensory receptors of sharks, whereas the diverging patterns are observed upstream of the hearing sensors of these animals [79]. Diverging riblet patterns (also called herringbone riblets) also appear on the secondary flight feathers of different species of birds [25].

Koeltzsch et al. [79] studied the flow in a pipe whose inner surface was fitted with riblet films arranged obliquely, with -45° yaw angle in one half of the pipe circumference and $+45^\circ$ yaw angle in the other. They observed an increase in the local streamwise velocity and a decrease in turbulent fluctuations over the diverging riblet pattern, and the opposite effect was found over the converging riblet pattern. Inspired by this finding, a series of experimental studies on convergent-divergent riblets has been carried out in a flat plate turbulent boundary layer at the University of Melbourne. Similar results to those reported by Koeltzsch et al. [79] were also obtained by Nugroho et al. [113]. Using a cross-wire, Nugroho et al. [114] revealed the presence of a large-scale counter-rotating roll mode in the time-averaged flow field in cross-stream planes. Their

finding was also confirmed and extended by Kevin et al. [72] with their stereoscopic PIV measurements. In accordance to the sense of rotation of the counter-rotating roll mode, the fluid in the region over the diverging line appears to be directed towards the wall (downwash), whereas the fluid in the region over the converging line is seen to be directed away from the wall (upwash).

There is an inherent difference between the vortical structures induced by convergent-divergent riblets and those induced by longitudinal (streamwise) riblets. The spanwise length scale of the vortical structures induced by longitudinal riblets has the same order as that of the riblet spacing s [28, 51]. The effects of longitudinal riblets are known to be confined in the vicinity of the riblet surface [40, 60] via suppression of streamwise vortical structures in the near-wall region [150, 54]. In contrast, the spanwise length scale of the vortical structures produced by the convergent-divergent riblets is comparable to the riblet wavelength Λ or the boundary layer thickness δ [72], which could be one or two orders of magnitude larger than that of the riblet spacing s. As such, the whole boundary layer can be affected [113].

The global effects of convergent-divergent riblets on a flow field have also been explored by some researchers. Chen et al. [25] carried out an experiment in a fully-developed turbulent pipe flow and reported that pipes covered with spanwise arrays of convergent-divergent riblets with diminishing heights towards their edges yield a drag reduction. With an optimal yaw angle of 30° and an optimal riblet height of 20 viscous wall units, a 21% skin-friction drag reduction was reported, which is significantly larger than what longitudinal riblets could ever offer ($\sim$ 8% in Walsh [161], 9.9% in Bechert et al. [15]). In a linear cascade experiment, Liu et al. [87] demonstrated that herringbone riblets fitted on blade suction surfaces were capable of reducing pressure losses by suppressing flow separation at low Reynolds numbers. Such flow control benefits have been attributed to the large scale streamwise vortical structures produced by convergent-divergent riblets. It is envisaged that convergent-divergent riblets could have a broad engineering application prospect including surface friction drag reduction, suppression of flow separation and heat transfer augmentation.

In contrast to the large quantity of studies on longitudinal riblets, there are only a very limited number of studies on convergent-divergent riblets, see Table 4.2. There has been no research investigating how the flow initially develops itself over these surface patterns. Such a study will be meaningful to practical applications, such as turbine blades, for which, due to their short streamwise extent, knowledge of the early stage of flow development over the riblet section is essential to maximise the effect of

the surface roughness to the flow. It is known that the convergent-divergent riblets act to divert some flow near the surface away from the converging region, leading to the generation of spanwise flow and the counter-rotating vortex pairs. However, there is a lack of understanding as to how the small-scale flow motion inside riblet channels contributes to the establishment of the large-scale motion. Furthermore, in most of the existing experimental studies the wavelength of the convergent-divergent riblets is chosen arbitrarily and hence it is not clear how the wavelength affects the strength and the characteristics of the induced secondary flow.

Therefore, in this paper the development of a flat plate laminar flow over a section of surface covered with convergent-divergent riblets of different wavelengths is investigated in a water flume. Dye visualisation technique is firstly used to visualise the small-scale fluid motion inside riblet valleys and the way that it interacts with the cross-flow over riblet crests. Mono PIV is then used to investigate the impact of the riblets on the boundary layer development over the converging region and diverging region respectively. Finally, stereoscopic PIV is employed to examine the vortical structures in the cross-stream plane. From the analysis of these results, the flow topology over convergent-divergent riblets is established and the effect of riblet wavelength on the strength and characteristics of the secondary flow is understood for the first time.

The use of a laminar boundary layer instead of a turbulent one in this study enables a clearer flow topology and hence allows a better understanding of the associated flow physics to be established without the interference of complex turbulent events. Considering the fact that convergent-divergent riblets are observed on both shark skin and bird feathers, such surface patterns are likely to find applications in both low Reynolds number flows where laminar flow exists and high Reynolds number flows where the flow is fully turbulent. Therefore, the finding from our study could directly benefit practical applications in low Reynolds number flows. Furthermore, understanding the impact of convergent-divergent riblets on a laminar boundary layer forms a logical first step towards understanding their effects on a turbulent boundary layer.

4.4 Experimental setting

In this section, the experimental settings of the water flume, convergent-divergent riblets, the dye visualisation system and PIV systems are described, and the nondimensionalisation of the coordinate system is provided.

Research	Model	Section (m)	Measure	Re	h (h^+) (μm)	s (s^+) (μm)	γ (deg)
Koeltzsch et al. [79]	pipe	0.2 (L), 0.07 (R)	HWA	5.2×10^5	152 (19)	152 (19)	45
Nugroho et al. [115]	plate	0.515 (L), 0.296 (W)	HWA	1900	500 (17)	675 (23)	30
Nugroho et al. [112]	plate	0.515 (L), 0.296 (W)	HWA	1300/2300	500 (13/24)	675 (18/32)	10
Nugroho et al. [113]	plate	$1-4$ (L), 0.296 (W)	HWA	$771-3120$	500 ($6.7-24.4$)	675 ($9-33$)	10/30
Chen et al. [24]	pipe	0.4 (L), 0.026 (R)	PG	$1.4-3.7\times10^5$	60 (19)	100	30
Chen et al. [25]	pipe	0.6 (L), 0.026 (R)	PG	$1.1-4.7\times10^5$	60 (19)	100	$0-60$
Kevin et al. [73]	plate	0.515 (L), 0.296 (W)	PIV	...	500 (18)	675 (24)	20
Kevin et al. [72]	plate	4 (L), 0.296 (W)	sPIV	3900	500 (18)	675 (24)	20

Table 4.2: A summary of experimental parameters in existing studies. In pipe flows, Reynolds number $Re_D = \overline{U}D/\nu$, where D is the hydraulic diameter. For flat plate flows, $Re_\tau = u_\tau L/\nu$, where u_τ is the friction velocity. HWA - hot-wire anemometry, PG - pressure gauge, PIV - (mono) particle image velocimetry, sPIV - stereoscopic particle image velocimetry.

4.4.1 Water flume

Our experiments are conducted in a water flume at the University of Manchester, which is depicted in Figure 4.2a. The water flume is $3.64m$ long and it has a $0.305m \times 0.305m$ cross-section. Both the side walls and the bottom floor of the test section are made of transparent glass to provide an optical access required for the PIV system. The fluid in the flume is driven by a centrifugal pump which draws water from the holding tank into the entry tank. To ensure a uniform flow with low turbulence level in the test section, the fluid is made to pass through a set of guiding vanes and a honeycomb before it goes through four metal screens arranged in a decreasing order of mesh size. The freestream velocity and water level in the test section are controlled by changing the rotating speed of the centrifugal pump with a digital inverter and an opening of the adjustable permeable grate installed at the outlet of the flume.

An aluminium flat plate ($1380mm$ long, $300mm$ wide, $6mm$ thick) is installed horizontally in the water flume with its test surface facing downward. In this setup, the use of a $1:5$ super-elliptical leading edge together with a negative inclination angle (-0.3°) of the flat plate is found to be effective in ensuring that an attached laminar boundary layer is obtained right from the leading edge [106]. A small gap is left between the flat plate and each side wall of the test section to restrain the growth of side wall boundary layers along the length of the flat plate. The stereoscopic PIV data of the baseline flow field (not shown here) confirms the $2D$ characteristics of the boundary layer flow across the width of the convergent-divergent riblet section. In this experiment, the freestream velocity is set as $U_{\infty} = 0.1m/s$ and the turbulence intensity in the freestream crossflow is about 0.2%. The Reynolds number based on the streamwise distance of the measurement station ($l = 715mm$) from the leading edge of flat plate ($Re_l = U_{\infty} l/\nu$) is 7.15×10^4, and the Reynolds number based on the momentum thickness ($Re_{\theta} = U_{\infty}\theta/\nu$) is 165. As shown in Figure 4.2b, the velocity profile measured at this location fits well with the Blasius solution obtained assuming that the boundary layer starts from the leading edge, confirming that the boundary layer under investigation is close to a zero-pressure-gradient laminar boundary layer.

4.4.2 Convergent-divergent riblets

The disc plate containing the convergent-divergent riblets is made with clear resin using $3D$ printing technique. It has a diameter $D = 132mm$ and it can be flush-mounted into the test plate as an insert. The centre of this disc is located at $715mm$ downstream

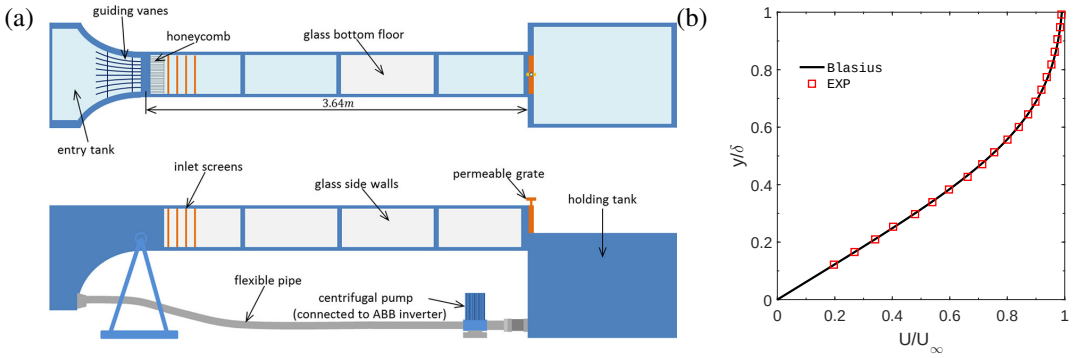

Figure 4.2: (a) Schematic diagram of the water flume in the top view (upper) and the side view (lower). (b) Comparison of the measured streamwise velocity profile in the experimental section at $x = 0.715mm$ with the Blasius solution.

of the leading edge of the test plate. The cross-sectional shape of the riblets is triangular with $s = 3mm$ and $h = 2.4mm$, see Figure 4.1. The protrusion height (h_p) of convergent-divergent riblets is $1.2mm$, which indicates that the smooth wall levels with half of the riblet height ($h_p = h/2$). The blockage ratio, i.e. the protrusion height of the riblets to the flat plate boundary layer thickness (h_p/δ_{FP}), is about 9% at the start of the riblet section. With both the layer thickness and the particles diameter being set as $25\mu m$, the resolution of $3D$ printing ($\sim 1\%$ of the riblet spacing or the riblet height) is considered excellent for the present setup. The angle between tilted riblets and the freestream direction is the yaw angle (γ). The optimal yaw angle of $\gamma = 30^\circ$ identified by Chen et al. [25] in their turbulent pipe flow experiment is adopted in this experiment. The overall length and width of the riblet section is $L = 90mm$ by $W = 90mm$. Riblet sections with a wavelength of $30mm$, $36mm$ and $45mm$ are tested in this experiment. The total number of riblet wavelengths accommodated on the disc plate is hence 3.0, 2.5 and 2.0 respectively.

4.4.3 Nondimensionalisation of coordinate system

The coordinate system is shown in Figures 4.1 and 4.3c, with axes x, y and z representing the streamwise, wall-normal and spanwise directions respectively, and the corresponding velocity components are u, v and w respectively. $x = 0$ is located at the beginning of the convergent-divergent riblet section, which is $670mm$ downstream of the leading edge of the flat plate. $y = 0$ is chosen to coincide with the smooth surface (level with the mid height of the riblets), and $z = 0$ is located at the converging/diverging line closest to the middle in the spanwise direction.

To provide nondimensional length scales, the three coordinate axes are normalised as follows. The streamwise coordinate x is normalised by the riblet spacing projected in the longitudinal plane ($s_x = s/sin\gamma = 3mm/sin30^\circ = 6mm$). Thus, x/s_x indicates the number of riblets in the streamwise direction. The wall-normal coordinate y is normalised by the local boundary layer thickness of the flat plate (δ_{FP}). The spanwise coordinate z is normalised by the wavelength of convergent-divergent riblets (Λ).

4.4.4 Dye visualisation system

The setup of the dye visualisation experimental system includes dye injection, illumination and image acquisition. In the present experiment, the dye is fed from a $3D$ printed cavity through five rubber tubes, which are connected to the five dye injection orifices on the disc plate located at a small distance of $10mm$ upstream of the riblet section. The dye flow rate through each rubber tube can be individually controlled using tube clips. The top side of the disc plate with convergent-divergent riblets remains translucent, whereas the bottom side is painted white to increase the contrast of dye images. The remaining part of the disc plate is painted black.

During the experiment, the riblet section is illuminated using four white light-emitting diode (LED) light sources through the glass side walls of the flume. To avoid producing shadows of dye streaklines on the riblet surface, lighting from the top is not used. The dye visualisation images are captured using a Canon $D70$ SLR camera fitted with a Canon EF-S $18-135mm$ F3.5 $-$ 5.6 IS lens. The camera is operated using a remote control mode to minimise its movement. The aperture of the camera lens is set as 11.0 in the side view and 5.6 in the top view. The smaller aperture used for the side view enables a larger depth of view across the span.

4.4.5 Particle image velocimetry system

The PIV system from TSI used in this experiment is composed of a New Wave Solo-PIV 120 laser generator, a laser pulse synchroniser (Model 610036) and two CCD cameras. The Solo-PIV 120 laser generator is capable of firing two laser pluses in a rapid succession with a maximum power of $135mJ$ and a pulse width of $3 \sim 5ns$ at a repetition rate up to $15Hz$. The CCD cameras have a 12-bit intensity dynamic range and a maximum resolution of 2352×1768 (4 Mega) pixels. The cameras are capable of recording images at a frame rate of up to $16Hz$. A $532 \pm 10nm$ bandpass filter is installed on the Nikon AF $50mm$ $f/1.8D$ camera lens to further improve the

image quality by reducing the intensity of the background light. The Dantec Dynamics HGS-10 (Hollow Glass Spheres) particles with a mean diameter of $10\mu m$ and density of $1.1 \times 10^3 kg/m^3$ are used as the seeding particles. The settling velocity of these particles is $5 \times 10^{-6} m/s$, ensuring that particles follow the motion of the fluid with high fidelity. To reduce the laser reflection and improve the quality of PIV images near the wall, the riblet section is coated with a matt black paint.

The layouts of the mono-PIV measurements in the longitudinal $(x-y)$ plane and the wall-parallel $(x-z)$ plane are shown in Figures 4.3a and 4.3b respectively. The aperture of the lens is set as $f/4.0$. The time interval between two laser pulses is chosen to be $6ms$ for the longitudinal plane and $2.5ms$ for the wall-parallel plane. The distance from the laser head to the measurement section is about $1m$. The width of the laser light sheet is around $1mm$. A total of 1250 image pairs are captured at an acquisition rate of $2Hz$, which is more than sufficient to ensure the convergence of the time-averaged flow field characteristics. In order to capture the flow field across the entire disc plate and beyond, mono-PIV measurements are taken on two overlapping longitudinal planes separately, as illustrated in Figure 4.4, and the data in these two planes are then merged together at the post-processing stage. In the wall-parallel plane, the centre of the laser light sheet is approximately $3mm$ from the smooth wall surface.

The PIV image pairs are processed using TSI InSight $4G$ software to obtain the velocity vector field. The first interrogation area is 96×32 pixels, and the final interrogation area is 32×32 pixels with 50% overlap. In the longitudinal plane, the field of view is $85mm \times 64mm$, yielding a velocity vector field with a spatial resolution of $0.58mm \times 0.58mm$. In the wall-parallel plane, the field of view is $138mm \times 104mm$, resulting in a spatial resolution of $0.94mm \times 0.94mm$. In the longitudinal plane, due to the high disparity in the displacements of particles between near-wall flow and the freestream, the image deformation algorithm is applied during post-processing. The measurement uncertainties in velocity components are estimated using the Peak Ratio (PR) method, which includes factors such as the particle seeding density, the preprocessing of images, the pixel displacement and other possible sources in determining the uncertainty [23]. For an instantaneous flow field, the expanded uncertainty in velocity components, i.e. 95.4% possibility of having the true value within the uncertainty bound, is estimated to be $0.43\%U_\infty$ in the longitudinal plane and $0.91\%U_\infty$ in the wall-parallel plane. In the averaged flow field of 1250 image pairs, the expanded uncertainty in velocity components is $0.05\%U_\infty$ in the longitudinal plane and $0.28\%U_\infty$ in the wall-parallel plane.

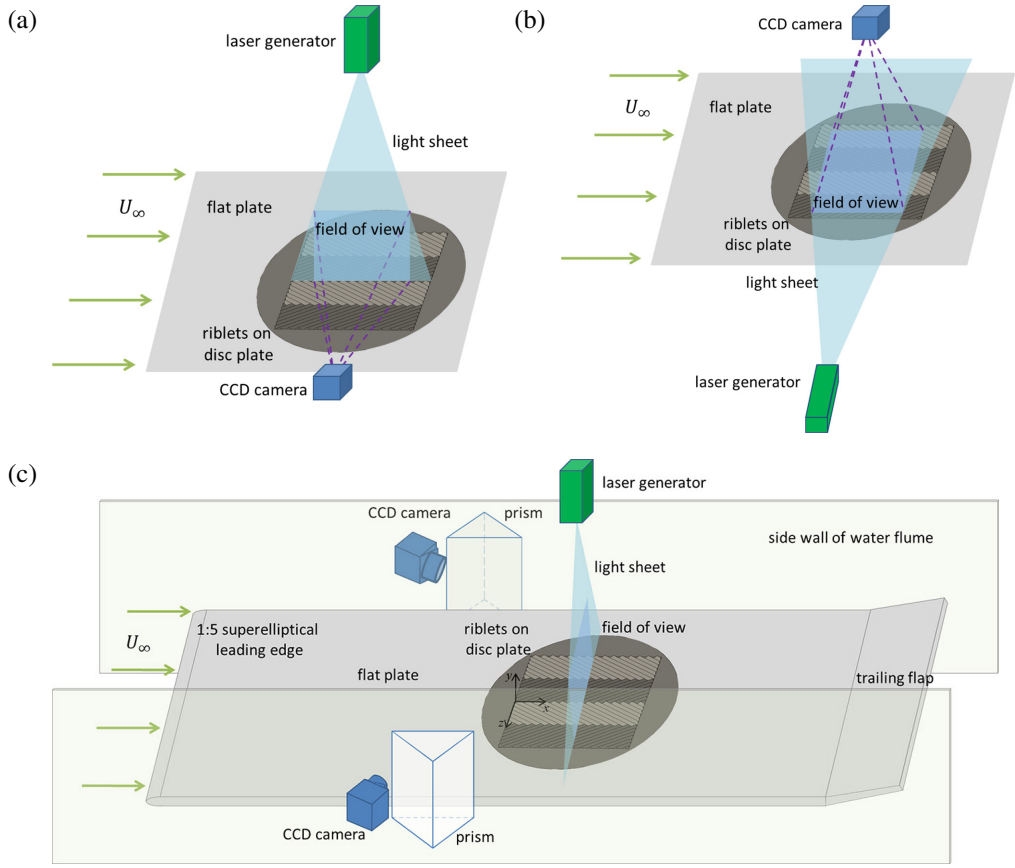

Figure 4.3: Mono PIV system arrangement in (a) the longitudinal plane, (b) the wall-parallel plane. (c) Schematic diagram of the stereoscopic PIV system in the cross-stream plane. The test surface is inverted to enable a better illustration of the setup.

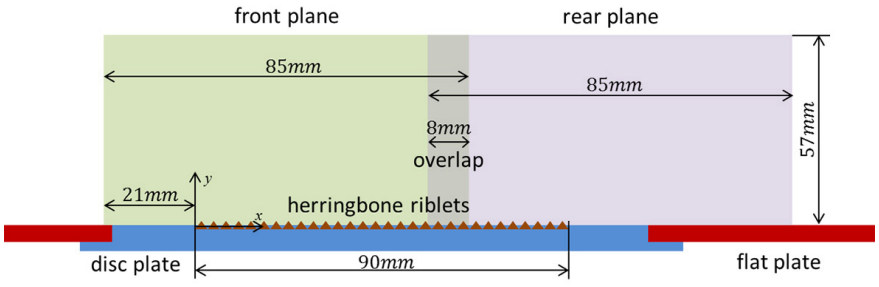

Figure 4.4: Schematic of two measurement planes with an overlapping region in mono-PIV measurements in the longitudinal plane.

In stereoscopic PIV, the cross-stream $(y-z)$ plane is located at $x = 12.5s_x$. One 4 Mega pixel CCD camera and a water-filled prism are installed at each side of the water flume, as shown in Figure 4.3c. The locations of the cameras are adjusted according to the Scheimpflug principle. The camera calibration is undertaken using a TSI $200mm \times 200mm$ calibration target plate, and the perspectives of cameras are optimised by the ensemble-averaged unwrapped velocity field. The time interval between the two laser pulses is set as $2.5ms$, and 1250 image pairs are captured at low acquisition rate of $1Hz$. The first interrogation area of 64×24 pixels and the final interrogation area of 24×16 pixels with 50% overlap are applied. The field of view, i.e. the intersection of two dewarped perspectives, is $87mm \times 40mm$. The perspective view leads to the gradation of spatial resolution, which is $0.59mm \pm 15\%$ in the spanwise direction and $0.24mm \pm 8\%$ in the wall-normal direction. For the averaged flow field of 1250 image pairs, the expanded uncertainty in velocity components is $0.16\%U_\infty$.

4.5 Micro-scale and large-scale vortical structures

Our experimental study starts with a dye visualisation of the flow over the riblet section and inside riblet valleys (micro-scale). The results are then correlated with the stereoscopic PIV data obtained in the cross-stream plane which reveal the large-scale vortical structures produced by the convergent-divergent riblets across the boundary layer. By synthesizing the findings from both the dye visualisation and the PIV measurement, the flow topology of convergent-divergent riblets is proposed.

4.5.1 Dye visualisation over riblet section

The dye visualisation experiment is carried out on convergent-divergent riblets with a wavelength of $45mm$. Figure 4.5a shows the side view and the top view of the dye visualisation images with the diverging line coinciding with the streamwise centreline of the disc plate. Red dye is injected through the central orifice D, which is located directly upstream of the diverging line. The images are instantaneous and they exhibit little changes in time indicating the steady nature of the flow. To illustrate the streaklines clearly, the side view is stretched vertically by a factor of 2.0.

It can be seen from the dye images in the top view that, when the dye released from the orifice encounters the foremost apex of riblet ridges located along the diverging line, it splits into two streams ($S3$), one on each side of the diverging line. Each

stream enters into a riblet valley and moves helicoidally along the valley till it reaches the converging line on the corresponding side. As the dye streamline reaches the converging line, it makes an abrupt turn and starts to flow in the streamwise direction. It is from this point ($PD1$) onwards that the dye starts to emerge from the riblet valley and to move above the riblet crest, making the streaklines becoming visible from the side view. As the dye flows through the riblet valley, a small portion of it spills over the riblet crest and is carried downstream by the main flow. The inner boundary of this overflow region over the riblet surface is indicated by the slant dashed lines. The overflow near the converging line is particularly strong producing further streaklines which are observed from the point $PD2$ in the side view.

Dye visualisation with the converging line coinciding with the streamwise centreline of the disc plate is also conducted by rotating the disc plate by 180°. This time, the dye is injected through an array of five orifices. The top view and the side view of the dye flow images are shown Figure 4.5b. The symmetric distribution of streaklines in the top view confirms the high quality in setting up the experiment.

In the top view, the dye from orifice C appears to follow the central converging line all the way downstream. The streakline from M is seen to split into two streams ($S1$ and $S2$) which enter the two adjacent riblet valleys respectively and flow towards the central converging line. Before arriving at the central converging line, a small portion of the dye ($S2$) spills over the riblet crest as overflow (gray dashed lines) and propagates downstream. The overflow of fluid above the riblet crest is unsteady, causing disturbances to the flow field. A majority of the dye reaches the converging line and becomes visible at $PM2$ in the side view. Similar to what has already been observed in Figure 4.5a, the dye streakline from orifice D is seen to be split into two streams ($S3$ and $S4$) when it encounters the foremost apex of riblet ridges. While $S3$ follows one riblet valley and flows towards the central converging line, $S4$ follows another riblet valley and flows towards another converging line located one wavelength apart at the edge of the riblet section. The slight asymmetric appearance in $S3$ and $S4$ seen in Figure 4.5b is due to the ending of the riblet section on one side which is absent in Figure 4.5a. To minimise the impact of the end effect on the results, the PIV data presented in this paper are always taken with the corresponding converging/diverging line as close to (if not on) the spanwise central line of the disc plate. In the top view, the overflow of the dye over the riblet crest lines as the dye flow through riblet valleys towards the converging lines can be observed clearly.

In the side view, one can see that the streakline originated from orifice C emerges

from the wall surface at *PC* and it continues to move further away from the wall as it propagates downstream. Since the dye below the riblet crest is invisible in the side view, there exists a small offset between the streamwise locations where the dye is seen to enter the converging line in the top view and where it becomes visible in the side view. Over this distance, the dye moves along the converging line in the streamwise direction and lifts up in the wall-normal direction before reaching the crest level. Upon reaching the central converging line, the streakline $S1$ lifts up vertically and becomes visible at $PM1$. Since the two streaklines from $PM1$ and $PM2$ are very close in wall-normal position, they appear as one streakline in the side view. The streakline $S3$ eventually appears in the side view at $PD1$.

From the direction of movement of the dye ($S1$, $S2$, and $S3$) in the top view, one can conclude that a secondary flow over the riblets from the diverging line towards the adjacent converging line is generated by convergent-divergent riblets. The flow gathers along the converging line and then lifts up away from the wall as revealed in the side view. Longitudinal riblets are known to stabilise the turbulent crossflow inside riblet valleys and to suppress near-wall momentum transfer in the spanwise direction [28, 150, 85]. The convergent-divergent riblets seem to affect the crossflow differently.

4.5.2 The helicoidal motion inside riblet valleys

The dye visualisation images in Figures 4.5a and 4.5b clearly show that the dye injected from the five orifices does not travel inside a riblet valley in a straight line; it moves from side to side and also up and down. In fact, it moves along a helicoidal path inside the riblet valley, i.e. the fluid rotates around an axis as it moves along the riblet valley. The flow inside the riblet valley can be regarded as a channel flow under the influence of a freestream crossflow with a yaw angle γ. The interaction between the crossflow and the axial flow along the valley generates a secondary flow inside the valley and hence the helicoidal motion. A close-up view of the streaklines of dye, which is injected through four orifices ($H1$ to $H4$) located at the bottom of riblet valleys next to the central diverging line, also confirms this. The (right-handed) helicoidal path of the dye is clearly revealed in Figure 4.6a and depicted schematically in Figure 4.6b. In the latter figure, the dashed line indicates the axis of the helix and the colour gradient indicates the spatial location in the plane perpendicular to the axis. The sense of rotation of the helicoidal path follows the right-hand rule.

In Figure 4.6a, it is also seen that the colour intensity of streaklines varies significantly along the helicoidal path, and between the converging and diverging line a

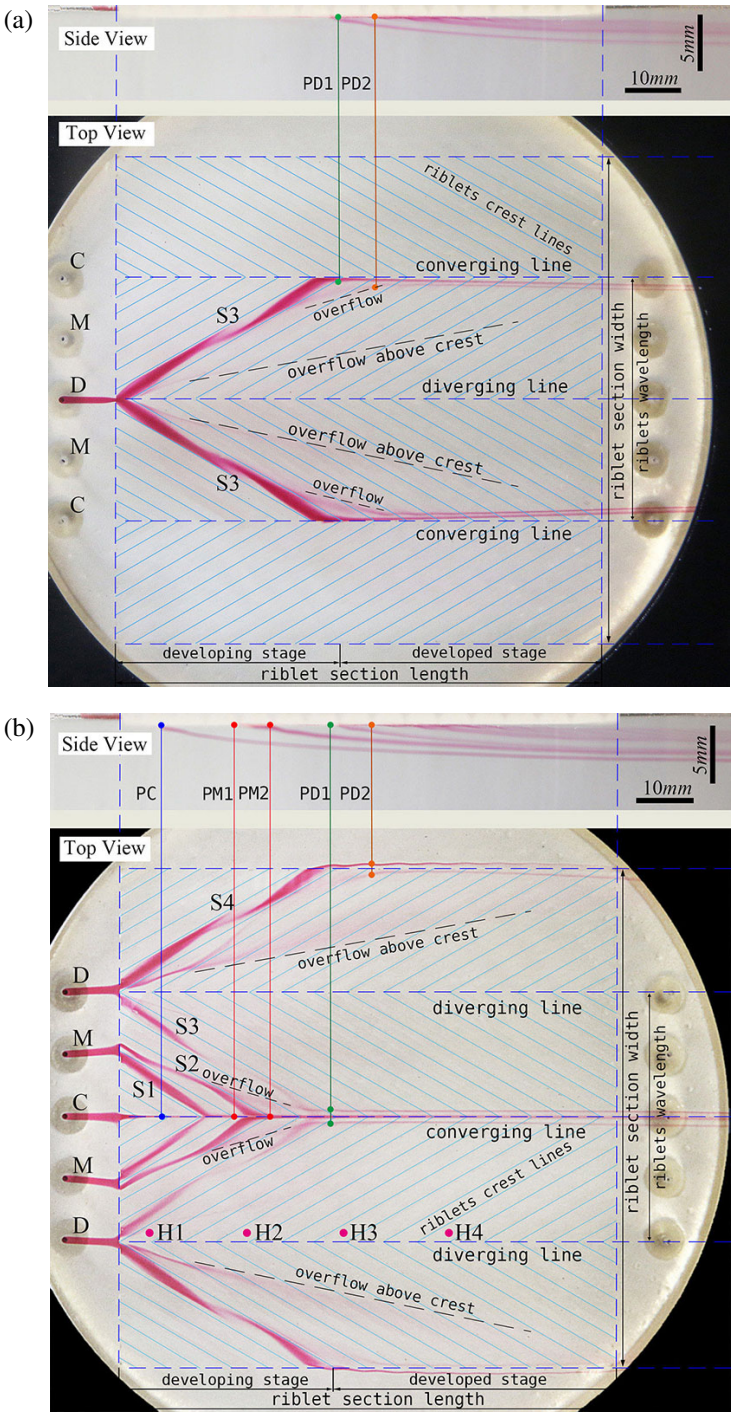

Figure 4.5: Dye visualisation in the side view (upper) and the top view (lower) with (a) the diverging line, (b) the diverging line coinciding with the streamwise centreline of the disc plate. Labels *C*, *D* and *M* indicate the dye orifices aligned with the converging line, the diverging line, and the middle section in between, respectively.

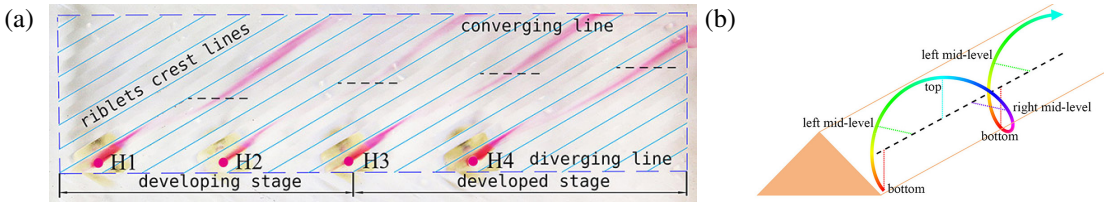

Figure 4.6: (a) Dye visualisation image of the helicoidal motion of the dye inside riblet valleys. Dye is injected to the bottom of the valleys through dye orifices $H1-H4$ [refer to Figure 4.5b for locations]. (b) Schematic diagram of the helicoidal path of the dye inside a riblet valley in $3D$ perspective.

portion of the streaklines even temporarily disappears. This is caused by variations in the velocity along the helicoidal path. Within the riblet valley, the portion of the streakline close to the wall surface has a lower velocity and hence is less stretched. Consequently, it appears to be darker in colour. In contrast, the portion of the streakline near the top of the valley travels faster, resulting in a reduction in the diameter of streakline and hence a lower dye concentration. As such, the colour of the dye becomes lighter and the streakline may seem to have disappeared temporarily. The streakline becomes visible again further along the valley as its velocity reduces when it dives down to the bottom of the valley again. In Figure 4.6a, the dashed lines indicate the locations when the streaklines originated from $H1$ to $H4$ touch the windward of each respective riblet valley. The pitch of the helicoidal motion is the distance along the valley covered by one complete rotation, which increases in the streamwise direction. An increase in pitch implies a higher axial component in the helicoidal motion.

4.5.3 Large-scale vortical structures in the cross-stream plane

The dye visualisation images mainly provide information about the flow both inside riblet valleys and slightly above riblet crests. In order to examine the impact of convergent-divergent riblets on the entire boundary layer, stereoscopic PIV measurements are conducted. Figure 4.7 shows the in-plane velocity vectors at $x = 12.5s/sin\gamma$ of convergent-divergent riblets with a wavelength of $30mm$, $36mm$ and $45mm$ respectively. The contours of the signed swirling strength $\langle\lambda_{ci}\rangle$ and streamlines are also superimposed on the velocity vector field to assist the identification of vortex cores, if they are present. The signed swirling strength $\langle\lambda_{ci}\rangle = (\omega/|\omega|)\cdot\lambda_{ci}$ was proposed by Zhou et al. [182] to analyte the local swirling motions, wherein λ_{ci} is the imaginary part of the complex-conjugate eigenvalue of velocity gradient tensor and ω is the in-plane vorticity. Here,

$\langle\lambda_{ci}\rangle$ is calculated for each instantaneous flow field, and all the instantaneous snapshots (1250 image pairs in total) are then averaged to derive the contour in Figure 4.7. Due to geometric symmetry, only the flow field over half of a wavelength of the convergent-divergent riblets is displayed. Triangles indicate the real geometries of the riblets. The dot/cross symbol indicates the centre of the primary/secondary vortex. There are 4.3, 5.2 and 6.5 riblets respectively across the spanwise width of half of a wavelength for the three different riblet wavelengths studied here. Note that the horizontal axes of this figure are normalised with the riblet wavelength (Λ), which is different among these three cases, and hence the flow structures are not scaled in physical size. In the spanwise direction, among every four velocity vectors only one vector is kept, and in the wall-normal direction every vector is plotted. The local boundary layer thickness of the flat plate is $\delta_{FP} = 13.2mm$.

In Figure 4.7, a spanwise flow from the diverging line to the converging line in the near-wall region is clearly revealed by the direction of velocity vectors and this is consistent with that observed in the dye visualisation images presented in Figures 4.5a and 4.5b. It is also established that this near-wall flow is part of a large-scale recirculating secondary motion in the cross-stream plane which extends itself across the entire boundary layer. In particular, an upwash motion dominates over the converging region whereas a downwash motion dominates over the diverging region. This observation is in agreement with the finding from previous experiments [113, 114, 72].

A comparison of the control effects between convergent-divergent riblets and synthetic jet is provided. In the active flow control experiments with synthetic jets, the upwash and downwash of fluid in the near-wall region are induced by the rotations of hairpin legs [179, 172], with an upwash leading to a decreased local skin friction and a downwash resulting in an increased one. For convergent-divergent riblets, the upwash and downwash in the near-wall region are produced by the highly directional spanwise surface patterns instead. Over the diverging line, the downward moving fluid is diverted along the valleys as it approaches the wall surface. The fluid subsequently collides over the converging region, leading to an increased skin friction drag whereas a decreased drag is obtained over the diverging line [114, 72].

A pair of co-rotating vortical structures with cores located at $y/\delta \approx 0.2$ can also be identified from the in-plane streamlines. For longitudinal riblets, such a large-scale vortical structure in the secondary flow is absent [85]. Note the magnitude of the wall-normal or the spanwise component is about two orders of magnitude smaller than the freestream velocity, implying that the strength of these two vortical structures is

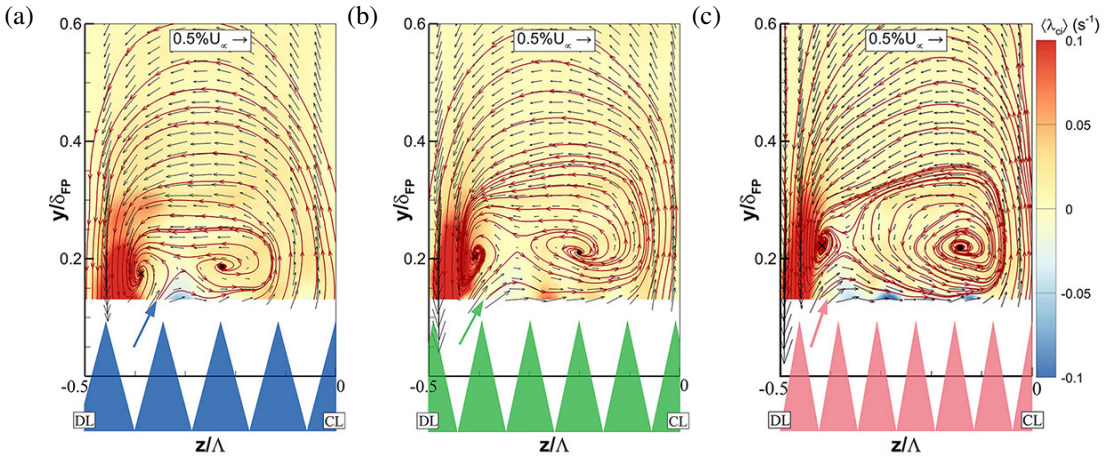

Figure 4.7: Signed swirling strength contour, in-plane velocity vectors and streamlines of the time-averaged flow field of convergent-divergent riblets with wavelength (a) $\Lambda = 30mm$, (b) $\Lambda = 36mm$, (c) $\Lambda = 45mm$ at $x = 12.5s_x$. The region with counter-clockwise swirling motion is red (positive), and the region with clockwise swirling motion is blue (negative).

quite weak. Furthermore, the signed swirling strength $\langle\lambda_{ci}\rangle$ has a high concentration at $y/\delta \approx 0.2$ near the diverging line whereas the magnitude of $\langle\lambda_{ci}\rangle$ is much lower near the converging line. Convergent-divergent riblets, with large-scale induced vortices in the secondary flow, may be applied to augment heat transfer [90, 101, 100].

In order to investigate the reason behind the presence of the two co-rotating vortices revealed by the streamlines in Figure 4.7, a zoom in view of the region near the diverging line is shown in Figure 4.8. The contour of the vertical velocity and streamlines are superimposed on the velocity vector field to aid the analysis. The spanwise coordinate z is normalised by the spanwise distance between adjacent riblets ($s_z = s/cos\gamma = 3mm/cos30^\circ = 3.46mm$).

It can been seen from Figure 4.8 that in all the three cases the vortex near to the diverging line is associated with the presence of an upwash located below it and slightly to its right. Under the combined influence of this upwash motion and the spanwise crossflow, the local velocity vectors are pointing upward at an inclined angle. The reason behind the presence of this upwash motion can be explained as follows. The fluid inside the riblet valley is mainly supplied by the downwash over the diverging line. Due to its downward momentum, the fluid strikes upon the bottom of the valley and then deflected upwards. As such, some of the fluid will spill over the riblet crests, creating a local upwash at $z/s_z \approx 1.2$, as seen in Figure 4.8. Here this upwash motion is termed 'the overflow-induced upwash'. It occurs at the windward of the riblet which

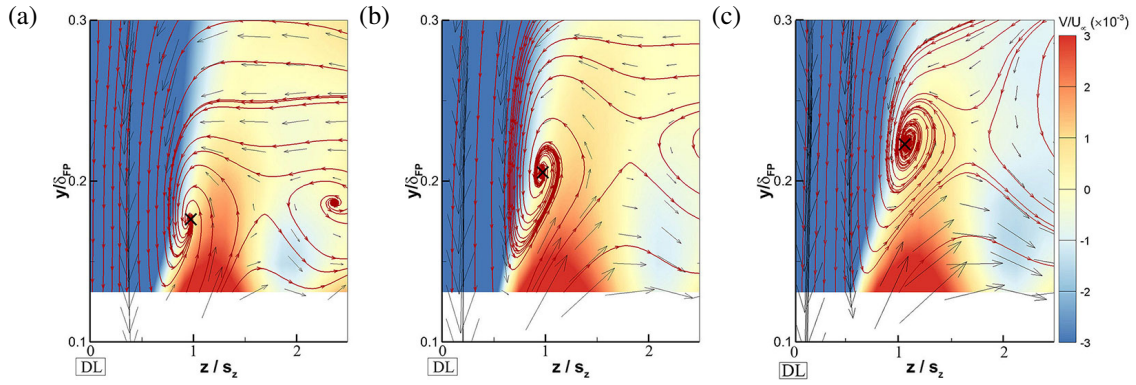

Figure 4.8: Zoom-in view of the time-averaged flow field near the diverging line of convergent-divergent riblets with wavelength (a) $\Lambda = 30mm$, (b) $\Lambda = 36mm$, (c) $\Lambda = 45mm$ at $x = 12.5s_x$. The contour of vertical velocity and streamlines are superimposed on the velocity vector field. The cross symbol indicates the centre of the secondary vortex near the diverging line.

intersects with the cross-stream PIV measurement plane. The vortex next to the diverging line (secondary vortex) is hence caused by the strong downwash over the diverging region and the overflow-induced upwash described above.

Immediately to the right of this upwash region along the span, there also exists a downwash region at $z/s_z \approx 2$ in which the velocity vectors are pointing downward at an inclined angle. This downwash motion is present as the result of the overflow-induced upwash, since a portion of the fluid from the crossflow needs to be entrained into the valley to satisfy the continuity requirement, and hence it is termed "the entrainment-induced downwash". In all these three cases, the location of the overflow-induced upwash is observed in the region around $1.0s_z$, whereas the region of the entrainment-induced downwash lies around $2.0s_z$. Their spanwise locations appear not affected by the riblet wavelength, suggesting that they are local to the downwash motion over the diverging line and the geometry of the riblets. The vortex close to the converging line (primary vortex) is caused by the strong upwash over the converging region and the entrainment-induced downwash described above.

It appears that as the riblet wavelength increases, the centre of this vortex pair moves upward above $y/\delta_{FP} = 0.2$ and the primary vortex becomes more dominant. In previous experiments [114, 72], only the primary vortex was observed and the secondary vortex close to the diverging region was not revealed. This could be attributed to the very large riblet wavelength ($\Lambda = 147.5mm$), more precisely the very large riblet wavelength to riblet spacing ($s = 0.675mm$) ratio, used in their experiments.

4.5.4 Flow topology and flow mechanism

In this section, the observations from the dye visualisation and PIV results are synthesised to form the flow topology of convergent-divergent riblets. The schematic diagram of the flow topology is shown in Figure 4.9a. Globally, it is established that a flow over the riblets from the diverging line towards the adjacent converging line is generated by convergent-divergent riblets [refer to Figures 4.5 and 4.7]. This consequently leads to formation of a weak recirculating secondary flow across the entire boundary layer that creates a downwash motion over the diverging region and an upwash motion over the converging region [refer to Figure 4.7]. The downwash over the diverging region provides feeding for the mass flow along the riblet valleys. Under the influence of the freestream crossflow above riblet crests, the fluid inside riblet valleys evolves along a helicoidal path [refer to the streaklines in Figures 4.5 and 4.6]. Two co-rotating vortical structures are identified in the cross-stream plane within half of a wavelength for the riblet geometry studied in the experiment [refer to Figure 4.7]. The secondary vortex close to the diverging region is generated by the downwash over the diverging line and the overflow-induced upwash at $z/s_z \approx 1$, whereas the primary vortex is caused by the upwash over the converging region and the entrainment-induced downwash at $z/s_z \approx 2$ [refer to Figure 4.8]. As the riblet wavelength increases, the primary vortex becomes more dominant [refer to Figure 4.7].

The flow topology over the surface of convergent-divergent riblets in Figure 4.9a is better illustrated using $2D$ sketches in the longitudinal planes at various representative spanwise stations as shown in Figures 4.9b to 4.9g. In the longitudinal plane at $z = 0$, the downwash dominates over the diverging line and under the influence of the freestream crossflow the local flow direction is pointing towards the windward side of the riblet valley, see Figure 4.9b. As the fluid shunts along the riblet valley ($0 < z/s_z < 0.6$), it is deflected upwards and towards the leeward side of the riblet valley, see Figure 4.9c. In Figure 4.9d, as the fluid impinges onto the leeward side and near the crest of the riblet valley ($0.7 < z/s_z < 1.7$), a portion of it is taken away by the crossflow resulting in the overflow-induced upwash (overflow-1). As the fluid propagates along the riblet valley, some of the crossflow fluid is entrained into the riblet valley to compensate for the loss of fluid within the valley, leading to the entrainment-induced downwash, see Figure 4.9e. Therefore, the entrainment-induced downwash ($1.8 < z/s_z < 2.2$) is a direct consequence of the overflow-induced upwash. The overflow-induced upwash in Figure 4.9d and the entrainment-induced downwash

in Figure 4.9e are the key contributing factors of the two co-rotating vortical structures seen in the cross-stream plane shown in Figure 4.9a. As the fluid continues to propagate along the riblet valley, the freestream crossflow supplies the energy to the tangential velocity component of the helicoidal motion on the top of the riblet valley, see Figure 4.9f. As the fluid on the top of the riblet valley is accelerated, a portion of the accelerated fluid moves above the riblet crest (overflow-2) from the windward side of the riblet valley. The overflow of fluid above the riblet crest is unsteady, causing disturbances to the flow field. In the longitudinal plane along the converging line ($z = \Lambda/2$), the upwash motion dominates, see Figure 4.9g.

4.5.5 Developing stage and developed stage

Finally, the flow field over a riblet section of a finite length can be classified into two stages, i.e. the developing stage and the developed stage, depending on the main source of the fluid that sustains the spanwise flow over the riblets from the diverging line to the converging line. The developing stage is defined as the region from the start of the riblet section ($x = 0$) to a downstream station, where the upwash flow in the converging region still comes from the crossflow boundary layer upstream of the riblet section. The developed stage is defined as the region where the flow reaches the converging line mainly comes from the downwash motion over the diverging line. The approximate boundary between these two stages is located roughly at the location of $PD1$ in Figures 4.5a and 4.5b. Therefore, the length of the developing stage ($\Lambda/(2 \cdot tan\gamma)$) depends on the riblet wavelength, with a longer wavelength resulting in a longer developing stage. The presence of the two stages has nothing to do with boundary layer transition. The difference in the flow characteristics in these two regions will be explored through the analysis of the PIV data obtained in longitudinal planes and a wall-parallel plane in Sections 4.6 and 4.7.

4.6 Effects of convergent-divergent riblets on the development of boundary layer

In this section, the development of the boundary layer over convergent-divergent riblets is examined using PIV in the longitudinal plane and the wall-parallel plane. The measurement is made on the convergent-divergent riblets with a $\Lambda = 45mm$ wavelength. The characteristics of the induced velocity and vortical structures are aligned with the

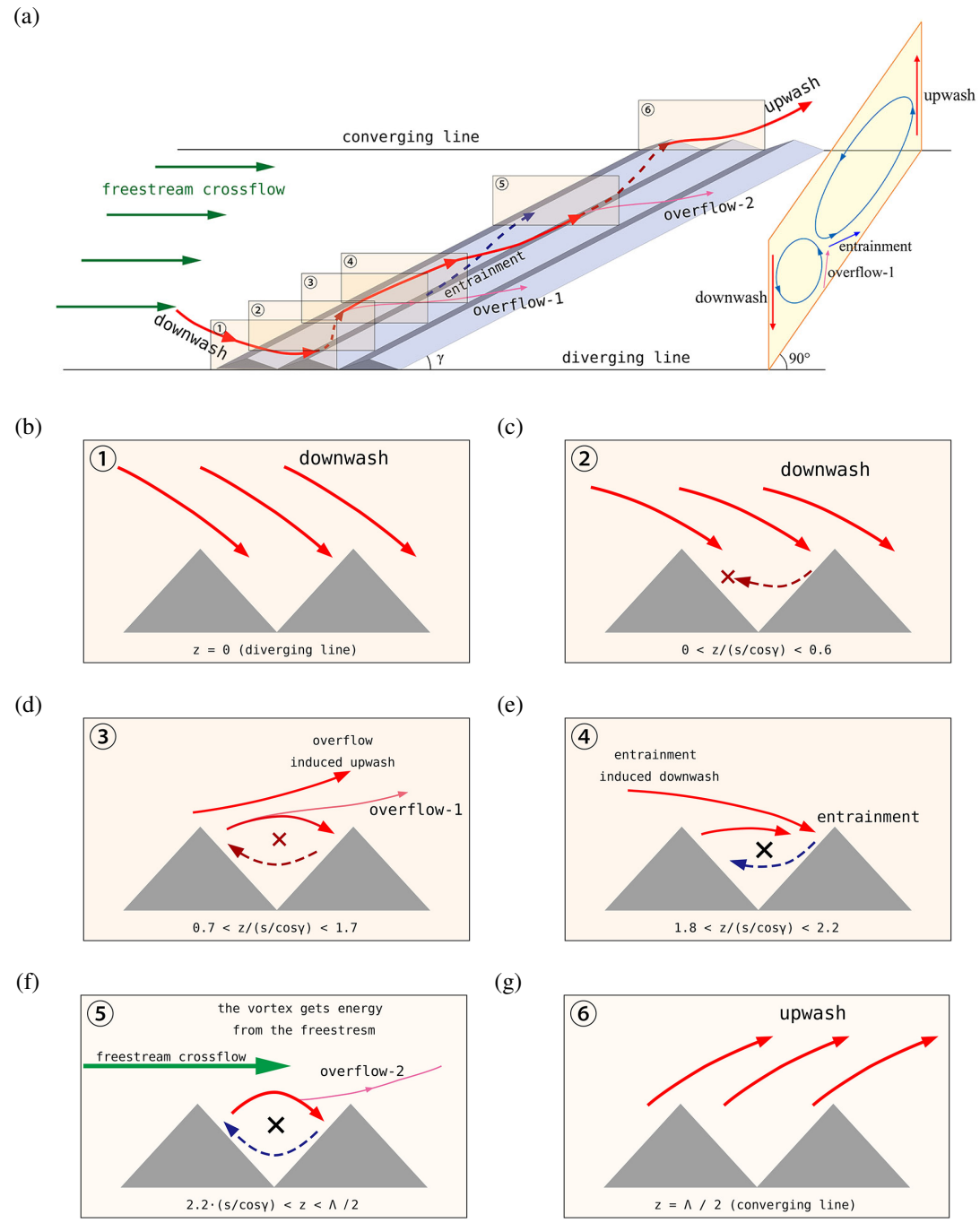

Figure 4.9: Schematic diagram of the flow topology of $\Lambda = 45mm$ convergent-divergent riblets in (a) $3D$ perspective, (b-g) multiple $2D$ longitudinal planes.

flow topology proposed in Figure 4.9.

4.6.1 Flow field in the longitudinal plane

Firstly, the time-averaged velocity field in the longitudinal plane of the convergent-divergent riblets are examined and shown in Figure 4.10. The vertical dashed line indicates the boundary of the developing stage and the developed stage. The y-coordinates are normalised by the local boundary layer thickness at $x = 0$ ($\delta_{FP} = 12.7mm$) and the x-coordinates by the projected riblet spacing in x direction ($s_x = s/sin\gamma = 6mm$).

The contours of the averaged streamwise velocity U in the longitudinal planes over the converging line and the diverging line are shown in Figures 4.10a and 4.10b respectively. PIV data very close to the riblet crest ($y/\delta_{FP} \leq 0.175$) are not available due to the surface reflection of the laser light sheet, and this is indicated by the region void of contours close to the wall. In the longitudinal plane over the converging line (Figure 4.10a), the region of low streamwise velocity (in blue) increases in height in the streamwise direction, indicating a reduction of the local velocity in the near-wall region. In contrast, over the diverging line (Figure 4.10b), the region of low streamwise velocity decreases in height in the streamwise direction, indicating an increase of the local velocity near the wall. Due to the lack of experimental data very close to the wall in the present experiment, the wall shear stress is not presented in this paper.

The magnitude of the vertical velocity is much smaller than that of the streamwise velocity component. An intense upward motion of the fluid (upwash) is observed in the region over the converging line (Figure 4.10c). The positive vertical velocity appears to be stronger over the leading edge of convergent-divergent riblets due to the blocking of convergent-divergent riblets. Furthermore, isolated vertical patches of positive vertical velocity are observed over the crests of convergent-divergent riblets. The upward motion appears to extend to the entire boundary layer with no clear physical upper boundary. For longitudinal riblets, the affected region is only limited to the vicinity of the riblet surface [60]. In contrast, a profound downward motion (downwash) is seen in the area over the diverging line (Figure 4.10d). The downwash appears to be confined within a finite region above the wall surface. It intensifies in the streamwise direction and decays abruptly once the riblet section ends. Over the diverging line, especially in the near-wall region, the magnitude of vertical velocity appears to increase in the streamwise direction indicating that the downwash motion is intensified further downstream. This is consistent with the observation of an increased helicoidal pitch along the streamwise direction as seen in Figure 4.6a. Furthermore,

isolated vertical patches of negative vertical velocity are observed over the valleys of convergent-divergent riblets. There is an expected strong correlation between the presence of an upwash/downwash and the reduction/increase of the streamwise velocity in the near-wall region.

Figures 4.10e and 4.10f show the contours of turbulence intensity Tu, which is the velocity fluctuation ($\sqrt{u'^2+v'^2}$) normalised by local in-plane velocity magnitude ($\sqrt{U^2+V^2}$). Over the converging line, a region with elevated velocity fluctuations is observed, which is absent over the diverging line. As revealed by the top views of the dye visualisation images in Figures 4.5a and 4.5b, the overflows of the fluid above riblet crests generate disturbances over the riblet section. Due to the spanwise flow which directs from the diverging line to the converging line, such disturbances are brought towards the converging region, causing a substantial increase in the turbulence intensity there.

Contours of the time-averaged vorticity ω_z indicating shear and rotation in the longitudinal plane of convergent-divergent riblets are shown in Figures 4.11a and 4.11b. The reversed colourbar is applied to highlight the high vorticity region. The level of vorticity in the boundary layer upstream of the riblet section ($x < 0$) can be considered as the baseline level. From Figure 4.11a, one can see that over the converging line the level of vorticity is significantly enhanced and the region with high vorticity is displaced upward becoming detached from the wall in the developed region. The uplift of vorticity ω_z seen in Figure 4.11a is a result of the upwash motion occurring over the converging region [refer to the side views in Figures 4.5a and 4.5b]. On the contrary, over the diverging line weakened vorticity and downward movement of the high vorticity region are observed in accordance with the presence of a downwash motion. Based on the results presented in Figures 4.11a and 4.11b, one can conclude that the fluid mixing is enhanced in the converging region and suppressed in the diverging region. Further analysis reveals that the enhancement or weakening of the shear mainly comes from the streamwise part of the fluid velocity rather than the vertical component.

In the vorticity ω_z shown in Figures 4.11a and 4.11b, the contribution from the shear to the averaged velocity field dominates. In order to isolate the local swirling motion from the shear, the contours of signed swirling strength $\langle\lambda_{ci}\rangle = (\omega_z/|\omega_z|)\cdot\lambda_{ci}$ are also examined. $\langle\lambda_{ci}\rangle$ is calculated firstly for each instantaneous flow field, and all the instantaneous snapshots (1250 image pairs in total) are then averaged to produce the contours shown in Figures 4.11c and 4.11d. Similar spatial periodicity in $\langle\lambda_{ci}\rangle$ can be obviously seen over the converging and diverging line. More intense vortical structures

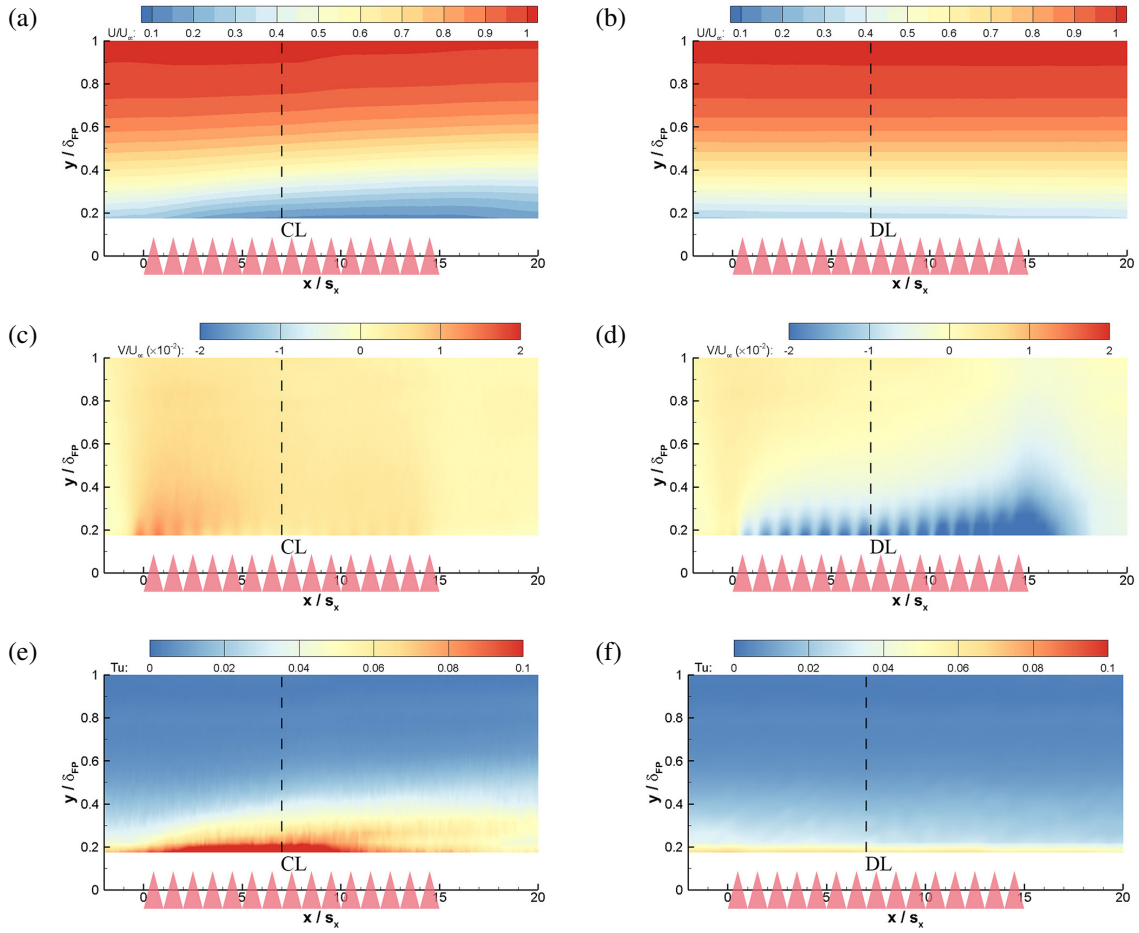

Figure 4.10: Contour of (a,b) time-averaged streamwise velocity U, (c,d) time-averaged vertical velocity V, (e,f) turbulence intensity Tu of $\Lambda = 45mm$ riblets in the longitudinal plane over the converging line (left) and the diverging line (right).

are observed over the diverging line than the converging line, which is consistent with the fact that the helicoidal motions within the riblet valleys are firstly generated over the diverging region and hence have a higher swirling strength.

4.6.2 Flow field in the wall-parallel plane

In the present experiment, in order to investigate the effects of convergent-divergent riblets on the secondary flow in the near-wall region, the PIV measurement is made in a wall-parallel plane very close to the wall surface. The exact location of the centre of the laser sheet used in this measurement cannot be measured easily in practice. However, it is possible to estimate its distance to the wall from the streamwise velocity on this plane ($0.035m/s$) by assuming that the local velocity profile in the baseline boundary

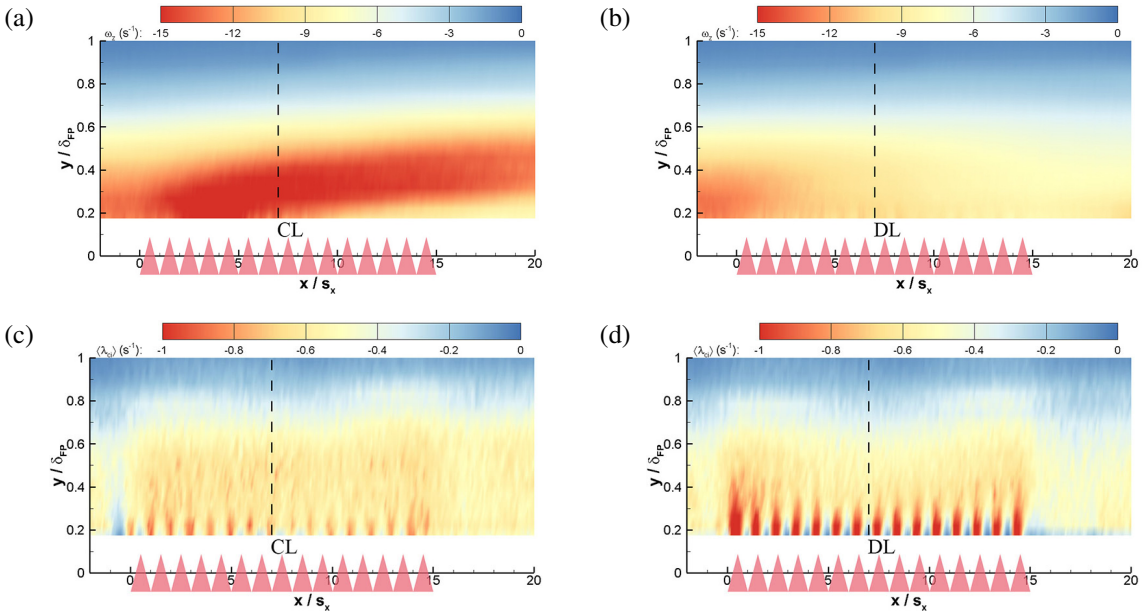

Figure 4.11: Contour of (a,b) the time-averaged vorticity ω_z, (c,d) the signed swirling strength $\langle\lambda_{ci}\rangle$ of $\Lambda = 45mm$ riblets in the longitudinal plane over the converging line (left) and the diverging line (right). The region with counter-clockwise rotational/swirling motion is blue (positive), and the region with clockwise motion is red (negative).

layer follows the Blasius profile. From this, the wall-parallel plane is estimated to be located at $3mm$ ($y/\delta_s = 0.23$) above the smooth wall surface or $1.8mm$ above the crest of convergent-divergent riblets.

Due to the longitudinal growth of the laminar boundary layer, the streamwise velocity in this wall-parallel plane decreases in the streamwise direction. The effect of streamwise variation can be removed by subtracting the streamwise velocity U_0 obtained in the boundary layer over the smooth wall from that measured over the convergent-divergent riblets. In Figures 4.12a and 4.12b, the contours of the induced streamwise velocity ($\Delta U = U - U_0$) reveal the presence of concentrated zones of streamwise velocity deficit/excess in stripy shape over the converging/diverging regions. The vertical dashed line indicates the boundary between the developing stage and the developed stage, and the horizontal dash-dot-dot lines indicate the overflow-induced upwash. Channelling of the flow with low-speed and high-speed pathways was also observed in the boundary layer over turbine blades covered with particle deposits [97] or convergent-divergent riblets [73]. The appearance of concentrated zones of streamwise velocity deficit/excess implies that the upwash/downwash motions occur predominantly over the converging/diverging region. They persist downstream of the

riblet section ($x > 15s_x$). It is also noticed that a slightly negative velocity occurs in the remaining region, indicating that the whole flow field is affected by the riblet section. The spanwise position of the overflow-induced upwash near the diverging region does not change in the developed stage, which is indicated by the green lines.

To illustrate the streamwise development, spanwise distributions of the induced streamwise velocity at different streamwise stations are shown in Figures 4.12c and 4.12d. Over the converging line, both the magnitude and the width of velocity deficit increase progressively till the end of the riblet section. Over the diverging region, both the magnitude and the width of velocity excess increase progressively and such an increase continues even after the end of the riblet section. It is noticed that the zone of velocity deficit is broader and has a higher maximum magnitude than that of the zone of velocity excess. A localised decrease in the streamwise velocity is also observed near the boundary of the velocity excess zone, which is indicated by the dotted circles in Figure 4.12d and associated with the overflow-induced upwash. The local upwash is also observed in the cross-stream plane, as indicated by the arrow in Figure 4.7c and the contour of vertical velocity in Figure 4.8c.

In Figure 4.13, the contour of vorticity ω_y and signed swirling strength $\langle\lambda_{ci}\rangle$ in the wall-parallel plane are shown. The vorticity in Figure 4.13a represents both shear and rotation of the averaged velocity field, whereas the signed swirling strength in Figure 4.13b indicates only the swirling motions. In Figure 4.13a, longitudinal pairs of high negative and positive vorticity straddle along the converging line and the diverging line due to the large local velocity gradient across these lines, see the bell-shaped profiles of the induced streamwise velocity in Figures 4.12c and 4.12d. Between the converging line and the diverging line, shear motions are very weak and the magnitude of vorticity is close to zero.

In Figure 4.13b, longitudinal pairs of high negative and positive swirling strength are seen to straddle along the converging/diverging line in a similar manner as in Figure 4.13a. However, with a closer examination of the zoom-in regions, one can see that in the developing stage in Figure 4.13c the intensity of $\langle\lambda_{ci}\rangle$ is low and appears to be featureless, whereas in the developed stage in Figure 4.13d the intensity of $\langle\lambda_{ci}\rangle$ increases to such an extent that isolated patches within each riblet valley with intense swirling strength appear. The regions with intense swirl are located between two adjacent crest lines, which can be interpreted as the imprints of the vortical structures inside riblet valleys on the wall-parallel plane. The swirling motions are more intense near the diverging line since vortical structures inside riblet valleys are initially generated

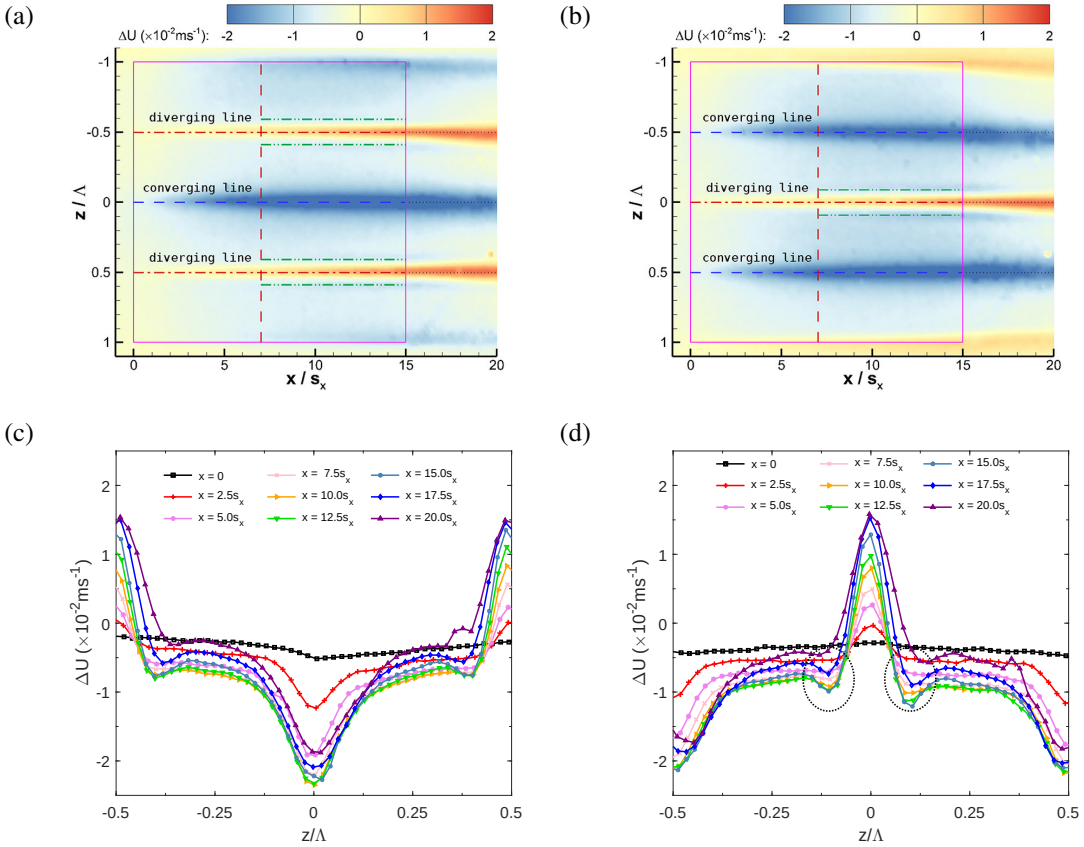

Figure 4.12: Contour and profile of the time-averaged induced streamwise velocity $\Delta U = U - U_0$ of $\Lambda = 45mm$ riblets in the wall-parallel plane with (a,c) the converging line at $z = 0$, (b,d) the diverging line at $z = 0$.

there. It is observed that although the strength of vorticity is maintained, the swirling motion decays more rapidly once the riblet section ends.

4.7 Effects of riblet wavelength

In this section, the effects of riblet wavelength on the flow field characteristics, including induced streamwise velocity, vorticity and swirling, are investigated using PIV measurements.

4.7.1 Parameters of induced velocity and vorticity

In order to enable a quantitative comparison of the amplitude and width of the upwash/downwash motion occurring over the converging/diverging region of riblets with

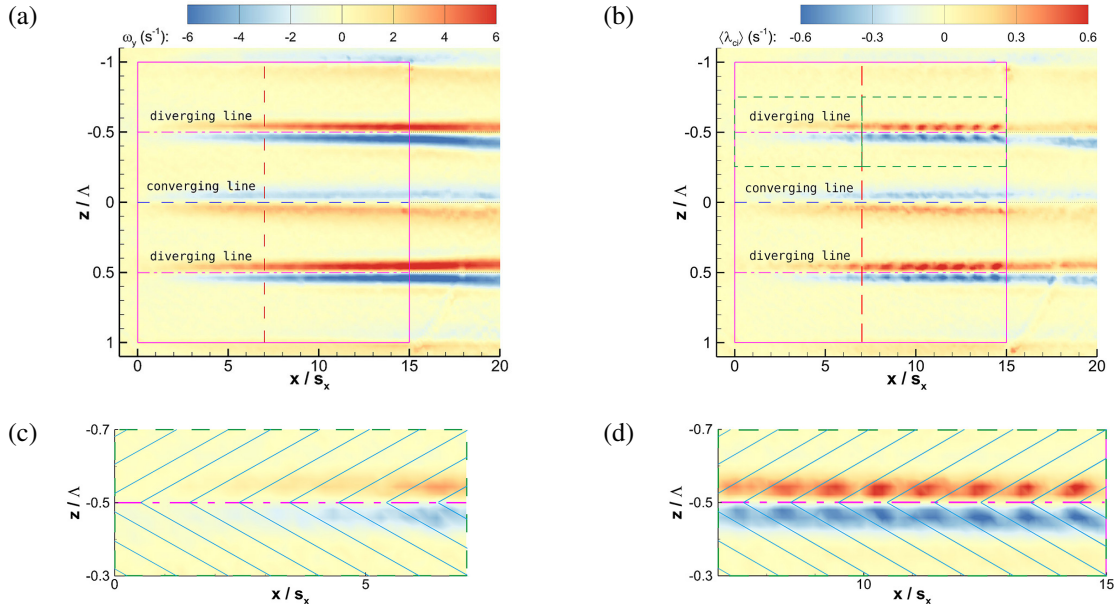

Figure 4.13: Contour of (a) the time-averaged vorticity ω_z and (b) the signed swirling strength $\langle\lambda_{ci}\rangle$, zoom-in region in (c) the developing stage and (d) the developed stage in the wall-parallel plane of $\Lambda = 45mm$ riblets with the converging line at $z = 0$. The region with counter-clockwise rotational/swirling motions is red (positive), and the region with clockwise motions is blue (negative).

different wavelengths, a parameter extraction algorithm for the bell-shaped velocity profiles obtained in the wall-parallel plane is developed. In Figure 4.14a, the C^2 continuity spline interpolation (curve) is applied to provide a smooth curve fit of the discrete data points (delta symbols). The base value is defined as the averaged value in the plateau region between converging line and diverging line, and the amplitude ($A_{\Delta U}$) represents the difference between the extreme value and the base value. The width of the upwash/downwash region over the converging/diverging line ($W_{\Delta U}$) is defined as the width of the curve with a 10% amplitude above the base value.

Figure 4.14b shows the variations of the amplitude of the induced streamwise velocity ($A_{\Delta U}$) along the converging and diverging line for convergent-divergent riblets with three different wavelengths. Along the converging line, the amplitude firstly increases continuously, and it then levels off after reaching the peak value. In contrast, along the diverging line the amplitude exhibits a continuous increase towards the end of the riblet section before it decreases slightly afterwards. This results in a stronger downwash over the diverging line than the upwash over the converging line towards the end of the riblet section. Interestingly, it is also found that the point where the amplitude begins to level off along the converging line approximately coincides with

the beginning of the developed stage. Furthermore, it is observed that an increase in riblet wavelength leads to a larger amplitude of the induced streamwise velocity over both the converging and the diverging regions.

Figure 4.14c shows the variations of the width of the induced streamwise velocity ($W_{\Delta U}$) along the converging and diverging line for convergent-divergent riblets with three different wavelengths. For all riblet wavelengths, the region with upwash centred at the converging line is substantially wider than the region with downwash straddling along the diverging line. The overflow near the converging line enhances the upwash, whereas the overflow close to the diverging region weakens the downwash. Downstream of the riblet section ($x > 15s_x$), the width of the downwash exhibits an increasing trend, whereas the width of the upwash remains basically constant. In the current wall-parallel plane, a larger wavelength leads to wider region with upwash centred at the converging line. An opposite trend is observed for the region with downwash over the diverging line, i.e. a larger wavelength leads to a narrower region.

Figure 4.15 compares the magnitude of vorticity A_{ω_y}, which is the mean magnitude of the positive and negative peaks in the spanwise vorticity profiles in the wall-parallel plane. Along the converging line, A_{ω_y} exhibits a continuous increase in the developing stage and then levels off in the developed stage. Along the diverging line, A_{ω_y} increases up to the end of the riblet section ($0 < x < 15s_x$) and it decreases rapidly further downstream ($x > 15s_x$). A higher A_{ω_y} close to the diverging line indicates more intense shear and rotation within that region. The wavelength of riblets has a negligible influence on A_{ω_y} over the converging region. On the other hand, a larger wavelength leads to a higher A_{ω_y} in the region over the diverging region. Over the diverging region, since the amplitude of the induced velocity is larger and the width in the diverging region is narrower [refer to Figures 4.14b and 4.14c], the shear and rotation are more intense than those near the converging line. In additional, it is also found that changes in riblet wavelength have a negligible influence on the spanwise width of vorticity peaks along both the converging and the diverging lines (the graph is not shown here for brevity).

The main contributor to the time-averaged vorticity ($\omega_y = \partial U/\partial z - \partial W/\partial x$) in Figure 4.13a is the spanwise gradient of the streamwise velocity, i.e. $\partial U/\partial z$. The effects of riblet wavelength on the amplitude and width of the induced streamwise velocity ΔU have been revealed in Figures 4.14b and 4.14c respectively. Along the diverging line, the amplitude $A_{\Delta U}$ increases whereas the width $W_{\Delta U}$ decreases as the riblet wavelength increases, leading to a dramatic increase in $\partial U/\partial z$. On the contrary, along the converging line, both the amplitude $A_{\Delta U}$ and the width $W_{\Delta U}$ increase as the riblet wavelength

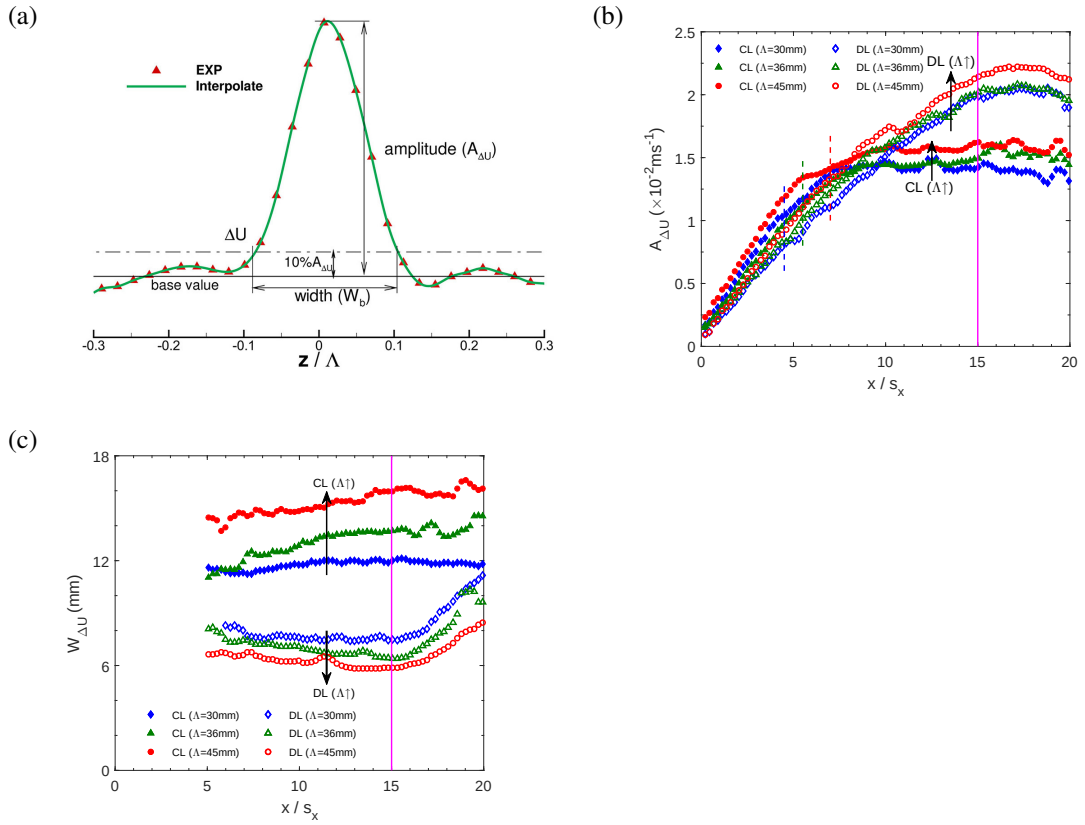

Figure 4.14: (a) Schematic of the definition of parameters, (b) amplitude $A_{\Delta U}$ and (c) width $W_{\Delta U}$ of the upwash region and the downwash region in the wall-parallel plane for convergent-divergent riblets with three different wavelengths.

increases. Thus, an increasing riblet wavelength is expected to have a negligible effect on A_{ω_y} in the converging region.

4.7.2 The deceleration effect

In Figure 4.12, contours of the induced streamwise velocity in the wall-parallel PIV measurement plane reveal changes in streamwise velocity introduced by the riblets with reference to that by a smooth wall. In order to quantify the effects of convergent-divergent riblets on the flow at each streamwise station in this plane, a new parameter is introduced, which is the integral of the induced streamwise velocity across one complete wavelength at the corresponding station, i.e. $TIU = \int_{-\Lambda/2}^{+\Lambda/2} \Delta U(z)dz$. The absolute value of TIU indicates the degree by which the flow is accelerated or decelerated by the convergent-divergent riblets. A positive TIU implies an acceleration effect whereas a negative value implies a deceleration effect across the span.

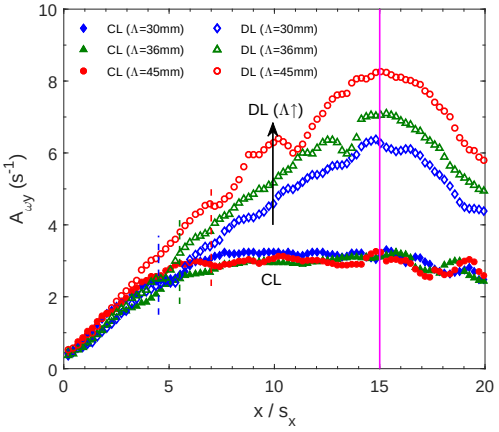

Figure 4.15: Comparison of the magnitude of vorticity A_{ω_y} in the wall-parallel plane for convergent-divergent riblets with three different wavelengths.

Based on the results shown in Figure 4.16, convergent-divergent riblets are found to generate a deceleration, with a larger riblet wavelength resulting in a more intense deceleration. The value of TIU decreases rapidly in the developing stage as the deceleration effect enhances. In the developed stage, the value of TIU first decreases slowly, and then increases slightly. Once the riblet section ends ($x > 15s_x$), the deceleration effect begins to weaken rapidly.

4.8 Conclusion

In this work, the development of a laminar boundary layer over a rectangular convergent-divergent riblet section with a finite streamwise length is studied experimentally using dye visualisation and PIV at a freestream velocity of $0.1m/s$ in a water flume. The flow topology over this highly directional spanwise roughness is established and the impact of riblet wavelength on vortical structures is also revealed for the first time. The key findings from this study are summarised as follows:

First, it is established that convergent-divergent riblets generate a flow close to the riblets from the diverging line towards the adjacent converging line. This consequently leads to the formation of a weak recirculating secondary flow in cross-stream plane across the entire boundary layer that creates a downwash motion over the diverging region and an upwash motion over the converging region. The downwash over the diverging region provides a feeding mechanism for the mass flow along riblet valleys. Under the influence of the crossflow above riblet crests, the fluid inside the riblet valley

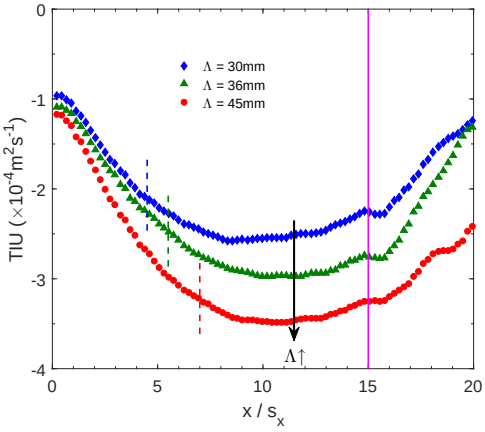

Figure 4.16: Streamwise variations in TIU for convergent-divergent riblets with three different wavelengths. The boundaries between the developing stage and the developed stage are indicated by the dashed vertical lines.

evolves along a helicoidal path. It also interacts with the crossflow boundary layer and hence plays a key role in determining the structure of the secondary flow across the boundary layer.

Secondly, in consistent with the findings from other researches, a reduction in the streamwise velocity and an increase in turbulence and vorticity is found in the longitudinal plane along the converging line and the opposite is observed in the longitudinal plane along the diverging line. Furthermore, the streamwise development of the flow over the riblet section can be divided into a developing stage followed by a developed stage. In the developing stage, the magnitudes of induced streamwise velocity and vorticity on the converging line continue to increase whereas in the developed stage the values of these parameters remain essentially unchanged.

Finally, it is found that a larger wavelength produces a higher magnitude of upwash/downwash in the converging/diverging region and hence leads to a more intense secondary flow. A more intense deceleration effect is also observed for riblets with larger wavelength. The effects of riblet wavelength on the parameters of the flow field are summarised in Table 4.3.

Properties	Converging Region	Diverging Region
$A_{\Delta U}$	$\uparrow$	$\uparrow$
$W_{\Delta U}$	$\uparrow$	$\downarrow$
A_{ω_y}	$\rightarrow$	$\uparrow$

Table 4.3: Variations of the flow field properties with increased wavelength of convergent-divergent riblets. The symbol $\uparrow$ indicates increase, $\downarrow$ denotes decrease, and $\rightarrow$ represents no significant effect.

4.9 Acknowledgements

The authors would like to thank the workshop technicians at School of Mechanical, Aerospace and Civil Engineering for their excellent technical supports during the setting up of our experimental rig. They also would like to acknowledge the timely technical advice provided by Dr. Amine Koched and Dr. Martin Hyde at TSI. Finally, the authors wish to thank the referees of this paper for their valuable review comments which have enabled us to make a substantial improvement to this paper.

Blank page

Chapter 5

Laminar Boundary Layer over Convergent-Divergent Riblets with Spanwise Height Variations

F. Xu, S. Zhong, and S. Zhang. Vortical structures of laminar boundary layer over convergent-divergent riblets with spanwise height variations. In *21st Australasian Fluid Mechanics Conference*, Adelaide, Australia, 2018.

Author	Fang Xu	Shan Zhong	Shanying Zhang
Rig design and setup	70%	15%	15%
Experimental measurement	70%	15%	15%
Paper writing	70%	15%	15%
Review feedback	70%	15%	15%
Overall	70%	15%	15%

Table 5.1: Author contribution to this peer-reviewed conference.

5.1 Abstract

In this paper, a laminar boundary layer over convergent-divergent riblets with a reduced riblet height in the converging region is investigated experimentally. The flow field in the longitudinal plane and the wall-parallel plane is measured using mono-particle image velocimetry (PIV). With a decreased riblet height along the converging line h_{CL}, the intensity of the induced secondary flow over the converging region is significantly reduced, while the flow field characteristics over the diverging region are basically

preserved. Detailed analysis on the in-plane flow field provides a deeper understanding of the flow topology of vortical structures. With a spanwise riblet height variation, a weak recirculating secondary flow still exists in the cross-stream plane.

5.2 Introduction

The nature-inspired surface pattern of convergent-divergent riblets (referred to as C-D riblets later on) is a new type of spanwise roughness heterogeneity which begins to attract attention more recently. Both vortical structures and the control effect of C-D riblets are inherently different from conventional longitudinal (streamwise) riblets. With large-scale vortical structures induced by the directional spanwise heterogeneity, this roughness pattern is expected to have a broad engineering application prospect in friction drag reduction and flow separation control [79, 114]. To date, there have been several researches on the flow topology of a boundary layer over C-D riblets with uniform riblet height rather than variable riblet height along the spanwise direction. Parameters of C-D riblets, including riblet height, riblet spacing, yaw angle and riblet wavelength, have been studied in several previous studies [113, 25, 173].

An increase in the skin friction drag is observed along the converging line while an opposite effect is obtained along the diverging line [113, 72]. A decrease in riblet height in the converging region, as observed on bird flying feathers, is expected to result in a less intense secondary flow, and consequently a reduction in the skin friction drag in that region. With SEM photos, Chen et al. revealed that the height of the surface roughness of mature pigeon feathers decreases by around three quarters from $130\mu m$ near the feather shaft to $30\mu m$ at the outer fringe [24]. Based on this intriguing characteristic, a spatial-3D configuration is proposed in Chen et al. [25], which has a zero height along the converging line and a linear variation of the riblet height in the spanwise direction. Chen et al. revealed the global drag reduction effect in a fully-developed turbulent pipe flow [25]. A drag reduction of about 20% is obtained for such spatial-3D configuration [25], in contrast to a net drag increase for the pattern with uniform riblet height along the spanwise direction [113].

To date, the influence of a spanwise variation in the riblet height on the flow field is not yet clear. To address this issue, we investigate a laminar boundary layer over C-D riblets with three types of spanwise height variations using mono-PIV measurement. The flow field characteristics in both the longitudinal plane and the wall-normal plane are analysed.

Parameter	Value	Parameter	Value
Λ	$45mm$	L	$90mm$
s	$3.0mm$	W	$90mm$
h_{DL} (h)	$2.4mm$	γ	30°

Table 5.2: Parameters of C-D riblets.

5.3 Experiment system

5.3.1 Water flume

The experiment is conducted in a $3.64m$ long water flume with a $305mm \times 305mm$ cross-section. A laminar boundary layer is generated over a $6mm$ thick flat plate which is submerged horizontally in the water flume, and a small negative inclination angle is applied to ensure an attached flow from the $1:5$ elliptical leading edge. The free-stream velocity is $0.1m/s$, and the turbulence intensity outside the boundary layer is around 0.2%. The velocity profile of the baseline laminar flow is aligned with the theoretical Blasius profile (not shown here for brevity). The Reynolds number $Re_x = U_\infty x/\nu$ at the measurement section is around 7×10^4.

5.3.2 Convergent-divergent riblets with spanwise height variation

The schematic diagram of C-D riblets with triangular riblet teeth is shown in Figure 5.1, and parameters of C-D riblets are listed in table 5.2. The riblet section starts at $x = 0.67m$ from the leading edge of the flat plate. To investigate the effect of spanwise riblet height variation, three types of C-D riblet patterns are designed, as shown in Figure 5.2. The riblet height along the diverging line $h_{DL} = h$ is $2.4mm$ for all three cases. The riblet height in the longitudinal plane along the converging line h_{CL}, as indicated in Figure 5.2, has three values of $2.4mm$ (uniform height), $1.2mm$ (half height) or 0 (zero height), and a linear variation of the riblet height is designed in the spanwise direction. The smooth wall levels with half of the adjacent riblet height, i.e. the protrusion height h_p is $h_{DL}/2$ ($h_{CL}/2$) for the wall surface adjacent to the diverging line (converging line). As shown in Figure 5.1, the streamwise, wall-normal and spanwise directions correspond to axes x, y and z, which are normalised by s_x ($6mm$, riblet spacing projected in x direction), δ_{FP} ($12.7mm$, $99\%U_\infty$ boundary layer thickness of the flat plate) and Λ ($45mm$, riblet wavelength) respectively.

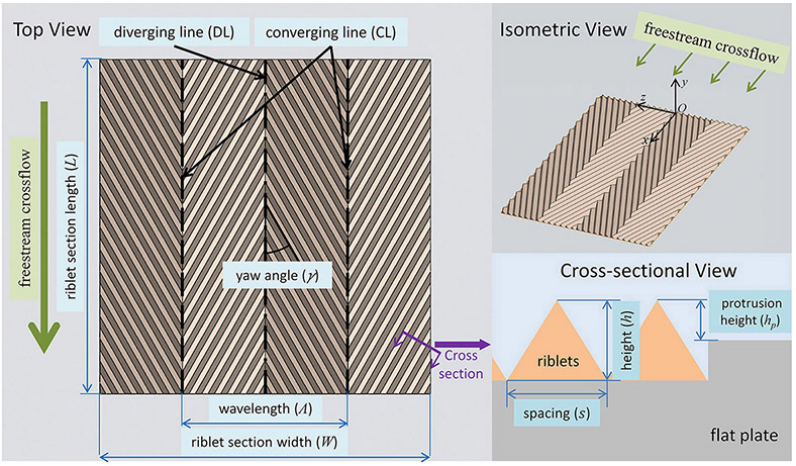

Figure 5.1: Schematic diagram of C-D riblets parameters [173]. The region close to the converging/diverging line is referred to as the converging/diverging region.

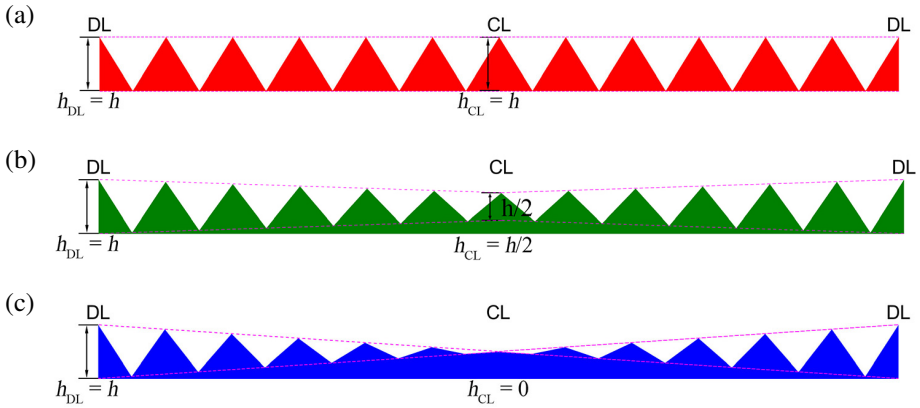

Figure 5.2: Cross-sectional view in the cross-stream (y-z) plane of C-D riblets with (a) $h_{CL} = h$, (b) $h_{CL} = h/2$, (c) $h_{CL} = 0$. Dashed lines indicate a linear variation of the riblet height along the spanwise direction.

5.3.3 Particle image velocimetry system

The mono-PIV system from TSI is composed of a New Wave Solo-PIV 120 laser generator, a laser pulse synchroniser (Model 610036) and a CCD camera (4 Mega pixels). The longitudinal (x-y) measurement plane covers the whole riblet section. The distance between the wall-parallel (x-z) measurement plane and the smooth wall surface is $3mm$. The laser pulse time interval is $6ms$ in the longitudinal plane or $8ms$ in the wall-parallel plane, and the width of the laser light sheet is around $1mm$. A total of 1250 image pairs are captured with an acquisition rate of $2Hz$ to ensure convergence of the time-averaged results.

In these measurement planes, PIV image pairs are processed using $64 \times 24/24 \times 24$

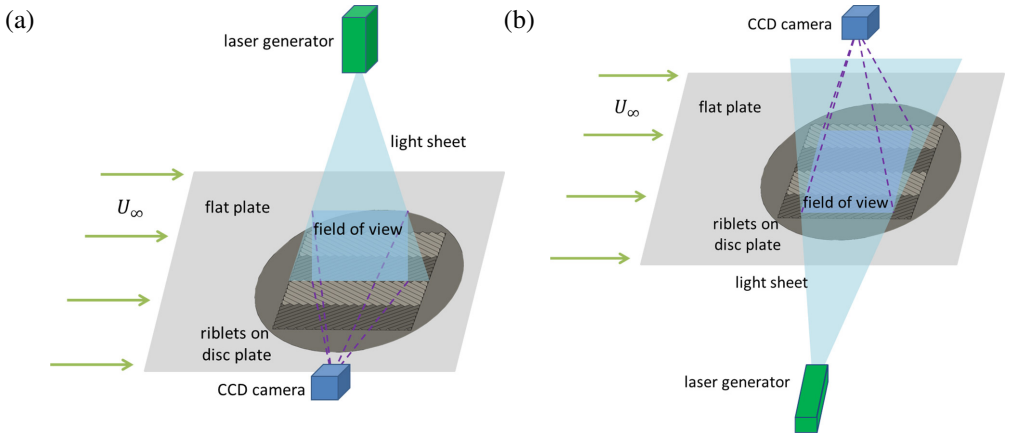

Figure 5.3: Mono PIV arrangement [173] in (a) the longitudinal plane, (b) the wall-parallel plane.

Plane	Field of view	Spatial resolution
Longitudinal (x-y)	117.32×88.19	0.60×0.60
Wall-parallel (x-z)	137.29×103.20	0.70×0.70

Table 5.3: Parameters of mono-PIV datasets (unit: mm^2).

as the first/final interrogation area with a 50% overlap. Table 5.3 lists parameters of the field of view and the spatial resolution of velocity vectors. The expanded uncertainties in the time-averaged velocity components, i.e. 95.4% possibility of having true value within the uncertainty bound, are $0.05\%U_\infty$ in the longitudinal plane and $0.28\%U_\infty$ in the wall-parallel plane.

5.4 Results and analysis

Figure 5.4 compares the distribution of time-averaged streamwise velocity contours of three types of spanwise height variations. For the uniform riblet height, the local streamwise velocity decreases rapidly in the near-wall region in Figure 5.4a. For $h_{CL} = h/2$, similar distributions of the velocity components are observed in Figure 5.4b, while the magnitudes are significantly smaller. For $h_{CL} = 0$, the distribution of the streamwise velocity in Figure 5.4c resembles the undisturbed boundary layer over a flat plate.

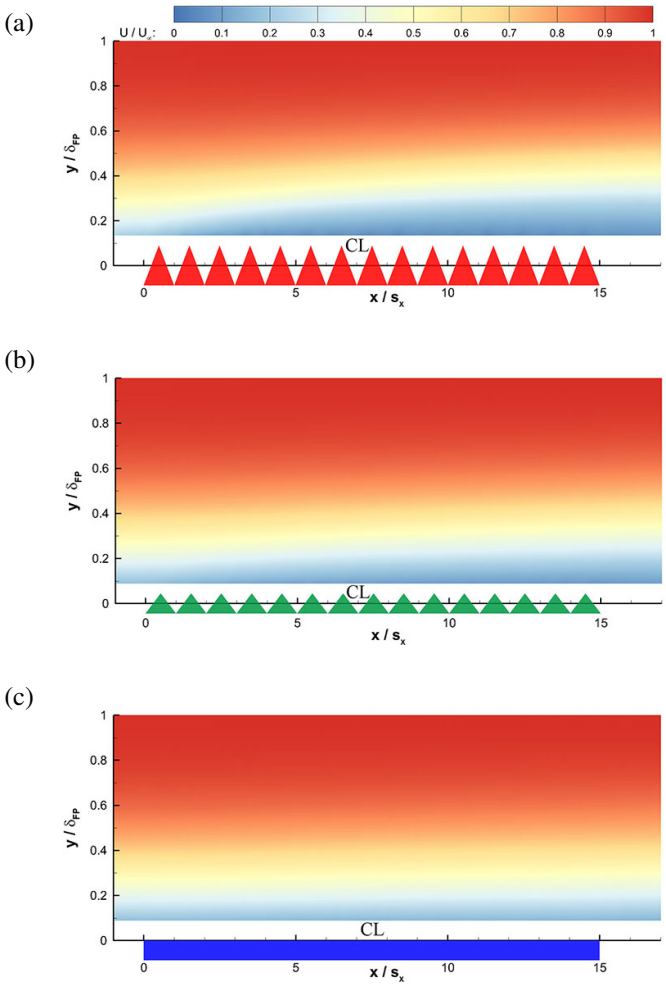

Figure 5.4: Time-averaged streamwise velocity over C-D riblets with (a) $h_{CL} = h$, (b) $h_{CL} = h/2$, (c) $h_{CL} = 0$.

Figure 5.5 compares the time-averaged streamwise velocity profiles at multiple streamwise stations over the converging line. The velocity profiles over the diverging line for three cases present only slight differences compared with those over the converging line, and thus are not shown here for the sake of brevity. Over the converging line, the streamwise velocity profile continues to evolve as a result of the progressive decrease in the streamwise velocity in the near-wall region and the gradual spreading of this region of reduced velocity towards the edge of the boundary layer. A decrease in h_{CL} leads to a narrower affected region in the wall-normal direction. The streamwise velocity profiles of the $h_{CL} = 0$ case resemble those over the flat plate, indicating ignorable flow disturbances over the converging region.

Figure 5.6 reveals the streamwise variations of the displacement thickness and the

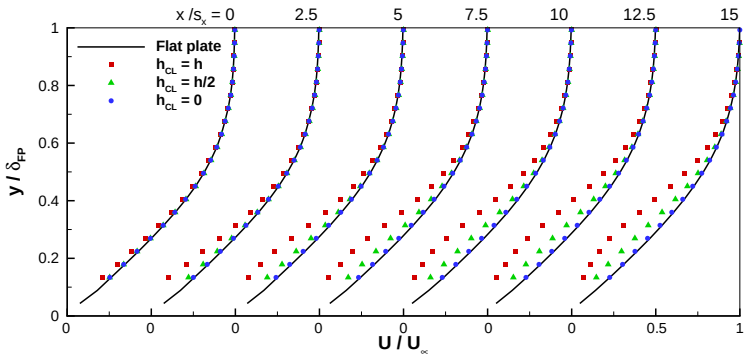

Figure 5.5: Time-averaged streamwise velocity profiles in the longitudinal plane along the converging line.

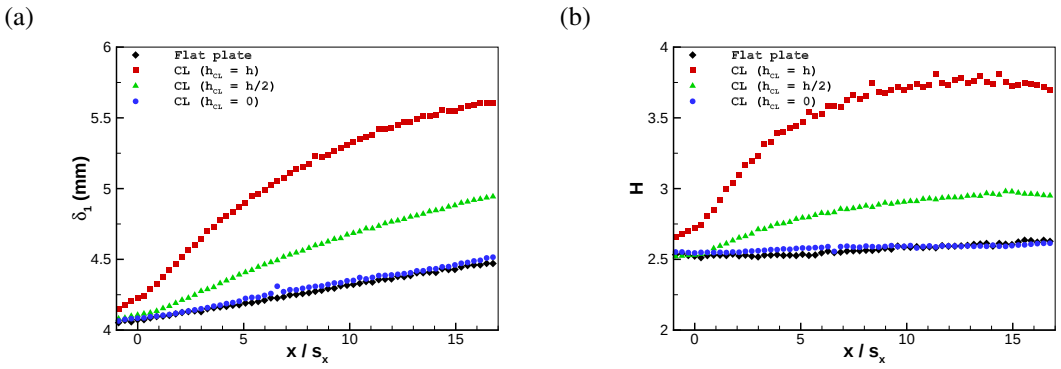

Figure 5.6: Comparison of (a) boundary layer displacement thickness δ_1, (b) shape factor H.

shape factor of the boundary layer along the converging line. Those parameters of a flat plate boundary layer are also included as a reference (black diamond). The boundary layer displacement thickness (δ_1) representing modification to the velocity shape is less sensitive to the free-stream velocity than the $99\%U_\infty$ boundary layer thickness (δ), which makes it more suitable to represent the changes in the local streamwise velocity within the boundary layer. Upstream of the riblet section ($x < 0$), a tiny increase in the displacement thickness is observed, which is caused by the blocking effect of the riblets above the smooth wall surface. In the region over the converging line, a lower local streamwise velocity leads to increased values of the displacement thickness and the shape factor than those of the baseline boundary layer. With an increased value of h_{CL}, a more substantial increase in δ_{CL} and H is observed, indicating that more low-velocity fluid is accumulated at the bottom of the boundary layer.

Figure 5.7 shows contours of the time-averaged induced streamwise velocity in the

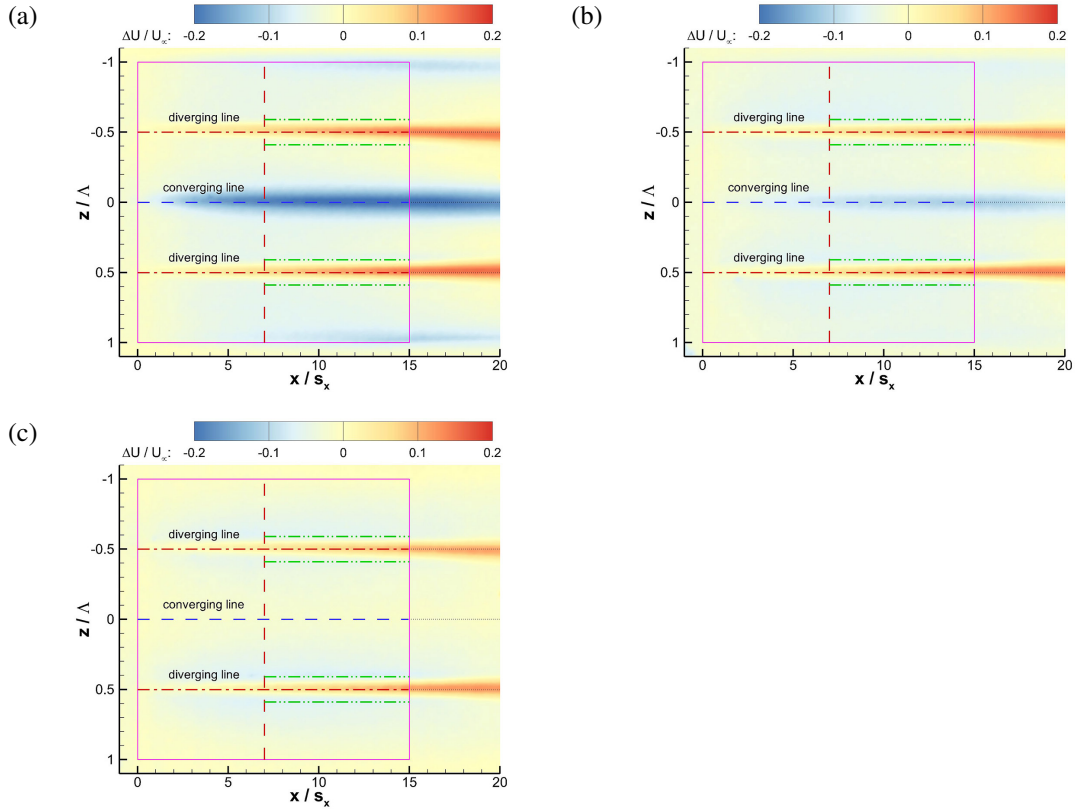

Figure 5.7: Time-averaged induced streamwise velocity over C-D riblets with (a) $h_{CL} = h$, (b) $h_{CL} = h/2$, (c) $h_{CL} = 0$ in the wall-parallel plane.

wall-parallel plane. Based on Figure 5.5, the streamwise velocity in the same wall-parallel plane over the flat plate is subtracted to reveal the induced velocity contour. In Figure 5.7a, a concentrated stripy zone with velocity defect (blue colour) is observed over the converging region, while stripy zones with velocity excess (red colour) are obtained over the diverging region. In comparison, with a reduced h_{CL} in Figures 5.7b and 5.7c, the intensity of induced streamwise velocity weakens over the converging region, while stripy shapes still exist over the diverging region.

Figure 5.8 shows contours of the time-averaged spanwise velocity in the wall-parallel plane. Based on the findings in Xu et al. [173], the development of a boundary layer over C-D riblets with uniform riblet height can be divided into a developing stage followed by a developed stage, with their separation locates at $x \approx 7s_x$. In Figure 5.8a, the distribution of the spanwise velocity indicates a distinct difference between these two stages. In the developing stage ($x < 7s_x$), the sign of the spanwise velocity component indicates a spanwise flow from the diverging line to the converging line, which is aligned with the spanwise direction of riblet valleys. In this stage, no recirculating

secondary flow is formed in the cross-stream plane. The fluid above the wall surface in the wall-parallel plane follows the fluid at a lower level which evolves along riblet valleys, as indicated in Figure 5.9a. In the developed stage ($x > 7s_x$), a spanwise flow opposite to the direction of riblet valleys is observed, which indicates the existence of a weak recirculating secondary flow in the cross-stream plane. The wall-parallel measurement plane in the present experiment is above the vortex centre of the recirculating secondary flow, and thus a reversed spanwise flow exists in the plane, as depicted in Figure 5.9b. With a decreased value of h_{CL} in Figures 5.8b and 5.8c, the weak recirculating secondary flow still exists in the cross-stream plane, although the intensity is expected to be lower.

Further analysis on the local characteristics of the time-averaged spanwise velocity in Figure 5.8a also provides a deeper understanding on the flow topology over C-D riblets (refer to Figure 9 in Xu et al. [173]). Close to the diverging line, there exist a few spotted zones which indicate local spanwise flow away from it. These spotted zones can be interpreted as the footprints of the fluid evolving inside riblet valleys in the wall-parallel plane. The streamwise distance between adjacent spotted zones is s_x, with each spotted zone corresponds to one riblet valley. The existence of these spotted zones indicates that the vortical structures in the cross-stream plane may vary slightly at different streamwise stations. Since the value of h_{CL} mainly affects the flow field characteristics over the converging region, the spotted zones close to the diverging line can still be observed in Figures 5.8b and 5.8c. Considering that the induced streamwise velocity is one to two orders of magnitude larger than the spanwise component, these spotted zones are not reflected in the contours of the streamwise velocity.

5.5 Conclusion

A laminar boundary layer over a spanwise roughness pattern of C-D riblets with a spanwise height variation, i.e. a reduced riblet height in the converging region, is analysed in multiple measurement planes in this paper. A reduced h_{CL} value leads to a less intense secondary flow, which includes a thinner boundary layer and a weaker induced streamwise velocity over the converging region. The induced flow field over the converging region is ignorable when the riblet height of this region is zero. In contrast, the flow field characteristics present only slight changes over the diverging region.

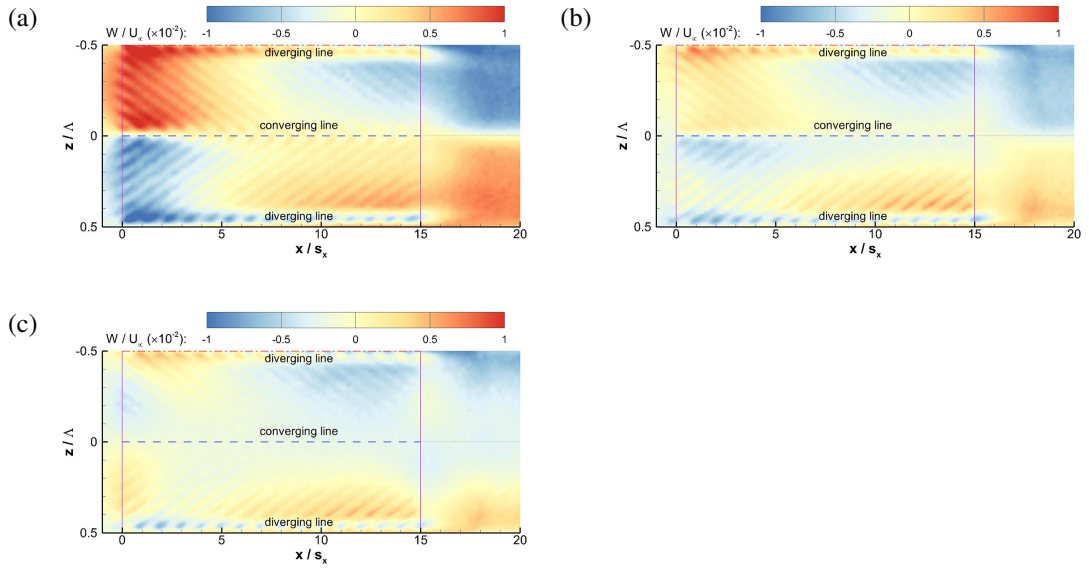

Figure 5.8: Time-averaged spanwise velocity over C-D riblets with (a) $h_{CL} = h$, (b) $h_{CL} = h/2$, (c) $h_{CL} = 0$ in the wall-parallel plane.

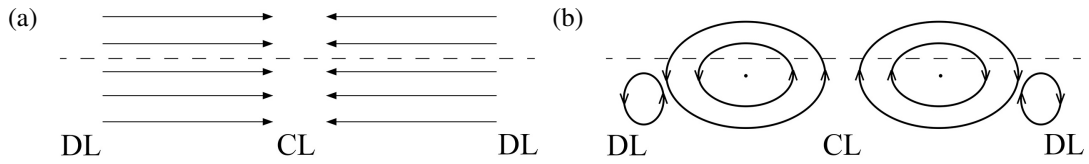

Figure 5.9: Schematic of the spanwise velocity and the relative position of the wall-parallel plane in the cross-stream plane in (a) the developing stage, (b) the developed stage. The dashed line indicates the station of the wall-parallel plane.

5.6 Acknowledgements

The authors would like to acknowledge the warm technical supports from the workshop technicians at the School of Mechanical, Aerospace and Civil Engineering.

Chapter 6

Statistical Analysis of Vortical Structures in Turbulent Boundary Layer over Directional Grooved Surface Pattern with Spanwise Heterogeneity

F. Xu, S. Zhong, and S. Zhang. Statistical analysis of vortical structures in turbulent boundary layer over directional grooved surface pattern with spanwise heterogeneity. *Physics of Fluids*, 31(8):085110, 2019.

Submitted: 14 May 2019

Accepted: 27 July 2019

Published Online: 16 August 2019

DOI: 10.1063/1.5110048

This paper was selected as *Featured Article*.

Author	Fang Xu	Shan Zhong	Shanying Zhang
Rig design and setup	60%	15%	25%
Experimental measurement	70%	10%	20%
Paper writing	60%	25%	15%
Review feedback	70%	15%	15%
Overall	60%	20%	20%

Table 6.1: Author contribution to this peer-reviewed paper.

6.1 Abstract

We examine the turbulent boundary layers developing over convergent-divergent riblets (C-D riblets) with three different heights ($h^+ = 8$, 14 and 20) at $Re_\theta = 723$ using particle image velocimetry. It is observed that although a logarithmic region presents in the velocity profiles over the converging and diverging line, Townsend's outer-layer similarity hypothesis is invalid. Compared to the smooth-wall case, C-D riblets with a height of 2.4% of the smooth-wall boundary layer thickness can cause a significant increase in the turbulence production activities over the converging region, as evidenced by a more than 50% increase in the turbulent shear stress and in the population of prograde and retrograde spanwise vortices. In contrast, the impact of riblets on the diverging region is much smaller. The slope of vortex packets becomes steeper and they are more streamwise stretched in the outer layer over the diverging region, whereas their shape and orientation is less affected over the converging region. Furthermore, the number of uniform momentum zones across the boundary layer increases over the converging region, causing a reduction in the thickness of uniform momentum zones in the outer part of the boundary layer. Overall, while an increased riblet height affects a large portion of the boundary layer away from the wall over the converging region, the impact on the diverging region is largely confined within the near-wall region. Such distinct differences in the response of the boundary layer over the diverging and converging region is attributed to the opposite local secondary flow motion induced by C-D riblets.

NOMENCLATURE

$A_g\ (m^2)$	groove cross section
$B\ (1)$	log-law constant
$H_y\ (m)$	wall-normal height
$h\ (m)$	riblet height
$K\ (1)$	acceleration parameter
$L_x\ (m)$	streamwise length scale
$N_{UMZ}\ (1)$	number of uniform momentum zones
$R\ (1)$	spatial correlation function
$Re_\tau\ (1)$	friction Reynolds number
$Re_\theta\ (1)$	momentum thickness Reynolds number

$S\ (m)$	spanwise spacing
$s\ (m)$	riblet spacing
$t_{UMZ}\ (m)$	thickness of uniform momentum zones
$U_\tau\ (ms^{-1})$	friction velocity
$U_c\ (ms^{-1})$	convection velocity
$u\ (ms^{-1})$	streamwise velocity
$v\ (ms^{-1})$	wall-normal velocity
$U_\infty\ (ms^{-1})$	freestream velocity
$W_x\ (m)$	streamwise width
$w_c\ (m)$	riblet crest width
$w_r\ (m)$	riblet root width
$x\ (m)$	streamwise coordinate
$y\ (m)$	wall-normal coordinate
$y_d\ (m)$	zero-plane displacement
$z\ (m)$	spanwise coordinate
$\alpha\ (1)$	inclination angle
$\Delta U\ (ms^{-1})$	difference in time-averaged streamwise velocity
$\delta\ (m)$	$99\%U_\infty$ boundary layer thickness
$\gamma\ (1)$	riblet yaw angle
$\kappa\ (1)$	von Kármán constant
$\Lambda\ (m)$	riblet wavelength
$\lambda_{ci}\ (s^{-1})$	swirling strength
$\langle\lambda_{ci}\rangle\ (s^{-1})$	signed swirling strength
$\nu\ (m^2s^{-1})$	kinematic viscosity
$\omega_z\ (s^{-1})$	vorticity in $x-y$ plane
$\Pi\ (1)$	population density of vortices
$\theta\ (m)$	boundary layer momentum thickness
$\sigma\ (1)$	standard deviation
$\lvert\cdot\rvert$	absolute value
$\rightarrow$	vector
$\bar{}$	ensemble average

Superscript

$+$	normalisation in wall units
$'$	fluctuating component

Subscript	
p	prograde vortex
r	retrograde vortex
ref	reference point of correlation origin
rms	root mean square
s	smooth wall

Abbreviation	
C-D riblets	convergent-divergent riblets
CL	converging line
DL	diverging line
PIV	particle image velocimetry
p.d.f.	probability density function
TNTI	turbulent/non-turbulent interface
UMZ	uniform momentum zone

6.2 Introduction

Convergent-divergent riblets (C-D riblets) are composed of a spanwise array of sections of left-yawed and right-yawed microgrooves arranged in an alternating manner [see Figure 6.1]. Due to their potential for reducing surface friction drag [25] and suppressing flow separation [87, 126], C-D riblets have attracted considerable research attentions in the recent few years [79, 113, 72, 173, 174, 71]. Similar to the patterns of spanwise alternating rough/smooth strips [166, 9] or longitudinal elevated/lower surfaces [108, 178, 66], C-D riblets are a type of surface patterns with spanwise heterogeneity, which are capable of generating a secondary flow in the boundary layers. A summary of the published work on C-D riblets can be found in Xu et al. [173].

As a result of the directional orientation of their microgrooves, C-D riblets generate inherently different flow structures in a boundary layer from those produced by longitudinal riblets [40, 54, 127, 176, 60, 109, 177]. While the effects of longitudinal riblets are known to be confined in the vicinity of the riblet surface, C-D riblets are capable of producing a profound modification to the entire boundary layer [79, 113, 72, 173]. Over the diverging region, the streamwise velocity in the near-wall region is increased

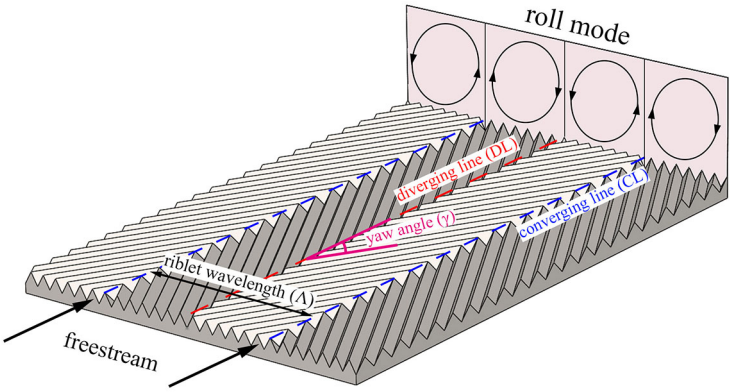

Figure 6.1: Schematic diagram of convergent-divergent riblets (C-D riblets) with definitions of diverging line (DL), converging line (CL), riblet wavelength (Λ) and yaw angle (γ). The time-averaged roll mode is shown in the cross-stream plane.

compared with that in the smooth-wall case, leading to a reduced boundary layer thickness, and the opposite occurs over the converging region [113, 173, 174]. Such a modification to the velocity field has been attributed to the presence of a weak time-averaged secondary flow motion (roll mode) in the cross-stream plane in the boundary layer, whereby an upwelling (downwelling) over the converging (diverging) region is created [see Figure 6.1] [72, 173]. The roll mode is essentially caused by the directional orientation of the yawed microgrooves which results in a surface flow directing from the diverging region to the converging region, as evidenced by the dye visualisation experiment conducted by Xu et al. [173].

The secondary flow motions created by C-D riblets are also found to radically modify both the time-averaged turbulence characteristics of the boundary layer and the coherent structures. While reduced near-wall turbulence intensity is observed over the diverging region, increased near-wall turbulence intensity is found over the converging region. This is in line with a reduction in the local skin friction coefficient over the diverging region and an increase over the converging region as estimated using the modified Clauser technique [113]. Based on single hot-wire measurements across the boundary layer and PIV measurements in the wall-parallel plane located in the logarithmic region, the roll mode seems to have gathered the low-speed fluid and relocated the very-large-scale streamwise structures and features with high vortical activities over the converging region of the C-D riblets [113, 114, 73, 72]. With a large field of view PIV measurements in all orthogonal planes, Kevin et al. [71] confirmed that C-D riblets result in formation of large-scale coherent structures over the converging region, which dictate the instantaneous behaviour of the roll mode and share some

characteristics, such as meandering and breaking, displayed by the superstructures observed in canonical smooth-wall flows.

It is known that a turbulent boundary layer at low Reynolds numbers is populated by horseshoe/hairpin vortices, which are typically composed of either one or two streamwise-oriented legs connected to a spanwise-oriented head whose rotation is of the same sense as the mean shear [3, 168]. Hairpin vortices are prevalent in the transitional flow and they may not retain a complete hairpin shape in a turbulent boundary layer at a high Reynolds number [41, 146]. In the longitudinal (streamwise wall-normal) plane, the presence of these vortices is manifested by the appearance of 'prograde' spanwise vortices and 'retrograde' spanwise vortices. Prograde vortices, whose rotation is in the same sense as the mean shear, are often associated with strong ejection and sweep events occurring in the lower upstream and upper downstream regions of their vortex centres, respectively [169]. Retrograde spanwise vortices, whose rotations are opposite to the mean shear direction, are believed to be the spatial signatures of bent necks of horseshoe/hairpin vortices [107]. The horseshoe/hairpin vortices are often grouped together in an orderly manner to form vortex packets, resulting in δ-scale coherent structures which are inclined downstream [3]. The superstructures, which have a streamwise length scale substantially larger than the local boundary layer thickness, are observed in the outer region, and their motion is a self-sustained process without drawing energy from the hairpin vortices in the near-wall region [67, 130]. As such, a hierarchy of vortical structures of different scales are observed in a turbulent boundary layer.

Based on the existing studies, as a type of spanwise heterogeneous surface pattern, C-D riblets generate a secondary flow motion due to directional arrangement of their microgrooves. This secondary flow subsequently results in a profound difference in the time-averaged flow field in the converging and diverging region and a redistribution of turbulent activities in the spanwise direction. Therefore, the way the coherent structures organise themselves in the converging and diverging region is expected to be distinctly different. So far, a fair amount of experimental data has become available enabling a good understanding of the time-averaged behaviour of the flow field developing over C-D riblets. However, a more detailed description of the activities of coherent structures of different scales is still lacking. Hence further studies are required to gain a new insight in this regard.

Some statistical techniques have been applied to analyse the characteristics of coherent structures in the boundary layer developing along smooth- or rough-wall surfaces [29, 156, 36]. A vortex identification technique was first proposed by Wu & Christensen [169] and Natrajan et al. [107], to study the population of prograde and retrograde spanwise vortices across a boundary layer. Spatial correlation maps have been widely used to extract the time-averaged shape of hairpin packets. The concept of uniform momentum zones (UMZs) in a turbulent boundary layer was put forwarded by Meinhart & Adrian [96] to infer the organised spatial distribution of hairpin vortices. The boundaries of a uniform momentum zone are found to pass through the heads of hairpin vortices [4], and hence they are associated with step changes in the instantaneous streamwise velocity profile across the boundary layer. However, these analytical techniques have not been applied to examine the turbulent boundary layer flow developing over C-D riblets or other types of surface patterns with spanwise heterogeneity.

Therefore, in this paper we perform a statistical analysis of the instantaneous velocity vector fields, focusing on the effects of C-D riblets on the characteristics of vortical structures over the diverging and the converging region. Particle image velocimetry (PIV) measurements are conducted on the turbulent boundary layer over C-D riblets with three different heights. The vortex identification technique is improved in efficiency and applied to study the population of prograde and retrograde spanwise vortices across the boundary layer. Spatial correlation maps are examined to extract the information about the streamwise coherence length and orientation of vortex packets. The number and thickness of uniform momentum zones in the boundary layer are also investigated. The effects of riblet height on these properties are summarised.

6.3 Experimental set-up

6.3.1 Water flume and flat plate

The present experiment was conducted in a low-speed water flume at the University of Manchester. The water flume has a test section measuring $305mm \times 305mm$ in cross-section. Four metal screens arranged in a decreasing order of mesh sizes were installed at the inlet of the flume to ensure a low level of background turbulence in the test section. Further details of the water flume can be found in our previous work [173].

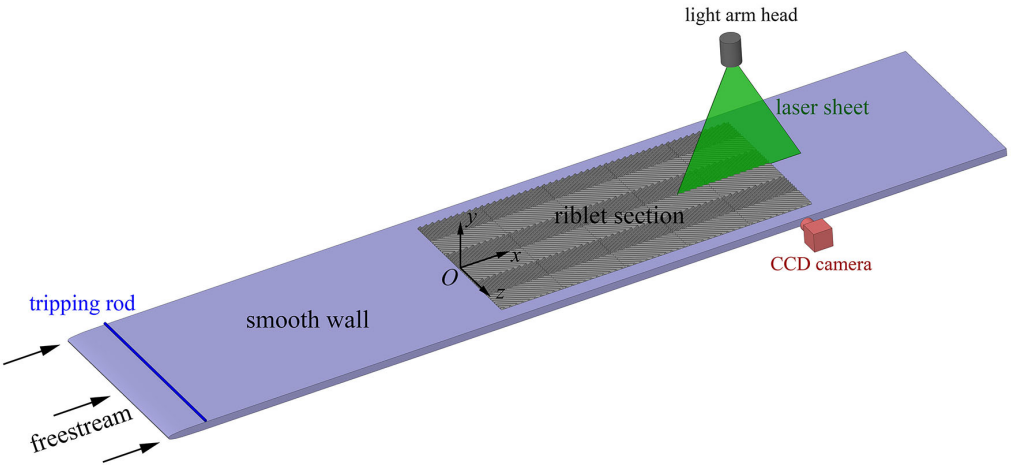

Figure 6.2: Schematic diagram of the mono-PIV system in the longitudinal plane. The riblet spacing and the riblet height are not drawn to scale.

To facilitate the experimental study, a 1350mm-long flat plate with its test section facing upward was designed [see Figure 6.2]. It has a super-elliptical leading edge to avoid flow separation from the leading edge. To minimise plate bending along the streamwise direction, the flat plate is strengthened by two angle irons attached to its bottom side. The inclination angle of the flat plate can be finely adjusted using the threads on the four steel legs mounted on the bottom floor of the water flume. There is a small gap between the flat plate and each side wall of the water flume, which restrains the growth of the side wall boundary layers along the flat plate. A cavity measuring $500mm \times 250mm \times 6mm$ (in length, width and depth respectively) starting at $550mm$ downstream of the leading edge was machined on the test plate. Rectangular tiles with either a smooth surface or rough pattern as the upper surfaces can be inserted into the cavity of the flat plate.

As shown in Figure 6.2, axes x, y and z represent the streamwise, wall-normal and spanwise directions respectively, while u, v and w denote the corresponding velocity components. The origin of the coordinate system is located at the beginning of the riblet section, and it levels with the smooth wall and coincides with the centre line of the test plate. The instantaneous velocity $\vec{u} = (u,v,w)$ is composed of the time-averaged component $\vec{U} = (U,V,W)$ and the fluctuating component $\vec{u'} = (u',v',w')$, i.e. $\vec{u} = \vec{U} + \vec{u'}$.

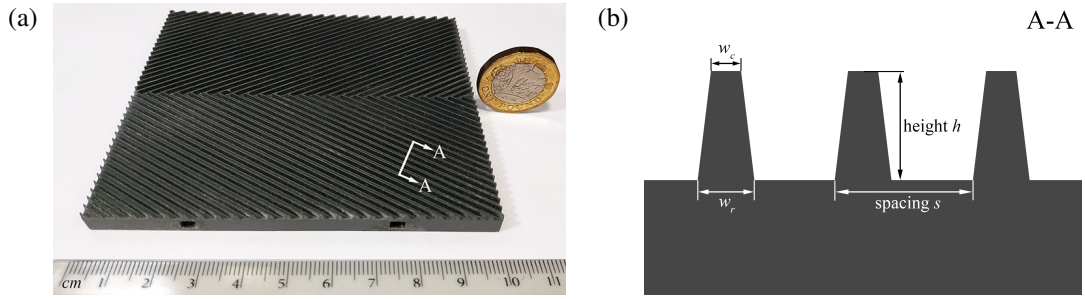

Figure 6.3: (*a*) Perspective view of a tile with C-D riblets on its upper surface. A £1 coin on its side is displayed for visual comparison. (*b*) Sectional view of C-D riblets along $A-A$, showing the trapezoidal profile of riblet teeth.

6.3.2 Parameters of convergent-divergent riblets

In the present experiment, C-D riblets were machined on rectangular tiles using 3D (three-dimensional) printing technique, as shown in Figure 6.3a. The layer thickness and particle diameter were set as $25\mu m$, and black resin was used to reduce the surface reflection of the laser light. These riblet tiles can be inserted into the cavity of the flat plate to form the surface pattern. The riblet section is $500mm$ in length and $250mm$ in width. The riblet wavelength (Λ) is $83.33mm$, which is 2.55 times of the turbulent boundary layer thickness over the smooth wall (δ_s) at the measurement station. Across the span of the cavity, three riblet wavelengths were accommodated. The yaw angle (γ), which is defined as the angle between the yawed grooves and the freestream direction, is selected as 30° based on the optimal value proposed by Chen et al. [25]. In our experiment, C-D riblets with three different heights (h), i.e. $0.8mm$, $1.4mm$ and $2mm$, and the same riblet spacing (s) of $2mm$ were tested. In all cases, the smooth wall is leveled with the mid height of the riblets. The blockage ratio, i.e. the riblet height to the boundary layer thickness of the smooth wall (h/δ_s), is 2.4%, 4.3% and 6.2% respectively at the measurement station. Over a homogeneous rough-wall surface, the outer-layer similarity is expected to hold for all these three height values (h/δ_s) [170, 47]. A flat instead of curved riblet surface was chosen, since the former is easier to machine in future engineering applications. As indicated in Figure 6.3b, to ensure durability, the riblets have trapezoidal teeth with a width of $0.4mm$ at the crest (w_c) and $0.8mm$ at the root (w_r).

The riblet height can be expressed in wall units using the local friction velocity (U_τ) and the kinematic viscosity (ν) as $h^+ = hU_\tau/\nu$. To ensure consistency, the friction velocity over the smooth wall ($U_{\tau s}$) is applied in the normalisation. Along the streamwise length of the riblet section, the normalised riblet height (h^+) in wall unit varies

by less than 6.3%. At the measurement station, the riblet height of $0.8mm$, $1.4mm$ and $2.0mm$ corresponds to approximately 8, 14 and 20 in wall units respectively, and the riblet spacing in wall units is $s^+ = sU_\tau/\nu = 20$. Hereafter, we refer to these C-D riblets as $h^+ = 8$, $h^+ = 14$ and $h^+ = 20$ riblets respectively. García-Mayoral & Jiménez [49] proposed to use the groove cross section (A_g) to characterise the drag reduction effects of longitudinal riblets. The values of $A_g^{+^{1/2}} = \sqrt{A_g\nu^2/U_\tau^2}$ for the trapezoidal riblets tested in our experiments are 10.6, 14 and 16.7 respectively. Unlike the $h^+ = 8$ or $h^+ = 14$ riblets which stay within the viscous sublayer and the buffer layer, the riblets with $h^+ = 20$ approach the lower bound of the log-law region [see Figure 6.4].

Note that the present study and the work by Nugroho et al. [113] investigate the effects of riblet height from two complementary aspects. In our study, the freestream velocity was kept the same (the same baseline turbulent boundary layer), and the change in h^+ was obtained by changing the physical height (h) of C-D riblets. Since the riblet spacing remained the same, the ratio h/s varied from 0.4 to 1.0. By contrast, in the work by Nugroho et al. [113], the height of riblets was kept constant, and the riblet height in wall units (h^+) was changed by varying the freestream velocity. In their study, the baseline turbulent boundary layers were different, whilst the ratio h/s remained constant [113].

6.3.3 Particle image velocimetry setup

The mono-particle image velocimetry (PIV) system used in our experiment is composed of a light-guiding arm, a New Wave Solo-PIV 120 laser generator, a laser pulse synchroniser (Model 610036), and a 4-mega pixel charge-coupled device (CCD) camera with 12-bit intensity. The maximum image-capturing frequency of the PIV system is $7.5Hz$. The resolution of the CCD camera is 2352×1768 pixels. The hollow glass seeding particles have a mean diameter of $10\mu m$ and a density of $1.1 \times 10^3 kg/m^3$, which were estimated to have a settling velocity of approximately $5 \times 10^{-6} m/s$.

Mono-PIV measurements were performed in the longitudinal ($x-y$) plane, located in the middle of the spanwise direction. The longitudinal measurement plane covers the region located between $12\delta_s$ and $15\delta_s$ downstream of the start of the riblet section, where δ_s is the boundary layer thickness over the smooth wall at $x = 450mm$ ($\delta_s = 32.5mm$). The aperture of the lens was set at $f/4.0$. The time interval between two laser pulses was set at $2ms$. The width of the laser light sheet is around $1mm$. A total of 6000 image pairs (snapshots) were captured to ensure statistical convergence. A low sampling frequency of $0.5Hz$, which corresponds to 12.3 times the turnover time

Parameter	U_∞	K	δ_s	$U_{\tau s}$	Re_θ	Re_τ
Value	$0.2m/s$	5×10^{-8}	$32.5mm$	$9.75\times10^{-3}m/s$	723	320

Table 6.2: Experimental parameters of the turbulent boundary layer.

scale in the smooth-wall boundary layer (δ_s/U_∞), was used to minimise the statistical dependence between adjacent snapshots.

The PIV image pairs were processed using the cross-correlation algorithm in the InSight 4G^{TM} software. The first interrogation area is 64×32 pixels, and the final interrogation area is 24×24 pixels with a 50% overlap. The field of view is around $100mm\times75mm$, which corresponds to a spatial resolution of $0.51mm\times0.51mm$, or approximately 5×5 in wall units. The streamwise length of the PIV field is approximately 1000 in wall units. The average particle image diameter is $2-3$ pixels, which ensures the sub-pixel accuracy. The image deformation algorithm is applied considering the high disparity in the displacements of particles at different wall-normal distances. The measurement uncertainties in velocity components are estimated using the Peak Ratio (PR) method incorporated in the InSight 4G^{TM} software. The expanded uncertainty in velocity components, i.e. 95.4% possibility of having the true value within the uncertainty bound, is estimated to be $0.47\%U_\infty$ for the instantaneous flow field and $0.03\%U_\infty$ for the time-averaged flow field.

6.3.4 Characterisation of the turbulent boundary layer over the smooth wall

The baseline turbulent boundary layer was tripped by a $4mm$ diameter rod installed $75mm$ downstream of the leading edge of the flat plate. The inclination angle of the flat plate was adjusted to zero degree to minimise the pressure gradient in the freestream direction. The freestream velocity (U_∞) is $0.2m/s$. The turbulence intensity in the freestream region is around 0.7%, which is acceptable considering the low Reynolds number of the flow. The acceleration parameter ($K=\nu(dU_\infty/dx)/U_\infty^2$) is approximately 5×10^{-8} in the measurement section, which ensures a streamwise quasi zero-pressure-gradient condition. At the measurement station of $x=450mm$, the boundary layer thickness (δ_s) is $32.5mm$ and the friction velocity ($U_{\tau s}$) is $9.75\times10^{-3}m/s$. The momentum thickness Reynolds number ($Re_\theta=U_\infty\theta/\nu$) is 723 and the friction Reynolds number ($Re_\tau=U_\tau\delta/\nu$) is 320. Table 6.2 lists experimental parameters of the baseline turbulent boundary layer.

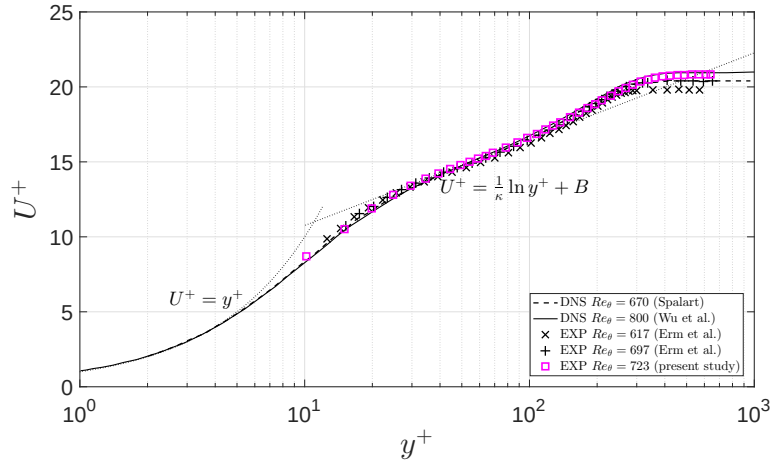

Figure 6.4: Time-averaged streamwise velocity profile U^+ as a function of inner coordinate y^+ of the turbulent boundary layer.

Figure 6.4 shows the time-averaged streamwise velocity profile (U^+) of the smooth-wall turbulent boundary layer. For clarity of presentation, not all the data points in the high y^+ region are presented. The friction velocity U_τ is estimated using the Clauser method with $\kappa = 0.4$ and $B = 5.0$ [32]. There exist a number of limitations in the Clauser method, including the selection of κ and B values and the subjectivity involved in selecting the data points in the logarithmic region [154]. The profiles of wind tunnel datasets at $Re_\theta = 617$ (Erm et al. [45]) and at $Re_\theta = 697$ (Erm et al. [44]) are included for comparison. DNS datasets at $Re_\theta = 670$ (Spalart [138]) and at $Re_\theta = 800$ (Wu & Moin [167]) are also used as references. It can be seen that the measured mean velocity profile obtained from our experiment follows the log-law in the region of $30 < y^+ < 120$. While there is a good consistency between our data and the references in the inner layer, some differences exist among these datasets in the wake region of $y^+ > 300$. Besides the minor difference in the Reynolds number, some other factors, e.g. differences in the numerical method used to introduce turbulence, numerical discretisation scheme and resolution in simulations or the tripping device used to trigger laminar-turbulent transition in the experiments [44], may also contribute to the discrepancies observed. Overall, the baseline streamwise velocity profile is in good agreement with the reference profiles.

Figure 6.5 compares our profiles of turbulence intensities of u'^+_{rms} and v'^+_{rms} (*rms* refers to the root mean square) with four reference datasets at similar Reynolds numbers. The outer coordinate is applied here to be consistent with reference datasets. Overall, the profiles of turbulence intensities in the present experiment exhibit a very

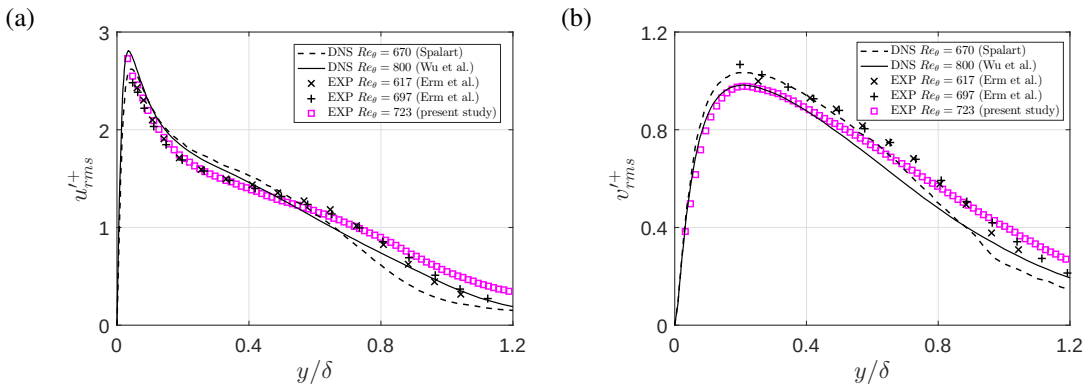

Figure 6.5: Turbulence intensity of (*a*) streamwise component u'^+_{rms} and (*b*) wall-normal component v'^+_{rms}, as a function of outer coordinate y/δ of the turbulent boundary layer.

similar trend as the reference profiles. The peak value and its vertical position are similar among these datasets. In the experiments of Erm et al. [45, 44], the lower near-wall peak of u'^+_{rms} could be attributed to the large value of the hot-wire etched length [22]. Interestingly, the present turbulence intensity profiles are closer to the published experimental data [45, 44] than the numerical simulation results [138, 167]. In the region outside the boundary layer, turbulence intensities of u'^+_{rms} and v'^+_{rms} in the present experiment are slightly larger than those in the other studies. We attribute this discrepancy to the slightly higher level of background freestream turbulence in our water flume.

Figure 6.6 compares profiles of the Reynolds shear stress ($-\overline{u'v'}^+$) of the turbulent boundary layer with four reference datasets [45, 138, 44, 167]. Despite the general agreement with these reference datasets in the profile shape, the peak value of $-\overline{u'v'}^+$ is slightly lower in the present experiment. At a low Reynolds number, Erm et al. [44] revealed that the Reynolds shear stress profile is sensitive to the tripping device. Thus, the minor variation of $-\overline{u'v'}^+$ may be attributed to the size and location of the tripping device used.

6.4 Statistical techniques

In this section, the statistical techniques used for extracting the characteristics of vortical structures are outlined. To identify spanwise vortices from PIV data, an efficient vortex recognition algorithm based on the queue data structure is utilised, which enables the population density of prograde and retrograde vortices to be computed. The spatial correlation of instantaneous velocity fields is applied to reveal the streamwise extent and inclination angle of vortex packets. The analytical technique to extract the

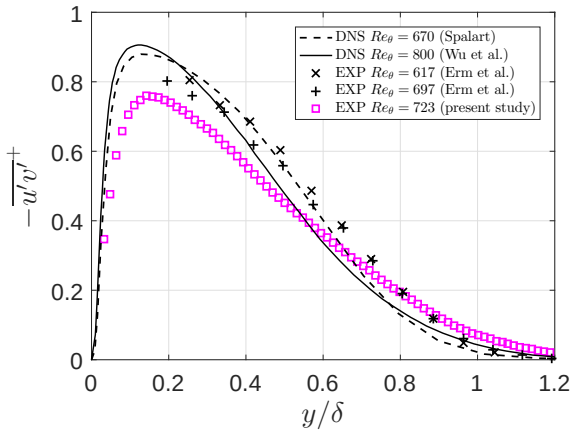

Figure 6.6: Reynolds shear stress $-\overline{u'v'}^+$ as a function of outer coordinate y/δ of the turbulent boundary layer.

features of uniform momentum zones in a turbulent boundary layer is also introduced.

6.4.1 Recognition and distribution statistics of spanwise vortices

Prograde and retrograde vortices are spanwise vortices which possess negative and positive values of the spanwise fluctuating vorticity, respectively. The signed swirling strength ($\langle\lambda_{ci}\rangle$), as proposed by Zhou et al. [182], can be applied to identify the instantaneous spanwise vortices by extracting local swirling motion from the mean shear flow. In the longitudinal plane, the definition of the signed swirling strength is given by

$$\langle\lambda_{ci}\rangle = \lambda_{ci}\frac{\omega_z}{|\omega_z|}, \tag{6.1}$$

where λ_{ci} is the imaginary part of the complex conjugate eigenvalue of the in-plane velocity gradient tensor, ω_z is the in-plane vorticity, and the operator $|\cdot|$ denotes the absolute value. The sign of the in-plane vorticity ($\omega_z/|\omega_z|$) indicates the rotational direction of the local swirling motion.

Figure 6.7 shows the distribution of spanwise vortices in a randomly selected instantaneous field obtained from the present study over the smooth wall. Due to the direction of the mean shear, there are more prograde vortices than retrograde vortices. The in-plane velocity vectors in Figure 6.7 are obtained using Galilean decomposition by subtracting a convection velocity of $U_c = 0.85U_\infty$. The vortical structures which have the same convection velocity can be identified by the closed streamline patterns, and the positions of these structures are aligned with the areas of high magnitude of

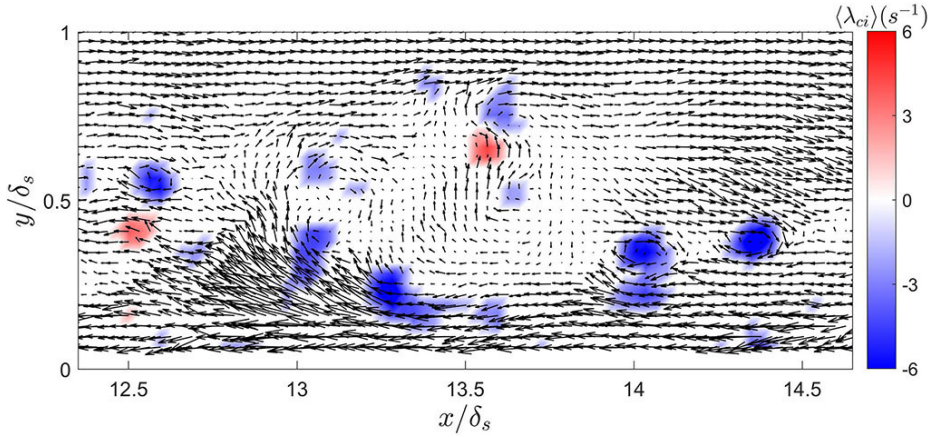

Figure 6.7: Sample contour of the instantaneous signed swirling strength $\langle\lambda_{ci}\rangle$ and in-plane velocity vectors $(u-U_c, v)$ revealing the distribution of prograde (blue) and retrograde (red) vortices.

$\langle\lambda_{ci}\rangle$.

The regions in the longitudinal plane constituting individual prograde/retrograde vortices can be identified by specifying predetermined thresholds of value and size. The vortex identification technique was first proposed by Wu & Christensen [169] and Natrajan et al. [107]. In order to further improve computational efficiency and reduce memory usage, a (breadth-first) vortex recognition algorithm based on a queue data structure is proposed. Compared with the brute force method, this algorithm improves efficiency and reduces computer memory usage by using dynamic data structures [34, 86]. Details of this algorithm are listed below.

S1. Scan each point in the instantaneous field to mark the points which exceed the threshold value(s) in terms of the signed swirling strength.

S2. Find a marked point in the field (e.g. the point with the largest $\langle\lambda_{ci}\rangle$), then enqueue (i.e. insert the point item at the back of the queue) and unmark it.

S3. While the queue is not empty, dequeue (i.e. remove) the first point. Then enqueue and unmark its adjacent marked points (four candidates are the points at the top, bottom, left and right). Repeat this operation until the queue is empty.

S4. The points dequeued in S3 constitute a connected area. Determine whether or not that area can be considered as a prograde/retrograde vortex by evaluating its spatial range.

S5. Repeat S2-S4 until there is no marked point left in the field.

To extract the centres of spanwise vortices found with the vortex recognition algorithm, the weighted average of the points constituting a prograde/retrograde vortex is calculated, with the local swirling strength λ_{ci} as the weighting coefficient. At a given wall-normal station, the threshold value of the vortex intensity is selected to be proportional to the root-mean-square of the local signed swirling strength, which accounts for the non-homogeneity of the flow in the wall-normal direction [169, 7]. In the following analysis, the threshold of the vortex intensity is selected as 1.5 times of the root-mean-square of $\langle \lambda_{ci}(y) \rangle$ over the smooth-wall case at the same location. In accordance to the choice of 22 wall units (three grid points) in Wu & Christensen [169], the threshold of vortex size is set as four grid points in the present study, which corresponds to approximately 20 wall units over the smooth wall. By using the same thresholds obtained from the smooth-wall case, we can quantitatively compare the population of prograde/retrograde vortices over C-D riblets with different riblet heights.

In our study, the population trends of prograde and retrograde vortices are presented as a function of the wall-normal distance. The population density of prograde (retrograde) vortices is defined as

$$\Pi_{p(r)} = \frac{N_{p(r)}}{H_y \cdot W_x / \delta_s^2}, \tag{6.2}$$

where $N_{p(r)}(y)$ is the ensemble-averaged number of prograde (retrograde) vortices whose centres are located in a rectangular area of $H_y \times W_x$. H_y is the wall-normal height which is selected as $0.1\delta_s$ (which equals 33 in wall units), and W_x is the streamwise width of the field of view of the PIV images. The centre of the rectangular area is located at a wall-normal station of y. The definition of population density in Eq. (6.2) is similar to the one proposed by Wu & Christensen [169]. Thus, $\Pi_{p(r)}(y)$ indicates the normalised population of prograde (retrograde) vortices within an area of $\delta_s \times \delta_s$ in the longitudinal plane.

6.4.2 Extraction of spatial correlation features

The vortex packet (hairpin packet), which is composed of a hierarchy of hairpin vortices arranged in an organised manner, can be analysed using spatial correlations of the instantaneous velocity fields in the longitudinal plane. The two-dimensional spatial

correlation function of streamwise fluctuating velocity fields is defined as

$$R_{u'u'}(\Delta x, y; y_{ref}) = \frac{\overline{u'(x, y_{ref})u'(x+\Delta x, y)}}{\sigma_{u'(y_{ref})}\sigma_{u'(y)}}, \tag{6.3}$$

where Δx is the streamwise separation, y_{ref} is the wall-normal distance at which the correlation is calculated, σ is the standard deviation, and the overline denotes an ensemble average of all PIV snapshots.

To quantitatively analyse the features of vortex packets, the streamwise length and the inclination angle can be extracted from the spatial correlation contour. With a reference to Christensen & Wu [29], the streamwise length scale (L_x) can be defined as the streamwise distance between the upstream location and the downstream location of the $R_{u'u'} = 0.5$ contour line at y_{ref}.

The inclination angle (α) is obtained by best fitting the $R_{u'u'}$ contour of a specific value with an ellipse which is centred at the location where the correlation is taken. The angle of the major axis of the ellipse forms with the streamwise direction is taken as the inclination angle [165]. In the present study, the overall inclination angel of the vortex packet is estimated by averaging the inclination angles of the $R_{u'u'} = 0.4$, 0.5 and 0.6 contours. The method of finding the inclination angle using the contour lines of intermediate values of correlation coefficients described above is found to yield more robust results than using the contour lines of low values of correlation coefficients. This is because this method is less susceptible to the noise in the correlation field. Christensen & Wu [29] reported that the inclination angle α of the $R_{u'u'}$ contour gives a good indication of the inclination angle of the vortex packet. The inclination angle is largely invariant over a wide range of Reynolds numbers [92].

6.4.3 Identification of uniform momentum zones

The presence of uniform momentum zones (UMZs) in the turbulent boundary layer was first revealed by Meinhart & Adrian [96] and further investigated by Adrian et al., [4] Kim & Adrian, [77] de Silva et al. [37, 36], etc. Within such a zone there is a relatively small momentum variation, and a significant momentum change only occurs across the boundary between adjacent zones. The UMZs are prevalent across a turbulent boundary layer, and they can persist for long distances along the streamwise direction [96].

Figure 6.8a illustrates the UMZs in a randomly selected instantaneous field obtained from the present study over the smooth wall. The solid black lines delimit UMZs, and the solid red line indicates the interface between the turbulent regime and the non-turbulent regime. The region between solid lines has an approximately uniform streamwise momentum. The turbulent/non-turbulent interface (TNTI) is identified using the kinematic energy criterion in the frame of reference moving with the freestream, as proposed by de Silva et al. [37].

Figure 6.8b compares the instantaneous and time-averaged streamwise velocity profiles along the vertical dotted line in Figure 6.8a. There exists a significant change in the instantaneous streamwise velocity across the boundary of UMZs. The horizontal dotted lines delineate the boundaries of UMZs, while the upper dotted line indicates the TNTI. In Figure 6.8c, the probability distribution function (p.d.f.) of the instantaneous streamwise velocity is applied to demarcate UMZs. The vertical dotted lines indicate the velocities which delimit UMZs, while the closed pentagrams indicate modal velocities. The entire field of view of the PIV snapshot in Figure 6.8a is accounted to make the probability distribution as smooth as possible. PIV data points in the non-turbulent region are excluded to avoid their dominance in p.d.f. statistics. In the histogram, the value at each peak point (modal velocity) delineates the characteristic velocity within a UMZ, whereas the value at each valley point corresponds to the boundary between adjacent UMZs.

In the present study, the entire PIV field of view which corresponds to $L^+ \approx 1000$, is taken into account to analysed features of UMZs, and the non-turbulent regime above the TNTI is excluded. Our parameter study using all PIV snapshots reveals that, when $L > \delta_s$ (i.e. $L^+ > 320$), the value of L has a negligible effect on the statistical characteristics of UMZs. This result is consistent with the finding of de Silva et al. [36], which indicates that a selection of L^+ greater than 300 does not affect the p.d.f. of N_{UMZ}.

6.5 Results and analysis

In this section, after briefly introducing the profiles of velocity and Reynolds shear stress, we reveal the effects of C-D riblets on the vortical structures in three interrelated aspects. The population densities of prograde/retrograde spanwise vortices are compared over C-D riblets and the smooth wall. The features of vortex packets, including the streamwise extent and the inclination angle, are extracted and compared. The effects of the newly created vortical structures on the uniform momentum zones

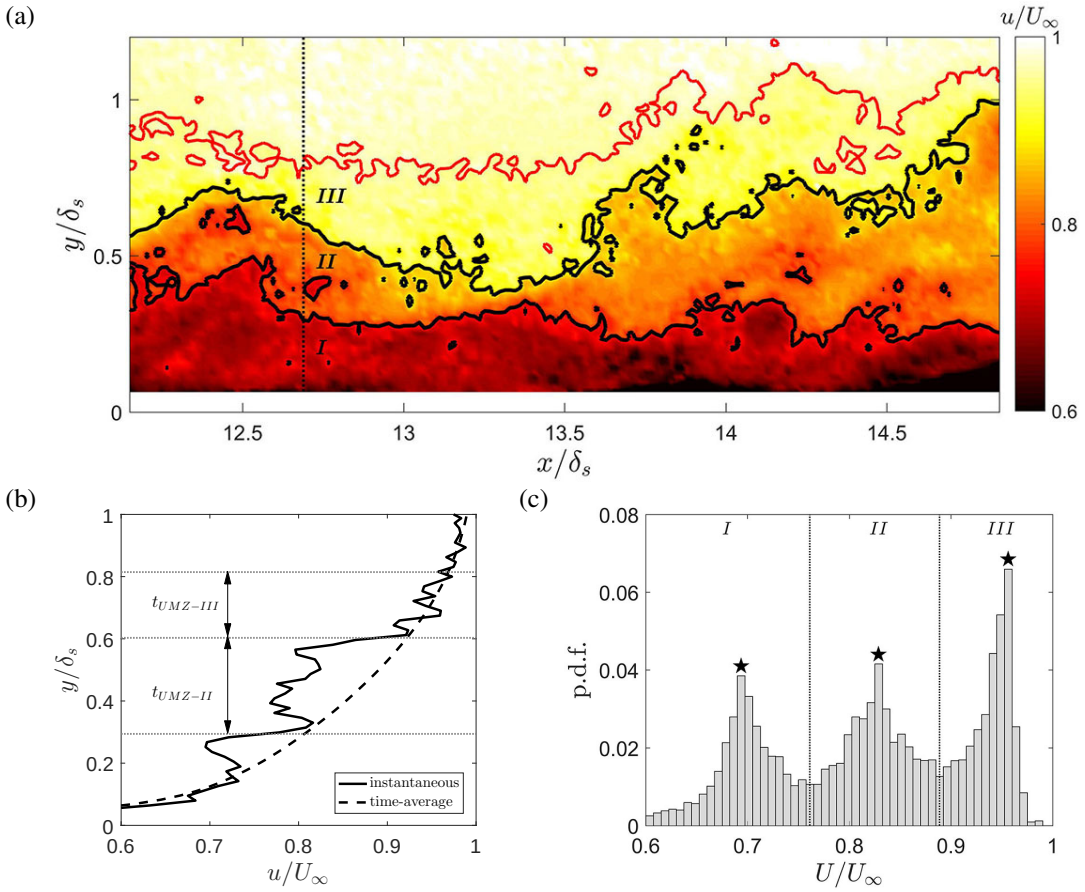

Figure 6.8: (*a*) Sample contour of the instantaneous streamwise velocity u revealing the presence of uniform momentum zones. (*b*) Profiles of the instantaneous and time-averaged streamwise velocity along the vertical dotted line. (*c*) P.d.f. of the instantaneous streamwise velocity normalised by U_∞.

are also analysed. The riblet height effects on these aspects are revealed by comparing three sets of C-D riblets with different heights.

6.5.1 Velocity and Reynolds shear stress

The effects of C-D riblets are first revealed by the time-averaged streamwise velocity profiles over the CL and the DL in Figure 6.9a. The converging line (CL) and the diverging line (DL) are defined by the C-D riblets geometry relative to the crossflow [see Figure 6.1]. Compared to the smooth-wall case, the local streamwise velocity decreases over the CL and increases over the DL. Over the CL, a decrease in the local streamwise velocity is observed in the entire boundary layer. By contrast, over the DL, the increase in the local streamwise velocity is only significant in the near-wall region.

Figure 6.9b shows the profiles in the time-averaged streamwise velocity difference ($\Delta U = U - U_s$) between C-D riblets and the smooth wall at the same wall distance. Over the CL, the magnitude of ΔU is larger (more negative) as the C-D riblets become higher. Over the DL, an increase in the riblet height primarily affects the near-wall region of $y/\delta_s < 0.1$. At a higher position of $y/\delta_s > 0.1$, the magnitude of ΔU is only slightly beyond zero. The difference between the affected regions, i.e. the entire flow field over the CL while only the near-wall region over the DL, is consistent with the previous observations in the laminar boundary layer [173] and the turbulent boundary layer [113, 72]. The mechanism can be attributed to the direction of vertical flow and the influence of wall surface [173].

Figure 6.9c compares profiles of the time-averaged wall-normal velocity (V) over the CL and the DL of C-D riblets and the smooth wall. Compared with the smooth-wall case, a strong upwelling occurs over the CL and an intense downwelling is seen over the DL in the time-averaged sense. It is found that the downwelling over the DL is more intense than the upwelling over the CL in the near-wall region, which is aligned with the previous observation in the laminar boundary layer [173]. Over the DL, as C-D riblets become higher, the magnitude of V increases continuously, while the vertical peak position remains essentially unchanged. An increased magnitude of V can be attributed to the increased cross-sectional area of the yawed grooves as the C-D riblets become higher. Over the CL, as the riblet height h^+ increases, the magnitude of V becomes larger, i.e, the upwelling turns more intense. The peak position of V over the CL shifts away from the wall as the riblet height increases, which is attributed to the more intense upwelling over this region.

Figure 6.9d compares profiles of the Reynolds shear stress ($-\overline{u'v'}$) over the CL and the DL of C-D riblets and the smooth wall. The Reynolds shear stress $-\overline{u'v'}$ indicates the wall-normal momentum transfer due to turbulent events [172]. Over the CL, $-\overline{u'v'}$ increases dramatically compared to that over the smooth wall, with a larger riblet height leading to a higher Reynolds shear stress. In a spanwise-periodic in-phase sinusoidal channel, ejection events are preferentially located near the peaks where there present upwelling secondary flows [153]. These ejection events serve as the main contributor to the high $-\overline{u'v'}$ observed at the peaks. With an increased riblet height, the vertical position of the Reynolds shear stress peak over the CL shifts away from the wall. The vertical shift of the peak may be attributed to the increased magnitude of the wall-normal velocity over the CL [see Figure 6.9c]. Over the DL, a less intense Reynolds shear stress than that over the smooth wall is observed, and the lowest riblet

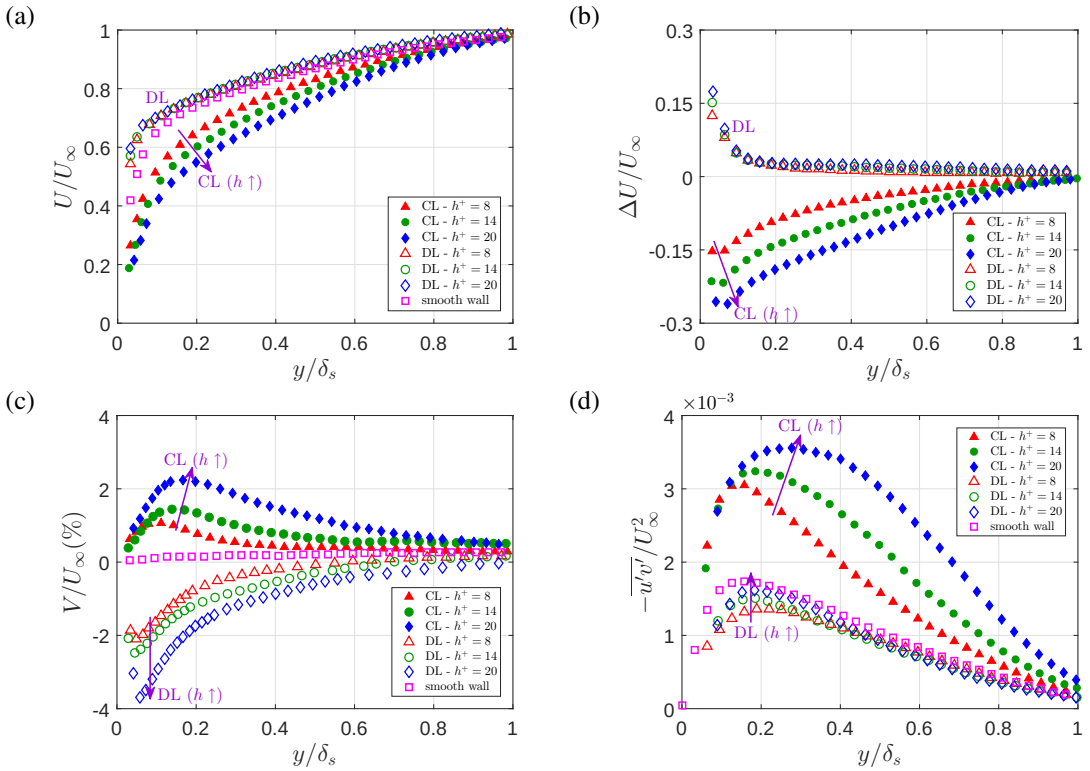

Figure 6.9: Profiles of (*a*) time-averaged streamwise velocity U, (*b*) time-averaged streamwise velocity difference $U - U_s$, (*c*) time-averaged wall-normal velocity V, and (*d*) the Reynolds shear stress $-\overline{u'v'}$, as a function of outer coordinate y/δ_s.

height $h^+ = 8$ (open triangle $\triangle$) corresponds to the lowest magnitude of $-\overline{u'v'}$. Since the region away from the wall has a lower magnitude of Reynolds shear stress, the downwelling over the DL transfers the fluid with low $-\overline{u'v'}$ downward, making the local $-\overline{u'v'}$ smaller than that of the smooth wall. The secondary flow in the turbulent boundary layer becomes more intense as the riblet height increases, which contributes to more fluctuations over the diverging region. Thus, as the riblet height becomes larger, the Reynolds shear stress over the DL slightly increases. A change in the riblet height influences the distribution of $-\overline{u'v'}$ in the entire boundary layer over the CL and affects only the region of $y/\delta_s < 0.5$ over the DL.

In summary, over the DL, C-D riblets lead to an increased local streamwise velocity, a downwelling and a reduced Reynolds shear stress, and the opposite applies to the CL. The secondary flow becomes more intense as the riblet height increases. For the streamwise velocity and the Reynolds shear stress, the impact of a changing riblet height is mainly reflected in the near-wall area over the DL and in the whole boundary layer over the CL. As the riblet height increases, the cross-sectional area of

the yawed microgrooves becomes larger, resulting in greater flow capability and more intense secondary flow.

6.5.2 Wall-shear stress and outer-layer similarity

To gain an insight on the local wall-shear stress, we analyse further profiles of the streamwise velocity over the CL/DL of C-D riblets and the smooth wall. Figure 6.10a compares profiles of the time-averaged streamwise velocity, wherein the friction velocity over the smooth wall ($U_{\tau s}$) is applied in the normalisation. It is clearly seen that the near-wall velocity increases over the DL and decreases over the CL, and a quasi-logarithmic region exists in all velocity profiles over the CL/DL. The slope of the quasi-logarithmic region is larger over the CL and smaller over the DL, and a larger riblet height enhances such a trend. The existence of the log-law region makes it possible to estimate the wall-shear stress using modified Clauser method. Since the time-averaged spanwise velocity is nominally zero over the CL/DL, such analysis could be regarded valid.

As revealed by Clauser [32], the surface pattern of uniformly distributed sand grits leads to an increased wall-shear stress and a downward shift of the mean flow in the logarithmic region of the boundary layer. In the modified Clauser method [122, 113, 95], the following equation is applied to the logarithmic law region of the streamwise velocity to estimate the wall-shear stress,

$$\frac{U}{U_\tau} = \frac{1}{\kappa}\ln\frac{(y-y_d)U_\tau}{\nu} + B - \Delta U^+, \tag{6.4}$$

where y_d is the zero-plane displacement, ΔU^+ is the roughness function which represents the vertical shift of the logarithmic region. The friction velocity can be determined by fitting the logarithmic law with three floating variables of U_τ, y_d and ΔU^+. A positive (negative) ΔU^+ represents a higher (lower) value of U_τ, and thus an increase (decrease) in wall-shear stress. The value of ΔU^+ depends on various parameters including the shape and configuration of the surface roughness. To eliminate the term ΔU^+, as proposed by Nugroho et al. [113], Eq. (6.4) is differentiated with respect to y, which leads to

$$\frac{\Delta U}{\Delta y} = \frac{U_\tau}{\kappa}\frac{1}{y-y_d}. \tag{6.5}$$

The friction velocity U_τ, along with the zero-plane displacement y_d, can be estimated by best fitting the time-averaged streamwise velocity with Eq. (6.5) in the logarithmic

h^+	8	14	20
CL	$+50\%$	$+58\%$	$+63\%$
DL	-21%	-24%	-29%

Table 6.3: Variation of wall-shear stress over the CL/DL compared to the smooth wall.

region.

The logarithmic region is manually selected using the linear section in Figure 6.10a. Figure 6.10b shows the same profiles of the time-averaged streamwise velocity presented in Figure 6.10a, with the local friction velocity applied in the normalisation. The most apparent feature is the downward shift of the velocity profile over the CL and the upward shift over the DL, which indicate an increased skin-friction drag over the CL and a decreased skin-friction drag over the DL respectively. The estimated changes of the wall-shear stress ($\tau_w = \rho U_\tau^2$) are listed in Table 6.3. The changing trend of the local wall-shear stress, i.e. an increase over the CL and a decrease over the DL, is consistent with the previous estimations [113, 72]. The overall wall-shear stress over C-D riblets is not available in the present experiment. For longitudinal riblets with the same height of $h^+ = 8$, 14 and 20 (the same trapezoidal riblet teeth with $s^+ = 20$), the variation of the wall-shear stress is estimated to be -6%, -5% and -1%, respectively [49]. Compared to the longitudinal riblets that exhibit spanwise homogeneity, C-D riblets result in a spanwise variation of the wall-shear stress. The spanwise variations in wall-shear stress over C-D riblets may be attributed to the flow topology in the yawed microgrooves observed by dye visualisation [173]. Over the diverging region, the fluid from the upper region is diverted away along the yawed microgrooves rather than directly impinging on the wall surface, resulting in a decrease in wall-shear stress. In contrast, over the converging region, the fluid being transported from both sides collides with each other there, and the wall-shear stress is increased correspondingly. As the riblet height increases, the drag variations compared to the smooth-wall case become more pronounced. With an increased riblet height, the drag increase over the converging region is more significant than the drag reduction over the diverging region. It should be mentioned that, as noted by Nugroho et al. [113], the estimation accuracy using the modified Clauser method is limited.

Over C-D riblets, the spanwise direction of the secondary flow is from the low wall-shear stress region (diverging region) to the high wall-shear stress region (converging region). Due to the low resistance, the fluid tends to flow in the direction parallel to the yawed microgrooves [89, 70, 173]. This contributes to the formation of the secondary

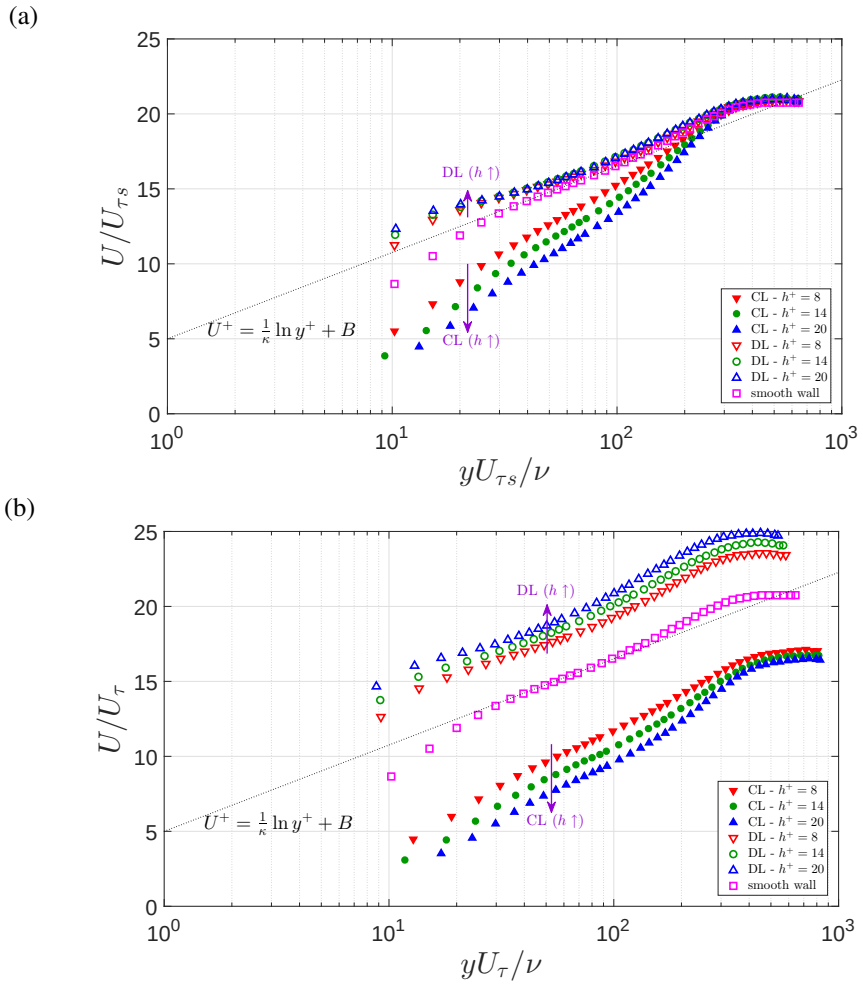

Figure 6.10: (*a*) Time-averaged streamwise velocity profile $U/U_{\tau s}$ as a function of inner coordinate $yU_{\tau s}/\nu$, where $U_{\tau s}$ is the friction velocity over the smooth wall. (*b*) Time-averaged streamwise velocity profile U/U_{τ} as a function of inner coordinate yU_{τ}/ν, where U_{τ} is the local friction velocity.

flow in order to satisfy the continuity requirement. The spanwise flow induced by the mean flow skewing has a contribution to the large-scale secondary flow over C-D riblets disregard of the state of boundary layer. It should also be mentioned that the turbulence contribution in generating the secondary flow cannot be ignored, especially in the boundary layers at high Reynolds numbers.

Townsend's outer-layer similarity hypothesis over C-D riblets, which states

$$\frac{U_\infty - U}{U_\tau} = f\left(\frac{y}{\delta}\right), \tag{6.6}$$

where $(U_\infty - U)/U_\tau$ is the normalised velocity decay, $f(\cdot)$ is assumed universal in the

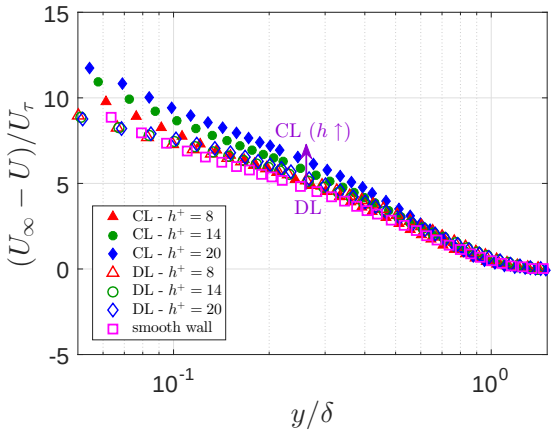

Figure 6.11: Velocity decay profile $(U_\infty - U)/U_\tau$ as a function of outer coordinate y/δ. The local friction velocity U_τ and boundary layer thickness δ are applied in the normalisation.

outer layer regardless of the surface pattern. Figure 6.11 shows the profiles of velocity decay in the outer region over C-D riblets. It can be clearly seen that the velocity profiles do not overlap in the outer region, which indicates that Townsend's outer-layer similarity is not valid over C-D riblets in the present study. The deviation from the baseline (smooth-wall case) is more severe over the CL than that over the DL. This phenomenon can be attributed to the upwelling over the converging region, which affects the velocity profile in the entire boundary layer. As the riblet height increases, the velocity decay profile over the CL moves upward and hence deviates further from the smooth-wall case. Even with a tentative adjustment of the local friction velocity, an overlap of the velocity decay profiles in the outer region cannot be obtained. Nugroho et al. [113] observed non-overlapping of velocity decay profiles over C-D riblets at a high yaw angle of $\gamma = 30^\circ$. The friction velocity (wall-shear stress) may not be estimated directly using Eq. (6.6) by assuming Townsend's outer-layer similarity. Furthermore, it was found that Townsend's outer-layer similarity hypothesis does not hold for other types of spanwise heterogeneous surface patterns, including spanwise alternating roughness strips [31] or surface elevation [95]. Thus, it is likely that the spanwise flow generated over a surface pattern with spanwise heterogeneity undermines the similarity in the outer layer.

In summary, C-D riblets lead to a significant change in the wall-shear stress, with an increase over the CL and a decrease over the DL. The drag variations compared to the smooth-wall case become more pronounced as the riblet height increases. Townsend's outer-layer similarity hypothesis is not valid over C-D riblets in the present study.

6.5.3 Population density of spanwise vortices

The population distribution of spanwise vortices is obtained by the recognition and statistical techniques described in Section 6.4.1. Figure 6.12 shows the population density of prograde vortices (Π_p) and retrograde vortices (Π_r). The population density of prograde vortices is larger than that of retrograde vortices, which can be attributed to the direction of the mean shear. In the turbulent boundary layer more prograde vortices which follow the direction of the mean shear are accounted [169, 3]. In general, an increased population density of prograde/retrograde vortices is observed (except for the DL with $h^+ = 8$), with a more significant increase over the CL than the DL. The greater population of spanwise vortices over the CL was also qualitatively observed by Kevin et al. [71]. Over the CL, the population density of spanwise vortices in the boundary layer increases by more than 50% (more than two times in most of the regions for $h^+ = 20$) as compared with the smooth-wall case, implying a significant increase in the turbulence production activities. Although the identified structures may be affected by the particular choice of structure and identification method, it is clear that the intensity of coherent motions over the converging region is significant increased. The significant increase over the CL confirms that there exists a creation of new coherent structures over the converging region, as proposed by Kevin et al. [71]. The change in the riblet height affects the whole boundary layer for prograde vortices and only the near-wall region of $y/\delta_s < 0.5$ for retrograde vortices, and the population density of the vortices presents a positive correlation with the riblet height. Over the CL, the vertical position with the maximum population density of retrograde vortices (Π_r) shifts away from the wall as the riblet height increases, while a vertical shift of the peak for prograde vortices (Π_p) is not apparent. The vertical shift of the Π_r peak over the CL can be attributed to the more intense upwelling secondary flow, which are essentially caused by the greater capacity of the spanwise flow with an increased riblet height. Over the DL, the population density of prograde and retrograde spanwise vortices remains almost unchanged in a large portion of the boundary layer except for some small changes in the near-wall area. We attribute these phenomena to the downwelling secondary flow, which transports the upper undisturbed fluid to the near-wall region. The population density of these spanwise vortices is not sensitivity to an increase in the riblet height over the DL.

In summary, the population and distribution of prograde and retrograde spanwise vortices are compared to analyse the features of vortical structures over C-D riblets.

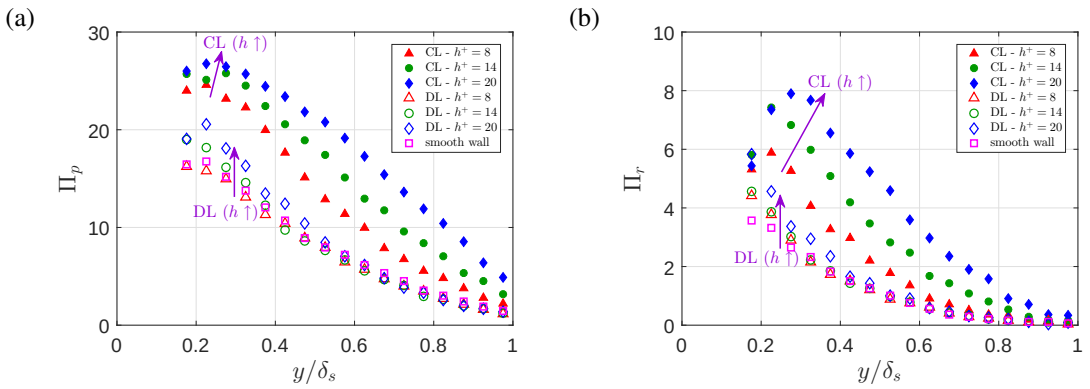

Figure 6.12: Population density of (a) prograde vortices Π_p and (b) retrograde vortices Π_r, as a function of outer coordinate y/δ_s.

The creation of new coherent structures can be confirmed by the significant modification of the population density of spanwise vortices over C-D riblets. Over the CL, the number of spanwise vortices is significantly increased by more than 50% over even the lowest C-D riblets. Over the DL, the change of the population density of spanwise vortices is far less significant. A height increase of C-D riblets leads to a larger population of spanwise vortices over both the CL and the DL. Over the DL, a variation in the riblet height is primarily reflected in the near-wall region.

6.5.4 Spatial correlation

The features of vortex packets are obtained by the spatial correlation analysis in the longitudinal plane described in Section 6.4.2. Figure 6.13 shows six representative contours of $R_{u'u'}$ over the CL/DL of $h^+ = 14$ C-D riblets and the smooth-wall case at two wall-normal stations of $y/\delta_s = 0.2$ and $y/\delta_s = 0.7$. Contour lines are between 0.3 and 0.8 with a spacing of 0.1. The central dots indicate the correlation origins, the solid line indicates the streamwise length scale L_x, and the dashed line shows the inclination angle α. Only the case of $h^+ = 14$ is provided in Figure 6.13, and the similar cases of $h^+ = 8$ and $h^+ = 20$ are not shown here for the sake of brevity. The boundary layer thickness over the smooth wall (δ_s) is applied to normalise the horizontal and vertical coordinates, which ensures a consistent physical station of correlation origins. If the local boundary layer thickness was applied to normalisation, a comparison of the length scales would be misleading. These contours indicate a distinct structure which is inclined at a shallow angle in the streamwise direction [29]. For the correlation origin at $y/\delta_s = 0.2$, the contour over the C-D riblets extends to a shorter streamwise distance in comparison with that over the smooth wall, and inclines at a steeper (shallower)

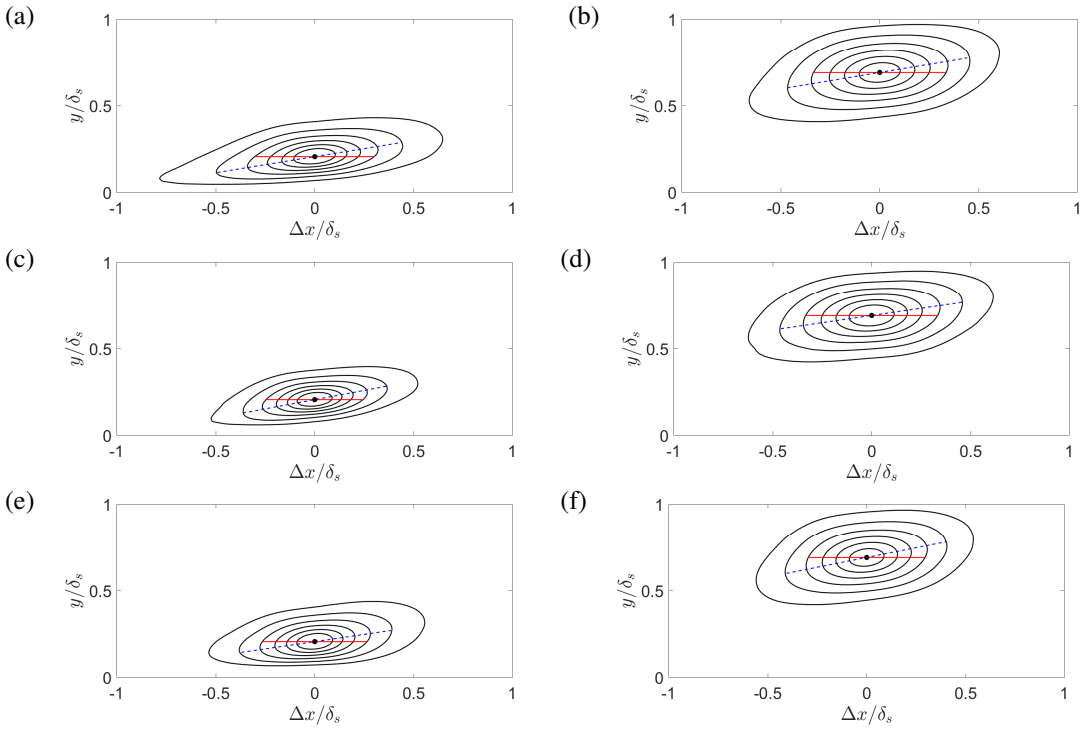

Figure 6.13: Correlation contours of the streamwise fluctuating velocity in the longitudinal plane along (*a*) smooth wall at $y/\delta_s = 0.2$, (*b*) smooth wall at $y/\delta_s = 0.7$, (*c*) $h^+ = 14$ - CL at $y/\delta_s = 0.2$, (*d*) $h^+ = 14$ - CL at $y/\delta_s = 0.7$, (*e*) $h^+ = 14$ - DL at $y/\delta_s = 0.2$, and (*f*) $h^+ = 14$ - DL at $y/\delta_s = 0.7$.

angle over the CL (DL), as indicated in Figure 6.13c (Figure 6.13e). The contour shape with the correlation origin at $y/\delta_s = 0.7$ is indicative of the spatial arrangement of vortex packets found in the outer region [4, 30]. The differences in the contour shapes over the CL in Figure 6.13d and the smooth wall in Figure 6.13b are not significant. Over the DL, the contour in Figure 6.13f extends to a shorter streamwise distance and inclines at a steeper angle.

To quantitatively extract the features of vortex packets, the preceding contours are analysed in terms of the streamwise length and the inclination angle. Figure 6.14a compares the streamwise length scale (L_x) extracted at the contour level of $R_{u'u'} = 0.5$. Over the smooth wall, L_x decreases rapidly in the region of $y/\delta_s < 0.2$, and then presents a slight increase followed by a mild decrease, with an approximate platform at $L_x \approx 0.65\delta_s$ in the region of $0.4 < y/\delta_s < 0.8$. Near the edge of the boundary layer, L_x decreases rapidly as a consequence of the low freestream turbulence. Both the changing trend and the platform value of L_x, including the rapid drop in the near-wall region, agree well with the result by Volino et al. [156]. For C-D riblets, over the

CL, L_x is significantly smaller in $y/\delta_s < 0.5$ and slight larger in $y/\delta_s > 0.65$ than that over the smooth wall, and the platform area does not exist. A lower (higher) value of L_x indicates a reduced (increased) streamwise spacing between consecutive vortices in the vortex packets [171]. The smaller L_x in the region of $y/\delta_s < 0.5$ over the CL can be attributed to the larger population of spanwise vortices as revealed in Figure 6.12, i.e. the creation of new coherent structures. Similarly, over the rough wall made of a woven mesh surface, Volino et al. [156] also observed a lower L_x in the near-wall region compared with the smooth wall. However, the mechanism of the rough wall is attributed to the destruction of the near-wall streaks, since no upwelling secondary flow occurs in the time-averaged sense. Due to the upwelling over the converging region, the area with a lower value of L_x over the CL of C-D riblets ($y/\delta_s < 0.5$) is much larger than that of the rough wall ($y/\delta_s < 0.1$). The riblet height has little effect on L_x over the CL, with an increased riblet height leading to a slightly larger value of the streamwise length in the outer region. Over the DL, a narrower streamwise length L_x of the $R_{u'u'}$ contour than that over the smooth wall is observed in the entire boundary layer, with an increased riblet height leading to a shorter streamwise length of vortex packets. The platform region of L_x exists over the DL, but does not present over the CL. A change in the riblet height corresponds to a significant variation of L_x over the DL. Volino et al. [156] showed that a homogeneous rough surface only modifies L_x in the near-wall area, whereas the feature of L_x in the outer flow remains essentially unchanged. In contrast, the C-D riblets profoundly modify the spatial distribution of coherent structures by introducing a large-scale secondary flow, leading to a significant change in L_x across the entire boundary layer.

Figure 6.14b shows the wall-normal variation of the inclination angle (α) over the C-D riblets and the smooth wall. Over the smooth wall, the inclination angle is approximately 10.5° for $0.2 < y/\delta_s < 0.7$ in the present study, which is close to the results obtained in other studies (e.g. 10° by Krogstad & Antonia [83], 12° by Adrian et al. [4], $12^\circ - 13^\circ$ by Christensen & Adrian [30], 11° by Christensen & Wu [29], $10.7^\circ - 15.7^\circ$ by Volino et al. [156]). Compared with the smooth wall, the inclination angle is larger (smaller) over the CL (DL) in the near-wall region of $y/\delta_s < 0.25$. The larger (smaller) inclination angle over the CL (DL) can be tentatively attributed to the upwelling (downwelling) in the near-wall region. Similarly, a larger inclination is observed over the upwelling (elevated) region over an elevation heterogeneity, which is attributed to the enhanced mixing within the high momentum pathways [8]. Away from the wall, the inclination angle in the region of $y/\delta_s > 0.25$ is larger over the DL

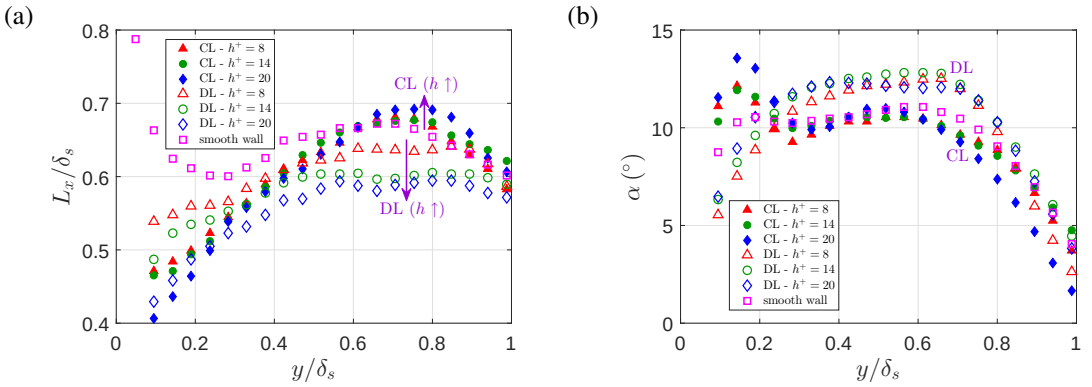

Figure 6.14: Profiles of (a) streamwise length scale L_x and (b) inclination angle α, of the streamwise velocity correlation contour as a function of outer coordinate y/δ_s.

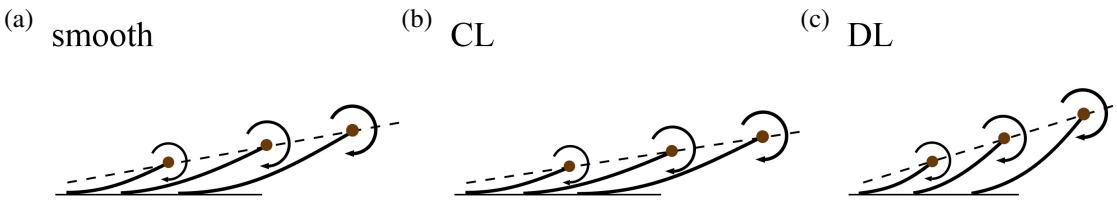

Figure 6.15: Schematic diagram of vortex packet in the outer region over (a) smooth wall, (b) CL of C-D riblets, and (c) DL of C-D riblets, indicating its streamwise length scale and inclination angle. The brown dots indicate the heads of hairpin vortices.

and slightly smaller over the CL compared with the smooth wall. The steeper hairpin packet in the outer region over the DL may be attributed to the smaller number of spanwise vortices, i.e. fewer hairpin vortices in the boundary layer. The riblet height has a negligible effect on the inclination angle in the region between $0.3\delta_s$ and $0.7\delta_s$. The rough wall is observed to lead to an inclination angle 1° to 3° larger than that over the smooth-wall case [105, 156]. For the C-D riblets, the changing trend of the inclination angle is inconsistent in the boundary layer, e.g. an increased α occurs only in the near-wall region over the CL and only in the outer region over the DL.

In summary, the spatial correlation characteristics in the longitudinal plane suggest that C-D riblets lead to a significantly modified spatial arrangement of vortex packets. By synthesizing figures. 6.14a and 6.14b, schematics of the shapes of vortex packets in the outer region are shown in Figure 6.15. In comparison with the smooth-wall case, while the δ-scale vortex packets are steeper and less stretched in the outer region over the diverging region, they are less affected (slightly flatter and a bit more stretched) over the converging region. An increase in the riblet height results in a further shortening of these packets in the streamwise direction over the diverging region.

6.5.5 Uniform momentum zones

The uniform momentum zones (UMZs) are identified by the technique described in Section 6.4.3. Figure 6.16a compares the p.d.f. of the number of UMZs (N_{UMZ}) over the C-D riblets and the smooth wall. The dominant number of UMZs, i.e. N_{UMZ} with the highest probability, changes from $N_{UMZ} = 2$ over the smooth wall or the DL to $N_{UMZ} = 3$ over the CL. The average number of UMZs ($\overline{N}_{UMZ}$) can be calculated by the probability weighted summation of N_{UMZ} in Figure 6.16a. As stated by de Silva et al. [36], $\overline{N}_{UMZ}$ presents a log-linear increase with increasing friction Reynolds number (Re_τ) at medium to high Reynolds numbers. The value of $\overline{N}_{UMZ}$ over the smooth wall at the present Reynolds number is 2.371, which also follows this log-linear relationship as indicated in Figure 6.16b. The consistency here provides further support to the hierarchical length scale distribution of vortical structures within the boundary layer [91]. $\overline{N}_{UMZ}$ is larger over the CL than the smooth wall, and the riblet height has a positive correlation with $\overline{N}_{UMZ}$ ($\overline{N}_{UMZ} = 2.567/2.608/2.658$ for C-D riblets with $h^+ = 8/14/20$ respectively). Over the CL, an increased riblet height leads to a more intense common-flow upwelling and a higher population density of hairpin vortices, which directly contribute to more UMZs. A similarity exists over the CL between the $h^+ = 8$ and $h^+ = 14$ cases, followed by a large difference to the $h^+ = 20$ case. On the contrary, $\overline{N}_{UMZ}$ is lower over the DL in comparison with the smooth wall ($\overline{N}_{UMZ} = 2.295/2.290/2.260$ for C-D riblets with $h^+ = 8/14/20$ respectively), while the riblet height has a negligible effect on the distribution of N_{UMZ}. The insensitivity of $\overline{N}_{UMZ}$ to the riblet height over the DL may be attributed to the time-averaged downwelling. The downwelling secondary flow, which transports the fluid from the upper region to the riblet surface, inhibits its direct influence on the spatial distribution of the upper vortical structures [173].

Figure 6.17a compares the p.d.f. of the mean thickness of UMZs ($\bar{t}_{UMZ}$) over the C-D riblets and the smooth wall. The calculation of the UMZ thickness at a certain streamwise station is indicated in Figure 6.8b, and its averaged value in the streamwise direction is defined as the mean UMZ thickness. Over the CL, the p.d.f. of the UMZ with a thickness of $\bar{t}_{UMZ}/\delta_s \approx 0.2$ increases dramatically. An increase in the riblet height leads to a higher probability of $\bar{t}_{UMZ}/\delta_s \approx 0.2$. The significant change over the CL can be primarily attributed to the rearrangement of the newly created coherent structures over the converging region [71]. The p.d.f. of the UMZ thickness over the DL remains basically unchanged compared with that over the smooth wall.

Figure 6.17b shows the wall-normal variation of the mean thickness of UMZs

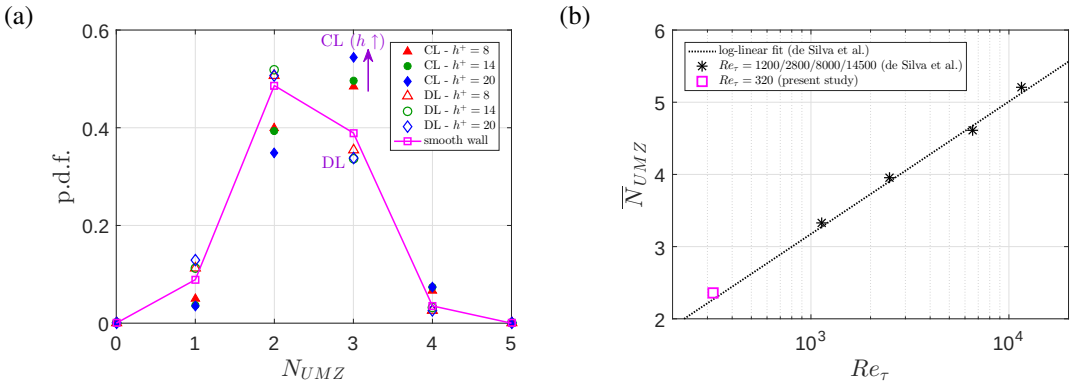

Figure 6.16: (*a*) P.d.f. of the number of UMZs N_{UMZ}. (*b*) Mean number of UMZs $\overline{N}_{UMZ}$ as a function of friction Reynolds number Re_τ.

($\bar{t}_{UMZ}$) over C-D riblets and the smooth wall. The wall-normal station of a UMZ in a snapshot is represented by the y coordinate of its geometric centre. For all cases, the normalised UMZ thickness ($\bar{t}_{UMZ}/\delta_s$) increases as its wall-normal station moves away from the wall. Over the CL, the mean UMZ thickness is significantly reduced in the region of $y/\delta_s > 0.2$, while in the near-wall region of $y/\delta_s < 0.2$ the difference from the smooth-wall case is negligible. The slope of the curves over the CL is significantly lower than that over the smooth wall or the DL. The reduced mean UMZ thickness over the CL in the region of $0.2 < y/\delta_s < 0.4$ helps explain the significantly increased probability of $\bar{t}_{UMZ}/\delta_s \approx 0.2$ as indicated in Figure 6.17a. An increase in the riblet height leads to a more significant decrease in the thickness of UMZs in the region away from the wall over the CL. As validated in Figure 6.12, due to the creation of new coherent structures, the population density of spanwise vortices increases significantly over the CL. The reduced $\bar{t}_{UMZ}/\delta_s$ over the CL is directly related to the reorganisation of these coherent structures. Over the DL, C-D riblets lead to a slight increase in the mean thickness of UMZs compared with the smooth-wall case, which is aligned with the slightly decreased value of $\overline{N}_{UMZ}$.

In summary, for the uniform momentum zones, C-D riblets result in a larger ensemble-averaged number over the CL and a slightly smaller number over the DL, compared with the smooth-wall case. The thickness of UMZs increases as the station moves away from the wall. Compared with the smooth-wall case, UMZs are thinner over CL especially in the area far above the wall, which is attributed to the upwelling and the spatial rearrangement of the newly created coherent structures. A greater riblet height results in a more profound modification to the UMZ features over the CL. Over the DL, the effects of C-D riblet on the thickness of UMZs are not significant.

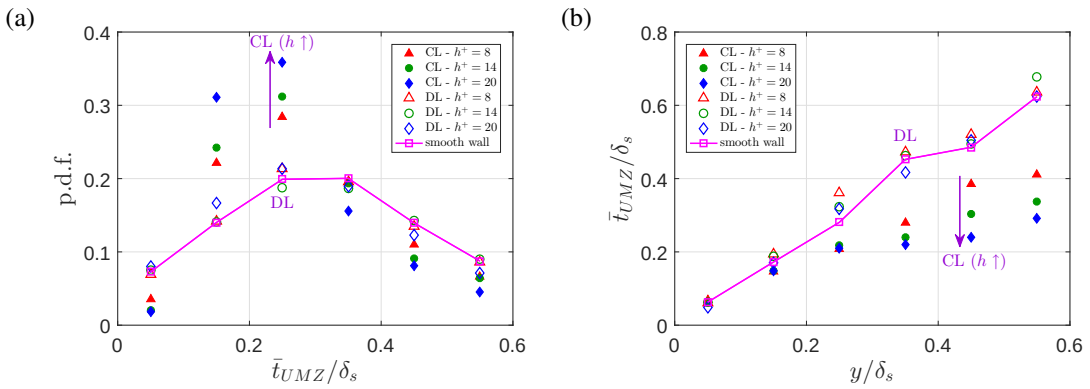

Figure 6.17: (*a*) P.d.f. of the mean thickness of UMZs $\bar{t}_{UMZ}$ normalised by δ_s. (*b*) Mean thickness of UMZs $\bar{t}_{UMZ}$ as a function of outer coordinate y/δ_s.

6.6 Conclusions

A particle image velocimetry (PIV) study of the turbulent boundary layers developing over convergent-divergent riblets (C-D riblets) of three different heights ($h^+ = 8$, 14 and 20) is undertaken at $Re_\theta = 723$. The purposes of this study are firstly to examine the effects of C-D riblets on the behaviours of turbulent structures in comparison to the smooth-wall case and the differences in such behaviours between the converging region and the diverging region in a more quantitative manner, and secondly to establish a better understanding of how riblet height affects such behaviours.

It is found that in comparison to the baseline case, an increase in the time-averaged streamwise velocity and a reduction in the time-averaged Reynolds shear stress are observed in the near-wall region over the diverging line. In contrast, the opposite occurs over the converging line and the impact extends across almost the entire boundary layer. An increase in riblet height enhances such a trend and affects the profiles of velocity and Reynolds shear stress more profoundly over the converging line. Furthermore, it is observed that although a logarithmic law region is present in the velocity profiles over the converging and diverging line, Townsend's outer-layer similarity hypothesis is invalid.

With a large sample size of PIV snapshots available, the population of prograde and retrograde spanwise vortices are investigated. It is found that with a riblet height of $h^+ = 8$ (2.4% of the baseline boundary layer thickness), the population densities of prograde and retrograde spanwise vortices are increased by more than 50% over the converging region compared to the smooth-wall case, implying a significant increase in the turbulence production activities. An increase in the height of C-D riblets results

in a substantial increase in the population of both prograde and retrograde spanwise vortices. Over the diverging region, except for the small changes in the near-wall region, the population density of prograde and retrograde spanwise vortices remains almost unaffected in a large portion of the boundary layer, and it appears to be much less sensitive to an increase in the riblet height.

The inclination angle and streamwise extent of vortex packets are also extracted from two-point correlations. In comparison with the smooth-wall case, while the δ-scale vortex packets are steeper and less stretched in the outer region over the diverging region, they are less affected over the converging region. The effects of an increasing riblet height are mainly manifested as a further shortening of these packets in the streamwise direction over the diverging region.

Finally, the zonal behaviour of uniform streamwise momentum in the boundary layer is examined. It is observed that, in comparison with the smooth-wall case, over the converging region while the probability of having three or four uniform momentum zones increases, the probability of having one or two uniform momentum zones decreases at the Reynolds number investigated in the present study. Correspondingly, the uniform momentum zones in the outer part of the boundary layer over the converging region become thinner. Again, an increase in the riblet height enhances such a trend.

Overall, it is observed that while an increase in the riblet height affects a large portion of the boundary layer away from the wall over the converging region, the impact on the diverging region is largely confined within the near-wall region. Such distinct differences in the response of the boundary layer over the diverging and converging region is attributed to the opposite local secondary flow motion induced by the riblets.

6.7 Acknowledgements

The first author wishes to acknowledge the President's Doctoral Scholar award from the University of Manchester. The authors would like to thank the technical supports from workshop technicians at the School of Mechanical, Aerospace and Civil Engineering. Finally, the authors would like to thank the referees of this paper for their valuable review comments.

Chapter 7

Secondary Flow in Turbulent Boundary Layer over Directional Grooves with Spanwise Heterogeneity

F. Xu, S. Zhong, and S. Zhang. Secondary flow in turbulent boundary layer over directional grooves with spanwise heterogeneity.

Author	Fang Xu	Shan Zhong	Shanying Zhang
Rig design and setup	60%	20%	20%
Experimental measurement	70%	10%	20%
Paper writing	60%	25%	15%
Overall	60%	20%	20%

Table 7.1: Author contribution to this manuscript.

7.1 Abstract

Convergent-divergent riblets (C-D riblets) are a novel type of grooved surface pattern with directionality and spanwise heterogeneity. In the cross-stream plane, we apply stereoscopic particle image velocimetry to study the characteristics of the secondary flow over C-D riblets. Three different heights of $h^+ = 8$, 14 and 20 are applied in the turbulent boundary layers at $Re_\theta = 723$ to reveal the effects of riblet height on the flow field. In the cross-stream plane, increasing the riblet height results in a wider down-welling region, a stronger spanwise flow, a narrower upwelling region and a stronger deceleration effect. Compared with the smooth-wall case, the magnitude of spanwise

velocity fluctuations is larger over the converging region. An increase in the riblet height enhances fluctuations, swirling motions and turbulent momentum transfer, especially over the converging region. The dispersive momentum transfer is primarily contributed by the secondary-flow-induced stress compared with the roughness-induced stress, and it becomes more intense as the riblet height increases. Compared with the smooth-wall case, the near-wall streamwise turbulent events are slightly wider over the diverging region and much narrower over the converging region. Overall, the higher C-D riblets generate a more intense secondary flow, and the mechanism of an increasing riblet height is attributed to the greater capability of deeper yawed microgrooves. In light of the results from our study, we propose a different way of categorising the surface patterns with spanwise heterogeneity from the perspectives of surface geometry, roll mode and secondary flow generation mechanisms.

NOMENCLATURE

$H_r\ (m)$	roughness element height
$h\ (m)$	riblet height
$L\ (m)$	streamwise length of riblet section
$L_z\ (m)$	spanwise width
$N\ (1)$	number of PIV snapshots
$p_{up}\ (1)$	probability of common-flow-up event
R	spatial correlation function
$Re_\tau\ (1)$	friction Reynolds number
$Re_\theta\ (1)$	momentum thickness Reynolds number
$S\ (m)$	spanwise spacing
$s\ (m)$	riblet spacing
$TKE\ (m^2s^{-2})$	turbulence kinetic energy
$U_\infty\ (ms^{-1})$	freestream velocity
$U_\tau\ (ms^{-1})$	friction velocity
$u\ (ms^{-1})$	streamwise velocity
$v\ (ms^{-1})$	wall-normal velocity
$W\ (m)$	spanwise width of riblet section
$W_r\ (m)$	high roughness strip width
$w\ (ms^{-1})$	spanwise velocity
$x\ (m)$	streamwise coordinate

$y\ (m)$	wall-normal coordinate
$z\ (m)$	spanwise coordinate
$\delta\ (m)$	$99\%U_\infty$ boundary layer thickness
$\gamma\ (1)$	riblet yaw angle
$\Lambda\ (m)$	riblet wavelength
$\lambda_{ci}\ (s^{-1})$	swirling strength
$\langle\lambda_{ci}\rangle\ (s^{-1})$	signed swirling strength
$\nu\ (m^2s^{-1})$	kinematic viscosity
$\omega_x\ (s^{-1})$	vorticity in $z-y$ plane
$\Phi\ (m^2s^{-2})$	spanwise-averaged momentum flux
σ	standard deviation
$\theta\ (m)$	boundary layer momentum thickness
$\rightarrow$	velocity vector
$\bar{}$	time averaging
$\tilde{}$	dispersive component
$\langle\cdot\rangle_\Lambda$	secondary-flow-scale spatial averaging
$\langle\cdot\rangle_r$	roughness-scale spatial averaging
$+$	normalisation in wall units
$'$	fluctuating component

Abbreviation	
C-D riblets	convergent-divergent riblets
CL	converging line
DL	diverging line
DNS	direct numerical simulation
DV	dye visualisation
HMP	high momentum pathway
HWA	hot-wire anemometry
LDA	laser Doppler anemometry
LES	large eddy simulation
LMP	low momentum pathway
OFI	oil film interferometry
PIV	particle image velocimetry
p.d.f.	probability distribution function
ref	reference point of correlation origin

rms	root mean square
s	smooth wall
sPIV	stereoscopic particle image velocimetry
UDV	ultrasonic Doppler velocimetry

7.2 Introduction

Spanwise heterogeneous surface patterns refer to the surface patterns with characteristic spanwise length scales comparable to the dominant length scale in a wall-bounded flow field, such as the boundary layer thickness, the channel height or the pipe diameter. Such surface patterns have received a considerable amount of research attention in the past two decades due to their potential as a means of promising passive flow control for wall-bounded flows. Examples of spanwise heterogeneous surface patterns, which have been studied, include spanwise alternating smooth and rough bed strips [162, 163], ridges of foreign-material deposition on turbine blades [97, 166], spanwise-periodic arrays of Lego® bricks [152], natural rough beds [5], etc.

Convergent-divergent riblets (C-D riblets), which are studied in this paper, are a type of directional surface patterns with spanwise heterogeneity. C-D riblets begin to attract research attention in the recent few years [79, 113, 72, 173, 71, 175], due to their potential in reducing surface friction drag [25] and suppressing flow separation [87, 126]. C-D riblets, as shown in Figure 7.1, are composed of a spanwise array of sections of left-yawed and right-yawed microgrooves arranged in an alternating manner. The converging line (CL) and the diverging line (DL) are defined intuitively from the geometry. The acute angle at which the microgrooves form with the diverging or converging line is referred to the yaw angle. Similar to the longitudinal riblets, the surface pattern of C-D riblets is inspired by nature. While the diverging riblet patterns are observed upstream of the hearing organs of sharks, the converging riblet patterns are found upstream of the sensory receptors of sharks [79]. Diverging riblet patterns are also observed on the secondary flight feathers of birds [25]. Except for the latest studies [16, 174, 71, 175], a summary of the published work on C-D riblets can be found in Xu et al. [173].

Based on the definition of yaw angle in Figure 7.1, longitudinal riblets may be regarded as the limiting case of C-D riblets with a zero yaw angle. Although both consisting of microgrooves, the flow structures and the impact on the boundary layer

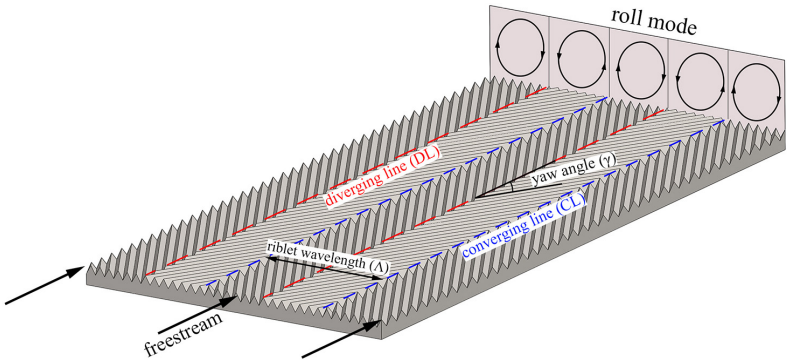

Figure 7.1: Schematic diagram of convergent-divergent riblets (C-D riblets) and the time-averaged roll mode in the perspective view. The converging and diverging regions are referred to the regions close to the converging and diverging lines, respectively.

flow produced by C-D riblets are inherently different from those produced by longitudinal riblets [40, 54, 127, 61, 60, 109, 177, 118, 128]. While the effect of longitudinal riblets is confined within the near-wall region, C-D riblets are capable of producing a profound modification to the entire boundary layer [79, 113, 72, 173]. Such an effect has been attributed to the creation of a weak time-averaged secondary flow motion (roll mode) in the cross-stream plane, whereby an upwelling/downwelling over the converging/diverging region is created in the boundary layer [72, 173]. In a laminar boundary layer, the roll mode is observed to be the consequence of a surface flow directing from the diverging region to the converging region driven by the yawed microgrooves [173]. The secondary flow motions lead to a significant difference in the time-averaged flow field over the converging and diverging regions. Over the diverging regions, the streamwise velocity in the near-wall region is increased compared with that in the smooth-wall case, leading to a reduced boundary layer thickness [113, 173, 174]. The opposite occurs over the converging regions.

With stereoscopic particle image velocimetry (PIV) measurements in the cross-stream plane, the instantaneous in-plane rotational motion is observed to be highly unsteady and much stronger than the time-averaged roll mode [72]. The secondary flow motion created by C-D riblets is found to radically modify both the time-averaged turbulence characteristics in the boundary layer and distributions of turbulent activities in the spanwise direction. While reduced near-wall turbulence intensity is observed over the diverging region, increased near-wall turbulence intensity is found over the converging region. This is in line with a reduction in the skin friction coefficient over the diverging region and an increase over the converging region as estimated using

the modified Clauser technique [113, 72, 175]. Based on single hot-wire measurements across the boundary layer and PIV measurements in the wall-parallel plane in the logarithmic region, Nugroho et al. [113, 114] found that the roll mode seemed to gather the very-large-scale streamwise structures and features with high vortical activities over the converging region of the C-D riblets. Kevin et al. [72] speculated that the directional surface roughness redistributes the large-scale energetic structures and preferentially arrange the large-scale motions over the converging region.

Xu et al. [175] studied the characteristics of a turbulent boundary layer developing over C-D riblets with three different heights of $h^+ = 8$, 14 and 20 at $Re_\theta = 723$ using mono-PIV. The results provide an insight of the distinct differences in the logarithmic velocity profile, the population of spanwise vortices, the orientation of vortex packets and the number of uniform momentum zones in the longitudinal planes over the converging line and the diverging line. It is also found that as the riblet height increases the coherent motions of vortical structures become more intense, and the influence of changing riblet height is observed primarily in the near-wall region over the diverging line and across a larger portion of the boundary layer over the converging line.

In this paper, we present the results obtained in the cross-stream plane using stereoscopic PIV from a complementary study undertaken at the same test conditions. The focus of this work is on the effect of riblet heights on the characteristics of the secondary flow and the time-averaged turbulence quantities in the cross-stream plane. In particular, the turbulent momentum flux transferred is decomposed into components related to the secondary flow motion and the roughness-induced motion, hence shedding some lights on the relative contributions from these two motions.

At present, there have been a number of categorisation methods on the surface patterns with spanwise heterogeneity [72, 95]. Medjnoun et al. [95] proposed that spanwise heterogeneous surface patterns can be classified into two types, one with spanwise roughness heterogeneity and the other with spanwise elevation heterogeneity. In their studies, C-D riblets were grouped together with spanwise alternating smooth and rough strips into the former. On the other hand, Kevin et al. [72] classified spanwise heterogeneous surface roughness into two categories based on the directionality of the local skin-friction, i.e. one is locally isotropic and the other is locally anisotropic. Hence, while the heterogeneous surface patterns with random surface roughness or surface elevation fall into the former, C-D riblets fall into the latter [72]. In light of the results from our study, we propose a different way of categorising the surface patterns with spanwise heterogeneity from the perspectives of surface geometry, roll mode and

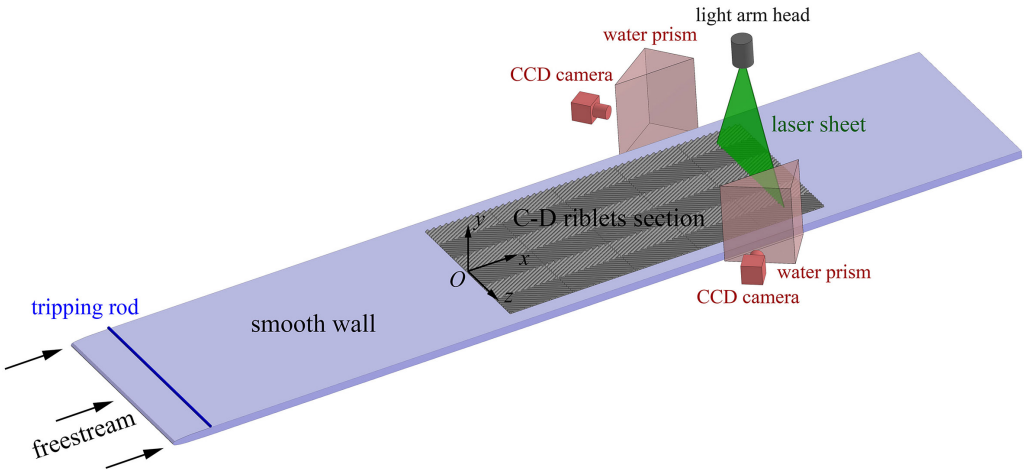

Figure 7.2: Schematic diagram of the stereoscopic PIV system in the cross-stream plane. The riblet spacing and the riblet height are not drawn to scale.

secondary flow generation mechanisms.

7.3 Experimental set-up

7.3.1 Water flume and flat plate

The present work was conducted in a low-speed water flume at the University of Manchester. The water flume has a length of 3640mm and a cross-section area of 305$mm \times 305mm$. To reduce the level of background turbulence, four metal screens are installed to the inlet of the water flume. Further details of the water flume can be found in Xu et al. [173, 175].

A flat plate with its test section facing upward was designed to facilitate the experimental study on the boundary layer flow over C-D riblets, as shown in Figure 7.2. The total length and width of the flat plate are 1350mm and 300mm, respectively. A rectangular cavity measuring $L = 500mm$ long and $W = 250mm$ wide was machined on the test plate starting at 550mm from the leading edge. The surface patterns (smooth wall or C-D riblets) are made on the upper surfaces of rectangular tiles, and these tiles can be inserted into the cavity of the flat plate. Note that the height (h) and spacing (s) of C-D riblets in Figure 7.2 are not drawn to scale.

In the present study, the freestream velocity is $U_\infty = 0.2m/s$, and the freestream turbulence intensity is approximately 0.7%. As shown in Figure 7.2, the axes x, y and z represent the streamwise, wall-normal and spanwise directions, respectively. The coordinate origin situates at the start of the cavity, levels with the upstream smooth

Parameter	L	W	Λ	s	h	γ
Value	$500mm$	$250mm$	$83.33mm$	$2.0mm$	$0.8/1.4/2.0mm$	30°

Table 7.2: Parameters of C-D riblets with three different riblet heights.

wall and locates at the centreline of the span. The instantaneous velocity $\vec{u} = (u, v, w)$ is the sum of the time-averaged component $\vec{\overline{u}} = (\overline{u}, \overline{v}, \overline{w})$ and the fluctuating component $\vec{u'} = (u', v', w')$. At the measurement station ($x = 450mm$), the boundary layer thickness is $\delta_s = 32.5mm$ and the friction velocity is $U_{\tau s} = 9.75 \times 10^{-3} m/s$. The momentum thickness Reynolds number is $Re_\theta = 723$ and the friction Reynolds number is $Re_\tau = 320$. The tripped turbulent boundary layer has a relatively short development length. The same baseline turbulent boundary layer has been characterised in our previous work [175], revealing a good agreement with reference datasets at similar Reynolds numbers.

7.3.2 Parameters of convergent-divergent riblets

The surface pattern of C-D riblets was machined on rectangular tiles using three-dimensional (3D) printing technique. Table 7.2 lists the parameters of C-D riblets with trapezoidal teeth and three different riblet heights. The parameters of C-D riblets applied to the present study are the same as those in our previous work [175]. Across the spanwise width of one riblet wavelength, there are around 36 riblet teeth. The blockage ratio, i.e. the riblet height to the boundary layer thickness of the smooth wall (h/δ_s), is 2.4%, 4.3% and 6.2%, respectively at the measurement station of $x = 450mm$. When the length scale is normalised in wall units by the local friction velocity over the smooth wall ($U_{\tau s}$) and the kinematic viscosity (ν) as $h^+ = hU_{\tau s}/\nu$, the riblet height of $0.8mm$, $1.4mm$ and $2.0mm$ corresponds to approximately $h^+ = 8$, 14 and 20. The riblet spacing in wall units is $s^+ = sU_{\tau s}/\nu = 20$. Later on, we refer to these C-D riblets as $h^+ = 8$, $h^+ = 14$ and $h^+ = 20$ riblets, respectively.

7.3.3 Particle image velocimetry setup

The particle image velocimetry (PIV) system is composed of a light-guiding arm, a New Wave Solo-PIV 120 laser generator, a laser pulse synchroniser (Model 610036), and two 4-mega pixel charge-coupled device (CCD) cameras. The maximum image-capturing frequency of the PIV system is $7.5Hz$. The CCD cameras have a resolution of 2352×1768 pixels and an intensity of 12 bits. The PIV seeding particles are hollow

glass spheres (HGS) with a mean diameter of $10\mu m$ and a density of $1.1 \times 10^3 kg/m^3$.

Figure 7.2 shows a schematic of the stereoscopic PIV system. The cross-stream $(z-y)$ measurement plane was located at $450mm$ downstream of the start of C-D riblets section, i.e. $x = 450mm$. Two water-filled prisms were placed on both sides of the water flume to reduce the optical aberration due to the different refractive indices of light in water and air. The locations of the two cameras were adjusted according to the Scheimpflug principle. The CCD cameras were calibrated using a dual-plane calibration plate, and the perspectives of the cameras were optimised by the ensemble-averaged de-wrapped velocity field. The time interval between two laser pulses was set at $1.2ms$, and 5000 image pairs were captured at an acquisition rate of $0.5Hz$ (i.e. 12.3 times of the turbulent turnover time scale of the smooth-wall boundary layer). The PIV image pairs were processed using the cross-correlation algorithm in InSight 4G^{TM} software. The first interrogation area of 64×32 pixels and the final interrogation area of 32×32 pixels with a 50% overlap were applied. The field of view, i.e. the intersection of two de-wrapped perspectives, was $98mm \times 38mm$, which covered more than one complete riblet wavelength. The perspective view leads to the gradation of spatial resolution, which is $0.66mm \pm 17\%$ in the spanwise direction and $0.35mm \pm 9\%$ in the wall-normal direction. The expanded uncertainty in velocity components, i.e. 95.4% possibility of having the true value within the uncertainty bound, is estimated to be $0.22\%U_\infty$ for the time-averaged flow field.

7.4 Results and analysis

In this section, we present the effects of the riblet height on the secondary flow in three inter-related aspects. The velocity fields are applied to reveal the time-averaged secondary flow, the instantaneous spanwise velocity distribution and the probability of vertical common-flow events. The distributions of the turbulent fluctuations and the decomposition of the total momentum flux are studied. The effects of C-D riblets on the spanwise width of streamwise turbulent events are also analysed.

7.4.1 Velocity fields

The vector fields of in-plane velocity components $(\overline{w}, \overline{v})$ over C-D riblets are shown in Figure 7.3. As a spanwise heterogeneous surface pattern, C-D riblets induce a counter-rotating roll mode occupying the entire boundary layer within the spanwise distance

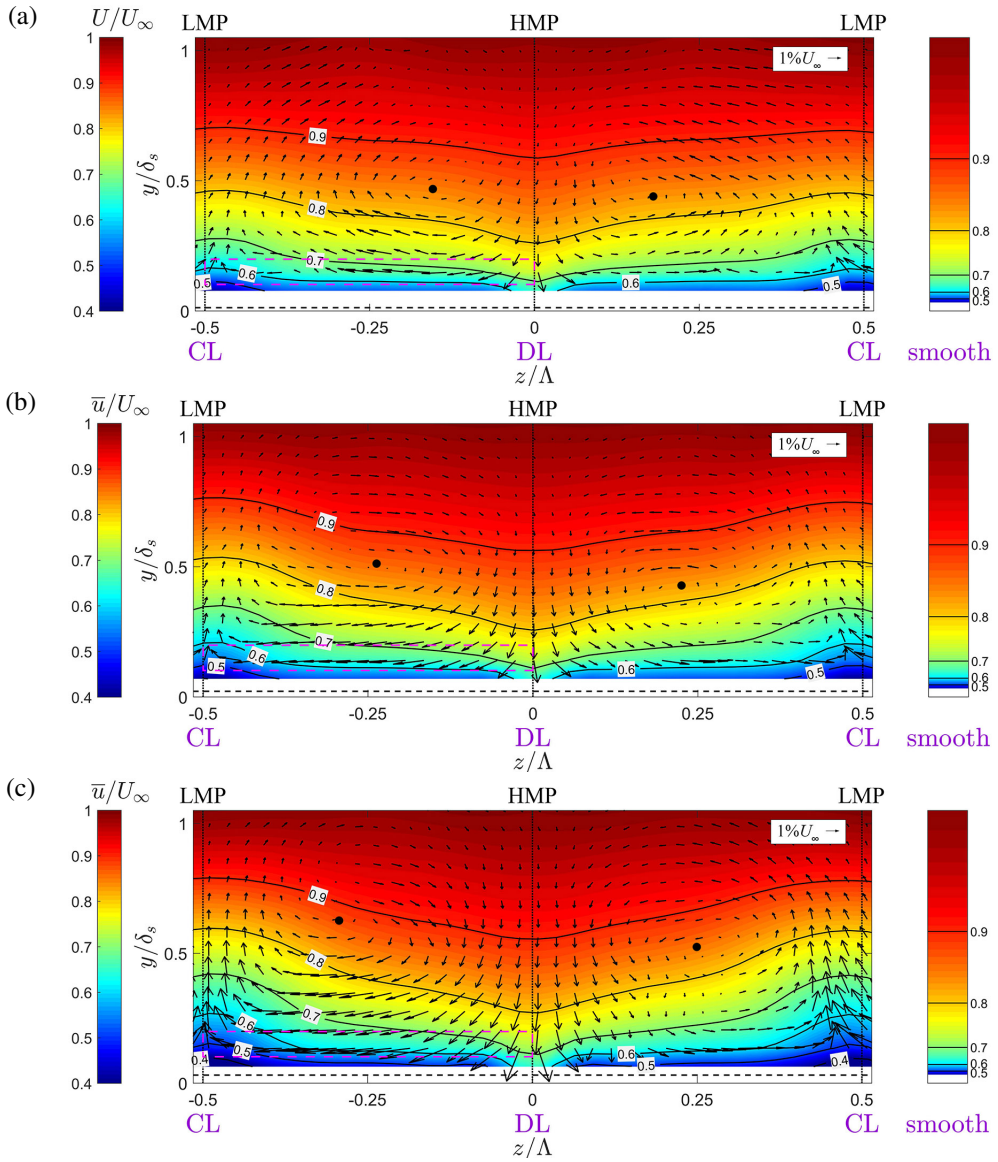

Figure 7.3: Contours of the time-averaged streamwise velocity $\overline{u}$ over C-D riblets with (*a*) $h^+ = 8$, (*b*) $h^+ = 14$, (*c*) $h^+ = 20$. The horizontal dashed lines indicate the riblet crest level, i.e. $y/\delta_s = 1.2\%$, 2.1% and 3.1%, respectively.

of one riblet wavelength, which is qualitatively similar to the roll mode found in the previous studies [114, 72]. The near-wall spanwise flow, as the driving force of the secondary flow [173], follows the direction of the yawed microgrooves, i.e. from the DL to the CL. The upwelling dominates the converging region, whereas the downwelling occurs over the diverging region. The spanwise flow in the near-wall region intensifies as the riblet height (flow capacity) increases. To provide a quantitative assessment, we analyse the spatial-averaged value of the time-averaged spanwise velocity magnitude

in the near-wall region of $-0.5 < z/\Lambda < 0$ and $0.1 < y/\delta_s < 0.2$, as indicated by the dashed rectangles in Figure 7.3. The values are $0.43\%U_\infty$, $0.67\%U_\infty$ and $1.03\%U_\infty$ for the C-D riblets with $h^+ = 8$, 14 and 20, respectively. The more intense spanwise flow in the near-wall region observed with an increased riblet height can be directly attributed to the increased flow capacity of the yawed microgrooves. Interestingly, the approximate centre of the time-averaged roll mode, as indicated by the dot symbols in Figure 7.3, moves away from the wall and closer to the CL as the riblet height increases. The movement trend of the vortex centre is closely related to the width of the downwelling region and the intensity of the near-wall spanwise flow. In a laminar boundary layer, a similar moving trend of the vortex centre with increasing riblet wavelength was observed [173].

Contours of the time-averaged streamwise velocity ($\overline{u}$) in the cross-stream plane are also shown in Figure 7.3. In the spanwise or wall-normal direction, among every five velocity vectors only one vector is plotted. The results from three sets of riblet height $h^+ = 8$, 14 and 20 are compared. The spanwise coordinate is normalised by the riblet wavelength (Λ), whereas the wall-normal coordinate is normalised by the boundary layer thickness of the smooth wall (δ_s). The contour of $\overline{u}$ over the smooth wall, which is homogeneous in the spanwise direction, is also shown on the right-hand side. The high-momentum pathways (HMPs) and low-momentum pathways (LMPs) refer to the regions where the time-averaged streamwise momentum is excessive and insufficient, respectively, as compared to the spatial-temporal-averaged (spanwise-time-averaged) streamwise momentum [98, 13]. In comparison with the smooth-wall case, the local streamwise velocity increases within a narrow area over the DL, and it decreases in the remaining areas in the cross-stream plane. Thus, there exist HMP and LMP over the diverging region and the converging region, respectively. As the riblet height increases, the streamwise velocity in the region over the CL exhibits a more dramatic decrease. This finding is consistent with that of Nugroho et al. [113] who varied the normalised riblet height (h^+) by changing the freestream velocity. A lower local streamwise velocity occurs at most of the spanwise stations. The spanwise averaged value based on the secondary-flow-scale domain, i.e. within one riblet wavelength, is

$$\langle \overline{u} \rangle_\Lambda(y) = \frac{1}{\Lambda} \int_{-\Lambda/2}^{\Lambda/2} \overline{u}(z,y) dz, \tag{7.1}$$

where Λ is the riblet wavelength, i.e. the spanwise spacing of C-D riblets. The wall-normal variation of the velocity difference is shown in Figure 7.4, indicating that C-D

riblets generate a global deceleration effect, with larger riblet height resulting in more intense deceleration. The near-wall region has a more intense deceleration than the outer layer due to the direction difference between the yawed grooves and the upper crossflow. The global deceleration effect in the near-wall region of C-D riblets has also been observed in laminar boundary layers [173].

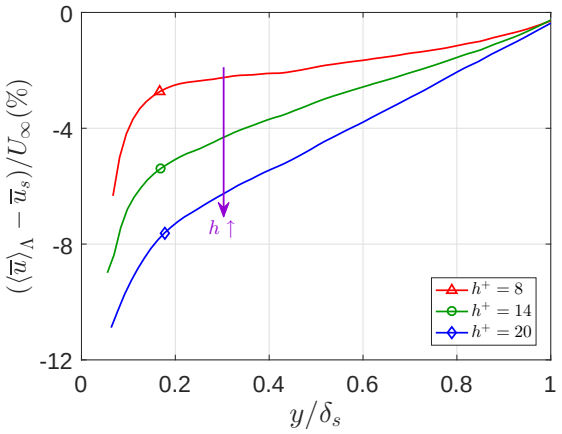

Figure 7.4: Profiles of streamwise velocity difference between spanwise averaged value and the smooth wall $\langle\overline{u}\rangle_\Lambda - \overline{u}_s$ as a function of outer coordinate y/δ_s.

The time-averaged roll mode in the cross-stream plane in Figure 7.3 represents an ensemble average. However, due to the unsteadiness of coherent structures, there may exist a dramatic difference between the time-averaged and the instantaneous flow fields in the turbulent boundary layer. As revealed by Kevin et al. [72, 71], the mean secondary flow generated by C-D riblets is only the time-averaged artefact of the unsteady large-scale roll modes. By contrast, in the laminar boundary layer, considering the steadiness of the baseline flow field, the time-averaged secondary flow over C-D riblets is believed to be more representative of the instantaneous flow fields [173]. Figure 7.5 shows the probability distribution function (p.d.f.) of the spanwise fluctuating velocity (w') at two wall-normal stations of $y/\delta_s = 0.2$ and $y/\delta_s = 0.7$ over the CL and the DL. The p.d.f. curves over the C-D riblets and the smooth wall present a bell-shaped distribution (not exactly the Gaussian distribution). The curves over the CL are lower and wider than those curves over the DL or the smooth wall, which indicates that the spanwise motions over the converging region are more intense. The curves at the higher wall-normal station of $y/\delta_s = 0.7$ are relatively narrower and taller than those at $y/\delta_s = 0.2$. Figure 7.6 shows the wall-normal variation of the spanwise turbulence intensity (w'_{rms}) over C-D riblets and the smooth wall. Over the CL, the spanwise turbulent motions are enhanced in the entire boundary layer, which is aligned with the

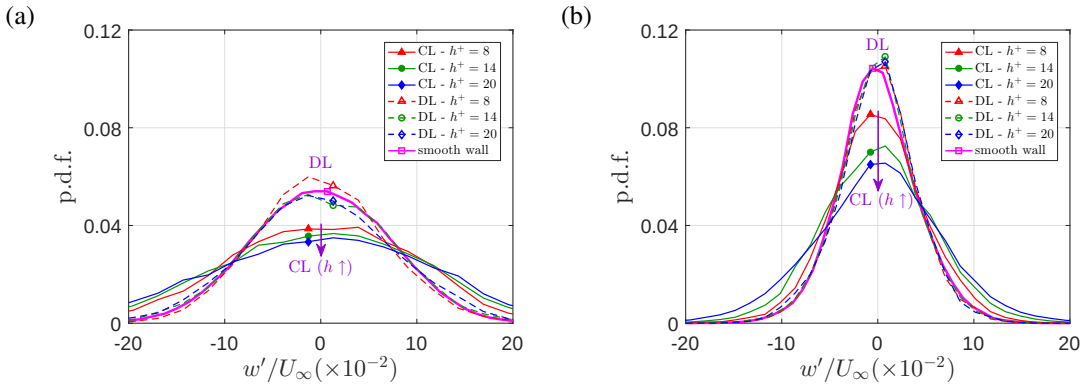

Figure 7.5: P.d.f. of the spanwise fluctuating velocity w' at the CL/DL about the wall-normal position of (a) $y/\delta_s = 0.2$, (b) $y/\delta_s = 0.7$.

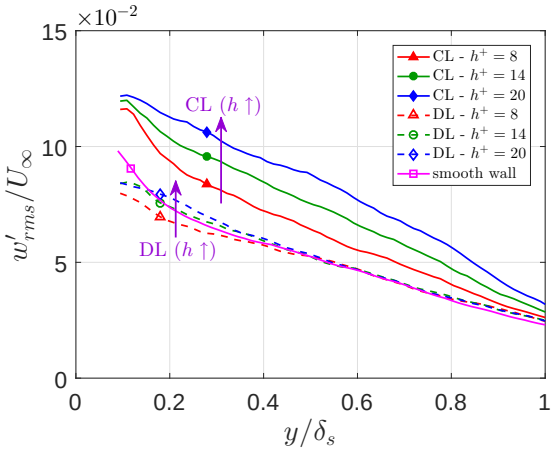

Figure 7.6: Profiles of turbulence intensity of spanwise velocity component w'_{rms} at the CL/DL as a function of outer coordinate y/δ_s.

observation by Kevin et al. [72]. In contrast, the slightly attenuated spanwise turbulent events are observed in the near-wall region over the DL than the smooth wall. While an increase in the riblet height affects a large part of the region away from the wall over the CL, its effect is limited in the near-wall region over the DL.

To quantitatively reveal the effects of riblet height on common-flow events, we analyse the proportion of the conditionally-averaged velocity fields based on the wall-normal velocity. A common-flow-up event at a certain location on the surface pattern is defined as the case in which the line integral of the instantaneous wall-normal velocity is positive, i.e. $\int_{y_l}^{y_h} v(z,y)dy > 0$. The proportion of samples (PIV snapshots) with

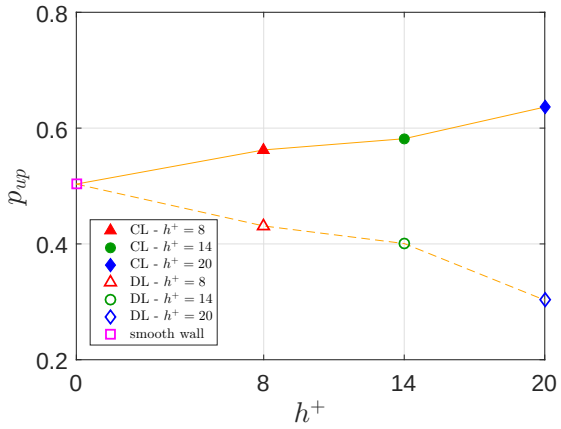

Figure 7.7: Probability of the snapshots with instantaneous common-flow-up event p_{up} at the CL/DL as a function of riblet height in wall units h^+.

common-flow-up events in a given signal series, $p_{up}(z)$, is defined as

$$p_{up}(z) = \frac{N|_{\int_{y_l}^{y_h} v(z,y)dy>0}}{N_{total}}, \tag{7.2}$$

where $N|_{\int_{y_l}^{y_h} v(z,y)dy>0}$ is the number of samples (PIV snapshots) which present common-flow-up events, y_l is confined by the available PIV data points closest to the wall surface, y_h is set as the smooth-wall boundary layer thickness δ_s, N_{total} is the total number of PIV samples in the present study. The value of $p_{up}(z)$ is in the range between 0 and 1, with a larger value indicating that the instantaneous flow field is more likely to present an upwelling (common-flow-up event) at a given spanwise station of z.

Figure 7.7 shows the probability of common-flow-up events (p_{up}) over the smooth wall and the CL/DL, where $z = \pm 0.5\Lambda$ and $z = 0$ at the CL and the DL, respectively. Compared with the smooth wall with $p_{up} \approx 50\%$, the value of p_{up} is higher over the CL and lower over the DL, i.e. the instantaneous flow field is more likely to present an upwelling over the CL and a downwelling over the DL. The sum of p_{up} over the CL and the DL is around unity, accounting the contradicting effect of upwelling and downwelling. Over the CL (DL), a positive (negative) correlation is seen between the upwelling probability (p_{up}) and the riblet height (h^+). There exists a widening difference between p_{up} as the riblet height increases, indicating that vertical motions are more directional for the C-D riblets with larger cross section. This phenomenon can be directly attributed to the greater flow capacity of the deeper yawed microgrooves as the riblet height increases.

In summary, the time-averaged secondary flow occupying the entire turbulent boundary layer is observed over C-D riblets. A larger riblet height, i.e. a greater flow capacity of yawed grooves, results in a wider downwelling region, a stronger spanwise flow and a narrower upwelling region, indicating a more intense secondary flow. An increase in the riblet height enhances the spanwise motions in the entire boundary layer over the CL, and suppresses the spanwise motions only in the near-wall region over the DL. The probability of common-flow events, i.e. common-flow-up events over the CL and common-flow-down events over the DL, is positively correlated with the riblet height.

7.4.2 Turbulent fluctuations and momentum flux decomposition

The turbulence kinetic energy (TKE) is defined as $(\overline{u'^2} + \overline{v'^2} + \overline{w'^2})/2$, which indicates the time-averaged kinetic energy associated with eddies in the turbulent flow. Figure 7.8 shows TKE contours in the cross-stream plane over C-D riblets. The distribution over the smooth wall is also shown on the right for comparison. The present results are qualitatively similar to other experimental observations [see Figure 10(e) in Kevin et al. [72]]. Compared with the distribution over the smooth wall, the TKE presents an increase within most of the regions over C-D riblets, except for a narrow area over the diverging region. In the cross-stream plane, the area over the converging region has the highest TKE, and such an area becomes wider and extends to the higher position as the riblet height increases (e.g. the region with a value of 10 and above). The mechanism of the high TKE area can be attributed to the characteristics of the secondary flow. Since the secondary flow is driven by the yawed microgrooves, a larger riblet height leads to a greater flow capacity, i.e. a larger amount of the fluid near the DL is transported towards the converging region from both sides and collides with each other there [175]. The upwelling over the CL also becomes more intense as the riblet height increases. The combined effect is that the high TKE area over the converging region turns wider and higher as the riblet height increases. Over two surface patterns of C-D riblets and spanwise alternating rough/smooth strips, the correlations between the vertical flow and the TKE distribution are reversed. For the alternating rough/smooth strips, the downwelling (upwelling) occurs in the region with a high (low) TKE [141], whereas the opposite correspondence occurs for C-D riblets. This result can be attributed to the different driving mechanisms of the secondary flow, i.e. driven by surface geometry for C-D riblets and driven by turbulence anisotropy for spanwise alternating rough/smooth strips. However, in both cases, the area with a high

(low) TKE locates over the high (low) wall-shear stress region. Besides the above-mentioned global features, a noteworthy local feature over C-D riblets is the presence of a small near-wall region with high TKE on each side of the DL at $z/\Lambda \approx \pm 0.06$. In the laminar flow experiment, Xu et al. [173] revealed the presence of a region of 'overflow-induced upwash' flanking the diverging region, which helps explain the high TKE regions adjacent to the DL in the present experiment.

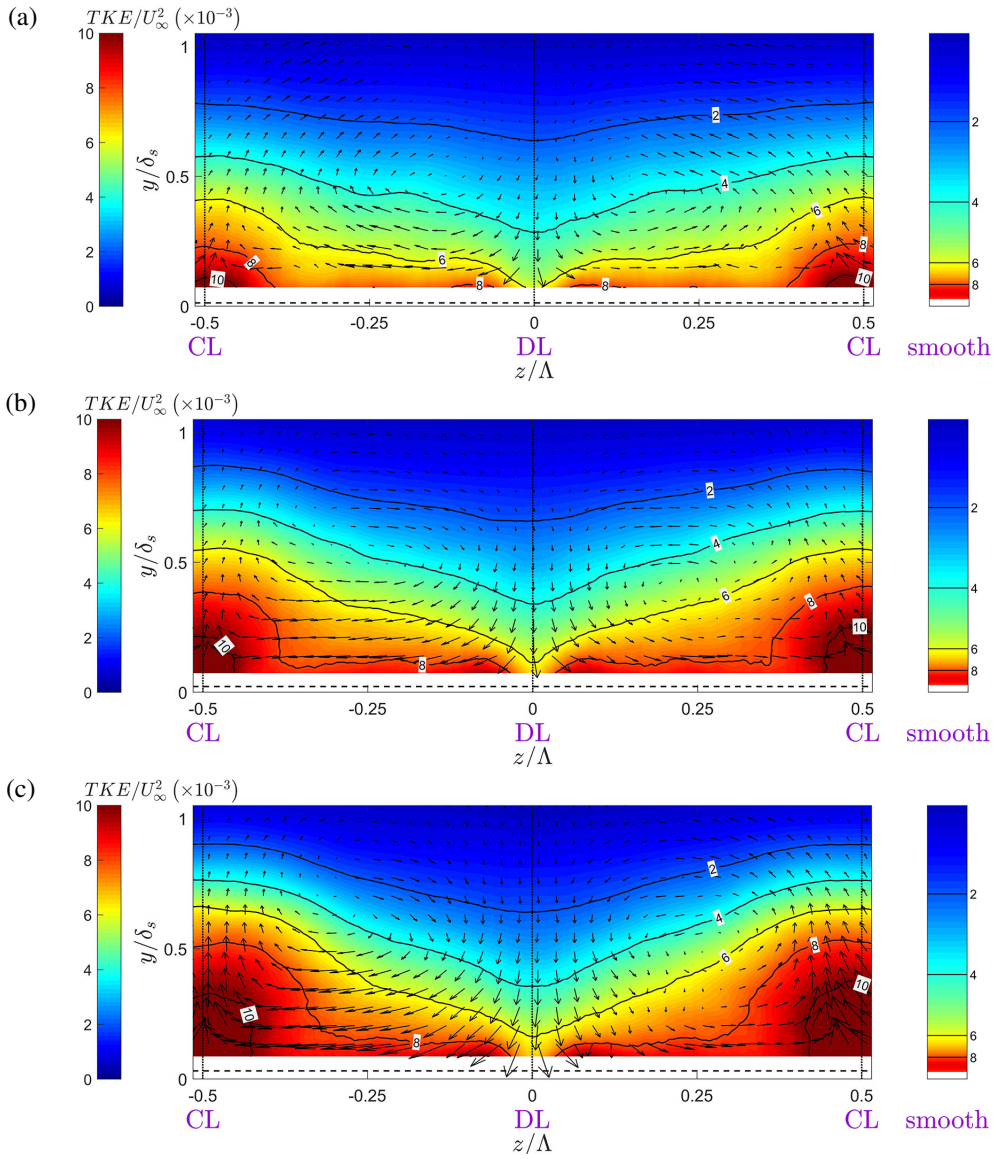

Figure 7.8: Contours of the time-averaged turbulence kinetic energy TKE over C-D riblets with (a) $h^+ = 8$, (b) $h^+ = 14$, (c) $h^+ = 20$. The horizontal dashed lines indicate the riblet crest level.

The signed swirling strength $\langle\lambda_{ci}\rangle = (\omega_x/|\omega_x|)\lambda_{ci}$ indicates the local swirling motions. The swirling strength (λ_{ci}), which isolates the local swirling motion from the shear, is defined as the imaginary part of the complex-conjugate eigenvalue of the velocity gradient tensor, and the direction of the in-plane vorticity ω_x is applied to represent the swirling direction [182]. Figure 7.10 shows contours of the time-averaged signed swirling strength ($\langle\overline{\lambda_{ci}}\rangle$) in the cross-stream plane over C-D riblets. The signed swirling strength ($\langle\lambda_{ci}\rangle$) is calculated for each PIV snapshot, and then all these instantaneous fields (5000 in total) are averaged to obtain the time-averaged contour in Figure 7.10. In the turbulent boundary layer, the regions with high rotational motions are observed on both sides of CL and DL. These high swirling regions are not aligned with the centres of the time-averaged secondary flow, since the time-averaging is an artificial superposition of instantaneous flow fields rather than a real presence [72]. A similar inconsistency between the high swirling region and the centre of the secondary flow has also been observed over the surface pattern with elevation heterogeneity [see Figure 3 in Awasthi et al. [8]]. Here we make an interesting comparison between the contours in the turbulent boundary layer [see Figure 7.10] and the laminar contour [see Figure 7.9]. To facilitate comparison, the laminar contour in Figure 7.9 is normalised using the original data of Figure 7 in Xu et al. [173]. The most dramatic difference is that we cannot observe the high swirling region near the CL in the laminar boundary layer. Thus, in the turbulent boundary layer the intense swirling motions close to the CL are completely associated with the turbulent coherent structures and the upwelling secondary flow. With larger riblet height, the population of vortical structures increases and the upwelling becomes more intense [175], making these high swirling regions wider and higher. The intensity of swirling motions in the turbulent flow is significantly higher than that in the laminar flow. Near the DL, the regions with intense swirling motions are partly related to the 'overflow-induced upwash'. The overflow-induced upwash is defined as the local upwash near the DL, which is related to the unsteady overflow above riblet crests, as revealed in the dye visualisation experiment [173]. These unsteady local events result in swirling motions adjacent to the DL in both laminar and turbulent boundary layers.

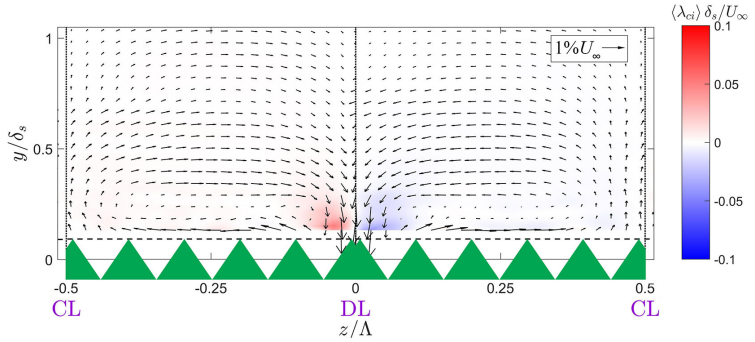

Figure 7.9: Reference case in the laminar boundary layer over C-D riblets with $\Lambda = 36mm$. Contour of the time-averaged signed swirling strength $\langle\overline{\lambda_{ci}}\rangle$ replotted by normalising data of Figure 7(b) in Xu et al. [175].

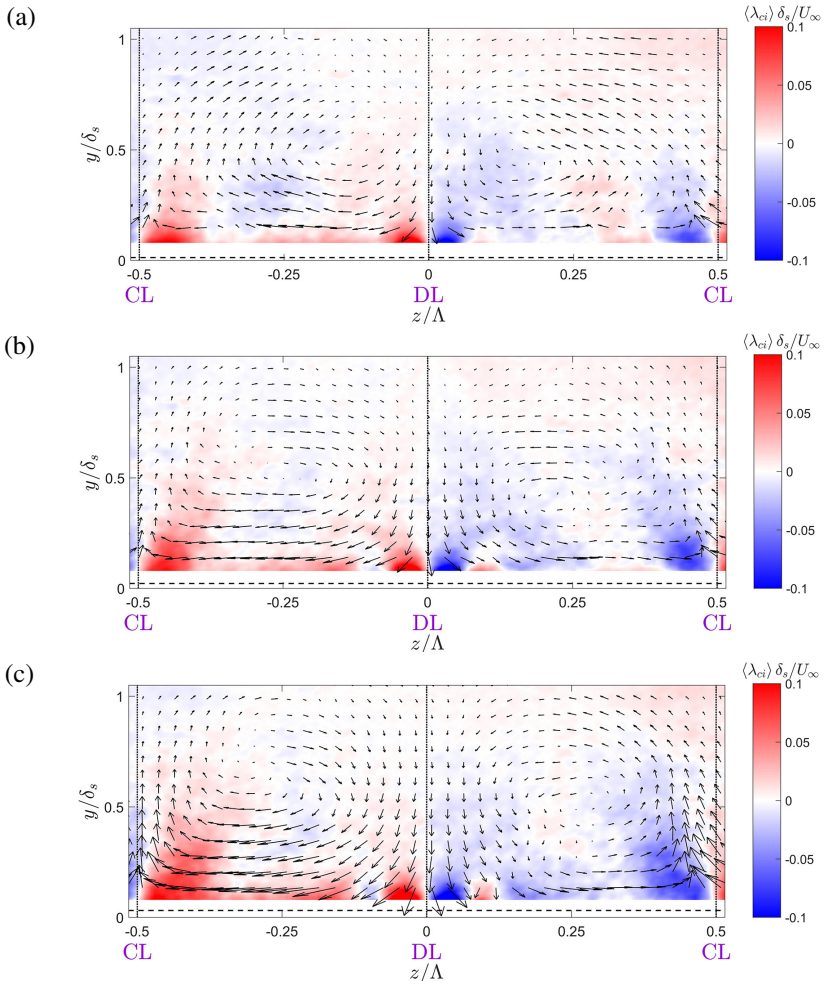

Figure 7.10: Contours of the time-averaged signed swirling strength $\langle\overline{\lambda_{ci}}\rangle$ over C-D riblets with (a) $h^+ = 8$, (b) $h^+ = 14$, (c) $h^+ = 20$. The horizontal dashed lines indicate the riblet crest level. The region with clockwise (counter-clockwise) swirling motion is red (blue).

The Reynolds shear stress ($-\overline{u'v'}$) indicates the extent of the wall-normal momentum transfer in the boundary layer. Figure 7.11 shows the time-averaged $-\overline{u'v'}$ contours in the cross-stream plane over C-D riblets. The distribution over the smooth wall, which is homogeneous in the spanwise direction, is also shown on the right as a reference. Compared with the smooth wall, the magnitude of the Reynolds shear stress increases within most of the regions over C-D riblets except for the narrow area directly over the diverging region. The area with the highest Reynolds shear stress locates over the converging region. With an increased riblet height, the high Reynolds shear stress areas (e.g. the region with a value of 2.5 and above) become wider and extend to a larger portion of the boundary layer in the cross-stream plane.

Following the wall-shear stress decomposition scheme proposed by Fukagata et al. [48], an inhibition of the Reynolds shear stress in the near-wall region is of primary importance for drag reduction. Thus, the larger (smaller) magnitude of the near-wall Reynolds shear stress over the converging (diverging) region as observed in Figure 7.11 is consistent with the higher (lower) wall-shear stress as estimated by Nugroho et al. [113] and Xu et al. [175]. The correspondence between the vertical flow and the Reynolds shear stress distribution over C-D riblets is contrary to that over the surface pattern of spanwise alternating rough/smooth strips. For the spanwise alternating strips, the downwelling (upwelling) region is situated over the rough (smooth) strip, which has a higher (lower) Reynolds shear stress [162, 141]. Thus, the near-wall spanwise flow is directed towards the region with low Reynolds shear stress. On the contrary, for C-D riblets, the region with downwelling (upwelling), i.e. the diverging (converging) region, has a relatively lower (higher) Reynolds shear stress [113, 175]. Over C-D riblets, the near-wall fluid flows from the region with low Reynolds shear stress to the region with high Reynolds shear stress.

In order to quantify the contribution of different factors to the momentum transfer, we decompose the total momentum flux here. With double-averaging based on the secondary-flow-scale domain [111], the total momentum flux can be decomposed as

$$\langle \overline{uv} \rangle_\Lambda = \langle \overline{u} \rangle_\Lambda \langle \overline{v} \rangle_\Lambda + \langle \overline{u'v'} \rangle_\Lambda + \langle \widetilde{\overline{u}}_\Lambda \widetilde{\overline{v}}_\Lambda \rangle_\Lambda, \tag{7.3}$$

where the overline denotes the time averaging, the tilde indicates the dispersive component, $\langle \cdot \rangle_\Lambda$ denotes the spatial averaging based on the secondary-flow-scale domain, i.e. within one riblet wavelength, and the dispersive velocities when using the secondary-flow-scale domain are defined as $\widetilde{\overline{u}}_\Lambda = \overline{u} - \langle \overline{u} \rangle_\Lambda$ and $\widetilde{\overline{v}}_\Lambda = \overline{v} - \langle \overline{v} \rangle_\Lambda$. The left-hand side term is the total momentum flux accounting the whole spanwise domain. On the

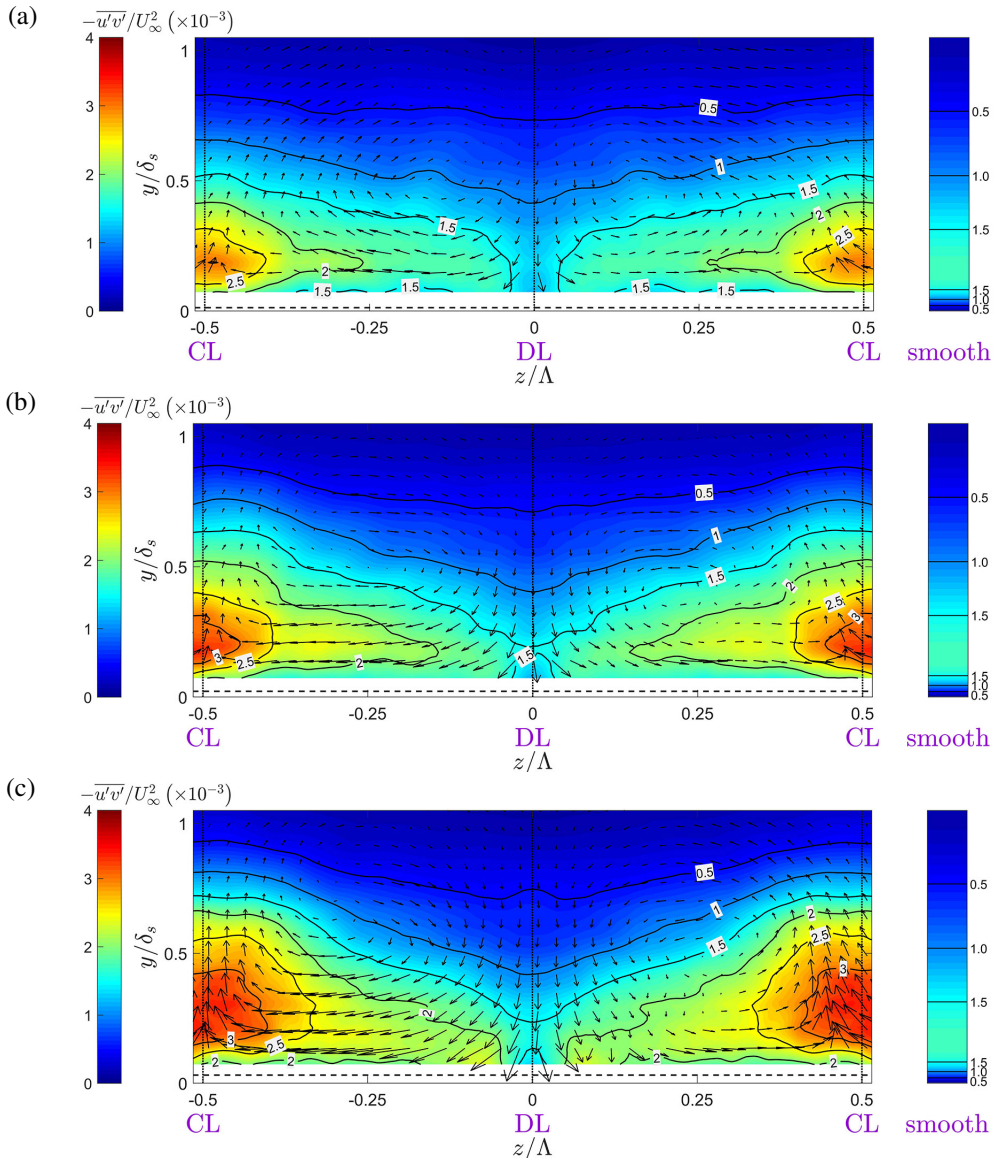

Figure 7.11: Contours of the time-averaged Reynolds shear stress $-\overline{u'v'}$ over C-D riblets with (a) $h^+ = 8$, (b) $h^+ = 14$, (c) $h^+ = 20$. The horizontal dashed lines indicate the riblet crest level.

right-hand side, the first term is the mean flow momentum flux ($\langle\overline{u}\rangle_\Lambda\langle\overline{v}\rangle_\Lambda$), the secondary term is the turbulent momentum flux ($\Phi_{turb} = \langle\overline{u'v'}\rangle_\Lambda$), and the third term is the total dispersive momentum flux ($\Phi_{disp} = \langle\widetilde{\overline{u}}_\Lambda\widetilde{\overline{v}}_\Lambda\rangle_\Lambda$). Based on the scheme proposed by Nikora et al. [110, 111], the total dispersive momentum flux can be further decomposed into the contributions of the roughness and the secondary flow, which are separated by considering the roughness-scale domain and the secondary-flow-scale domain, respectively. In this way, the total dispersive flux is further decomposed into the

roughness-induced stress and the secondary-flow-induced stress,

$$\langle \widetilde{\overline{u}}_\Lambda \widetilde{\overline{v}}_\Lambda \rangle_\Lambda = \langle \widetilde{\overline{u}}_r \widetilde{\overline{v}}_r \rangle_\Lambda + \langle \widetilde{\langle \overline{u} \rangle}_r \widetilde{\langle \overline{v} \rangle}_r \rangle_\Lambda, \tag{7.4}$$

where $\langle \cdot \rangle_r$ denotes the spatial averaging based on the roughness-scale domain, the roughness-induced stress is $\Phi_{rough} = \langle \widetilde{\overline{u}}_r \widetilde{\overline{v}}_r \rangle_\Lambda$, and the secondary-flow-induced stress is $\Phi_{sec} = \langle \widetilde{\langle \overline{u} \rangle}_r \widetilde{\langle \overline{v} \rangle}_r \rangle_\Lambda$. The dispersive velocities when using the roughness-scale domain are defined as $\widetilde{\overline{u}}_r = \overline{u} - \langle \overline{u} \rangle_r$ and $\widetilde{\overline{v}}_r = \overline{v} - \langle \overline{v} \rangle_r$. The dispersive velocities due to the secondary flow are $\widetilde{\langle \overline{u} \rangle}_r = \widetilde{\overline{u}}_\Lambda - \widetilde{\overline{u}}_r = \langle \overline{u} \rangle_r - \langle \overline{u} \rangle_\Lambda$ and $\widetilde{\langle \overline{v} \rangle}_r = \widetilde{\overline{v}}_\Lambda - \widetilde{\overline{v}}_r = \langle \overline{v} \rangle_r - \langle \overline{v} \rangle_\Lambda$.

Over C-D riblets, the spanwise averaging based on the secondary-flow-scale domain is calculated over one complete riblet wavelength (Λ), while the roughness-scale averaging is extracted across the spanwise width of the projected riblet spacing ($s/cos\gamma$). In the present study, the roughness-scale averaging is calculated across five spanwise points (23.5 in wall units), which is close to the targeted value of the spanwise projected riblet spacing ($s^+/cos\gamma = 22.4$). The profiles of the spanwise-averaged turbulent momentum flux (Φ_{turb}) and dispersive momentum flux (Φ_{disp}) over C-D riblets are shown in Figure 7.12a. It can be clearly seen that the turbulent momentum flux is significantly larger than the dispersive momentum flux, which is consistent with its dominance observed in the rough-wall open-channel flows [111, 5]. The larger spanwise-averaged turbulent momentum flux over riblets than that over the smooth wall indicates that C-D riblets enhance turbulent momentum transfer globally. An increase in the riblet height leads to a more intense turbulent momentum transfer. The effect of the riblet height is pronounced on the profiles of the dispersive momentum flux (Φ_{disp}). A decomposition of the dispersive momentum flux using Eq. (7.4) is shown in Figure 7.12b, revealing that the dispersive momentum flux over C-D riblets is substantially all contributed by the secondary-flow-induced stress (Φ_{sec}), while the roughness-induced stress (Φ_{rough}) is several orders of magnitude smaller. Therefore, in terms of the turbulent momentum flux or the dispersive momentum flux, the secondary flow becomes more intense as the riblet height turns larger.

In summary, compared with the smooth-wall case, turbulent fluctuations including the Reynolds shear stress, swirling motions and the turbulence kinetic energy are stronger over C-D riblets, and are the most pronounced over the converging region. The intense swirling motions straddling the converging region are completely associated with coherent structures and the upwelling. The increase in the riblet height significantly enhances the dispersive momentum transfer, wherein the secondary-flow-induced stress far exceeds the roughness-induced stress.

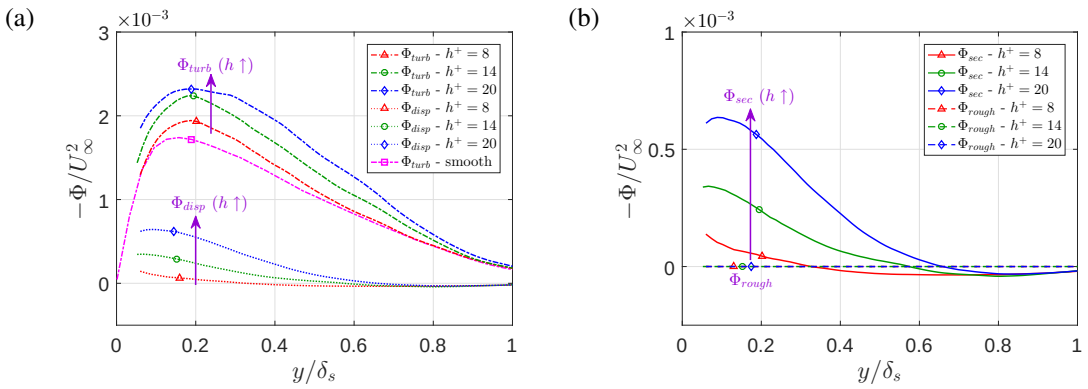

Figure 7.12: Profiles of (a) spanwise-averaged turbulent momentum flux $\Phi_{turb} = \langle\overline{u'v'}\rangle_\Lambda$ and dispersive momentum flux $\Phi_{disp} = \langle\widetilde{\overline{u}}_\Lambda\widetilde{\overline{v}}_\Lambda\rangle_\Lambda$, (b) spanwise-averaged roughness-induced dispersive momentum flux $\Phi_{rough} = \langle\widetilde{\overline{u}}_r\widetilde{\overline{v}}_r\rangle_\Lambda$ and secondary-flow-induced dispersive momentum flux $\Phi_{sec} = \langle\widetilde{\langle\overline{u}\rangle}_r\widetilde{\langle\overline{v}\rangle}_r\rangle_\Lambda$ as a function of outer coordinate y/δ_s.

7.4.3 Spatial correlation

In the cross-stream plane, the spatial correlation function can be applied to study the turbulent events. The two-dimensional spatial correlation function of the streamwise fluctuating velocity field is defined as

$$R_{u'u'}(\Delta z,\Delta y;z_{ref},y_{ref}) = \frac{\overline{u'(z_{ref},y_{ref})u'(z_{ref}+\Delta z,y_{ref}+\Delta y)}}{\sigma_{u'(z_{ref},y_{ref})}\sigma_{u'(z_{ref}+\Delta z,y_{ref}+\Delta y)}}, \tag{7.5}$$

where Δz is the spanwise separation, Δy is the wall-normal separation, (z_{ref},y_{ref}) is the position at which the correlation is calculated, and σ is the standard deviation. Specifically, for the smooth wall, the spatial correlation function is averaged along the spanwise direction due to homogeneity.

To analyse the spanwise width of streamwise turbulent events, we calculate the spatial correlation $(R_{u'u'})$ as a function of Δz about a given position (z_{ref},y_{ref}), i.e. $R_{u'u'}(\Delta z,0;z_{ref},y_{ref})$. Figure 7.13a shows the profiles of $R_{u'u'}$ at $y_{ref}/\delta_s = 0.2$ over the smooth wall and the CL/DL. Compared with the smooth-wall case, the profile is narrower over the CL and wider over the DL, indicating narrower (wider) streamwise turbulent events over the CL (DL) at $y_{ref}/\delta_s = 0.2$. To quantitatively representative the width of a correlation profile, we define the spanwise width (L_z) as the spanwise separation (Δz) at which the profile first intersects with the horizontal axis, i.e. $L_z = min(\Delta z|_{R_{u'u'}=0})$, as illustrated by the two-way arrow in Figure 7.13a.

Figure 7.13b shows the wall-normal variation of the spanwise width (L_z) over C-D

riblets and the smooth wall. Over the smooth wall, due to the development of coherent structures, the spanwise width increases as the position moves away from the wall surface. In the region between $0.15\delta_s$ and $0.9\delta_s$, there exists a quasi-linear relation between L_z and y for all these curves, which indicates a linear growth in the eddy geometry within this region. Compared with the smooth wall, the spanwise width (L_z) is slightly larger over the DL in the near-wall region of $y/\delta_s < 0.3$ and significantly smaller over the CL in the region of $y/\delta_s < 0.4$. The narrower spanwise width of streamwise turbulent events over the CL may be attributed to the secondary flow. As indicated in Figure 7.3, in the near-wall region, the time-averaged spanwise flow directs towards the CL, resulting in a compression of coherent structures over the converging region. The effect of a changing riblet height on the spanwise width (L_z) is negligible for both cases in the entire boundary layer. An increase in the riblet height results in a stronger secondary flow and a larger population of vortical structures [175], which have conflicting contributions to the changing trend of the spanwise width.

Figure 7.13b shows the wall-normal variation of the spanwise width scale (L_z) over C-D riblets and the smooth wall. Due to the development of coherent structures, the spanwise width scale increases as the reference station moves away from the wall surface. An increasing spanwise width scale with the wall distance is consistent with the hypothesis in the attached eddy model [149, 94]. Over the smooth wall, quasi-linear relations between the spanwise width scale (L_z) and the wall distance (y) are indicated by the dotted lines. The value of L_z varies linearly with respect to y in the near-wall region of $y/\delta_s < 0.15$, while a new constant growth rate is observed at a higher distance of $y/\delta_s > 0.15$. The position of $y = 0.15\delta_s$ indicates the upper limit of the logarithmic layer, and the coherent structures above this height cannot retain their coherence [91]. Similar trends of L_z against y have been observed in boundary layers at higher Reynolds numbers [147, 63] as well as in channel flows and pipe flows [62, 103]. Compared with the smooth wall, the spanwise width scale (L_z) in the near-wall region is slightly larger over the DL and much smaller over the CL. The narrower streamwise turbulent events over the CL can be primarily attributed to the newly created coherent structures, as evidenced by the significant increase in the population of spanwise vortices [175] and the intense swirling motions [see Fig. 7.10] over the converging region. A direct result of these new small-scale vortical structures is a decrease in coherence in the spanwise direction. In addition, the slope change over the CL occurs at $y/\delta_s \approx 0.4$, as compared with the smooth-wall case at $y/\delta_s \approx 0.15$. The higher wall-normal position indicates that the logarithmic layer over the converging region extends further into the boundary

layer. The effect of a changing riblet height on the spanwise width scale is negligible over both the CL and the DL in the entire boundary layer.

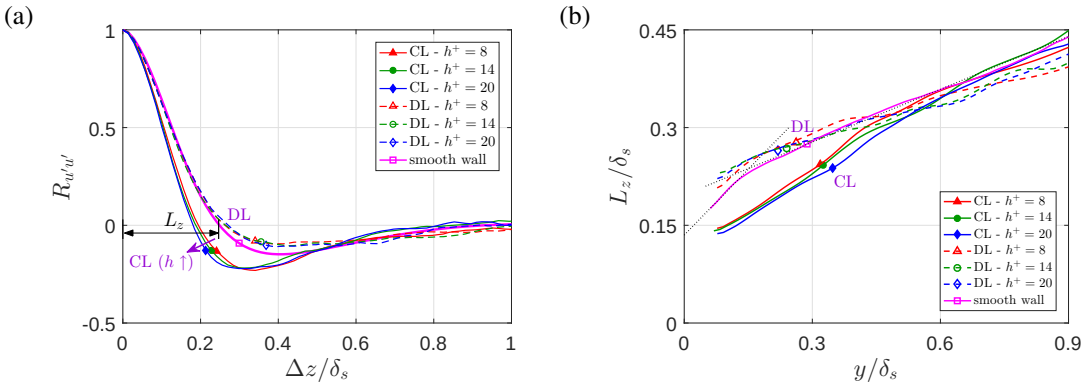

Figure 7.13: (*a*) Profiles of the spatial correlation coefficient $R_{u'u'}$ at the CL/DL about $y_{ref}/\delta_s = 0.2$ and $\Delta y = 0$ as a function of spanwise separation Δz. (*b*) Profiles of the spanwise width L_z at the CL/DL as a function of outer coordinate y/δ_s.

In summary, compared with the smooth-wall case, the spanwise width scale of near-wall streamwise turbulent events increases slightly over the DL and decreases significantly over the CL. The narrower width over the CL is due to the newly created coherent structures over the converging region. In the outer region of $y/\delta_s > 0.5$, the spanwise width scale of the streamwise coherent structures over C-D riblets remains essentially unchanged.

7.5 Categorisation of spanwise heterogeneous surface patterns

In this section, we elaborate the differences in the known types of spanwise heterogeneity from the perspectives of surface geometry, roll mode and generation mechanism of the secondary flow, emphasising the distinction of C-D riblets from the other two types. By synthesising available classification methods [72, 95], we propose to have three types of spanwise heterogeneous surface patterns: type I - spanwise heterogeneity due to spanwise variations in surface roughness level or slip condition; type II - spanwise heterogeneity due to spanwise variations in elevation; type III - spanwise heterogeneity due to spanwise variations in directionality.

Type	Research	Surface roughness patterns	Research method(s)	Model	S/δ_s	S/W_r	H_r/δ_s (%)
I	Wang et al. [162]	roughness strips	LDA	channel	2	2	-
I	Willingham et al. [166]	roughness strips	LES	plate	3	3, 5, 15	0.1
I	Turk et al. [151]	free-slip/no-slip surface	DNS	channel	0.048−3.12	1.33−4	-
I	Anderson et al. [6]	roughness strips	LES	plate	3	5	0.1
I	Stoesser et al. [141]	roughness strips	LES	channel	2	2	-
I	Stroh et al. [142]	free-slip/no-slip surface	DNS	channel	0.6−1.4	1.75−2.34	-
I	Bai et al. [9]	roughness strips	PIV, sPIV	plate	2.73	3	0.77
I	Chung et al. [31]	wall-shear stress variation	DNS	channel	0.39−6.28	2	-
II	Wang et al. [163]	rectangular ridges	LDA, UDV	channel	2	2, 3	6.7, 13.3
II	Mejia-Alvarez et al. [97]	surface with deposition	sPIV	plate	≈ 0.75	-	4.1, 4.5
II	Barros et al. [13]	surface with deposition	sPIV	plate	≈ 0.75	-	4.5
II	Vanderwel et al. [152]	Lego® bricks	sPIV	plate	0.3−1.76	2−12	8.9
II	Hwang et al. [66]	rectangular ridges	DNS	plate	0.57−2.39	2−16	0.16
II	Yang et al. [178]	pyramidal obstacles	LES	channel	0.1−6.28	1.3−113	5, 6.7
II	Medjnoun et al. [95]	rectangular ridges	OFI, HWA	plate	0.8, 1.6, 3.2	2, 4, 8	10
II	Awasthi et al. [8]	raised topography	LES	channel	3.14	-	5, 10
III	Nugroho et al. [113]	C-D riblets	HWA	plate	2.84	2	0.96
III	Benschop et al. [16]	C-D riblets	DNS	channel	0.1−12.9	2	2.4
III	Kevin et al. [72]	C-D riblets	sPIV	plate	1.53	2	0.52
III	Xu et al. [173, 174]	C-D riblets	DV, PIV, sPIV	plate	2.27−3.41	2	18.2
III	Kevin et al. [71]	C-D riblets	PIV	plate	2.5	2	0.9
III	Xu et al. [175], Present	C-D riblets	PIV, sPIV	plate	2.56	2	2.4, 4.3, 6.2

Table 7.3: A summary of experimental parameters in existing studies on C-D riblets.

Table 7.3 summarises some representative studies on surface patterns with spanwise heterogeneity including those on C-D riblets (type III). Here, S is the spanwise spacing or riblet wavelength, W_r is the spanwise width of the high roughness strip, the elevated strip or the riblet strip, H_r is the height of the roughness element and δ_s is the boundary layer thickness over the smooth wall, which is replaced by the channel height H for an open channel flow. In these studies, the spanwise spacing (S) is comparable to the dominant length scale in the flow field (δ_s), despite the values of S/W_r and H_r/δ_s being more scattered.

7.5.1 Surface geometry

Figure 7.14 shows the typical surface geometries of the aforementioned three types of spanwise heterogeneous patterns in both perspective view and cross-sectional view. The most distinct difference among these three types lies in the change of surface geometry at the interface between alternating strips. In type I, there exists an abrupt change in the height of random surface roughness across the interface between smooth and rough strips, whereas in type II there is a step change [163, 152] or a gradual transition [8] in the surface elevation across the interface. For C-D riblets, while there is no step change in the surface roughness level or the averaged surface elevation across strips of left-yawed and right-yawed microgrooves, a step change in the orientation of the microgrooves exists across the interface. It is the directionality of the microgrooves that makes the geometric characteristics of C-D riblets inherently different from those of type I and type II spanwise heterogeneity surface patterns.

7.5.2 Roll mode

Each of these three types of spanwise heterogeneous surface patterns generates a roll mode with a scale comparable to the dominant length scale in the flow field. In Figure 7.14, the typical appearance of the time-averaged roll modes of the secondary flow in the cross-stream plane generated by the three different types of spanwise heterogeneous surface patterns is illustrated. The freestream is from the bottom left to the top right, i.e. along x direction. The roll modes presented here are representative of most reported cases, though variations from them do exist. The intensity of the secondary flow is influenced by the spanwise spacing (S). When S takes a value near the boundary layer thickness (δ_s), the intensity of secondary flow reaches the maximum for both type I [31] and type II [95] surface patterns.

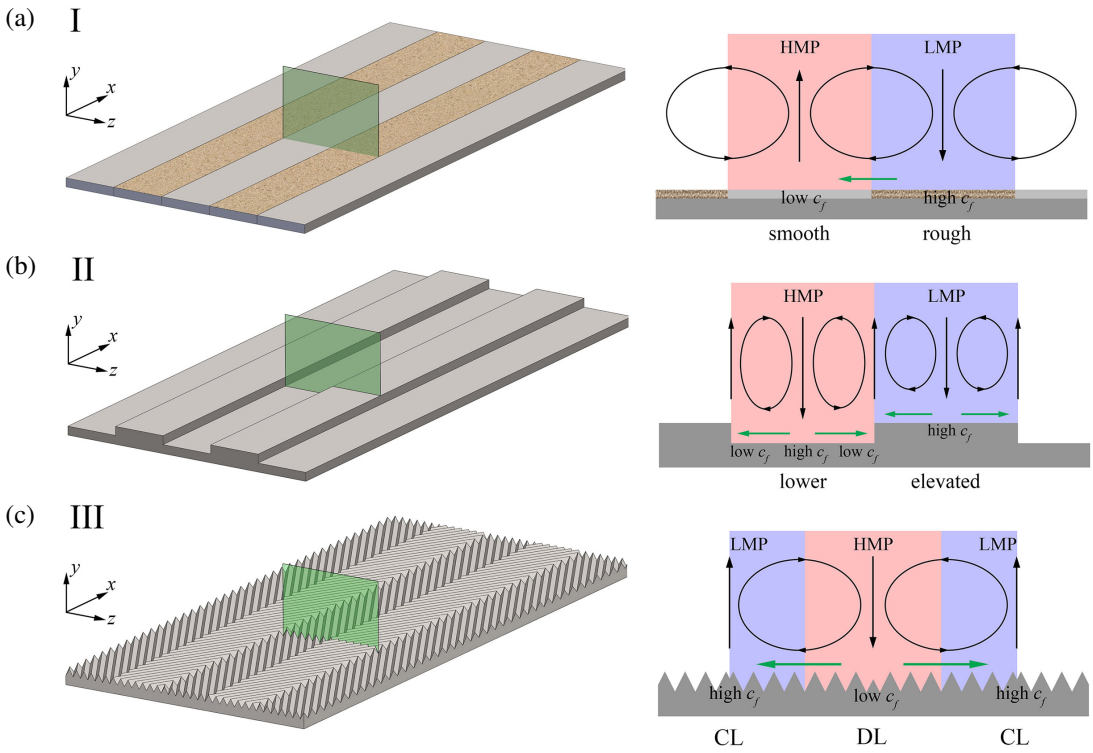

Figure 7.14: Surface geometry (left) and corresponding secondary flow in the cross-stream plane (right) of representative spanwise heterogeneous surface patterns in three categories. (*a*) Spanwise alternating smooth and rough strips (type I, roughness heterogeneity), (*b*) streamwise-aligned elevated strips (type II, elevation heterogeneity), (*c*) convergent-divergent riblets (type III, directionality heterogeneity).

For the spanwise alternating rough/smooth strips (type I), the spanwise flow over the surface is directed from the rough region to the smooth region. This leads to a roll mode as depicted in Figure 7.14a, with an upwelling occurring over the smooth region and a downwelling over the rough region [162, 31, 9]. There exist streamwise-elongated spanwise-alternating LMPs and HMPs above the smooth and rough strips, respectively [99, 13, 6]. For spanwise alternating free-slip/no-slip strips (type I) where the free-slip area is superhydrophobic, numerical simulations indicate that the appearance of roll mode is not definite but influenced by the spanwise width of these strips [151, 142].

For type II spanwise heterogeneous surface pattern, the fluid in the near-wall region flows towards the spanwise step [163]. There exists a pair of counter-rotating roll mode over each lower/elevated strip as depicted in Figure 7.14b, with a downwelling at the middle station of the lower surface area and an upwelling over the interface where a step change in surface elevation occurs [163]. However, in some cases, the roll

mode across the type II heterogeneity may become indiscernible [152]. The upwelling at the interface further induces a tertiary flow with a local recirculating motion over the area of higher elevation and hence a downwelling over its middle station [66]. Spanwise-alternating HMPs and LMPs are observed over the lower and upper surfaces, respectively [8]. When the elevated strip is relatively narrow in relation to the spanwise spacing (i.e. large value of parameter S/W_r in Table 7.3), an upwelling dominates the region over the elevated strip whereas an intense downwelling is observed only in the vicinity of the elevated wall surface, and the middle part of the lower surface is less disturbed [152, 66, 178].

For C-D riblets (type III), the spanwise flow is directed from the DL towards the CL, leading to a roll mode as depicted in Figure 7.14c [114, 72, 173]. In the boundary layer, the HMPs and LMPs occur above the diverging and converging regions, respectively [72, 175]. The directions of the vertical velocity over two types of surface interfaces (CL and DL) are different, i.e. an upwelling over the CL and a downwelling over the DL.

7.5.3 Generation mechanism

For all these three types of spanwise heterogeneous surface patterns, a secondary flow across the span is generated via introducing a changing wall boundary condition in the spanwise direction. The direction of the spanwise flow in the near-wall region and its correspondence with the local wall-shear stress are shown in Figure 7.14. The secondary flow over spanwise alternating rough/smooth strips (type I) is induced by a spanwise variation in the surface frictional drag. The near-wall fluid tends to flow from the rough strip to the smooth strip, i.e. from the high-resistance region to the low-resistance region. For the lower/elevated strips (type II), the skin friction on the surface near the step change is smaller compared to the middle section of the lower or elevated surface [95]. The near-wall fluid flows from the region with high-resistance to the region with low-resistance in the spanwise direction. In the case of C-D riblets (type III), a spanwise surface flow is directly caused by the tendency of fluid to follow the direction of the minimum flow resistance and hence the direction of the microgrooves [89]. Thus, the inherent driving force of the secondary flow over C-D riblets is attributed to the directionality of the yawed riblets.

Prandtl classified the secondary flows into two categories based on generation mechanisms [19, 43]. Prandtl's first kind is caused by the mean flow being skewed

away from the streamwise direction by a geometric means, and it occurs in both laminar and turbulent flows. By contrast, Prandtl's second kind, also known as turbulence-driven secondary flow, is caused by the heterogeneity of turbulence and occurs only in the turbulent flow. The secondary flows generated by spanwise heterogeneous surface patterns can be further explained according to these criteria.

The secondary flow generated by spanwise alternating smooth and rough strips (type I) belongs to Prandtl's second kind [6]. Here, the difference in the level of turbulent stress across the smooth-/rough-wall interface leads to a spanwise pressure gradient and hence the secondary flow. Hinze [58, 59] stated that an imbalance between the local production rate and the local dissipation rate of the turbulence kinetic energy results in a radial (normal to the wall surface) motion of the fluid. As such, an upwelling occurs in the region where dissipation exceeds production, whereas a downwelling occurs in the area where production exceeds dissipation. By analysing the transport equation of turbulence kinetic energy, Hwang et al. [66] showed that the secondary flow over a surface pattern with elevation heterogeneity (type II) also belongs to Prandtl's second kind. It is not known whether the secondary flow is present in a laminar flow over the spanwise heterogeneous surface pattern of type I or type II.

By contrast, the secondary flow induced by C-D riblets in a boundary layer may not be directly categorised as Prandtl's second kind, especially at relatively low Reynolds numbers. With less resistance in the direction parallel to the microgrooves, the fluid tends to flow along the yawed microgrooves [89, 70, 173], leading to the formation of a secondary flow as seen in the cross-stream plane in order to satisfy the continuity requirement. Such a phenomenon has been observed in both laminar [173] and turbulent boundary layers [72]. Therefore, the spanwise flow induced by the mean flow skewing, i.e. the highly directional riblet surface, also contributes to the large-scale secondary flow disregard of the state of boundary layer. Based on the estimated wall-shear stress [113, 72, 175], the near-wall fluid over C-D riblets flows spanwise from the low-resistance region towards to the high-resistance region. It is speculated that as the Reynolds number increases, the contribution of turbulence heterogeneity to the secondary flow becomes relatively more important. In order to verify Prandtl's first kind or Prandtl's second kind of secondary flow over C-D riblets, we need to investigate the dominance of the mean shear skewing term or the turbulence heterogeneity terms, respectively, on the right-hand side of the Reynolds-averaged streamwise vorticity transport equation (details provided in Appendix 7.8). However, a verification using the current non-time-resolved PIV data in the cross-stream $(z-y)$ plane is not

feasible because the spatial gradients along the streamwise direction ($\partial/\partial x$) are not available.

In summary, based on the above analysis, it can be seen that C-D riblets exhibit very different geometric characteristics from those of type I and type II surface patterns with spanwise heterogeneity. C-D riblets also produce a roll mode of a different nature. Furthermore, unlike type I or type II surface patterns with spanwise heterogeneity which generate the secondary flow of Prandtl's second kind, C-D riblets also have a non-negligible contribution from the geometrical skewing by the yawed microgrooves. The inherent differences between type I and type II have also been explained in the above-mentioned three aspects. Thus, we propose to categorise the surface patterns with spanwise heterogeneity into three types [see Figure 7.14], with C-D riblets being classified as type III.

7.6 Conclusions

We apply stereoscopic particle image velocimetry to study the secondary flow in the turbulent boundary layer developing over convergent-divergent riblets (C-D riblets) at $Re_\theta = 723$. The effect of riblet height on the secondary flow is revealed in the cross-stream plane by comparing three different heights of $h^+ = 8$, 14 and 20. The secondary flow which occupies the entire boundary layer becomes more intense as the riblet height increases. A larger riblet height corresponds to a wider downwelling region, a stronger spanwise flow, a narrower upwelling region and a more intense deceleration. Spanwise turbulent fluctuations are more intense over the converging line than the smooth wall, and an increase in the riblet height further enhances fluctuations. On the contrary, in the near-wall region over the diverging line, spanwise fluctuations are slightly inhibited. As the riblet height increases, the likelihood of common-flow events is higher, i.e. more common-flow-up events over the converging region while more common-flow-down events over the diverging region. In addition to the divergent region, more severe turbulent fluctuations, including Reynolds shear stress and turbulence kinetic energy, are observed on the C-D riblets compared with the smooth wall. Intense swirling motions are observed over the converging region, which are entirely attributable to the turbulent coherent structures and the upwelling. An increase in the riblet height further enhances these turbulent fluctuations. The momentum flux decomposition shows that an increase in the riblet height enhances the transfers of both

turbulent and dispersive momentum. For the dispersive momentum flux, the contribution of the secondary-flow-induced stress far exceeds the roughness-induced stress. The spanwise width scale of near-wall turbulent events increases slightly over the diverging region and decreases significantly over the converging region. Overall, for the time-averaged roll mode and the instantaneous vortical structures, an increase in the riblet height results in a stronger secondary flow over C-D riblets. The mechanism of an increased riblet height is attributed to the greater capability of the deeper yawed microgrooves in driving the surface flow from the diverging region to the converging region in the spanwise direction.

Besides, by examining three aspects including surface geometry, roll mode and secondary flow generation mechanism, we propose to categorise the surface patterns with spanwise heterogeneity into three different types. These three types are termed as roughness heterogeneity (type I) [see Figure 7.14a], elevation heterogeneity (type II) [see Figure 7.14b] and directionality heterogeneity (type III) [see Figure 7.14c]. The geometrical skewing of the directional microgrooves makes a key contribution to the secondary flow over C-D riblets.

7.7 Acknowledgements

The first author wishes to acknowledge the President's Doctoral Scholar award from the University of Manchester. The authors would like to thank the technical supports from workshop technicians at the School of Mechanical, Aerospace and Civil Engineering.

7.8 Appendix: Mechanism of secondary flow

The classification of Prandtl's first kind or Prandtl's second kind of secondary flow over C-D riblets in the turbulent boundary layer still needs further verification. Here, we present the procedure to verify the kind of secondary flow over C-D riblets based on the mean streamwise vorticity transport equation [121, 19]. The time-averaged streamwise vorticity ($\overline{\omega}_x = \partial\overline{w}/\partial y - \partial\overline{v}/\partial z$), which is exactly zero for a spanwise homogeneous flow, can be applied to indicate the intensity of the secondary flow. For an incompressible flow, the transport equation for the mean streamwise vorticity is

$$\overline{u}\frac{\partial\overline{\omega}_x}{\partial x} + \overline{v}\frac{\partial\overline{\omega}_x}{\partial y} + \overline{w}\frac{\partial\overline{\omega}_x}{\partial z} = \nu\nabla^2\overline{\omega}_x + \overline{\omega}_x\frac{\partial\overline{u}}{\partial x} + P_1 + P_2 + P_3 + P_4, \tag{7.6}$$

where

$$P_1 = \frac{\partial \overline{u}}{\partial z}\frac{\partial \overline{v}}{\partial x} - \frac{\partial \overline{u}}{\partial y}\frac{\partial \overline{w}}{\partial x}, \tag{7.7}$$

$$P_2 = \frac{\partial}{\partial x}\left(\frac{\partial \overline{u'v'}}{\partial z} - \frac{\partial \overline{u'w'}}{\partial y}\right), \tag{7.8}$$

$$P_3 = \frac{\partial^2}{\partial y \partial z}\left(\overline{v'^2} - \overline{w'^2}\right), \tag{7.9}$$

$$P_4 = \left(\frac{\partial^2}{\partial z^2} - \frac{\partial^2}{\partial y^2}\right)\overline{v'w'}. \tag{7.10}$$

The left-hand side terms in Eq. (7.6) represent the convection of streamwise vorticity by the primary flow and the secondary flow. On the right-hand side in Eq. (7.6), the first term accounts for the viscous diffusion, while the second term represents the streamwise vortex stretching. The term P_1 describes the production of streamwise vorticity through deflection or skewing of the mean shear by a transverse pressure gradient. The term P_1 represents an inherently inviscid process, and the secondary flow dominated by this mechanism is categorised as Prandtl's first kind. The last three terms, i.e. $P_2+P_3+P_4$, which represent the effect of the time-averaged convection and production of turbulent vorticity, are responsible for generating the secondary flow of Prandtl's second kind. These three terms are non-zero only in the turbulent flow, with a transverse imbalance of turbulent stresses reflected in terms P_3 and P_4.

In the turbulent boundary layer, the categorisation of the secondary flow (Prandtl's first kind or Prandtl's second kind) over C-D riblets needs to be validated by investigating the relative contribution of P_1 and $P_2+P_3+P_4$ in Eq. (7.6). The assumption of streamwise heterogeneity ($\partial/\partial x = 0$) is not valid for C-D riblets, otherwise there would exist no secondary flow in the laminar boundary layer [173]. Due to the spanwise flow in the near-wall region, the components $\partial\overline{v}/\partial y$ and $\partial\overline{w}/\partial x$ are expected to have non-zero values in the near-wall region, i.e. the term P_1 is non-zero. For the current stereoscopic PIV data, the spatial gradient along the streamwise direction ($\partial/\partial x$) is not available. Thus, the terms P_1 and P_2 cannot be estimated using the present data due to the lack of the streamwise gradients. In the future, either numerical simulation or tomographic PIV measurement can be applied to study the generation mechanism of the secondary flow over C-D riblets.

Chapter 8

Conclusions and Future Work

8.1 Conclusions

The objective of this research work is to explore the characteristics of boundary layer flows over the spanwise heterogeneous surface pattern of convergent-divergent riblets (C-D riblets). To achieve this objective, a series of experimental work has been carried out using different measurement technique including dye visualisation and mono-/stereoscopic particle image velocimetry (PIV).

8.1.1 Characteristics of laminar flow over C-D riblets

The development of a laminar boundary layer over a rectangular riblet section is studied experimentally using dye visualisation and mono-/stereoscopic PIV. C-D riblets are observed to generate a surface flow from the diverging region towards the adjacent converging region. A weak recirculating secondary flow is formed in cross-stream plane across the entire boundary layer, creating a downwelling over the diverging region and an upwelling over the converging region. The downwelling over the diverging region adds the mass flow into riblet valleys. The fluid inside riblet valleys evolves along a helicoidal path considering the crossflow above yawed riblet. The micro-scale flow inside riblet valleys interacts with the crossflow boundary layer and hence plays a key role in determining the structure of the secondary flow across the boundary layer.

A reduction in the streamwise velocity and an increase in fluctuations and vorticity is found over the diverging region, and the opposite is observed over the diverging region. The streamwise development of the flow over C-D riblets is divided into a developing stage and a developed stage. Over the converging region, the magnitudes

of induced streamwise velocity and vorticity increase in the developing stage while remain essentially unchanged in the developed stage.

The effect of riblet wavelength on the flow field characteristics is revealed. A larger wavelength produces a higher magnitude of upwelling/downwelling over the converging/diverging region and hence a more intense secondary flow. For the streamwise velocity (momentum flux), a more intense deceleration effect is also observed for riblets with larger wavelength.

8.1.2 Effects of spanwise variation of riblet height on laminar flow

A laminar boundary layer over C-D riblets with a spanwise riblet height variation, i.e. a reduced riblet height in the converging region, is analysed in the longitudinal plane and the wall-parallel plane using mono-PIV. A reduced riblet height over the converging region leads to a less intense secondary flow including a thinner boundary layer and a weaker induced streamwise velocity. When the riblet height over the converging region is zero, the induced flow field is ignorable compared with the smooth-wall case. In contrast, the flow field characteristics present only slight changes over the diverging region.

In the developing stage, the fluid flows in the spanwise direction of riblet valleys in the wall-parallel plane, i.e. from the diverging line to the converging line. In the developed stage, a spanwise flow opposite to the directions of riblet valleys is observed in the same wall-parallel plane. The time-averaged vortical structures in the cross-stream plane are inferred from the distribution of the spanwise velocity. It is believed that he weak recirculating large-scale vortical structures exist in the developed stage but does not exist in the developing stage.

8.1.3 Characteristics of turbulent boundary layer over C-D riblets in the longitudinal plane

The turbulent boundary layers developing over C-D riblets of three different heights of $h^+ = 8$, 14 and 20 is measured in the longitudinal plane at $Re_\theta = 723$ using mono-PIV. Compared to the baseline case, an increase in the time-averaged streamwise velocity and a reduction in the time-averaged Reynolds shear stress occur in the near-wall region over the diverging line. In contrast, the opposite is observed over the converging line and the impact extends across the entire boundary layer. An increase in riblet height enhances such a trend and affects the profiles of velocity and Reynolds shear

stress more profoundly over the converging line. Although a logarithmic law region is present in the velocity profiles, Townsend's outer-layer similarity hypothesis is invalid.

The population of prograde and retrograde spanwise vortices is investigated. With a riblet height of $h^+ = 8$ (2.4% of the baseline boundary layer thickness), the population of spanwise vortices increase by more than 50% over the converging region compared to the smooth-wall case, implying a more intense in the turbulence production activities. An increase in the height of C-D riblets results in a substantial increase in the population of both prograde and retrograde vortices. Over the diverging region, the population density of spanwise vortices remains almost unaffected in the boundary layer except for the near-wall region, and it is insensitive to the riblet height increase.

The characteristics include the inclination angle and the streamwise extent of vortex packets are extracted from two-point spatial correlations. In comparison with the smooth-wall case, while the δ-scale vortex packets are steeper and less stretched in the outer region over the diverging region, they are less affected over the converging region. An increasing riblet height further shortens of these packets in the streamwise direction over the diverging region.

The zonal behaviour of uniform streamwise momentum in the boundary layer is examined. In comparison with the smooth-wall case, over the converging region while the probability of having three or four uniform momentum zones increases, the probability of having one or two uniform momentum zones decreases at the Reynolds number investigated in the present study. Correspondingly, the uniform momentum zones in the outer part of the boundary layer over the converging region become thinner. Again, an increase in the riblet height enhances such a trend.

Overall, while an increase in the riblet height affects a large portion of the boundary layer away from the wall over the converging region, the impact on the diverging region is largely confined within the near-wall region. We attribute such distinct differences to the opposite local secondary flow motion induced by the C-D riblets.

8.1.4 Characteristics of turbulent boundary layer over C-D riblets in the cross-stream plane

The secondary flow in the turbulent boundary layer developing over C-D riblets is studied in the cross-stream plane using stereoscopic PIV. The effects of riblet height on the secondary flow are revealed by measuring C-D riblets with three different heights of $h^+ = 8$, 14 and 20.

The boundary-layer-scale secondary flow becomes more intense as the riblet height increases. A larger riblet height corresponds to a wider downwelling region, a stronger spanwise flow, a narrower upwelling region and a more intense deceleration effect. Spanwise turbulent fluctuations are more intense over the converging line than the smooth wall, and an increase in the riblet height enhances fluctuations. On the contrary, in the near-wall region over the diverging line, spanwise fluctuations are slightly inhibited. As the riblet height increases, the probability of common-flow events is higher, i.e. more common-flow-up events over the converging region while more common-flow-down events over the diverging region.

The turbulent fluctuations including the Reynolds shear stress and the turbulence kinetic energy are more intense over C-D riblets in addition to the diverging region. Intense swirling motions are observed over the converging region, as completely attributed to the turbulent coherent structures and the upwelling. An increase in the riblet height further enhances these turbulent fluctuations. The momentum flux decomposition reveals that an increase in the riblet height enhances both turbulent and dispersive momentum transfers. For the dispersive momentum flux, the secondary-flow-induced stress far exceeds the roughness-induced stress over C-D riblets. The spanwise width of streamwise turbulent events, as indicated by the characteristics of the spatial correlation function, in the near-wall region slightly increases over the diverging region and significantly decreases over the converging region.

Overall, for the time-averaged roll mode and the instantaneous vortical structures, an increase in the riblet height results in a stronger secondary flow over C-D riblets. The mechanism of an increased riblet height is attributed to the greater capability of deeper yawed microgrooves in driving the spanwise surface flow from the diverging region to the converging region.

Besides, by examining three complementing aspects including surface geometry, time-averaged roll mode and secondary flow generation mechanism, we propose to categorise the surface patterns with spanwise heterogeneity into three different types. These three types are termed as roughness heterogeneity (type I), elevation heterogeneity (type II) and directionality heterogeneity (type III). Considering the presence of secondary flow in the laminar boundary layer over C-D riblets, the geometrical skewing of the directional microgrooves makes a key contribution to the roll mode over C-D riblets.

8.2 Future work

8.2.1 On the drag reduction effect

In the thesis, the wall-shear stress over C-D riblets is estimated by the modified Clauser method using the time-averaged streamwise velocity profile. C-D riblets lead to a significant change in the wall-shear stress, with an increase over the converging line and a decrease over the diverging line. However, the modified Clauser method has a number of limitations, including the choice of constant values (κ and B) and the subjectivity of selecting data points in the logarithmic region [175]. The grooved surface of C-D riblets inhibits the application of a film-based technique. Thus, it is very promising to study the total wall-shear stress using force balance.

8.2.2 On the spanwise height variation

On the secondary flight feathers of birds, there is a height variation in the spanwise direction, with the maximum height over the middle (diverging) region and a height reduction away from the middle region [25]. In the thesis, the effect of spanwise height variation of C-D riblets on the flow field is examined in the laminar boundary layer in Chapter 5. The characteristics of coherent structures in the turbulent boundary layer over a similar configuration may be examined in the future.

8.2.3 On the heat transfer characteristics

The boundary-layer-scale secondary flow induced by C-D riblets may affect the heat transfer characteristics. It is expected that the vertical mass transfer, i.e. downwelling over the diverging region and the upwelling over the converging region, will enhance heat transfer in the corresponding region. Considering the low roughness height relative to the boundary layer thickness, the surface pattern of C-D riblets may be applied to enhance local heat transfer in certain areas without introducing excessive resistance. A practical engineering application is needed to promote the project.

8.2.4 On the separation inhibition

To study the control effects of C-D riblets on flow separation, the ramp configuration can be applied to produce a mildly separated turbulent boundary layer. The surface pattern of C-D riblets can be mounted upstream of the ramp to create a secondary

flow above the shear layer. In the boundary layer wind tunnel, the ramp has been designed and machined to study the separation control effects of synthetic jets [180, 181]. The same configuration may be applied to study the separation control effects of C-D riblets. Potential experimental measurements include hot wire anemometer, particle image velocimetry, laser Doppler velocimetry and pressure gauge. Beside, the configuration of an airfoil at high angle of attack can be applied to explore the possibility of delaying the separation by C-D riblets.

Bibliography

[1] M. S. Acarlar and C. R. Smith. A study of hairpin vortices in a laminar boundary layer. Part 1. Hairpin vortices generated by a hemisphere protuberance. *J. Fluid Mech.*, 175:1–41, 1987.

[2] M. S. Acarlar and C. R. Smith. A study of hairpin vortices in a laminar boundary layer. Part 2. Hairpin vortices generated by fluid injection. *J. Fluid Mech.*, 175:43–83, 1987.

[3] R. J. Adrian. Hairpin vortex organization in wall turbulence. *Phys. Fluids*, 19(4):041301, 2007.

[4] R. J. Adrian, C. D. Meinhart, and C. D. Tomkins. Vortex organization in the outer region of the turbulent boundary layer. *J. Fluid Mech.*, 422:1–54, 2000.

[5] G. Alfonsi, D. Ferraro, A. Lauria, and R. Gaudio. Large-eddy simulation of turbulent natural-bed flow. *Phys. Fluids*, 31(8):085105, 2019.

[6] W. Anderson, J. M. Barros, K. T. Christensen, and A. Awasthi. Numerical and experimental study of mechanisms responsible for turbulent secondary flows in boundary layer flows over spanwise heterogeneous roughness. *J. Fluid Mech.*, 768:316–347, 2015.

[7] M. Atzori, R. Vinuesa, A. Lozano-Durán, and P. Schlatter. Characterization of turbulent coherent structures in square duct flow. *J. Phys. Conf. Ser.*, 1001:012008, 2018.

[8] A. Awasthi and W. Anderson. Numerical study of turbulent channel flow perturbed by spanwise topographic heterogeneity: Amplitude and frequency modulation within low- and high-momentum pathways. *Phys. Rev. Fluids*, 3(4):044602, 2018.

[9] H. L. Bai, Kevin, N. Hutchins, and J. P. Monty. Turbulence modifications in a turbulent boundary layer over a rough wall with spanwise-alternating roughness strips. *Phys. Fluids*, 30(5):055105, 2018.

[10] B. J. Balakumar and R. J. Adrian. Large- and very-large-scale motions in channel and boundary-layer flows. *Philos. Trans. R. Soc. A Math. Phys. Eng. Sci.*, 365(1852):665–681, 2007.

[11] P. Ball. Shark skin and other solutions. *Nature*, 400(6744):507–508, 1999.

[12] P. Bandyopadhyay. Large structure with a characteristic upstream interface in turbulent boundary layers. *Phys. Fluids*, 23(11):2326–2327, 1980.

[13] J. M. Barros and K. T. Christensen. Observations of turbulent secondary flows in a rough-wall boundary layer. *J. Fluid Mech.*, 748:R1, 2014.

[14] D. W. Bechert and M. Bartenwerfer. The viscous flow on surfaces with longitudinal ribs. *J. Fluid Mech.*, 206:105–129, 1989.

[15] D. W. Bechert, M. Bruse, W. Hage, J. G. T. Van der Hoeven, and G. Hoppe. Experiments on drag-reducing surfaces and their optimization with an adjustable geometry. *J. Fluid Mech.*, 338:59–87, 1997.

[16] H. O. G. Benschop and W. P. Breugem. Drag reduction by herringbone riblet texture in direct numerical simulations of turbulent channel flow. *J. Turbul.*, 18(8):717–759, 2017.

[17] R. F. Blackwelder and R. E. Kaplan. On the wall structure of the turbulent boundary layer. *J. Fluid Mech.*, 76(1):89–112, 1976.

[18] H. Blasius. Grenzschichten in Flüssigkeiten mit kleiner Reibung. *Zeitschrift für Math. und Phys.*, 56(1):1–37, 1908.

[19] P. Bradshaw. Turbulent secondary flows. *Annu. Rev. Fluid Mech.*, 19:53–74, 1987.

[20] C. Brossard, J. C. Monnier, P. Barricau, F. X. Vandernoot, Y. Le Sant, F. Champagnat, and G. Le Besnerais. Principles and applications of particle image velocimetry. *Aerosp. Lab J.*, 1:1–11, 2009.

[21] G. L. Brown and A. S. W. Thomas. Large structure in a turbulent boundary layer. *Phys. Fluids*, 20(10):S243–S252, 1977.

[22] J. D. Cameron, S. C. Morris, S. Bailey, and A. J. Smits. Effects of hot-wire length on the measurement of turbulent spectra in anisotropic flows. *Meas. Sci. Technol.*, 21(10):105407, 2010.

[23] J. J. Charonko and P. P. Vlachos. Estimation of uncertainty bounds for individual particle image velocimetry measurements from cross-correlation peak ratio. *Meas. Sci. Technol.*, 24(6):065301, 2013.

[24] H. Chen, F. Rao, X. Shang, D. Zhang, and I. Hagiwara. Biomimetic drag reduction study on herringbone riblets of bird feather. *J. Bionic Eng.*, 10(3):341–349, 2013.

[25] H. Chen, F. Rao, X. Shang, D. Zhang, and I. Hagiwara. Flow over bio-inspired 3D herringbone wall riblets. *Exp. Fluids*, 55:1698, 2014.

[26] H. Choi, P. Moin, and J. Kim. On the effect of riblets in fully developed laminar channel flows. *Phys. Fluids A Fluid Dyn.*, 3(8):1892–1896, 1991.

[27] H. Choi, P. Moin, and J. Kim. Direct numerical simulation of turbulent flow over riblets. *J. Fluid Mech.*, 255:503–539, 1993.

[28] K. Choi. Near-wall structure of a turbulent boundary layer with riblets. *J. Fluid Mech.*, 208:417–458, 1989.

[29] K. Christensen and Y. Wu. Characteristics of vortex organization in the outer layer of wall turbulence. In *Fourth Int. Symp. Turbul. Shear Flow Phenom.*, pages 1025–1030. Begel House Inc., 2005.

[30] K. T. Christensen and R. J. Adrian. Statistical evidence of hairpin vortex packets in wall turbulence. *J. Fluid Mech.*, 431:433–443, 2001.

[31] D. Chung, J. P. Monty, and N. Hutchins. Similarity and structure of wall turbulence with lateral wall shear stress variations. *J. Fluid Mech.*, 847:591–613, 2018.

[32] F. H. Clauser. Turbulent boundary layers in adverse pressure gradients. *J. Aeronaut. Sci.*, 21(2):91–108, 1954.

[33] E. R. Corino and R. S. Brodkey. A visual investigation of the wall region in turbulent flow. *J. Fluid Mech.*, 37(1):1–30, 1969.

[34] T. H. Cormen, C. E. Leiserson, R. L. Rivest, and C. Stein. *Introduction to algorithms*. The MIT Press, third edition, 2009.

[35] E. Coustols and V. Schmitt. Synthesis of experimental riblet studies in transonic conditions. In E. Coustols, editor, *Turbul. Control by Passiv. Means*, pages 123–140. 1990.

[36] C. M. de Silva, N. Hutchins, and I. Marusic. Uniform momentum zones in turbulent boundary layers. *J. Fluid Mech.*, 786:309–331, 2016.

[37] C. M. de Silva, J. Philip, K. Chauhan, C. Meneveau, and I. Marusic. Multiscale geometry and scaling of the turbulent-nonturbulent interface in high Reynolds number boundary layers. *Phys. Rev. Lett.*, 111(4):044501, 2013.

[38] B. Dean and B. Bhushan. Shark-skin surfaces for fluid-drag reduction in turbulent flow: a review. *Philos. Trans. R. Soc. A Math. Phys. Eng. Sci.*, 368(1929):4775–4806, 2010.

[39] J. C. del Álamo, J. Jiménez, P. Zandonade, and R. D. Moser. Self-similar vortex clusters in the turbulent logarithmic region. *J. Fluid Mech.*, 561:329–358, 2006.

[40] L. Djenidi, F. Anselmet, J. Liandrat, and L. Fulachier. Laminar boundary layer over riblets. *Phys. Fluids*, 6(9):2993–2999, 1994.

[41] G. Eitel-Amor, R. Örlü, P. Schlatter, and O. Flores. Hairpin vortices in turbulent boundary layers. *Phys. Fluids*, 27(2):025108, 2015.

[42] O. A. El-Samni, H. H. Chun, and H. S. Yoon. Drag reduction of turbulent flow over thin rectangular riblets. *Int. J. Eng. Sci.*, 45:436–454, 2007.

[43] P. Erhard, D. Etling, U. Müller, U. Riedel, K. R. Sreenivasan, and J. Warnatz. *Prandtl-essentials of fluid mechanics*, volume 158 of *Applied Mathematical Sciences*. Springer New York, third edition, 2010.

[44] L. P. Erm and P. N. Joubert. Low-Reynolds-number turbulent boundary layers. *J. Fluid Mech.*, 230:1–44, 1991.

[45] L. P. Erm, P. N. Joubert, and A. J. Smits. Low Reynolds number turbulent boundary layers on a smooth flat surface in a zero pressure gradient. In F. Durst, B. E. Launder, J. L. Lumley, F. W. Schmidt, and J. H. Whitelaw, editors, *Turbul. Shear Flows 5*, pages 186–196, Cornell University, Ithaca, New York, USA, 1985. Springer.

[46] R. E. Falco. Coherent motion in the outer region of turbulent boundary layers. *Phys. fluids*, 20(10):S124–S132, 1977.

[47] K. A. Flack, M. P. Schultz, and J. S. Connelly. Examination of a critical roughness height for outer layer similarity. *Phys. Fluids*, 19(9):095104, 2007.

[48] K. Fukagata, K. Iwamoto, and N. Kasagi. Contribution of Reynolds stress distribution to the skin friction in wall-bounded flows. *Phys. Fluids*, 14(11):L73–L76, 2002.

[49] R. García-Mayoral and J. Jiménez. Drag reduction by riblets. *Philos. Trans. R. Soc. A Math. Phys. Eng. Sci.*, 369(1940):1412–1427, 2011.

[50] R. García-Mayoral and J. Jiménez. Hydrodynamic stability and breakdown of the viscous regime over riblets. *J. Fluid Mech.*, 678:317–347, 2011.

[51] D. Goldstein, R. Handler, and L. Sirovich. Direct numerical simulation of turbulent flow over a modeled riblet covered surface. *J. Fluid Mech.*, 302:333–376, 1995.

[52] D. B. Goldstein and T. C. Tuan. Secondary flow induced by riblets. *J. Fluid Mech.*, 363:115–151, 1998.

[53] H. L. Grant. The large eddies of turbulent motion. *J. Fluid Mech.*, 4(2):149–190, 1958.

[54] G. R. Grek, V. V. Kozlov, S. V. Titarenko, and B. G. B. Klingmann. The influence of riblets on a boundary layer with embedded streamwise vortices. *Phys. Fluids*, 7(10):2504–2506, 1995.

[55] M. Guala, S. E. Hommema, and R. J. Adrian. Large-scale and very-large-scale motions in turbulent pipe flow. *J. Fluid Mech.*, 554:521–542, 2006.

[56] A. H. Haidari and C. R. Smith. The generation and regeneration of single hairpin vortices. *J. Fluid Mech.*, 277:135–162, 1994.

[57] M. R. Head and P. Bandyopadhyay. New aspects of turbulent boundary-layer structure. *J. Fluid Mech.*, 107:297–338, 1981.

[58] J. O. Hinze. Secondary currents in wall turbulence. *Phys. Fluids*, 10(9):S122–S125, 1967.

[59] J. O. Hinze. Experimental investigation on secondary currents in the turbulent flow through a straight conduit. *Appl. Sci. Res.*, 28(1):453–465, 1973.

[60] H. Q. Ho and M. Asai. Experimental study on the stability of laminar flow in a channel with streamwise and oblique riblets. *Phys. Fluids*, 30(2):024106, 2018.

[61] J. Hou, B. Vajdi Hokmabad, and S. Ghaemi. Three-dimensional measurement of turbulent flow over a riblet surface. *Exp. Therm. Fluid Sci.*, 85:229–239, 2017.

[62] S. Hoyas and J. Jiménez. Scaling of the velocity fluctuations in turbulent channels up to $Re_\tau = 2003$. *Phys. Fluids*, 18(1):011702, 2006.

[63] N. Hutchins, W. T. Hambleton, and I. Marusic. Inclined cross-stream stereo particle image velocimetry measurements in turbulent boundary layers. *J. Fluid Mech.*, 541:21–54, 2005.

[64] N. Hutchins and I. Marusic. Evidence of very long meandering features in the logarithmic region of turbulent boundary layers. *J. Fluid Mech.*, 579:1–28, 2007.

[65] N. Hutchins and I. Marusic. Large-scale influences in near-wall turbulence. *Philos. Trans. R. Soc. A Math. Phys. Eng. Sci.*, 365(1852):647–664, 2007.

[66] H. G. Hwang and J. H. Lee. Secondary flows in turbulent boundary layers over longitudinal surface roughness. *Phys. Rev. Fluids*, 3(1):014608, 2018.

[67] Y. Hwang and C. Cossu. Self-sustained process at large scales in turbulent channel flow. *Phys. Rev. Lett.*, 105(4):044505, 2010.

[68] J. Jiménez. Cascades in wall-bounded turbulence. *Annu. Rev. Fluid Mech.*, 44:27–45, 2012.

[69] J. Jiménez and A. Pinelli. The autonomous cycle of near-wall turbulence. *J. Fluid Mech.*, 389:335–359, 1999.

[70] K. Kamrin, M. Z. Bazant, and H. A. Stone. Effective slip boundary conditions for arbitrary periodic surfaces: the surface mobility tensor. *J. Fluid Mech.*, 658:409–437, 2010.

[71] K. Kevin, J. Monty, and N. Hutchins. Turbulent structures in a statistically three-dimensional boundary layer. *J. Fluid Mech.*, 859:543–565, 2019.

[72] K. Kevin, J. P. Monty, H. L. Bai, G. Pathikonda, B. Nugroho, J. M. Barros, K. T. Christensen, and N. Hutchins. Cross-stream stereoscopic particle image velocimetry of a modified turbulent boundary layer over directional surface pattern. *J. Fluid Mech.*, 813:412–435, 2017.

[73] K. Kevin, B. Nugroho, J. P. Monty, and N. Hutchins. Wall-parallel PIV measurements in turbulent boundary layers with highly directional surface roughness. In *19th Australas. Fluid Mech. Conf.*, Melbourne, Australia, 2014.

[74] H. T. Kim, S. J. Kline, W. C. Reynolds, and D. W. C. Reynolds. The production of turbulence near a smooth wall in a turbulent boundary layer. *J. Fluid Mech.*, 50(1):133–160, 1971.

[75] J. Kim. Physics and control of wall turbulence for drag reduction. *Philos. Trans. R. Soc. A Math. Phys. Eng. Sci.*, 369(1940):1396–1411, 2011.

[76] J. Kim and P. Moin. The structure of the vorticity field in turbulent channel flow. Part 2. Study of ensemble-averaged fields. *J. Fluid Mech.*, 162:339–363, 1986.

[77] K. C. Kim and R. J. Adrian. Very large-scale motion in the outer layer. *Phys. Fluids*, 11(2):417–422, 1999.

[78] S. J. Kline, W. C. Reynolds, F. A. Schraub, and P. W. Runstadler. The structure of turbulent boundary layers. *J. Fluid Mech.*, 30(4):741–773, 1967.

[79] K. Koeltzsch, A. Dinkelacker, and R. Grundmann. Flow over convergent and divergent wall riblets. *Exp. Fluids*, 33(2):346–350, 2002.

[80] L. S. G. Kovasznay, V. Kibens, and R. F. Blackwelder. Large-scale motion in the intermittent region of a turbulent boundary layer. *J. Fluid Mech.*, 41(2):283–325, 1970.

[81] A. G. Kravchenko, H. Choi, and P. Moin. On the relation of near-wall streamwise vortices to wall skin friction in turbulent boundary layers. *Phys. Fluids A Fluid Dyn.*, 5(12):3307–3309, 1993.

[82] A. Krein and G. Williams. Flightpath 2050: Europe's vision for aviation. In D. Knörzer and J. Szodruch, editors, *Innov. Sustain. Aviat. a Glob. Environ.*, pages 63–71, Madrid, Spain, 2012. IOS Press.

[83] P. A. Krogstad and R. A. Antonia. Structure of turbulent boundary layers on smooth and rough walls. *J. Fluid Mech.*, 277:1–21, 1994.

[84] J. Krüger, B. Habbel, and T. Erich. The history of Lufthansa Technik. Technical report, 2015.

[85] S. J. Lee and S. H. Lee. Flow field analysis of a turbulent boundary layer over a riblet surface. *Exp. Fluids*, 30(2):153–166, 2001.

[86] L. Li, S. Erfani, and C. Leckie. A pattern tree based method for mining conditional contrast patterns of multi-source data. In *2017 IEEE Int. Conf. Data Min. Work.*, pages 916–923, New Orleans, LA, 2017. IEEE.

[87] Q. Liu, S. Zhong, and L. Li. Reduction of pressure losses in a linear cascade using herringbone riblets. In *Proc. ASME Turbo Expo 2017 Turbomach. Tech. Conf. Expo.*, Charlotte, North Carolina, USA, 2017.

[88] S. S. Lu and W. W. Willmarth. Measurements of the structure of the Reynolds stress in a turbulent boundary layer. *J. Fluid Mech.*, 60(3):481–511, 1973.

[89] P. Luchini, F. Manzo, and A. Pozzi. Resistance of a grooved surface to parallel flow and cross-flow. *J. Fluid Mech.*, 228:87–109, 1991.

[90] Y. Ma, R. Mohebbi, M. M. Rashidi, and Z. Yang. Study of nanofluid forced convection heat transfer in a bent channel by means of lattice Boltzmann method. *Phys. Fluids*, 30(3):032001, 2018.

[91] I. Marusic. On the role of large-scale structures in wall turbulence. *Phys. Fluids*, 13(3):735–743, 2001.

[92] I. Marusic and W. D. C. Heuer. Reynolds number invariance of the structure inclination angle in wall turbulence. *Phys. Rev. Lett.*, 99(11):114504, 2007.

[93] I. Marusic, R. Mathis, and N. Hutchins. High Reynolds number effects in wall turbulence. *Int. J. Heat Fluid Flow*, 31(3):418–428, 2010.

[94] I. Marusic and J. P. Monty. Attached eddy model of wall turbulence. *Annu. Rev. Fluid Mech.*, 51:49–74, 2019.

[95] T. Medjnoun, C. Vanderwel, and B. Ganapathisubramani. Characteristics of turbulent boundary layers over smooth surfaces with spanwise heterogeneities. *J. Fluid Mech.*, 838:516–543, 2018.

[96] C. D. Meinhart and R. J. Adrian. On the existence of uniform momentum zones in a turbulent boundary layer. *Phys. Fluids*, 7(4):694–696, 1995.

[97] R. Mejia-Alvarez, J. M. Barros, and K. T. Christensen. Structural attributes of turbulent flow over a complex topography. In G. Venditti, J. L. Best, M. Church, and R. J. Hardy, editors, *Coherent Flow Struct. Earth's Surf.*, pages 25–41. John Wiley & Sons, Ltd, 2013.

[98] R. Mejia-Alvarez and K. T. Christensen. Low-order representations of irregular surface roughness and their impact on a turbulent boundary layer. *Phys. Fluids*, 22(1):015106, 2010.

[99] R. Mejia-Alvarez and K. T. Christensen. Wall-parallel stereo particle-image velocimetry measurements in the roughness sublayer of turbulent flow overlying highly irregular roughness. *Phys. Fluids*, 25(11):115109, 2013.

[100] R. Mohebbi, H. Lakzayi, N. A. C. Sidik, and W. M. A. A. Japar. Lattice Boltzmann method based study of the heat transfer augmentation associated with Cu/water nanofluid in a channel with surface mounted blocks. *Int. J. Heat Mass Transf.*, 117:425–435, 2018.

[101] R. Mohebbi, M. M. Rashidi, M. Izadi, N. A. C. Sidik, and H. W. Xian. Forced convection of nanofluids in an extended surfaces channel using lattice Boltzmann method. *Int. J. Heat Mass Transf.*, 117:1291–1303, 2018.

[102] P. Moin and J. Kim. The structure of the vorticity field in turbulent channel flow. Part 1. Analysis of instantaneous fields and statistical correlations. *J. Fluid Mech.*, 155:441–464, 1985.

[103] J. P. Monty, J. A. Stewart, R. C. Williams, and M. S. Chong. Large-scale features in turbulent pipe and channel flows. *J. Fluid Mech.*, 589:147–156, 2007.

[104] J. Murlis, H. M. Tsai, and P. Bradshaw. The structure of turbulent boundary layers at low Reynolds numbers. *J. Fluid Mech.*, 122:13–56, 1982.

[105] S. Nakagawa and T. J. Hanratty. Particle image velocimetry measurements of flow over a wavy wall. *Phys. Fluids*, 13(11):3504–3507, 2001.

[106] R. Narasimha and S. N. Prasad. Leading edge shape for flat plate boundary layer studies. *Exp. Fluids*, 17(5):358–360, 1994.

[107] V. K. Natrajan, Y. Wu, and K. T. Christensen. Spatial signatures of retrograde spanwise vortices in wall turbulence. *J. Fluid Mech.*, 574:155–167, 2007.

[108] I. Nezu and H. Nakagawa. Cellular secondary currents in straight conduit. *J. Hydraul. Eng.*, 110(2):173–193, 1984.

[109] J. H. Ng, R. K. Jaiman, and T. T. Lim. Interaction dynamics of longitudinal corrugations in Taylor-Couette flows. *Phys. Fluids*, 30(9):093601, 2018.

[110] V. Nikora, F. Ballio, S. Coleman, and D. Pokrajac. Spatially averaged flows over mobile rough beds: definitions, averaging theorems, and conservation equations. *J. Hydraul. Eng.*, 139(8):803–811, 2013.

[111] V. I. Nikora, T. Stoesser, S. M. Cameron, M. Stewart, K. Papadopoulos, P. Ouro, R. McSherry, A. Zampiron, I. Marusic, and R. A. Falconer. Friction factor decomposition for rough-wall flows: theoretical background and application to open-channel flows. *J. Fluid Mech.*, 872:626–664, 2019.

[112] B. Nugroho, N. Hutchins, and J. P. Monty. Effects of diverging and converging roughness on turbulent boundary layers. In *18th Australas. Fluid Mech. Conf.*, Launceston, Australia, 2012.

[113] B. Nugroho, N. Hutchins, and J. P. Monty. Large-scale spanwise periodicity in a turbulent boundary layer induced by highly ordered and directional surface roughness. *Int. J. Heat Fluid Flow*, 41:90–102, 2013.

[114] B. Nugroho, Kevin, J. Monty, N. Hutchins, and E. Gnanamanickam. Roll-modes generated in turbulent boundary layers with passive surface modifications. In

52nd Aerosp. Sci. Meet., pages AIAA 2014–0197, National Harbor, Maryland, 2014.

[115] B. Nugroho, V. Kulandaivelu, Z. Harun, N. Hutchins, and J. P. Monty. An investigation into the effects of highly directional surface roughness on turbulent boundary layers. In *17th Australas. Fluid Mech. Conf.*, Auckland, New Zealand, 2010.

[116] G. R. Offen and S. J. Kline. Combined dye-streak and hydrogen-bubble visual observations of a turbulent boundary layer. *J. Fluid Mech.*, 62(2):223–239, 1974.

[117] G. R. Offen and S. J. Kline. A proposed model of the bursting process in turbulent boundary layers. *J. Fluid Mech.*, 70(2):209–228, 1975.

[118] K. Okabayashi, K. Hirai, S. Takeuchi, and T. Kajishima. Direct numerical simulation of turbulent flow above zigzag riblets. *AIP Adv.*, 8(10):105227, 2018.

[119] R. L. Panton. Overview of the self-sustaining mechanisms of wall turbulence. *Prog. Aerosp. Sci.*, 37(4):341–383, 2001.

[120] S. Park and J. M. Wallace. Flow alteration and drag reduction by riblets in a turbulent boundary layer. *AIAA J.*, 32(1):31–38, 1994.

[121] H. J. Perkins. The formation of streamwise vorticity in turbulent flow. *J. Fluid Mech.*, 44(4):721–740, 1970.

[122] A. E. Perry and J. D. Li. Experimental support for the attached-eddy hypothesis in zero-pressure-gradient turbulent boundary layers. *J. Fluid Mech.*, 218:405, 1990.

[123] A. E. Perry, T. T. Lim, and E. W. Teh. A visual study of turbulent spots. *J. Fluid Mech.*, 104:387–405, 1981.

[124] A. K. Praturi and R. S. Brodkey. A stereoscopic visual study of coherent structures in turbulent shear flow. *J. Fluid Mech.*, 89(2):251–272, 1978.

[125] C. J. A. Pulles, K. K. Prasad, and F. T. M. Nieuwstadt. Turbulence measurements over longitudinal micro-grooved surfaces. *Appl. Sci. Res.*, 46(3):197–208, 1989.

[126] P. Quan, S. Zhong, Q. Liu, and L. Li. Attenuation of flow separation using herringbone riblets at $M_\infty = 5$. *AIAA J.*, 57(1):142–152, 2019.

[127] S. Raayai-Ardakani and G. H. McKinley. Drag reduction using wrinkled surfaces in high Reynolds number laminar boundary layer flows. *Phys. Fluids*, 29(9):093605, 2017.

[128] S. Raayai-Ardakani and G. H. McKinley. Geometric optimization of riblet-textured surfaces for drag reduction in laminar boundary layer flows. *Phys. Fluids*, 31(5):053601, 2019.

[129] M. Raffel, C. E. Willert, F. Scarano, C. J. Kähler, S. T. Wereley, and J. Kompenhans. *Particle image velocimetry*. Springer International Publishing, third edition, 2018.

[130] S. Rawat, C. Cossu, Y. Hwang, and F. Rincon. On the self-sustained nature of large-scale motions in turbulent Couette flow. *J. Fluid Mech.*, 782:515–540, 2015.

[131] J. Reneaux. Overview on drag reduction technologies for civil transport aircraft. In P. Neittaanmäki, T. Rossi, S. Korotov, E. Oñate, J. Périaux, and D. Knörzer, editors, *Eur. Congr. Comput. Methods Appl. Sci. Eng. (ECCOMAS 2004)*, Jyväskylä, Finland, 2004.

[132] J. P. Robert. Drag reduction: an industrial challenge. Technical report, 1992.

[133] S. K. Robinson. Coherent motions in the turbulent boundary layer. *Annu. Rev. Fluid Mech.*, 23:601–639, 1991.

[134] W. S. Saric, A. L. Carpenter, and H. L. Reed. Passive control of transition in three-dimensional boundary layers, with emphasis on discrete roughness elements. *Philos. Trans. R. Soc. A Math. Phys. Eng. Sci.*, 369(1940):1352–1364, 2011.

[135] P. Schlatter, Q. Li, G. Brethouwer, A. V. Johansson, and D. S. Henningson. Simulations of spatially evolving turbulent boundary layers up to $Re_\theta = 4300$. *Int. J. Heat Fluid Flow*, 31(3):251–261, 2010.

[136] P. Schlatter, R. Örlü, Q. Li, G. Brethouwer, A. V. Johansson, P. H. Alfredsson, and D. S. Henningson. Progress in simulations of turbulent boundary layers. In

J. K. Eaton and S. Tavoularis, editors, *Seventh Int. Symp. Turbul. Shear Flow Phenom.*, pages 1–10, Ottawa, 2011.

[137] A. J. Smits, B. J. McKeon, and I. Marusic. High-Reynolds number wall turbulence. *Annu. Rev. Fluid Mech.*, 43:353–375, 2011.

[138] P. R. Spalart. Direct simulation of a turbulent boundary layer up to $Re_\theta = 1410$. *J. Fluid Mech.*, 187:61–98, 1988.

[139] P. R. Spalart and J. D. McLean. Drag reduction: enticing turbulence, and then an industry. *Philos. Trans. R. Soc. A Math. Phys. Eng. Sci.*, 369(1940):1556–1569, 2011.

[140] V. Stenzel, Y. Wilke, and W. Hage. Drag-reducing paints for the reduction of fuel consumption in aviation and shipping. *Prog. Org. Coatings*, 70(4):224–229, 2011.

[141] T. Stoesser, R. McSherry, and B. Fraga. Secondary currents and turbulence over a non-uniformly roughened open-channel bed. *Water*, 7(9):4896–4913, 2015.

[142] A. Stroh, Y. Hasegawa, J. Kriegseis, and B. Frohnapfel. Secondary vortices over surfaces with spanwise varying drag. *J. Turbul.*, 17(12):1142–1158, 2016.

[143] Y. Suzuki and N. Kasagi. Turbulent drag reduction mechanism above a riblet surface. *AIAA J.*, 32(9):1781–1790, 1994.

[144] G. I. Taylor. The spectrum of turbulence. *Proc. R. Soc. A Math. Phys. Eng. Sci.*, 164(919):476–490, 1938.

[145] T. Theodorsen. Mechanism of turbulence. In *Proc. Mid-western Conf. Fluid Mech.*, Columbus, OH, 1952.

[146] H. Tian, J. Zhang, N. Jiang, and Z. Yao. Effect of hierarchical structured superhydrophobic surfaces on coherent structures in turbulent channel flow. *Exp. Therm. Fluid Sci.*, 69:27–37, 2015.

[147] C. D. Tomkins and R. J. Adrian. Spanwise structure and scale growth in turbulent boundary layers. *J. Fluid Mech.*, 490:37–74, 2003.

[148] A. A. Townsend. Equilibrium layers and wall turbulence. *J. Fluid Mech.*, 11(1):97–120, 1961.

[149] A. A. Townsend. *The structure of turbulent shear flow*. Cambridge University Press, Cambridge, UK, second edition, 1976.

[150] S. Tullis and A. Pollard. The time dependent flow over V- and U-groove riblets of different sizes. *Phys. Fluids*, 6(3):1310–1314, 1994.

[151] S. Türk, G. Daschiel, A. Stroh, Y. Hasegawa, and B. Frohnapfel. Turbulent flow over superhydrophobic surfaces with streamwise grooves. *J. Fluid Mech.*, 747:186–217, 2014.

[152] C. Vanderwel and B. Ganapathisubramani. Effects of spanwise spacing on large-scale secondary flows in rough-wall turbulent boundary layers. *J. Fluid Mech.*, 774:R2, 2015.

[153] A. Vidal, H. M. Nagib, P. Schlatter, and R. Vinuesa. Secondary flow in spanwise-periodic in-phase sinusoidal channels. *J. Fluid Mech.*, 851:288–316, 2018.

[154] R. Vinuesa and R. Örlü. Measurement of wall-shear stress. In S. Discetti and A. Ianiro, editors, *Exp. Aerodyn.*, pages 393–428. CRC Press, 2017.

[155] P. R. Viswanath. Aircraft viscous drag reduction using riblets. *Prog. Aerosp. Sci.*, 38(6-7):571–600, 2002.

[156] R. J. Volino, M. P. Schultz, and K. A. Flack. Turbulence structure in rough- and smooth-wall boundary layers. *J. Fluid Mech.*, 592:263–293, 2007.

[157] P. Vukoslavcevic, J. M. Wallace, and J. L. Balint. Viscous drag reduction using streamwise-aligned riblets. *AIAA J.*, 30(4):1119–1122, 1992.

[158] J. M. Wallace, H. Eckelmann, and R. S. Brodkey. The wall region in turbulent shear flow. *J. Fluid Mech.*, 54(1):39–48, 1972.

[159] M. Walsh. Turbulent boundary layer drag reduction using riblets. In *20th Aerosp. Sci. Meet.*, pages AIAA 82–0169, Orlando, Florida, 1982. American Institute of Aeronautics and Astronautics.

[160] M. Walsh and A. Lindemann. Optimization and application of riblets for turbulent drag reduction. In *22nd Aerosp. Sci. Meet.*, pages AIAA 84–0347, Reno, Nevada, 1984.

[161] M. J. Walsh. Riblets as a viscous drag reduction technique. *AIAA J.*, 21(4):485–486, 1983.

[162] Z. Wang and N. Cheng. Secondary flows over artificial bed strips. *Adv. Water Resour.*, 28(5):441–450, 2005.

[163] Z. Wang and N. Cheng. Time-mean structure of secondary flows in open channel with longitudinal bedforms. *Adv. Water Resour.*, 29(11):1634–1649, 2006.

[164] F. M. White. *Viscous fluid flow*. McGraw-Hill, third edition, 2006.

[165] O. J. H. Williams, D. Sahoo, M. L. Baumgartner, and A. J. Smits. Experiments on the structure and scaling of hypersonic turbulent boundary layers. *J. Fluid Mech.*, 834:237–270, 2018.

[166] D. Willingham, W. Anderson, K. T. Christensen, and J. M. Barros. Turbulent boundary layer flow over transverse aerodynamic roughness transitions: Induced mixing and flow characterization. *Phys. Fluids*, 26(2):025111, 2014.

[167] X. Wu and P. Moin. Direct numerical simulation of turbulence in a nominally zero-pressure-gradient flat-plate boundary layer. *J. Fluid Mech.*, 630:5–41, 2009.

[168] X. Wu and P. Moin. Forest of hairpins in a low-Reynolds-number zero-pressure-gradient flat-plate boundary layer. *Phys. Fluids*, 21(9):091106, 2009.

[169] Y. Wu and K. T. Christensen. Population trends of spanwise vortices in wall turbulence. *J. Fluid Mech.*, 568:55–76, 2006.

[170] Y. Wu and K. T. Christensen. Outer-layer similarity in the presence of a practical rough-wall topography. *Phys. Fluids*, 19(8):085108, 2007.

[171] Y. Wu and K. T. Christensen. Spatial structure of a turbulent boundary layer with irregular surface roughness. *J. Fluid Mech.*, 655:380–418, 2010.

[172] F. Xu, Z. Gao, X. Ming, L. Xia, Y. Wang, W. Sun, and R. Ma. The optimization for the backward-facing step flow control with synthetic jet based on experiment. *Exp. Therm. Fluid Sci.*, 64:94–107, 2015.

[173] F. Xu, S. Zhong, and S. Zhang. Vortical structures and development of laminar flow over convergent-divergent riblets. *Phys. Fluids*, 30(5):051901, 2018.

[174] F. Xu, S. Zhong, and S. Zhang. Vortical structures of laminar boundary layer over convergent-divergent riblets with spanwise height variations. In *21st Australas. Fluid Mech. Conf.*, Adelaide, Australia, 2018.

[175] F. Xu, S. Zhong, and S. Zhang. Statistical analysis of vortical structures in turbulent boundary layer over directional grooved surface pattern with spanwise heterogeneity. *Phys. Fluids*, 31(8):085110, 2019.

[176] N. Yadav, S. W. Gepner, and J. Szumbarski. Instability in a channel with grooves parallel to the flow. *Phys. Fluids*, 29(8):084104, 2017.

[177] N. Yadav, S. W. Gepner, and J. Szumbarski. Flow dynamics in longitudinally grooved duct. *Phys. Fluids*, 30(10):104105, 2018.

[178] J. Yang and W. Anderson. Numerical study of turbulent channel flow over surfaces with variable spanwise heterogeneities: topographically-driven secondary flows affect outer-layer similarity of turbulent length scales. *Flow, Turbul. Combust.*, 100(1):1–17, 2018.

[179] S. Zhang and S. Zhong. Experimental investigation of flow separation control using an array of synthetic jets. *AIAA J.*, 48(3):611–623, 2010.

[180] S. Zhang and S. Zhong. Turbulent flow separation control over a two-dimensional ramp using synthetic jets. *AIAA J.*, 49(12):2637–2649, 2011.

[181] S. Zhong and S. Zhang. Further examination of the mechanism of round synthetic jets in delaying turbulent flow separation. *Flow, Turbul. Combust.*, 91(1):177–208, 2013.

[182] J. Zhou, R. J. Adrian, S. Balachandar, and T. M. Kendall. Mechanisms for generating coherent packets of hairpin vortices in channel flow. *J. Fluid Mech.*, 387:353–396, 1999.